UNIVERSITY
OF OSLO

Faculty of Mathematics and Natural Sciences

Justyna Czekirda

Ground thermal regime and periglacial slope processes in Norway and Iceland

2024

UiO : University of Oslo

Justyna Czekirda

GROUND THERMAL REGIME AND PERIGLACIAL SLOPE PROCESSES IN NORWAY AND ICELAND

Thesis submitted for the degree of Philosophiae Doctor

Department of Geosciences

Faculty of Mathematics and Natural Sciences

2024

Series of dissertations submitted to the
Faculty of Mathematics and Natural Sciences, University of Oslo
No. 2750

ISSN 1501-7710

Cover: UiO.
Print production: Graphic Centre, University of Oslo.

ABSTRACT

The ground thermal regime substantially influences geomorphological processes operating in periglacial environments, although the connection may not be straightforward. Recent studies provide more evidence for enhanced rockfall activity and accelerating rockslides in terrain underlain by thawing permafrost. In contrast, there is an ongoing debate on the periglacial imprint for long-term landscape evolution. Furthermore, the concept of "frost cracking window", which refers to an optimal ground temperature range for frost weathering, was established over two decades ago to describe in a simple way the connection between frost weathering and ground temperature. Therefore, knowledge of the ground thermal regime is essential in the geomorphological context on both short- and long-term scales. This dissertation employs permafrost modelling, modelling of frost weathering, space-borne and ground-based remote sensing approaches as the main methods to investigate various concepts within cold-region geomorphology.

Ground temperature is modelled using a one-dimensional heat flow model for Iceland and a two-dimensional heat flow model for rock walls in Norway. This modelling showed that Iceland's shallow and warm permafrost and Norway's rock wall permafrost are susceptible to the atmospheric warming that has been lasting since the 1980s. The number of cells with simulated permafrost in Iceland decreased by approximately 40 % between the 1980s and 2010–2016. The average warming of Norway's rock walls has been 0.2 °C per decade at 20 m depth since the 1980s. Recent permafrost thawing in Norway and Iceland may have consequences for slope stability, rockslide and rock glacier dynamics, and lead to the disappearance of palsas.

Sites with enhanced frost weathering were identified using the two-dimensional modelling of frost cracking performed for steep rock walls in Jotunheimen, southern Norway. Such sites are typically found between the rock wall and melting ice sheet or glaciers, as well as where the snow depth changes abruptly, resulting in large thermal gradients. Therefore, bedrock may be gradually weakened by segregation ice weathering during deglaciation, in addition to the effects of glacial debuttressing. The Younger Dryas climate was suitable for intense segregation ice weathering in the coastal areas of Norway and Iceland, according to the frost cracking modelling conducted using a one-dimensional approach. This implies that high rates of segregation ice weathering may have contributed to the formation of talus-derived rock glaciers. The enhanced segregation ice weathering at that time also compares favourably to previous studies on the timing of rockfall accumulations in Norway.

Furthermore, short-term and long-term rock wall retreat rates are estimated in the Kjelen rock wall, southern Norway, using point cloud differencing and sediment volume estimation for a nearby ice-cored moraine. The average rate of rock wall retreat since deglaciation was only two times greater than the current average rate for the study period, which was limited though to only one year. Most of the detected rockfalls occurred during summer, and most of the material was lost from frequently shaded rock wall sections.

In addition, slow mass movements are measured using satellite radar interferometry for the Juvflye hillslope, southern Norway. The observed displacements are related to the solifluction processes, as demonstrated by the high correlation between the temporal variations in displacement and the thaw depth from borehole temperatures. The distribution of active solifluction areas was primarily governed by ground temperature and a vegetation index from multispectral satellite images, with increasing activity for the lowest ground temperatures and sparsely vegetated areas.

The presence of ground ice has a profound impact on geomorphological processes, which slowly contribute to the long-term landscape denudation in Norway and Iceland. However, the contribution of periglacial processes to the development of the high-elevation, low-relief surfaces in southern Norway remains highly uncertain.

ACKNOWLEDGEMENTS

First and foremost, I would like to express my deepest gratitude to my main supervisor Bernd Etzelmüller (University of Oslo, UiO) for the guidance during my PhD and for inspiring many of the ideas presented in this work. Bernd has been very enthusiastic about my work and open-minded about my scientific ideas. Bernd always seemed to find time to answer my emails, despite his very busy schedule. As the section and department head, Bernd has also been very understanding of my personal issues, when I really needed extra time off. I also want to thank my subsidiary supervisor Andreas Kääb (UiO), who helped me especially with InSAR and other remote sensing topics. Furthermore, I want to thank Sebastian Westermann (UiO) for helping me with the various snow and permafrost modelling aspects. I am also very grateful to Alan Rempel (University of Oregon) for his scientific input to the third paper.

Furthermore, I acknowledge that Trond Eiken (UiO) collected point clouds from the Kjelen rock wall using terrestrial laser scanning during several summers, the last time even without me as his field assistant. Trond also conducted the additional differential GNSS measurements in the field and did initial post-processing of the LIDAR point clouds before sending them to me. I also want to thank Luc Girod (UiO), who collected drone imagery from the Kjelen rock wall in August 2021. I also want to acknowledge the co-authors of the second paper, Ketil Isaksen from the Meteorological Institute of Norway and Florence Magnin (EDYTEM, Université Savoie Mont-Blanc, CNRS). I am also grateful to Lene Kristiansen and Pierrick Sylvain Nicolet (both the Norwegian Water Resources and Energy Directorate), who gave me feedback on the initial point cloud processing for rockfall source detection. Other acknowledgements are included in the published papers.

A special thanks is to my fiancé for always believing in me and his unwavering support throughout my whole PhD. I also want to thank my friends and family for their support.

LIST OF PAPERS

PAPER I

Czekirda, J., Westermann, S., Etzelmüller, B., and Jóhannesson, T. (2019). Transient Modelling of Permafrost Distribution in Iceland. *Frontiers in Earth Science*, 7. doi: 10.3389/feart.2019.00130

PAPER II

Czekirda, J., Etzelmüller, B., Westermann, S., Isaksen, K., and Magnin, F. (2023). Post-Little Ice Age rock wall permafrost evolution in Norway. *The Cryosphere*, 17, 2725–2754. doi: 10.5194/tc-17-2725-2023

PAPER III

Czekirda, J., Rempel, A. W., Etzelmüller, B., and Westermann, S. (2024). Spatiotemporal variations in frost cracking measures in two dimensions: A case study for rock walls in Jotunheimen, southern Norway. *Geomorphology*, 453, 109112. doi: 10.1016/j.geomorph.2024.109112

NOMENCLATURE

ABBREVIATIONS

AOI	Area Of Interest
DEM	Digital Elevation Model
HTM	Holocene Thermal Maximum
InSAR	SAR Interferometry
LIA	Little Ice Age
LIDAR	Light Detection and Ranging
LOS	Line Of Sight
M3C2	Multiscale Model to Model Cloud Comparison
MintPy	Miami INsar Time-series software in PYthon
PB	Preboreal
SAR	Synthetic Aperture Radar
YD	Younger Dryas

GREEK CHARACTERS

α	Power-law exponent (frost damage model)	[–]
Δn	Porosity change (frost damage model)	[–]
ΔT	Undercooling $\Delta T = T_m - T$	[°C]
ΔT_c	Undercooling for frost cracking	[°C]
κ	Thermal diffusivity	[$\mathrm{mm^2\ s^{-1}}$]
λ	Depth-integrated porosity change (frost damage measure)	[mm]
∇T	Temperature gradient	[$\mathrm{°C\ m^{-1}}$]
ρ_i	Ice density	$920\ \mathrm{kg\ m^{-3}}$
θ_j	Volumetric content of a soil component j	[–]
θ_{inc}	Incidence angle	[°]
θ_{slp}	Slope angle	[°]

LATIN CHARACTERS

A	Annual amplitude of surface temperature	[°C]
C	Volumetric heat capacity	[J m^{-3} K^{-1}]
c	Initial crack radius	[cm]
C_{eff}	Effective volumetric heat capacity	[J m^{-3} K^{-1}]
D	Diffusivity for frost weathering	[mm^2 s^{-1}]
d	Swelling depth (frost damage measure)	[m]
FCW	Frost cracking window	[°C]
GST	Ground surface temperature	[°C]
GT	Ground temperature	[°C]
K	Thermal conductivity	[W m^{-1} K^{-1}]
k_0	Unfrozen permeability	[m^2]
K_{IC}	Mode I critical stress intensity factor (fracture toughness)	[Pa $m^{1/2}$]
L	Specific latent heat of fusion of water	334 kJ kg^{-1}
$MAAT$	Mean annual air temperature	[°C]
$MAGST$	Mean annual ground surface temperature	[°C]
MTA	Maximum triangle area	[m^2]
$NDVI$	Normalised Difference Vegetation Index	[–]
nF	Freezing n-factor	[–]
nT	Thawing n-factor	[–]
r^2	Coefficient of determination	[–]
$RMSE$	Root mean square error	Various units
SAT	Surface air temperature	[°C]
SO	Surface offset	[°C]
T	Temperature	[°C]
t	Time	[s]
T_m	Normal bulk melting temperature	273.15 K
$TTOP$	Mean annual temperature at the top of permafrost	[°C]
TWI	Topographic Wetness Index	[–]
z	Depth	[m]

CONTENTS

I OVERVIEW

II PAPERS

III APPENDIX

I

OVERVIEW

1. INTRODUCTION

1.1 MOTIVATION

The term "periglacial" refers to "cold, nonglacial" areas in the geographical, climatic and geomorphological sense, with the latter concerning environments with distinctive landform and landscape evolution that is significantly influenced by frost action and sometimes also by permafrost occurrence (Ballantyne, 2018). Even though azonal geomorphological processes are common in periglacial environments, such processes are conditioned by seasonal and perennial ground ice in these areas (Berthling and Etzelmüller, 2011). Permafrost is a subsurface thermal phenomenon defined as ground that remains at or below 0 °C for at least two consecutive years (Associate Committee on Geotechnical Research, 1988). Modelling estimates suggest that contemporary permafrost underlies ~15 % of the exposed land area in the Northern Hemisphere (Figure 1.1; Obu *et al.*, 2019).

Permafrost temperature serves as a climate indicator by providing an attenuated signal of surface temperature variability ranging from annual-scale variations at a few metres depth to centennial-scale variations at several hundred metres depth (Lachenbruch and Marshall, 1986). The Intergovernmental Panel on Climate Change has identified permafrost as one of the cryospheric components vulnerable to both rising atmospheric temperatures and changing precipitation (Vaughan *et al.*, 2013). In polar and mountain regions, permafrost has been warming since around 1980 at varying regional rates, typically 0.2–0.8 °C per decade (Smith *et al.*, 2022). Although local factors like vegetation and snow cover may influence permafrost response to a warming environment, permafrost warming trends are consistent with air temperature trends (Smith *et al.*, 2022). As a result of the likely continuation of climate warming and seasonal snow cover changes, climate projection scenarios indicate shrinkage of the near-surface permafrost (within 3–4 m) extent by between 24 ± 16 % (RCP2.6) and 69 ± 20 % (RCP8.5) by 2100 (IPCC, 2019). Permafrost is one of the largest so-called vulnerable carbon pools, storing two times more organic carbon than the entire atmosphere holds presently (Schuur *et al.*, 2008). Permafrost degradation may further amplify atmospheric warming as a positive climate feedback mechanism through the emission of greenhouse gases since microbial decomposition that follows thawing of the organic-rich permafrost releases radiatively active gases such as carbon dioxide (CO_2), methane (CH_4) (Zimov *et al.*, 2006; Schuur *et al.*, 2009; Lee *et al.*, 2010; Schaefer *et al.*, 2011) and nitrous oxide (N_2O) (Marushchak *et al.*, 2011).

With increasing air and ground temperatures (*GTs*), arctic and alpine regions may experience rapid geomorphological changes, with the largest rates since the last glacial period (Ballantyne, 2018). The presence of permafrost may delay erosive processes by keeping sediments frozen and unavailable for further transport (Etzelmüller and Frauenfelder, 2009). The scale at which such delay occurs may perhaps be even up to millennia (Hilger *et al.*, 2021), if permafrost persists throughout

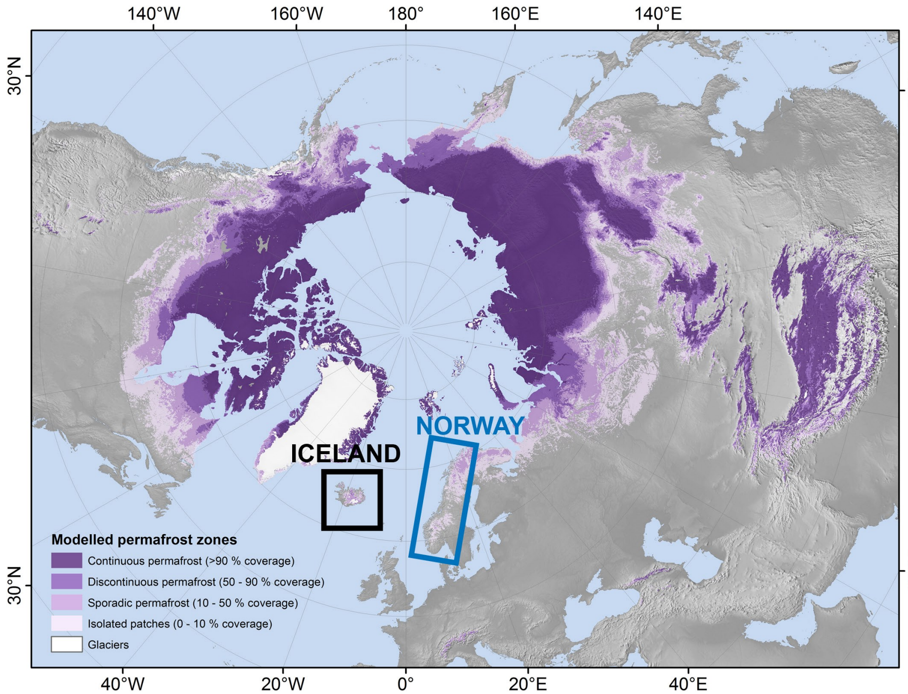

Figure 1.1: Modelled permafrost zones in the Northern Hemisphere. Modified from Obu *et al.* (2019).

long periods. However, permafrost may also facilitate frost processes and increase sediment transport during permafrost degradation (Etzelmüller and Frauenfelder, 2009). In the European Alps, inventories suggest that rockfalls and rock avalanches from permafrost rock walls have increased in frequency since the 1990s and 2000s, particularly at the lower permafrost limit (Ravanel and Deline, 2011; Fischer *et al.*, 2012). Unusual rockfall activity in the European Alps during the extremely hot summers of 2003 and 2015 was most likely caused by permafrost degradation (Gruber *et al.*, 2004; Ravanel *et al.*, 2017). It has already been reported with high confidence that the slope stability has decreased as a result of permafrost thaw and glacier retreat, and the decreasing slope stability is projected to continue (IPCC, 2019). Ice-filled fractures are supposed to stabilise the permafrost-underlain slopes (e.g. Dramis *et al.*, 1995) and thawing may lead to a significant drop in rock strength (Krautblatter *et al.*, 2013). Frost weathering processes contribute to the generation of weakness planes or widening fractures in frost-affected rocks; hence, they gradually damage permafrost bedrock over timescales up to millennia (Gruber and Haeberli, 2007; Matsuoka and Murton, 2008; Krautblatter *et al.*, 2013). The ground thermal regime is an important factor for periglacial weathering, as shown in other studies relating segregation ice weathering to climate (Anderson, 1998; Hales and Roering, 2007; Rempel *et al.*, 2016).

Permafrost thaw-related instabilities have also occurred in Iceland and Norway. Ice-cemented debris within the landslide deposits was observed for the first time in Iceland in 2011, and two similar events have subsequently been reported in other parts of the country (Saemundsson *et al.*, 2018). Permafrost warming has also likely influenced the dynamics of several slope failures in Norway, e.g. the Gámanjunni-3 instability in Northern Norway that accelerated recently (Böhme *et al.*, 2019; Etzelmüller *et al.*, 2022), the Polvartinden rock avalanche in Northern Norway in 2008 (Frauenfelder *et al.*, 2018) or possibly also Veslemannen in 2019 (Kristensen *et al.*, 2021). Permafrost had likely stabilised rock slopes in Norway for several millennia following deglaciation (Hilger *et al.*, 2021). According to Magnin *et al.*'s (2019) estimation, discontinuous and continuous permafrost underlies 11 % of Norway's potentially unstable slopes. The recent landslides in Iceland and Norway that were induced by permafrost thaw mostly occurred in unpopulated areas; however, similar types of landslides may occur in the future in other regions, thus posing a risk to infrastructure, inhabitants, grazing animals, or tourists.

Since permafrost is a subsurface phenomenon, mapping of permafrost distribution and its depth, as well as investigating permafrost changes during ongoing climate change, are challenging. Boreholes provide valuable information about rising permafrost temperatures at various sites; however, it is impossible to install a dense GT monitoring network across the world, and hence alternative methods have to be used. The assessment of permafrost conditions is further complicated by the highly heterogeneous permafrost distribution in mountains. It is even more challenging to investigate GT changes in steep rock walls, where drilling a borehole is almost impossible, although it has been accomplished at very few locations (e.g. Magnin *et al.*, 2017). Permafrost modelling offers the possibility to assess permafrost distribution at various spatial and temporal scales (e.g. Henry and Smith, 2001; Gruber, 2012; Jafarov *et al.*, 2012; Westermann *et al.*, 2015b; Gisnås *et al.*, 2017; Myhra *et al.*, 2017) and such an approach is used in this work. The knowledge of contemporary and paleo-permafrost distributions allows for various analyses. The ground thermal regime has a large influence on geomorphological processes, although its role is not always understood. In this thesis, I focus especially on the connection between the ground thermal regime and frost weathering, together with periglacial slope processes such as rockfalls and solifluction.

1.2 AIM AND OBJECTIVES

The research aim of this thesis is to **gain an increased understanding of the impact of the ground thermal regime on the geomorphological processes in mountain environments on both short- and long-term scales, with examples from Norway and Iceland.** To achieve this aim, the following objectives are set:

1. Provide a regional permafrost map for the gentle terrain in Iceland for the period 1960–2016 and analyse the spatiotemporal changes in permafrost extent (objective achieved in Paper I)
2. Investigate the spatiotemporal variations in GTs in steep rock walls in Norway on an inter-decadal scale (objective achieved in Paper II)
3. Evaluate the postglacial spatiotemporal distribution of frost weathering in a rock wall (objective achieved in Paper III)
4. Provide a regional map of frost weathering potential for rock walls in Norway and Iceland, together with an analysis of the postglacial variations in frost weathering potential for talus-derived rock glaciers (unpublished; objective achieved in Sections 4.4 and 5.4)
5. Estimate short- and long-term rock wall retreat rates and evaluate rockfall sources with regard to potential incoming shortwave radiation (unpublished; objective achieved in Sections 4.5 and 5.5)

6. Measure very slow displacements on a periglacial hillslope and analyse the temporal displacements, together with identification of the most important environmental variables governing spatial activity (unpublished; objective achieved in Sections 4.6 and 5.6)

I address the main goals by conducting numerical modelling, using or conducting field measurements, and employing remote sensing techniques. Numerical modelling of GT and frost cracking potential is conducted in both one and two dimensions for both Norway and Iceland at various spatial and temporal scales. Collected field measurements include temperature data from boreholes in Iceland and Norway, together with multi-temporal LIDAR point clouds and drone imagery from a rock wall in Jotunheimen, southern Norway. The collected terrestrial LIDAR data is further used in the remote sensing technique of point cloud differencing to estimate the short-term rock wall retreat rates. Furthermore, space-borne differential synthetic aperture radar interferometry is used to measure very slow displacement rates on a hillslope in Jotunheimen, southern Norway. Finally, statistical modelling is employed to evaluate spatial patterns of activity on a periglacial slope.

1.3 OUTLINE

Part I Overview

Chapter 1 Introduction – This chapter provides background information on permafrost and its vulnerability under climate change. The aim of this work and the research objectives are defined.

Chapter 2 Scientific background – This chapter presents the state of knowledge concerning the modelling of permafrost and frost weathering at geomorphic scales. It begins with an overview of the aspects that are important for the ground thermal regime. The following subsections focus on transient permafrost modelling, where two permafrost models, CryoGrid 2 and CryoGrid 2D, are described in detail. Periglacial landforms that occur in Iceland and Norway are also mentioned. The subsequent part of the chapter describes the frost weathering theory and the frost weathering model employed in this work. Finally, the basics of satellite radar interferometry are provided.

Chapter 3 Setting – This chapter describes Iceland's climate, bedrock and Quaternary geology, and permafrost distribution, including the permafrost boreholes and the occurrence of landforms indicative of permafrost. The second part of the chapter focuses on Norway's climate, bedrock and Quaternary geology, the distribution of permafrost in gentle terrain and rock walls, rock glaciers and a very short description of the study sites.

Chapter 4 Methods and data – This chapter provides the research methodology employed in this dissertation. Methods for each paper are described separately. Furthermore, I include a description of additional methods that are used for the work within this thesis that is not included in journal papers: (1) one-dimensional frost cracking indices for Iceland and Norway, (2) rockfall source detection and estimation of rock wall retreat rates, and (3) measuring solifluction using SAR interferometry and identification of the most important environmental variables governing solifluction.

Chapter 5 Results – This chapter presents the findings of this thesis in the order corresponding to the methods described in the previous chapter.

Chapter 6 Discussion – This chapter discusses the findings of this dissertation, together with the uncertainties and limitations of the methods.

Chapter 7 Conclusions – This chapter summarises the findings of this dissertation.

Part II Papers

Paper I, Paper II and Paper III, which form the basis of this dissertation, are included. All papers are peer-reviewed and published.

Part III Appendix

This part includes supplementary figures and tables, along with a list of peer-reviewed journal publications and conference publications.

2. SCIENTIFIC BACKGROUND

2.1 GROUND THERMAL REGIME

The two non-mutually exclusive terrestrial permafrost environments occur at high latitudes (latitudinal or polar permafrost), mainly in Siberia, Canada, Alaska, and at high elevations (mountain permafrost). Depending on the area underlain by permafrost, Brown *et al.* (1997) divided permafrost into continuous (90–100 % area), discontinuous (50–90 %), sporadic (10–50 %) and isolated permafrost (0–10 %) zones. In general, thicker permafrost develops in locations with lower mean annual air temperature ($MAAT$), whereas the thickness of the active layer, the seasonally thawing and freezing layer above permafrost, decreases with a lower $MAAT$. Figure 2.1 shows an example of a profile with the active layer above permafrost.

The heat and moisture exchange between the atmosphere and the ground surface, as well as the thermal characteristics of the ground materials and the local geothermal heat flow, determine the ground thermal regime (Williams and Smith, 1989). The ground surface receives heat from both the Sun through the atmosphere and Earth's interior, with the former being around three orders of magnitude greater than the latter (Yershow, 2004). Energy exchanges affect how much the ground surface temperature (GST) fluctuates, whereas their downward propagation is governed by the thermal characteristics of the ground. The geothermal heat flux from the Earth's interior also affects the temperature of the ground; however, this impact is less significant in the top soil layers, where the thermal regime is controlled by the surface energy balance (Lunardini, 1981). Nevertheless, in volcanic regions like Iceland, the strong geothermal heat fluxes may be able to limit permafrost thickness (Etzelmüller *et al.*, 2007). The surface offset (SO) (Smith and Riseborough, 2002) between surface air temperature (SAT) and GST results from the interplay of atmospheric climate and topoclimatic site-specific elements such as vegetation, snow cover, soil moisture, and terrain (Williams and Smith, 1989; Gisnås, 2016). These factors determine the temperature of the near-surface ground layers, which in turn affects the active layer depth and permafrost thickness. Conduction, convection, phase change, and moisture transport are possible geophysical phenomena associated with energy transfer in the ground (Lunardini, 1981). Although convection may be essential in locations with groundwater flow and hydrothermal circulation, the study of GT is most often based on the heat conduction theory since heat conduction is the dominant mode of heat transfer in the ground (Williams and Smith, 1989). The thermal characteristics of the ground may change significantly below the ice-water transition temperature because the thermal conductivity, which describes the rate of conductive heat flow, and the volumetric heat capacity, which determines the change in volume's heat content per unit temperature change, depend on the soil moisture phase. The thermal offset between GST and permafrost temperatures arises from the difference in thermal conductivities between the ground's frozen and thawed states, caused by the fact that the ice thermal conductivity $\left(2.2\,\mathrm{W\,m^{-1}\,K^{-1}}\right)$ is around

Figure 2.1: Profile of 72 cm thick active layer and underlying permafrost developed in volcanic tephra deposits in Iceland. Source: Harris *et al.* (2018).

four times larger than the thermal conductivity of water $\left(0.57\,\mathrm{W\,m^{-1}\,K^{-1}}\right)$ (Smith and Riseborough, 2002). The magnitude of the thermal offset is therefore dependent on the water content of the soil, and it is often negligible in bedrock. Moreover, across a range of negative temperatures until most of the unfrozen water freezes, latent heat of fusion is released (Williams and Smith, 1989). Because the latent heat effect dominates the heat capacity during the phase transition (also known as the apparent heat capacity), a substantially greater amount of heat must be lost to cool the ground during freezing. As the active layer freezes in the autumn, the release of latent heat leads to the zero-curtain effect, when the temperature stays at 0 °C for an extended length of time. In soils with higher water content, the zero-curtain effect lasts longer (Williams and Smith, 1989).

2.2 PERMAFROST MODELLING

Two transient heat conduction models CryoGrid 2 (Westermann *et al.*, 2013) and CryoGrid 2D (Myhra *et al.*, 2017), both developed at the Department of Geosciences, University of Oslo, are employed in this dissertation. The CryoGrid 2 is a one-dimensional version, whereas the CryoGrid 2D is a two-dimensional version.

Permafrost model types – Empirical and process-based (analytical and numerical) permafrost models are the two primary subcategories of permafrost models (Riseborough *et al.*, 2008). In contrast to numerical models, which may simulate the ground's transient response, analytical and empirical models, such as $TTOP$ (Temperature at the top of permafrost; Smith and Riseborough, 2002) and Frost Index, assume that permafrost conditions are in equilibrium with climatic conditions. Whereas equilibrium models generate simple outputs, such as permafrost occurrence or mean annual GT, transient permafrost models yield the evolution of a subsurface temperature profile (Riseborough *et al.*, 2008). Equilibrium models may be employed in applications with little complexity or when transient effects are insignificant (Jafarov *et al.*, 2012). The numerical solution is required to account for the transient impacts of the phase change caused by the ground freezing and thawing. As a result, transient models require significantly more computer resources than equilibrium models. Nonetheless, using transient permafrost models that take the effects of latent heat into account, the GT and the phase change boundary dynamics may be reproduced rather well (Jafarov *et al.*, 2012). However, more input data are required due to the model's rising complexity and the number of addressed processes. Permafrost models may simulate an index or a GT profile for a single location in one dimension, a transect in two dimensions, or a 2.5D space (Riseborough *et al.*, 2008). These latter models are spatial permafrost models that consist of a grid of single-point locations and ignore lateral heat fluxes between the points. Spatial permafrost models may be applied at the continental, regional or mountain scales (Riseborough *et al.*, 2008). Three-dimensional models for ground heat flow in permafrost areas have also been developed (Noetzli *et al.*, 2007; Noetzli and Gruber, 2009).

Transient permafrost models – In the transient permafrost models, the ground thermal state is typically calculated using data defining the climate and the surface and subsurface properties of the soil. The modelling space, the starting point in time, the upper and lower boundary conditions, and other parameters must also be specified in a numerical model. Space and time are divided into discrete space grid and time increments. In spatial transient permafrost models, the vertical resolution of the snow column is often constant, whereas the vertical spacing of the soil domain typically increases with depth. At the lower and higher boundaries, temperature or heat flow must be specified for each time step. Under the so-called Dirichlet boundary condition, the temperature (SAT or GST) is specified as the upper boundary (e.g. Jafarov *et al.*, 2012). Another strategy uses surface energy balance models at the upper boundary (e.g. Zhang *et al.*, 2003, 2006). The Neumann boundary condition is commonly used at the lower boundary, where the geothermal heat flux is assigned (e.g. Zhang *et al.*, 2006; Jafarov *et al.*, 2012). Furthermore, it is necessary to specify the values needed to calculate the ground and snow thermal characteristics, as well as the initial temperature profile at each point in the profile. Based on the thermal properties of the snow and soil, the temperature profile from the previous step, and the boundary conditions, the temperature profile is computed for each time step (Riseborough *et al.*, 2008).

Model validation – To ensure that the numerical modelling findings accurately reflect geophysical reality, they must be validated (e.g. Nicolsky *et al.*, 2017). The measured temperatures from deep or shallow boreholes may be used to validate the model temperatures. The observed active layer thicknesses ($ALTs$) may also be used to validate the simulated $ALTs$ (e.g. Jafarov *et al.*, 2012). It is possible to determine the measures of model performance, such as root mean square error ($RMSE$), mean absolute error (MAE), and mean bias error (MBE). Overall error is shown by MAE, under- or overestimation of the true value is quantified by MBE, and non-systematic error is estimated by $RMSE$ (Jafarov *et al.*, 2012). Visual comparisons between maps of permafrost extent and modelled permafrost distribution are also possible ways of model validation (Zhang *et al.*, 2006). Results of permafrost modelling may also be validated based on the occurrence of landforms indicative of permafrost (e.g. Westermann *et al.*, 2013).

Limitations – The uncertainties in the forcing data, the thermal properties of the subsurface and snowpack, model initialisation, model physics, and spatial scale limit the capability of transient models to simulate accurately the GT (Westermann *et al.*, 2013). The equilibration or "spin-up" procedures are typically used to derive the initial GT profile; however, the accuracy of these techniques has been questioned (Riseborough *et al.*, 2008). The spatial transient permafrost models usually only take into account conductive heat transfer when calculating GT, disregarding other physical processes such as, for example, advective heat transfer from infiltration of snowmelt or rainfall (Hinzman *et al.*, 1998), convective heat transfer of air in the blockfields, scree and along the fractures, or percolation and refreezing of water at the bottom of the snowpack (Westermann *et al.*, 2013). Additionally, in high alpine locations where topographic heterogeneity has a significant impact on the subsurface thermal field, disregarding lateral heat transfer between neighbouring cells may provide unsatisfactory outcomes (Etzelmüller, 2013). Moreover, the poor spatial resolution of the forcing data makes it difficult to obtain the variation in GT in alpine regions (Etzelmüller, 2013). Because of the different spatial resolutions of the validation data and modelled outcomes, model validation may also have limitations. For example, Zhang *et al.* (2006) attempted to compare predicted permafrost extent with higher-resolution permafrost maps, emphasising that the findings are not directly comparable. The findings from a single cell that covers a larger area of e.g. one square kilometre may not be suitable for validation against the point borehole data (Westermann *et al.*, 2013).

2.2.1 ONE-DIMENSIONAL PERMAFROST MODEL CRYOGRID 2

Several studies have previously employed the numerical permafrost model CryoGrid 2 to simulate GTs (Westermann *et al.*, 2013, 2015a, 2017). The CryoGrid 2 model calculates the evolution of a one-dimensional temperature profile in a layered soil column and overlying snowpack (Figure 2.2). The required model forcing consists of data sets of SAT and snow depth. The one-dimensional model equations may be applied to a single grid cell or several individual grid cells as a spatially distributed model. The latter approach ignores the lateral heat fluxes since there is no interaction between the adjacent cells. Furthermore, the model neglects water and water vapour movements and external water inputs such as meltwater or rain; thus, the only factors affecting variations in soil water content are freezing and thawing (Westermann *et al.*, 2013).

Ground thermal model – The one-dimensional transient heat conduction equation, which is derived from the fundamental law of heat conduction known as Fourier's law, serves as the mathematical foundation for the model. The main model equation also takes into consideration latent heat effects from ice–water phase changes, which have a significant impact on GT in areas subject to seasonal freezing and permafrost conditions. The following one-dimensional equation allows for the computation of the temperature field $T(z,t)$ over depth z and time t in the subsurface:

$$C_{eff}(z,T)\frac{\partial T}{\partial t} = \frac{\partial}{\partial z}\left(K(z,T)\frac{\partial T}{\partial z}\right), \tag{2.1}$$

where C_{eff} [$\mathrm{J\,m^{-3}\,K^{-1}}$] is the effective volumetric heat capacity and K [$\mathrm{W\,m^{-1}\,K^{-1}}$] is the thermal conductivity (Westermann *et al.*, 2013). The effective volumetric heat capacity term in Equation (2.1) includes the release or absorption of latent heat that

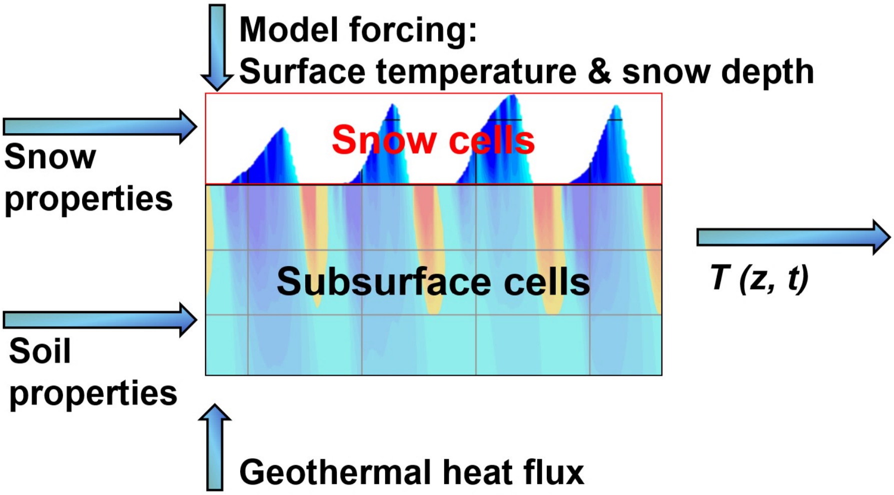

Figure 2.2: CryoGrid 2 transient permafrost model with the required parameters and boundary conditions.

results from ground freezing or thawing:

$$C_{eff} = C(T,z) + \rho_w L \frac{\partial \theta_w}{\partial T}, \tag{2.2}$$

where $C(T,z)$ [J m^{-3} K^{-1}] is the volumetric heat capacity of the ground, ρ_w [kg m^{-3}] is the water density, L [J kg^{-1}] is the specific latent heat of fusion of water, and θ_w [–] is the volumetric liquid water content.

Thermal conductivity, volumetric heat capacity and freezing curve – Functions of the thermal properties of the individual soil constituents j (water, ice, organic, mineral, air) and their respective volumetric fractions θ_j estimate thermal properties of the soil layers. Volume-weighted sum of the heat capacity of the soil components C_j yields $C(T,z)$ as follows:

$$C(T,z) = \sum_j \theta_j(T,z)\, C_j. \tag{2.3}$$

CryoGrid 2 uses the quadratic parallel model from Cosenza *et al.* (2003) to approximate overall ground thermal conductivity:

$$K = \left(\sum_j \theta_j \sqrt{K_j}\right)^2. \tag{2.4}$$

The ground thermal conductivity varies with temperature because volumetric water and ice contents are temperature-dependent variables. CryoGrid 2 takes into account seasonal variations in thermal conductivity that cause thermal offsets (Westermann *et al.*, 2013). The liquid water and ice contents are obtained from the functions described by Dall'Amico *et al.* (2011), which relate liquid water content, temperature and soil saturation degree, by applying the "freezing=drying" assumption. This assumption implies, among other things, that (1) the freezing or thawing of water is comparable to evaporation or condensation of water, and (2) the soil water and ice contents may be connected with the soil matric potential through the soil water retention curve (Dall'Amico *et al.*, 2011). CryoGrid 2 employs the soil water retention curve and the soil freezing characteristic $\theta_w(T)$ from Van Genuchten (1980). The permafrost model includes the Van Genuchten parameters for three soil textures (sand, silt and clay).

Snowpack thermal model – CryoGrid 2 also includes a snow domain, where the only heat transfer process is heat conduction. The thermal impact of the processes in snow, such as water infiltration, snow melting or refreezing of melt- or rainwater, is excluded. Snow cells, all of them with the same thermal properties, may be removed or added according to the changes in snow depth. The volumetric heat capacity of snow C_s is obtained as a function of the snow density ρ_s:

$$C_s = \frac{\rho_s}{\rho_i} C_i, \tag{2.5}$$

where C_i is the heat capacity of ice and ρ_i is the density of ice (Westermann *et al.*, 2013). The thermal conductivity of snow K_s may be estimated from a formula derived by Yen (1981):

$$K_s = K_i \left(\frac{\rho_s}{\rho_w} \right)^{1.885}, \tag{2.6}$$

where K_i is the thermal conductivity of ice.

Numerical solution, boundary conditions and model initialisation – CryoGrid 2 uses the method of lines (Schiesser, 1991) to solve numerically the partial differential equation for heat flow (Equation 2.1), with time being the sole independent variable. The SUNDIALS package's CVODE solver (Hindmarsh *et al.*, 2005) is employed to solve numerically the resulting ordinary differential equations. Upper boundary conditions include SAT series (Dirichlet boundary condition), while lower boundary conditions are constant geothermal heat flux (Neumann boundary condition).

The initial temperature profile is generated using the five-step initialisation procedure based on the first five years of the modelling period (see Westermann *et al.*, 2013). The model initialisation procedure captures the impact of nival (snow) and thermal offsets on the temperature of deeper ground layers, as well as the annual temperature cycles of the upper soil layers. The derivation of the initial profile is based on the equilibrium model, and $TTOP$ (Smith and Riseborough, 1996) is set as the surface temperature; hence, there are some uncertainties associated with the initial profile. Nonetheless, the initial temperature profile has the most influence at the beginning of the main run, e.g. first ten years (Westermann *et al.*, 2013).

2.2.2 TWO-DIMENSIONAL PERMAFROST MODEL CRYOGRID 2D

CryoGrid 2D is a transient two-dimensional permafrost model that has previously been used to simulate GT in steep rock walls in Norway (Myhra *et al.*, 2017) as well as conductive heat flow between rock walls and talus slopes (Myhra *et al.*, 2019). In contrast to CryoGrid 2, CryoGrid 2D only includes a subsurface domain (Figure

2.3), i.e. the model lacks a snow domain. Hence, the evolution of the 2D thermal field in the ground is computed in the CryoGrid 2D model by forcing the model with sets of GST along the upper boundary, i.e. the temperature at the air-ground interface below snow cover (Figure 2.3). Since the model includes only two dimensions, it assumes translational symmetry along the third dimension, making it most suitable for applications where the heat flow occurs mainly in two dimensions.

Ground thermal model – In the CryoGrid 2D model, the two-dimensional heat conduction equation that includes the latent heat effects due to ground freezing or thawing is solved for vertices with the Cartesian coordinates x and y:

$$C_{eff}(x,y,T)\frac{\partial T}{\partial t} = \frac{\partial}{\partial x}\left(K(x,y,T)\frac{\partial T}{\partial x}\right) + \frac{\partial}{\partial y}\left(K(x,y,T)\frac{\partial T}{\partial y}\right), \tag{2.7}$$

where C_{eff} is the same as in CryoGrid 2 as defined by Equation (2.2), except it is in two dimensions. The CryoGrid 2D model was built on CryoGrid 2; hence, the thermal properties of the subsurface regions, together with soil freezing dynamics, are parameterised in the same way as in CryoGrid 2 (see Subsection 2.2.1 for more details). CryoGrid 2D is a conductive model; thus, non-conductive heat transfer, such as convective water- or airflow, is unaccounted for.

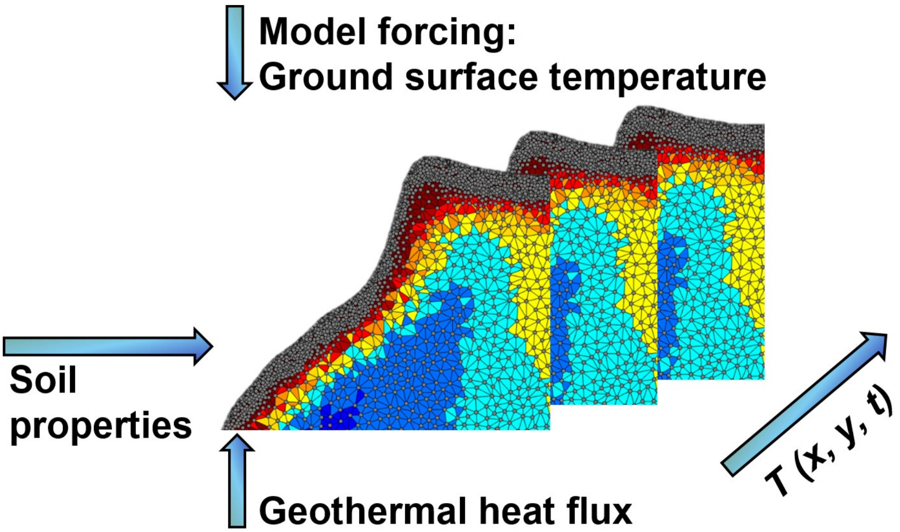

Figure 2.3: CryoGrid 2D transient permafrost model with the required parameters and boundary conditions.

Numerical solution – Equation (2.7) is numerically solved using the finite element method (FEM) solver MILAMIN (Dabrowski *et al.*, 2008). One of the main advantages of the FEM is that it may be applied to complex geometries, making it highly suitable for heat flow problems in steep rock walls below mountain plateaus (Myhra *et al.*, 2017). The original version of the MILAMIN solver only accounts for the steady state; hence, it had to be modified in CryoGrid 2D to include transient heat flow (Myhra, 2016). Time is discretised using the finite difference backward Euler scheme, which is unconditionally stable for any time step. The transient implementation was successfully benchmarked against the analytical solution by Myhra (2016).

The model domain is constructed as a 2D slice through a slope down to several thousand metres depth. An unstructured triangular mesh is generated in CryoGrid 2D using the 2D mesh generator Triangle (Shewchuk, 1996), where the spatial resolution of various subsurface regions depends on the maximum triangle area (MTA). MTA typically increases with depth in order to keep the total node number as small as possible (usually less than 1.5 million nodes), which is required by the model for an efficient numerical solution. Furthermore, the model allows for subsurface domain segmentation in terms of regions with distinct volumetric contents of soil constituents (mineral, organic, air, water, ice), and hence various thermal properties. This allows for including any ground composition in the model, such as e.g. scree, blockfields or porous bedrock.

Boundary conditions and model forcing – GST series are specified as upper boundary conditions for each surface node (Dirichlet boundary condition), whereas a constant geothermal heat flux is set at the lower boundary. Zero heat flux boundary conditions are assumed along the left and right vertical boundaries. To account for SOs and obtain GST, SAT is linked with GST using empirical scaling factors, so-called freezing n-factor nF and thawing n-factor nT (e.g. Smith and Riseborough, 2002), which are defined as ratios between annual accumulated freezing or thawing degree days at the ground surface (FDD_S or TDD_S) and in the air (FDD_A or TDD_A):

$$nF = \frac{FDD_S}{FDD_A} \text{ and} \tag{2.8}$$

$$nT = \frac{TDD_S}{TDD_A}. \tag{2.9}$$

GST is then computed as follows:

$$GST = \begin{cases} nF\ SAT & \text{if } SAT \leq 0\,^{\circ}\text{C} \\ nT\ SAT & \text{if } SAT > 0\,^{\circ}\text{C}. \end{cases} \tag{2.10}$$

nF-factor accounts for the nival offset, and nT-factor accounts for the summer SO, arising from, among other things, vegetation shading effects, topographic shading effects, potential incoming radiation and soil moisture (Gisnås, 2016).

Model initialisation – The initial temperature field is obtained by running the 2D steady-state version of the model using the geothermal heat flux at the bottom of the domain and the average GST for e.g. the first 10 years of the simulation period (Myhra *et al.*, 2017). Subsequently, a spin-up procedure is used for the same initialisation period, i.e. the transient version of the model is run as many times as needed until the specified initialisation conditions are reached. The latter may be defined as the maximum allowable difference between subsequent runs (Myhra *et al.*, 2017).

2.3 PERIGLACIAL AND PERMAFROST-RELATED LANDFORMS

Certain periglacial landforms, together with their activity state, may be used as proxies for the occurrence of contemporary or paleo-permafrost. For contemporary permafrost, examples of such landforms are active rock glaciers, stable ice-cored moraines and palsas. For paleo-permafrost, for instance relict rock glaciers may be used.

Rock glaciers – Rock glaciers (Figure 2.4) are defined as *"debris landforms generated by the former or current creep of frozen ground (permafrost), detectable in the landscape with the following morphologies: front, lateral margins and optionally ridge-and-furrow surface topography"* (RGIK, 2023). Active rock glaciers creep slower than glaciers, typically with velocities of 0.1–1 $\mathrm{m\ a^{-1}}$ (Barsch, 1996). Rock glacier front is fairly steep, ranging from 35° to 45°. The sides are also steep, with a height of more than 10 m. The total volume of a typical rock glacier with dimensions of 100–200 m in width, several hundred m in length, and 50 m in depth is larger than 10^6 $\mathrm{m^3}$. Furrow and ridge topography with a relative surface relief of between 1 and 10 m characterise rock glacier surface. In rock glaciers, differentiation between coarse and fine material (<2 mm) is quite common. The outer mantle (2–5 m deep) consists usually of blocks, while the core consists of fine material where blocks are rare. As a rock glacier forms, frost sorting is most likely in action, dividing material into fine and coarse layers. Typically, there should be between 40 and 60 % ice inside rock glaciers, with the remaining material coming from talus or moraines. They may become "climatically inactive" due to ice melt-out or "dynamically inactive" due to a reduction in talus and ice incorporation. Rock glaciers are described as "relict" or "fossil" glaciers when the ground ice melts out entirely (Barsch, 1996). According to their origin, either from periglacial talus or material of glacial origin, rock glaciers are divided into "talus-derived rock glaciers" and "moraine-derived rock glaciers", respectively (Frauenfelder *et al.*, 2003).

Ice-cored moraines – The interaction of glaciers with permafrost allows for the formation of stable ice-cored moraines (Etzelmüller and Hagen, 2005). The incorporation of sediments into the basal ice is facilitated by the transition zone between cold and temperate ice at the beds of polythermal glaciers. The material is then carried to the ice surface along shear planes englacially (i.e. within a glacier's body). As long as the depth of the active layer is shallower than the thickness of the accumulated supraglacial debris (i.e. debris at a glacier's surface), permafrost prevents the ice core from melting and allows prominent ice-cored moraines to develop (Etzelmüller and Hagen, 2005). Ice-cored moraines may also be found in temperate glacial environments; however, these unstable landforms normally disappear after a few decades (Krüger and Kjær, 2000).

Palsas – Palsas are peaty mounds that may be up to 150 metres wide and 12 metres high. They have a permafrost nucleus, and consist of frozen peat and mineral soil

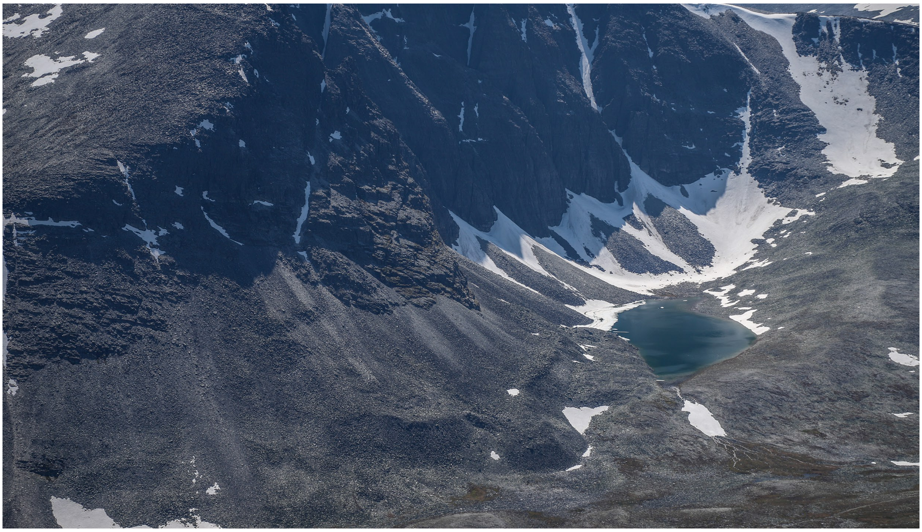

Figure 2.4: Active talus-derived rock glaciers and talus slopes under rock walls of Rondslottet, the Rondane mountain range, southern Norway. Photograph by Jaroslav Obu.

(Seppälä and Kujala, 2009). Their formation is associated with the thermal properties of peat, which has a high thermal conductivity when wet or frozen and a low thermal conductivity when dry. Hence, severe frost penetration occurs in winter when the snow cover is thin, whereas dry peat insulates the ground and prevents the frozen core from thawing in summer (Seppälä and Kujala, 2009). Palsas naturally collapse according to their cyclic behaviour; however, if there is widespread palsa degradation in a particular area, it is most likely related to environmental or climatic change (Zuidhoff and Kolstrup, 2000).

Solifluction lobes and terraces – Solifluction is *"the slow downslope movement of soil due to cyclic freezing and thawing of the ground"* (Ballantyne, 2018). Several components of solifluction have been recognised, and each of them is characterised by a distinct movement profile associated with ice lens formation at certain depths during frost heaving and the frequency of freeze-thaw cycles: (1) needle-ice creep component due to diurnal freezing has the superficial velocity profile, (2) diurnal frost creep has a deeper velocity profile than the needle-ice creep, (3) annual frost creep or gelifluction due to one-sided seasonal freezing is deeper than the aforementioned components, and (4) plug-like flow due to two-sided seasonal freezing has the deepest velocity profile and mostly occurs in cold permafrost areas (Matsuoka, 2001b). Frost creep is *"the ratchetlike downslope movement of particles as the result of frost heaving of the ground and subsequent settling upon thawing, the heaving being predominantly normal to the slope and the settling more nearly vertical"* (Washburn, 1967). Frost heave occurs parallel to the surface primarily as ice lenses grow in frost-susceptible soils and lead to volumetric expansion (Ballantyne, 2018). Potential frost creep PFC, which is equivalent to potential downslope movement, may be computed from frost heave amount H_F and slope angle θ_{slp} as follows: $PFC = H_F \tan(\theta_{slp})$ (Matsuoka, 2001b). Part of solifluction that cannot be attributed to the potential frost creep, as computed from the latter equation, is often due to gelifluction (e.g. Kinnard and Lewkowicz, 2005). Gelifluction was in earlier research connected with a slow viscous flow of water-saturated soils (e.g. Washburn, 1967); however, recent studies follow Harris *et al.* (2003) and define it rather as elasto-plastic deformation due to elevated water pressure (Ballantyne, 2018). Furthermore, an additional component of retrograde movement may occur during thawing due to cohesion between soil particles. Surface displacement rates associated with solifluction seldom exceed 10 $\mathrm{cm\,a^{-1}}$ in permafrost areas and may be up to 60 $\mathrm{cm\,a^{-1}}$ in non-permafrost areas with frequent freeze-thaw cycles (Matsuoka, 2001b).

Solifluction often leads to the formation of characteristic landforms, such as turf- or stone-banked solifluction lobes or terraces. Solifluction lobes are less than 25 m wide, whereas terraces are up to hundreds of metres wide (Ballantyne, 2018). Both lobes and terraces have up to a 2 m high frontal riser that develops due to retardation of soil movement (Ballantyne, 2018). The riser height is correlated with the maximum depth of soil movement and the dominant type of freeze-thaw action (Matsuoka, 2001b). Turf-banked solifluction lobes or terraces have vegetation cover only on the riser or both on the riser and tread, whereas stone-banked solifluction landforms lack vegetation cover on the riser (Matsuoka, 2001b).

2.4 FROST WEATHERING THEORY

Frost weathering is a type of mechanical weathering defined as rock breakdown due to the freezing of water. Shattered rocks are typical material resulting from frost weathering producing coarser material (cm to m scale), so-called macrogelivation, whereas finer debris (μm to cm scale) results from granular disintegration and flaking, so-called microgelivation (Matsuoka, 2001a). Shattered rocks are common in the Arctic and are also often found in mountainous environments. In Norway and Iceland, the most common landforms with angular rocks are blockfields, talus slopes and talus-derived rock glaciers (e.g. Figure 2.4). The importance of frost weathering for their formation is not always certain (e.g. French, 2007).

2.4.1 VOLUMETRIC EXPANSION

The frost weathering process was initially interpreted as a result of the 9 % volumetric expansion of water when it freezes to ice in situ, so-called "freeze-thaw weathering" (e.g. McGreevy and Whalley, 1982), since the generated pressure should be sufficient for crack expansion and ultimately rock breakdown. Since such a process necessitates a closed system with saturated bedrock and water is prone to migrate in rocks, the most current research undermines this explanation. Volumetric expansion is still perceived by some geomorphologists as a type of frost weathering that occurs in saturated rocks that are subject to fast freezing near the surface, in water-filled joints, or in rocks with a small specific surface area (e.g. Matsuoka, 1990; Matsuoka and Murton, 2008), while other research nearly entirely rejects the concept of "freeze-thaw weathering" in nature (e.g. Hallet *et al.*, 1991). The frost weathering indices that are described later do not consider volumetric expansion, and this process is omitted in this work.

2.4.2 ICE SEGREGATION

According to the most recent school of thought on frost weathering, crack widening during freezing is caused by ice segregation in rocks. Such a process allows for an open system. The term "ice segregation" describes the formation of segregated ice as a result of unfrozen water migrating through a frozen fringe towards the ice-filled cracks (also known as "cryosuction"). The more well-known analogous phenomenon in fine-grained soils is called frost heave. Since the publication of Walder and Hallet's (1985) pioneering work titled *"A theoretical model of the fracture of rock during freezing"* in 1985, many studies on frost weathering have been influenced by the theory of ice segregation in rocks. The authors presented a numerical model for "penny-shaped" crack growth due to ice segregation in rocks during freezing, where frost-induced rock damage is a result of ice pressure inside the slowly growing ice-filled cracks (Figure 2.5). Water transport is the key element limiting crack formation, according to Walder and Hallet (1985), who also noted that freeze-thaw cycles are not essential for effective frost weathering; however, they may be relevant for water supply (Walder and Hallet, 1986).

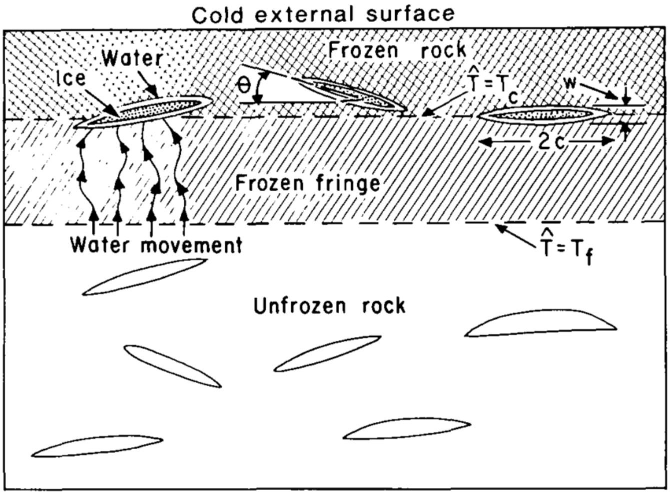

Figure 2.5: Idealised freezing of rock with cracks of radius c and width w. Ice-filled cracks are shown here as analogous to ice lenses in soils, and crack width is exaggerated. Source: Walder and Hallet (1986).

Mechanics of crack growth – The term "stress-intensity factor" arose from the analysis of the stresses in the vicinity of a crack tip, and it quantifies the intensity of the singular stress field (Rossmanith, 1983). According to the principles of fracture mechanics for brittle, elastic solids, a crack will fail after the critical stress-intensity factor, the so-called fracture toughness K_C, has been reached. K_C is a constant value depending on the rock or material type. Experiments show, however, that stable crack extension may occur at stress intensity below K_C, the so-called subcritical crack growth, most likely through stress corrosion cracking ("environmental cracking"), which is *"the weakening of strained bonds at crack tips by the chemical action of an environmental agent, such as water ..."* (Atkinson, 1984). In terms of ice growth, only the mode-I stress-intensity factor is considered (Walder and Hallet, 1985). Mode-I stress-intensity factor describes the crack-opening mode (tension mode), where the displacement of the crack's tip occurs perpendicular to its plane (Rossmanith, 1983). The crack growth rate in Walder and Hallet's (1985) model is a function of the mode-I stress-intensity factor, expressed as a function of internal ice pressure in the cracks and the initial radius of the penny-shaped cracks. Crack growth occurs in Walder and Hallet's (1985) model, if the stress-intensity factor exceeds 30 % of K_C ("stress-corrosion limit"); hence, subcritical crack growth is considered in their model, although it is only based on the empirical power laws between the crack growth rate and stress-intensity factor.

Premelting of ice – The phase behaviour called "interfacial melting" or "interfacial premelting" allows for the existence of very thin (nanometre-scale), unfrozen liquid water films ("premelted films") between the ice-filled cracks and rock matrix at subfreezing temperatures (e.g. Dash *et al.*, 2006). The intermolecular forces that give rise to premelting are the same forces that disjoin the rock and ice surface ("disjoining forces"; Rempel *et al.*, 2001). The net thermomolecular force that disjoints rock matrix and ice surface is balanced by the net force governing the liquid pressure gradients, which are usually parallel to temperature gradients (Dash *et al.*, 2006; Rempel *et al.*, 2016). The thickness of premelted liquid films increases with increasing temperature, leading to a decrease in the thermomolecular pressure (Wettlaufer and Worster, 2006). As a result, while the external pressure remains constant, the fluid pressure drops as the temperature decreases, and premelted liquid has a propensity to flow from warmer to colder areas, so that the pore water is drawn from the surrounding rock towards the solidification front, where it will eventually freeze (Wettlaufer and

Worster, 2006). Consequently, at sufficiently low temperatures, ice exerts pressure on the rock matrix, and the disjoining forces are held responsible for the high stress concentration at the crack tips and ultimately the frost damage (Walder and Hallet, 1985; Rempel *et al.*, 2016). As temperature drops, the hydraulic permeability in the frozen rock matrix drops substantially, and the water flux must drop as well (Rempel *et al.*, 2016).

Frost cracking window – According to Walder and Hallet's (1985) findings, frost cracking is most effective between -15 and -4 °C (the so-called "frost cracking window", FCW, Anderson, 1998) for granite and marble. The FCW varies with the size of the initial crack and the bedrock's hydraulic and fracture-mechanical characteristics. At temperatures higher than the upper limit of FCW, thermodynamic limitations prevent water freezing in thin films and microcracks; hence, ice pressure and the stress-intensity factor are too low for crack growth, whereas at lower temperatures, the low hydraulic conductivity of the frozen fringe inhibits crack growth (Walder and Hallet, 1985).

Laboratory experiments – The laboratory measurements of microfracture activity for frozen sandstone specimens later validated Walder and Hallet's (1985) theoretical model for crack propagation, showing that the majority of frost damage occurred in FCW between -6 and -3 °C (Hallet *et al.*, 1991). More recent laboratory experiments by Murton *et al.* (2006) on wet chalk specimens revealed that (1) contrary to what the older school of thought predicted, the frost heave was associated with ice segregation during thawing cycles rather than freezing cycles, (2) fractures due to frost weathering were parallel to the cooling surfaces, (3) ice lenses were formed, and (4) the depth of fracture occurrence depends on whether they are the result of bi- or unidirectional freezing. Ice segregation may also occur in harder rock types, as demonstrated by the first laboratory experiment carried out using hard, intact gneiss specimens, presented in Duca *et al.* (2014). The latter investigation found that the microcracking took place at temperatures between -2.7 and -0.5 °C, which is greater than what would be anticipated for tougher rocks (e.g. Matsuoka and Murton, 2008).

2.5 ONE-DIMENSIONAL FROST DAMAGE INDICES

Cold-region geomorphologists are particularly interested in the optimal climatic range for frost weathering in order to evaluate its role in the evolution of landscapes through periglacial erosion. From the geomorphological point of view, the two frost weathering concepts provide different climatic conditions for frost cracking. The volumetric expansion (freeze-thaw) model requires frequent oscillations about 0 °C, whereas the ice segregation model implies that most frost cracking occurs in the FCW (Hales and Roering, 2007). The potential for frost cracking caused by ice segregation in rocks has been hitherto linked to climate using a few simple frost-cracking indices. These measures have only been applied in one dimension. All the indices are applicable to horizontal bedrock surfaces; however, they may also be applied to rock walls by assuming that the 1D profiles are perpendicular to the rock wall surface. The frost cracking indices require GT evolution, which is often solved using the analytical solution of a 1D conduction problem with sinusoidal temperature variation at the upper boundary as a function of $MAAT$ and its annual amplitude. Several studies employed the frost cracking indices mentioned below (e.g. Hales and Roering, 2009; Scherler, 2014; Andersen *et al.*, 2015; Savi *et al.*, 2015; Marshall *et al.*, 2021).

Anderson's (1998) index – The first frost cracking measure (Anderson, 1998) takes into account time spent within the assumed FCW between -8 and -3 °C. The largest limitation of this model is that it has unreasonably large frost cracking potential at large depths e.g. for $MAAT$ of -5 °C and depths below 5 m, frost cracking occurs throughout the entire year (Rempel *et al.*, 2016).

Hales and Roering's (2007) index – The assumption that the chemical potentials causing frost cracking are proportional to GT gradients, along with simple considerations regarding water supply, served as the foundation for Hales and Roering's (2007) frost weathering index. They calculated the cumulative annual temperature gradients at a certain depth as a proxy for the intensity of frost cracking. This model shows the largest frost cracking potential for $MAAT$ of 0 °C for shallower depths; however, frost cracking is also large for $MAAT$ of -7.5 °C, when it reaches half of the total frost cracking intensity at 4.5 m depth (Figure 2.6).

Anderson et al.'s (2013) index – The latter model (Hales and Roering, 2007) was modified by Anderson *et al.* (2013) who added a penalty function that restricts how far water may flow to the frost cracking sites. The penalty function moderates the frost cracking intensity from Hales and Roering (2007), and it also leads to much shallower frost cracking (Figure 2.6). Both models presented in Hales and Roering

(2007) and Anderson *et al.* (2013) suggest that frost weathering does not occur for $MAAT < -10\,^{\circ}$C, assuming $MAAT$ amplitude of 10 °C (Figure 2.6).

Rempel et al.'s (2016) index – Lastly, in the Rempel *et al.*'s (2016) model, the crack growth is assumed to be correlated with porosity changes that accompany gradients in water flux. It is described in detail in the following subsection since this is the model I employ in this dissertation. The Rempel *et al.*'s (2016) model predicts the maximum frost potential for $MAAT$ that is slightly lower than the assumed upper limit for frost cracking (Figure 2.6). The swelling depths, where half of the frost cracking occurs, are quite similar to the depths from the Anderson *et al.*'s (2013) model for the chosen upper limit for frost cracking shown in Figure 2.6.

2.5.1 FROST DAMAGE MODEL BY REMPEL *et al.* (2016)

The frost damage model by Rempel *et al.* (2016) uses spatiotemporal porosity increase Δn due to the liquid water supply to growing ice as a proxy for relative frost-induced damage in rocks. The model assumes that saturated conditions always prevail in rock pores (Rempel *et al.*, 2016).

Assumptions from the generalised Clapeyron equation – The decreasing temperature T leads to an increase in the undercooling ΔT, defined as $\Delta T = T_m - T$, where T_m equals the normal bulk melting temperature (273.15 K) (Rempel *et al.*, 2016).

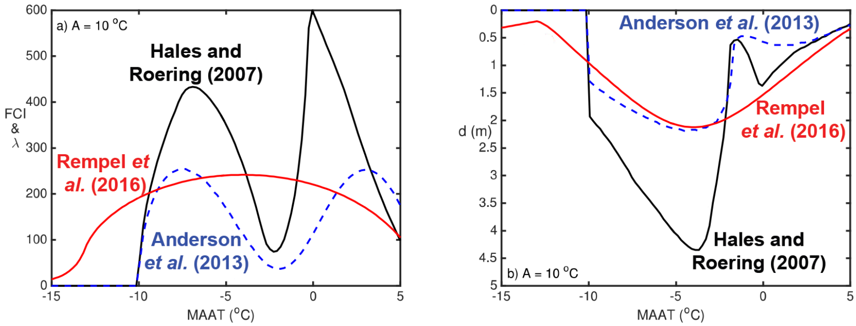

Figure 2.6: Comparison of various frost cracking indices. a) Frost cracking potential measures. FCI - the frost cracking intensity from Hales and Roering (2007) and Anderson *et al.* (2013). λ - the integrated porosity change from Rempel *et al.* (2016). b) Swelling depth d, where half of the frost cracking potential occurs. Rempel *et al.*'s (2016 runs were computed using the upper limit for frost cracking of -3 °C. A - annual amplitude of $MAAT$. Modified from Supplementary Information in Rempel *et al.* (2016).

According to the generalised Clapeyron equation, ΔT is approximately proportional to the difference in pressure ΔP between the ice pressure acting on the crack walls and the relatively lower liquid pressure present in premelted films, which drives the liquid water supply:

$$\Delta P \approx \frac{\rho_i \, L}{T_m} \Delta T. \tag{2.11}$$

Consequently, the model makes the assumption that when ice is present, liquid water must be available (Rempel *et al.*, 2016).

Assumptions about the upper-temperature limit for frost damage – Rock damage may only occur when the net pressure on the rock matrix exceeds the critical cracking pressure P_c. P_c is assumed to depend on mode-I (tensile) fracture toughness K_{IC} and initial crack radius c:

$$P_c = \frac{\sqrt{\pi}}{2} \frac{K_{IC}}{\sqrt{c}}. \tag{2.12}$$

P_c dictates the upper-temperature limit for frost cracking ΔT_c, so-called "undercooling for frost cracking", i.e. the absolute temperature difference between T_m and the upper-temperature threshold for the onset of frost-induced porosity increase. Including the assumption from Equation (2.11), ΔT_c may be approximated as follows:

$$\Delta T_c \approx \frac{T_m}{\rho_i \, L} P_c \approx \frac{T_m}{\rho_i \, L} \frac{\sqrt{\pi}}{2} \frac{K_{IC}}{\sqrt{c}}. \tag{2.13}$$

Assumptions about the permeability – Liquid water is redistributed according to Darcy's law with a temperature-dependent permeability $k(T)$ that is parameterised using the power-law function:

$$k(T) = k_c \left(\frac{\Delta T_c}{\Delta T} \right)^{\alpha}, \tag{2.14}$$

where α is the unitless power-law exponent (usually ~4), and k_c denotes the permeability at ΔT_c, typically between 10^{-24} and 10^{-16} m^2 (Rempel *et al.*, 2016). Equation (2.14) implies that k decreases dramatically as temperature drops and ice formation inhibits water movement. This assumption justifies the lack of an explicit lower temperature limit for frost cracking in the model, i.e. the equivalent of the lower temperature threshold in FCW. The unfrozen hydraulic permeability k_0 may be used to estimate k_c:

$$k_c \equiv k_0 \left(\frac{\Delta T_f}{\Delta T_c} \right)^{\alpha}, \tag{2.15}$$

where ΔT_f – the undercooling for ice formation is 0.1 °C (Rempel *et al.*, 2016).

Main model equation – The temporal changes in porosity n are assumed to be equal to the divergence in the flow rate $\boldsymbol{q}$ as defined by Darcy's law:

$$\frac{\partial n}{\partial t} = -\nabla \cdot \boldsymbol{q} = \nabla \cdot \left(\frac{k}{\mu} \nabla P \right) = \mu^{-1} \left(\frac{\partial k}{\partial T} \nabla T \cdot \nabla P + k \nabla^2 P \right), \tag{2.16}$$

where ∇P is the hydrodynamic pressure gradient, ∇T is the temperature gradient, and μ is water dynamic viscosity (1.8 mPa s) (Rempel *et al.*, 2016). The first term in the brackets accounts for porosity evolution due to temperature-dependent permeability variations, whereas the second term arises from the effects of variations in the liquid pressure gradient. The model assumes that ice pressure equals a fixed P_c, hence defining the hydrodynamic pressure gradient as $\nabla P = \rho_i L / T_m \nabla T$. This implies that when frost cracking occurs (Rempel *et al.*, 2016):

$$\frac{\partial n}{\partial t} = \frac{\rho_i L}{T_m \mu} \left(\frac{\partial k}{\partial T} (\nabla T)^2 + k \nabla^2 T \right), \tag{2.17}$$

where $\nabla^2 T$ is the Laplacian. Equation (2.17) may be applied in 1D, 2D and 3D.

One-dimensional model for frost damage – Equation (2.17) is further simplified in Rempel *et al.*'s (2016) study to the one-dimensional case, where GT is modelled using the analytical solution. The final model for spatiotemporal porosity changes $\Delta n(z,t)$ [–] in one dimension is as follows:

$$\Delta n(z,t) = \frac{D}{\Delta T_c^2} \int_{t_c}^{t} \left(\frac{\Delta T_c}{\Delta T} \right)^{\alpha+1} \left(\frac{\partial T}{\partial z} \right)^2 dt + \frac{D}{\kappa} \frac{(\Delta T_c / \Delta T)^{\alpha-1} - 1}{\alpha(\alpha-1)}, \tag{2.18}$$

and the cumulative porosity increase at a particular depth $\Delta n(z)$ is:

$$\Delta n(z) = \frac{D}{\Delta T_c^2} \int_{\Delta T > \Delta T_c, 1 year} \left(\frac{\Delta T_c}{\Delta T} \right)^{\alpha+1} \left(\frac{\partial T}{\partial z} \right)^2 dt, \tag{2.19}$$

where κ [mm^2 s^{-1}] is the thermal diffusivity and D [mm^2 s^{-1}] is the frost weathering diffusivity parameter, defined as follows:

$$D = \frac{\alpha \rho_i L k_c \Delta T_c}{T_m \mu}. \tag{2.20}$$

The magnitude of the second term in Equations (2.17) or (2.18) is much smaller in comparison with the first term, and if GT is modelled analytically (Carslaw and Jaeger, 1959), the second term is zeroed after 1 year, and it disappears in Equation (2.19). The frost-induced porosity change is only accumulated for time steps when the GT for a given depth is below the threshold value of $-\Delta T_c$. The frost damage is thus a function of: (1) rock strength parameters through ΔT_c that dictates the frost cracking onset (Equation (2.13)), (2) D that determines the rock susceptibility to frost damage (Equation (2.20)), (3) GT, and (4) α that shapes the hydraulic permeability decline with the decreasing GT. The total depth-integrated annual porosity change or the total expansion λ [mm] for one location may also be computed (Rempel *et al.*, 2016):

$$\lambda = \int_z \Delta n(z)\, dz. \tag{2.21}$$

In addition, another parameter describes variations in frost cracking, the so-called swelling depth d [m], which is the depth z over which the cumulative integral is equal to half λ (Rempel *et al.*, 2016):

$$d = z \text{ where } \left(\int_0^d \Delta n(z)\, dz = \frac{\lambda}{2} \right). \tag{2.22}$$

2.6 SAR INTERFEROMETRY

Synthetic Aperture Radar – Synthetic Aperture Radar (SAR) is a coherent type of radar where both phase and amplitude (or intensity) are registered (Hanssen, 2001). The term "radar" (an acronym for "RAdio Detection And Ranging") refers to a device that sends out microwave or radio pulses and detects reflected pulses in the line of sight (LOS), as well as a method that allows for range estimation based on the time it takes for the pulses to travel forth and back and how strongly the amount of backscattered energy varies depending on the physical characteristics of the illuminated objects (Hanssen, 2001). The capacity of radar to penetrate cloud cover and its independence from sunlight are its two key advantages over passive optical sensors. The processing of the returned echoes in a SAR system, the so-called "synthetic aperture technique" (Elachi and Van Zyl, 2006), synthetically creates an artificially long antenna by using the displacement of a smaller (physical) antenna along the track. As a result, azimuth (along-track) resolution may be three orders of magnitude finer than that of early imaging radars such as real-aperture radar (Hanssen, 2001). Imaging radars produce 2-D radar images, similar to optical imagery; however, their generation is different. In SAR images, the cross-track dimension (in "slant range") stems from the time delay between the backscattered echoes, and the azimuth dimension results from the separation of echoes based on their Doppler history (Elachi and Van Zyl, 2006). Radar images have particular geometric distortions, such as layover, shadow, or foreshortening due to the radar antenna's oblique viewing geometry. Space-borne SARs operate in X- (e.g. TanDEM-X 9.65 GHz), L- (e.g. JERS-1 1.275 GHz, ALOS PALSAR-2 1.2GHz) or C-band frequencies (e.g. ERS-1 5.3 GHz, ASAR 5.331 GHz, RADARSAT-2 5.405 GHz, Sentinel-1 5.405 GHz).

Differential InSAR (DInSAR) – The concept behind SAR interferometry (InSAR) is that the distance between the antenna and the target can be related to the phase information from at least two complex SAR observations ("multiplicative interferometry"), from two antennas on a single platform ("single-pass interferometry"), or from repeated overpasses ("repeat-pass interferometry" or "differential interferometry") (Hanssen, 2001). Although interferometry was primarily employed for topographic mapping, later applications demonstrated that repeat-pass configuration may successfully be utilised for deformation monitoring. Nevertheless, when the distance between two antennas, the so-called effective or perpendicular baseline (B in Figure 2.7), is greater than zero, the acquired displacement signals are combined with topographic signals. The technique of differential SAR interferometry (DInSAR), which removes the topographic phase contribution to the total interferometric phase, and enables the creation of "differential interferograms" solves this issue (Hanssen, 2001). Using DInSAR allows potentially for measuring displacements at mm precision because the fractions of 2π cycle are determined (Rott, 2009). However, the main limitations of the method are its inability to detect movement along the flight path and the orientation of the motion. Therefore, DInSAR measurements from the descending and ascending satellite orbits are sometimes combined to obtain the 3D movement vector, although further assumptions are still necessary (Rott, 2009).

Repeat-pass interferometric phase – The interferometric phase $\Delta\phi$ between two SAR signals, acquired by antennas separated by the spatial baseline B [m] (Figure 2.7), is a function of the transmitted radar wavelength λ_r [m] and the path length difference between two radar beams with geometric distances R_2 [m] and R_1 [m] (Hanssen, 2001; Rott, 2009):

$$\Delta\phi = \phi_2 - \phi_1 = \frac{4\pi}{\lambda_r}(R_2 - R_1) = \frac{4\pi}{\lambda_r}\Delta R. \tag{2.23}$$

Equation (2.23) is strictly valid only when the scattering characteristics of a cell are the same in both acquisitions (Hanssen, 2001). In the case of repeat-pass interferometry, the interferometric phase results from the following summands (Rott, 2009; Schneevoigt *et al.*, 2012):

$$\Delta\phi = \Delta\phi_{flat} + \Delta\phi_{topo} + \Delta\phi_{LOS\ d} + \Delta\phi_{atm} + \Delta\phi_{noise}, \tag{2.24}$$

where $\Delta\phi_{flat}$ [rad], $\Delta\phi_{topo}$ [rad], $\Delta\phi_{LOS\ d}$ [rad], $\Delta\phi_{atm}$ [rad], $\Delta\phi_{noise}$ [rad] are the contributions to the interferometric signal due to the flat Earth trend (curvature of the

Earth), topography, line-of-sight displacement, atmospheric delay in the troposphere and ionosphere, and phase noise, respectively. The other summands in Equation (2.24) need to be subtracted to calculate the LOS displacement $\Delta\phi_{LOS\ d}$. The LOS motion-related phase $\Delta\phi_{LOS\ d}$ is given by (Rott, 2009):

$$\Delta\phi_{LOS\ d} = \frac{4\pi}{\lambda_r}\Delta R, \tag{2.25}$$

where ΔR [m] is the component of the displacement in LOS, which may be measured as a fraction of the wavelength. According to Equation (2.25), the spatial baseline does not influence the $\Delta\phi_{LOS\ d}$. The topographic component is a function of the spatial baseline. The shorter baselines are therefore a better choice for DInSAR because the topographic contribution is smaller (Hanssen, 2001).

Coherence and decorrelation – Satellite interferometry requires the phase stability of the targets at the ground surface between two SAR measurements, estimated by

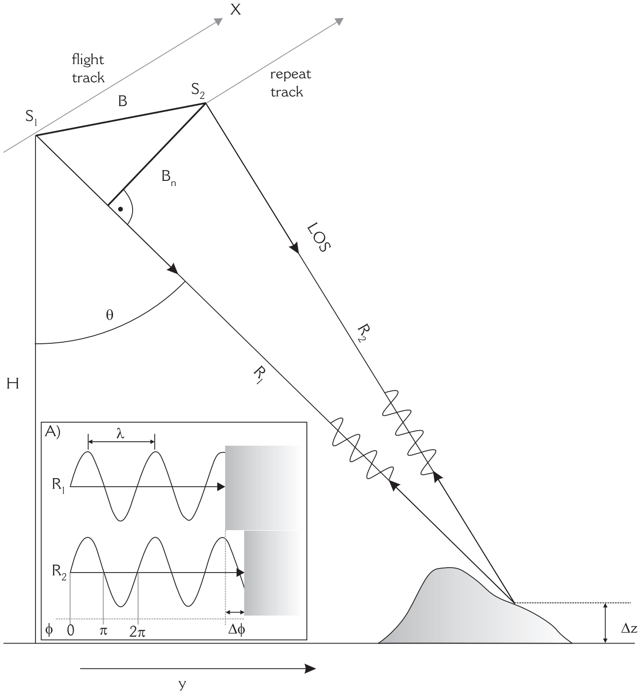

Figure 2.7: Across-track InSAR geometry. S_1, S_2 denote the sensor positions in two overpasses and R_1, R_2 denote their antenna distances, B is the baseline, B_n is the perpendicular (or effective) baseline, θ is the look angle between the instrument and its line of sight; A. The difference between two radar beams yields $\Delta\phi$. Adapted from Rott (2009).

calculating so-called "coherence" from both amplitude and phase information of a SAR pair (Weydahl, 2001). The degree of the coherence degrades due to decorrelating factors, such as radar system noise, coregistration of a SLC pair, baseline (geometric) decorrelation, volume decorrelation and temporal decorrelation (Woodhouse, 2006). Volume decorrelation is associated with the volume scattering properties of the imaged targets, which is especially significant in vegetated areas and sometimes also ice and snow surfaces because the radar signal is able to penetrate into such media. Temporal decorrelation depends on the electromagnetic similarity of the target area between two SAR acquisitions. Various surfaces decorrelate within different timescales. Water and forest may decorrelate within seconds, whereas rocks, stony deserts and glaciers decorrelate within months to years (Woodhouse, 2006); however, surface changes due to precipitation, snow melting or wind redistribution of snow may lead to faster coherence degradation (Weydahl, 2001). Furthermore, temporal decorrelation due to fast motion may occur (Barboux *et al.*, 2014). Another important issue in the interferometric measurements is thus the temporal baseline, selected as a trade-off between the magnitude of motion and the temporal decorrelation of the target surface.

Generation of a single differential interferogram – A pair of two focused complex SAR images, the so-called Single-Look Complex (SLC) is used as an input in the interferometric SAR processing. Assuming the data is prepossessed, SLCs need to be coregistered at a sub-pixel level in two steps of coarse and fine coregistration. Subsequently, a complex interferogram is created by the complex multiplication of two SLC data sets on a pixel basis (Hanssen, 2001). The various summands in Equation (2.24) are removed from the interferogram. The contribution of the topography is computed in the two-pass method using a digital elevation model (DEM) (Hanssen, 2001). The influences of $\Delta\phi_{tropo}$, $\Delta\phi_{iono}$ and $\Delta\phi_{noise}$ are difficult to correct for, and their contribution is often removed using multi-temporal techniques. Before phase unwrapping, the signal-to-noise ratio may be increased by filtering the interferogram, e.g. using the Goldstein filter algorithm (Goldstein and Werner, 1998) or multi-looking (averaging the multiple looks). The interferogram's phase difference, $\Delta\phi$ [rad], is ambiguous to within modulo 2π (Figure 2.7A). The term "fringe" is frequently used to describe a 2π phase cycle. After successful visual investigation of the final "wrapped" interferogram, $\Delta\phi$ values have to be unwrapped to remove 2π ambiguity by adding integer multiples of 2π to the initial $\Delta\phi$ values when phase changes from 2π to 0, using one of the techniques for phase unwrapping (see e.g. Rosen *et al.*, 2000 for a review of the algorithms). So far, the analysis has been conducted using the radar coordinates. Finally, the processed data, e.g. wrapped and unwrapped interferograms, coherence information, in the radar coordinates may be transformed into a geodetic reference system.

Multi-temporal InSAR – Multi-temporal InSAR approaches were invented to minimise displacement-unrelated phase terms, particularly atmospheric delays and temporal decorrelation. Such approaches allow for increased measurement accuracy in comparison with the single interferogram approach. Time series InSAR provides the temporal evolution of displacement as a displacement relative to a chosen date, usually the first date in the stack.

Two main time series InSAR techniques emerged: (1) permanent or persistent scatterer (PS) method, employing the pixels with particularly strong and temporally consistent natural reflectors (PSs) and especially useful for urban areas and rocky terrain (Ferretti *et al.*, 2001), and (2) distributed scatterer (DS) methods, where many scatterers may contribute to the sum of the returned signal from one pixel. One of the subcategories of the DS methods is small baseline subsets (SBAS; Berardino *et al.*, 2002), which employs a network of interferograms with small temporal and spatial baselines. The main drawback of the PS method is that it only measures point-wise information for PSs, whereas DS methods may also measure other areas as long as spatial coherence is sufficient.

3. Setting

3.1 Mainland Norway

3.1.1 Climate

The mainland of Norway has several climate types according to the Köppen–Geiger climate classification for 1981–2010 (Rubel and Kottek, 2017): (1) Cfb (warm temperate, fully humid, warm summer) and Cfc (warm temperate, fully humid, cool summer) in the lower areas in southern Norway, (2) Dfb (snow, fully humid, warm summer) and Dfc (snow, fully humid, cool summer) in the areas at a slightly higher elevation than the latter zone in southern Norway and the lower elevation areas in northern Norway, and (3) ET (polar tundra) climate type in mountains in both southern and northern Norway. $MAAT$ ranges from less than -6 °C in the highest mountains up to 8 °C in the warmest coastal areas (1971–2000; Lussana, 2020). The annual range of mean monthly air temperature is <18 °C in Western Norway and >18 °C in the inland areas. Precipitation distribution in Norway arises from the prevailing western winds and the coast-parallel mountains, which form an orographic barrier, leading to orographic precipitation in areas west of the main water divide and rain shadow effects in areas east of the main water divide. Hence, climate of Western Norway is maritime, with annual precipitation sums of >2000 mm (Lussana, 2018). The Jotunheimen Massif area further east receives less precipitation than Western Norway, with the mean precipitation typically less than 1000 mm a^{-1} (1971–2000; Lussana, 2018). Climate in northern Norway is mostly subarctic in the lowlands and tundra-type in the mountains. Northern Norway's climate varies from maritime in the coastal areas, with the largest precipitation sums in the Nordland county (> 2000 mm in 1971–2000; Lussana, 2018), to a more continental character further inland.

3.1.2 BEDROCK GEOLOGY

The Fennoscandian Shield, a very stable section of the Earth's crust that Norway is a part of, is composed of Precambrian basement rocks (Ramberg *et al.*, 2013). The oldest dated rock in Norway is 2 900 Ma gneiss from Sør-Varanger, northern Norway. The Precambrian rocks are in general younger in southern Norway and formed in various plate-tectonic environments from 1700 to 900 Ma, and later some of them were metamorphosed, especially during the Sveconorwegian Orogeny (1 130–900 Ma). The Western Gneiss Region, Western Norway, is composed of e.g. granitic gneisses and migmatites, which formed 1 850–950 Ma and underwent metamorphism during the Caledonian orogeny (Ramberg *et al.*, 2013).

During the Cambro-Silurian, when Norway was often below sea level, thin sediment layers were deposited in the shallow ocean (Ramberg *et al.*, 2013). The Caledonian orogeny (500–405/400 Ma) due to the compressional tectonic settings, when Laurentia (Greenland, North America) collided with Baltica, caused the transport of rock masses from the sea and the continent margins over Baltica as nappes (thrust sheets), together with pressing down the Precambrian rocks to depth and compression of the Cambro-Silurian deposits. The present-day Scandinavian Caledonides are remnants of the mountains formed at that time. The thrust-sheet complexes are divided into Lower, Middle, Upper and Uppermost Allochthons, with the shortest transported rocks lying lower in the sequence. The Lower Allochthon is composed of sedimentary deposits that underwent low-grade metamorphism, e.g. phyllites. The Middle Allochthon includes the Precambrian rocks, which underwent a higher grade of metamorphism than the Lower Allochthon, e.g. the Juvflye area with metagabbro and metamonzonite and the Rondane Mountains with metasandstone and quartzite. The Upper Allochthon encompasses various rocks formed in the Iapetus Ocean with various grades of metamorphism, e.g. gabbro, greenstone, and mica schist. The Uppermost Allochthon includes granite, shale, and volcanic rocks from the Laurentian margin or the microcontinent in the Iapetus Ocean. After the collision stopped, the mountains collapsed and their denudation started, being levelled to a plain in the Carboniferous (359–299 Ma) (Ramberg *et al.*, 2013).

3.1.3 QUATERNARY GEOLOGY

The Pleistocene glaciations (2.58 Ma–11.7 ka) are responsible for Norway's characteristic landscape with alpine mountains, deep glacial valleys and fjords. During the first phase of the Pleistocene, the ice sheets were quite small, and glacial epochs lasted 41

000 or 23 000 years. Longer glacial epochs started 0.9 Ma, with a frequency of 100 000 years (Ramberg *et al.*, 2013). Larger-scale landforms are a cumulative effect of many glaciations, whereas smaller-scale landforms resulted mainly from the action of the Fennoscandian Ice Sheet of the Weichselian glaciation (117–11.7 ka) (Fredin *et al.*, 2013). Multiple mountain and full-sized Fennoscandian ice sheets linearly eroded the pre-existing fluvially eroded valleys and led to the formation of the fjords and U-valleys (Kleman *et al.*, 2008). Scandinavia's inland was a net deposition area in the early and middle Quaternary, and experienced minimal glacial erosion during the later Quaternary due to cold-based ice (Kleman *et al.*, 2008). Today, this area is covered by glacial drift with thick or intermediate thickness (Kleman *et al.*, 2008). Blockfields in southern Norway were also preserved under non-erosive ice sheets at high-mountain plateaus (Goehring *et al.*, 2008), where negative thermal anomaly in blockfields could enhance the formation of permafrost and cold basal conditions (Juliussen and Humlum, 2007).

After the Last Glacial Maximum (25–18 ka), deglaciation started. Many coastal areas in Norway were already deglaciated in the Allerød Interstadial (14–12.8 ka). Climate amelioration in the Younger Dryas Stadial (YD, 12.8–11.7 ka) led to a re-advance of the Fennoscandian Ice Sheet, leaving behind many moraines from that period (Hughes *et al.*, 2016). Climate deterioration in Preboreal (PB; ~11.7–10.2 ka) led to a rapid ice retreat, which lasted around 1000 years, although smaller ice re-advances also occurred in this period (Ramberg *et al.*, 2013). The Holocene Thermal Maximum (HTM; 11–5 ka) was a relatively warm period in the Holocene (11.7 ka–present), during which all glaciers melted completely in Norway, although the timing of the melt-out varies (Nesje *et al.*, 2008). The glaciers formed again during the Neoglaciation, a period of renewed glaciation that started around ~6–5 ka in Norway. During the Holocene, glaciers had their maximum extent during the Little Ice Age (LIA), which culminated around 1750 in Norway.

3.1.4 PERMAFROST

Permafrost in gentle terrain – Around four decades ago, King (1986) recognised that large mountain areas in southern Norway (Jotunheimen and Rondane) are underlain by widespread permafrost. The first borehole was drilled in Jotunheimen in 1982 (Odegård *et al.*, 1992), and in August 1999, as part of the PACE project (Harris *et al.*, 2001), the deepest permafrost borehole (129 m) in Norway was drilled in the continuous permafrost zone at Juvvasshøe (1894 m) in Jotunheimen ("PACE" in Figure 3.1D). Additional boreholes were drilled in August 2008 across southern Norway (Farbrot *et al.*, 2011), e.g. in Jotunheimen ("BH-X" in Figure 3.1D). Numerous studies concerning permafrost in the gentle parts of southern Norway have been published since the 1980s, attributing mountain permafrost distribution to $MAAT$ (Etzelmüller *et al.*, 2003), elevation (Sollid *et al.*, 2003; Heggem *et al.*, 2005), snow cover (Farbrot *et al.*, 2008, 2011; Isaksen *et al.*, 2011; Gisnås *et al.*, 2017), blockfield cover or surface sediments (Farbrot *et al.*, 2011; Gisnås *et al.*, 2017), and vegetation cover (Farbrot *et al.*, 2013; Gisnås *et al.*, 2017). The lower limit of mountain permafrost is at 900–1100 m in eastern southern Norway (Heggem *et al.*, 2005; Juliussen and Humlum, 2007) and at 1300–1550 m in central and western parts of southern Norway (Etzelmüller *et al.*, 2003). The differences in the lower permafrost limit are due to snow cover and distribution of surface sediments, according to Farbrot *et al.* (2011).

Several permafrost studies have been conducted in northern Norway, where both miniature temperature data loggers and borehole temperature strings were installed to monitor ground thermal conditions (Isaksen *et al.*, 2008; Christiansen *et al.*, 2010; Farbrot *et al.*, 2013). Farbrot *et al.* (2013) distinguished three permafrost regions in northern Norway: (1) maritime mountain permafrost in the western part of Troms county, (2) continental permafrost in Finnmark, mainly in palsa mires, and (3) Low Arctic permafrost at the Varanger Peninsula. The lower permafrost limits decrease from 800–900 m in the western areas of Troms to around 200–300 m in the continental parts of Finnmark and Troms (Farbrot *et al.*, 2013).

Rock wall permafrost – The earliest rock wall permafrost investigations in Norway were systematic field observations at selected sites in the Jotunheimen Mountains (Figure 3.1D, Hipp *et al.*, 2014). The rock wall temperatures were also measured on small rock cliffs in Troms, northern Norway (Frauenfelder *et al.*, 2018). From 2015 through 2017, other sites across southern and northern Norway were also logged (Figure 3.1, Magnin *et al.*, 2019). Steiger *et al.* (2016) presented the first-order rock wall permafrost map for mainland Norway based on a statistical permafrost model relating permafrost distribution to both elevation and potential incoming short-wave radiation. Later, Myhra *et al.* (2017) presented the first 2D modelling for three north-facing rock walls in Norway, based on the interpolated air temperature, variable snow cover and presence of glaciers. Magnin *et al.* (2019) improved the earlier approaches for the statistical rock wall permafrost modelling in Norway by using $MAAT$ as an explanatory variable instead of elevation. The lower rock wall permafrost limits in Norway may be at present expected at 1300–1400 m in north-facing slopes (Magnin *et al.*, 2019). The discontinuous permafrost limit in the north faces occurs above an elevation of 1300–1400 m in southern and 750 m in northern Norway (Magnin *et al.*, 2019).

Rock glaciers in Norway – The first inventory of rock glaciers in Norway suggested there were at least 150 rock glaciers in Norway (Sollid and Sørbel, 1992). The subsequent rock glacier inventories extended the number to around 240 (Lilleøren and Etzelmüller, 2011) and 900 rock glaciers (Hestad, 2021). Hestad's (2021) mapping indicated that ~90 % of the rock glaciers were talus-derived, ~60 % of the landforms are fossil, and the main area of rock glacier occurrence is close to Tromsø in northern Norway. The relict rock glaciers in northern Norway are located mainly outside the YD end moraines (Sollid and Sørbel, 1992), in the vicinity of the contemporary coastline (Lilleøren and Etzelmüller, 2011). Lilleøren and Etzelmüller (2011) explained that the low number of rock glaciers in Norway is due to the quite small area of alpine relief in Norway and limited debris availability.

3.1.5 STUDY SITES

The Juvflye area – The Juvflye area in the Jotunheimen Mountains represents one of the highest mountain areas in Norway. The Juvflye area is one of the main areas of interest in this dissertation. Permafrost distribution is modelled in two mountains in the area: Veslpiggen (2369 m) and Galdhøe (2283 m) (Figure 3.1D). Frost weathering potential in the Veslpiggen Plateau is also modelled. Other data were also collected in the Juvflye area, e.g. the LIDAR and drone data from the Kjelen rock wall (Figure 3.1D; Figure 3.2). The LIDAR data is used in multi-temporal point cloud differencing in order to identify rockfall sources and estimate short-term rock wall retreat rates. Furthermore, long-term rock wall retreat rates are estimated from a nearby ice-cored moraine (Figure 3.2). Displacement of solifluction lobes (Figure 3.3) in the Juvflye area is also investigated.

Ramnanosi – Ramnanosi (1421 m) is a mountain peak in the Flåm Valley (Figure 3.1C). Ramnanosi is part of a larger, unstable rock slope Stampa. Around the Ramnanosi mountain, both gravitational faults and fractures were mapped, and below a west-facing 200-m-high slide scar, there are deposits from the rock avalanche and rockfall events (Blikra *et al.*, 2006; Böhme *et al.*, 2012, 2013).

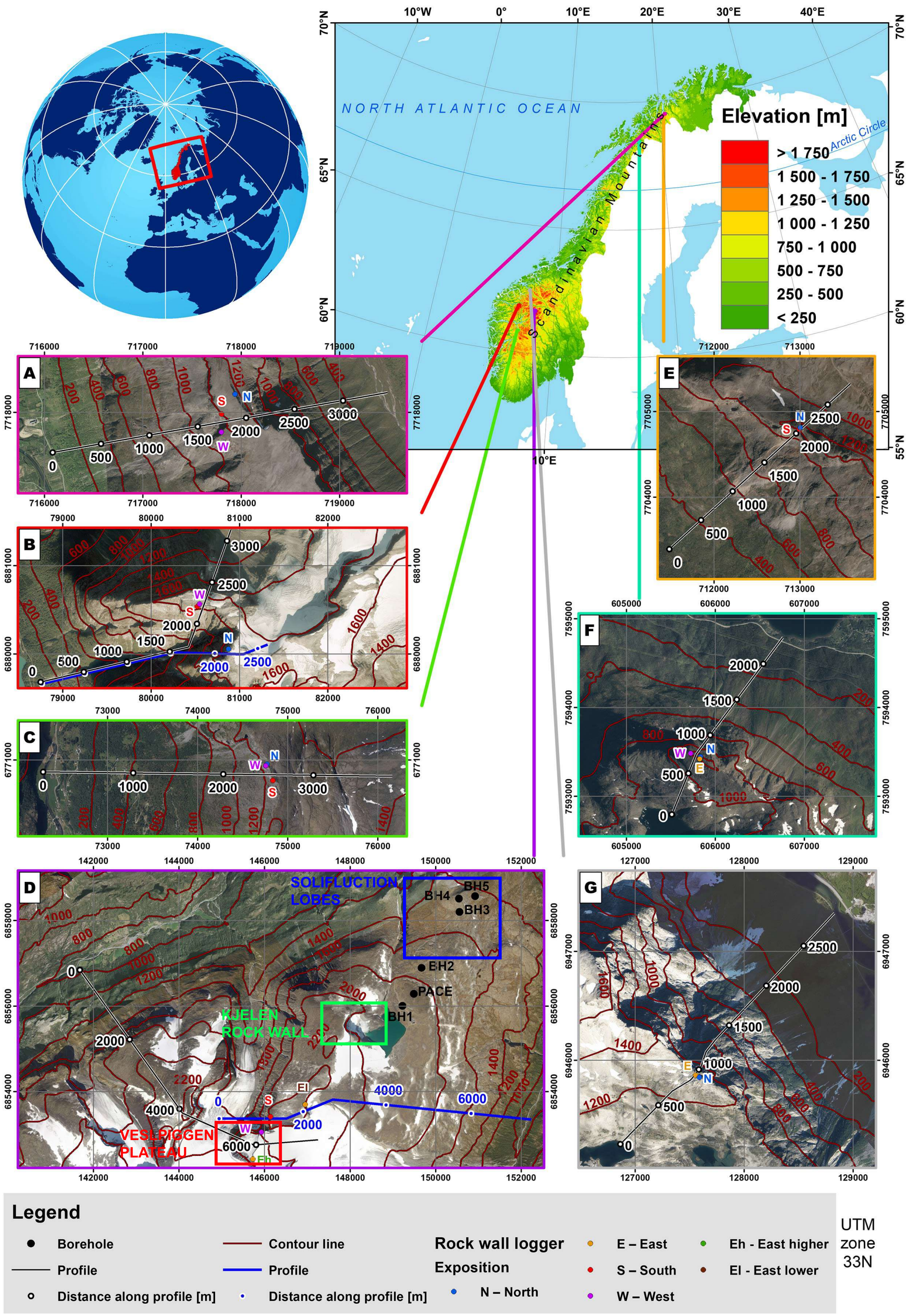

Figure 3.1: Study sites in Norway, together with the transects for the 2D ground temperature modelling: A) Gámanjunni 3, Kåfjord, B) Hogrenningsnibba (the black line) and Kvernhusfjellet (the blue line), Stryn, C) Ramnanosi, Aurland, D) Veslpiggen (the black line) and Galdhøe (the blue line), the Jotunheimen Mountains, E) Ádjit, Storfjord, F) Rombakstøtta, Narvik, and G) Mannen, Rauma. Map background credits: ©Statens kartverk, Geovekst og kommunene.

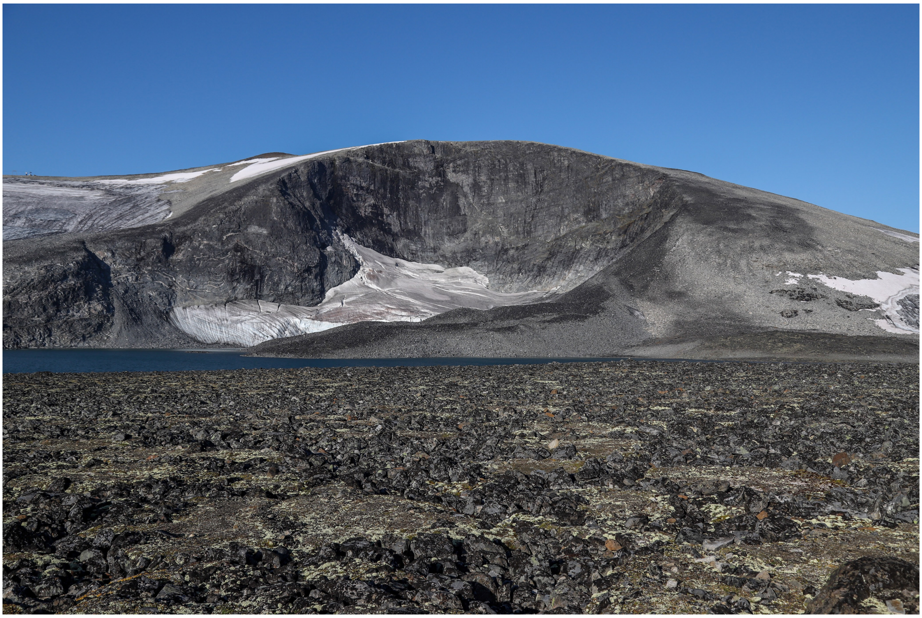

Figure 3.2: The Kjelen rock wall and cirque glacier, together with an ice-cored moraine. Photograph by Jaroslav Obu.

Figure 3.3: Stone-banked solifluction lobes in the Juvflye area. Photograph by Jaroslav Obu, taken at an elevation of ~1525 m.

Hogrenningsnibba and Kvernhusfjellet – Hogrenningsnibba (1670 m) and Kvernhusfjellet (1740 m) are two mountains located above the Raudalen valley north of the Jostedalsbreen ice cap, on the eastern side of Lovatnet Lake (Figure 3.1B).

Mannen – Mannen (1294 m) is the name of both a mountain peak and a large active rockslide in the Møre og Romsdal county (Figure 3.1G), which activated during the HTM around 8 ka (Hilger *et al.*, 2021), leading to the formation of a 20-m-high backscarp.

Gámanjunni 3 – Gámanjunni 3 in Manndalen, west of Tromsø (Figure 3.1A), is one of the most unstable rock slopes in Norway, moving recently up to 60 mm a^{-1} (Böhme *et al.*, 2016, 2019). The unstable part has moved approximately 150 m down since the end of the HTM (Böhme *et al.*, 2019; Hilger *et al.*, 2021).

Ádjit – Ádjit is a mountain ridge in the Skibotn Valley in Troms (Figure 3.1E), where below its south-western rock wall several periglacial and mass movement landforms were mapped, such as e.g. active and inactive talus-derived rock glaciers (Nopper, 2015; Eriksen, 2018).

Rombakstøtta – Rombakstøtta (1230 m) is a steep mountaintop located a few kilometres east of Narvik, Nordland (Figure 3.1F). The north-facing part of the mountain, east of our profile, displays open tension cracks, and it has been subjected to investigations due to its potential for instabilities (Gauer *et al.*, 2016; Morken, 2017).

3.2 ICELAND

3.2.1 CLIMATE

Iceland's climate and weather are influenced by the topography as well as the atmospheric and oceanic conditions in the North Atlantic (Einarsson, 1984). Iceland has maritime climate with mild winters and cool summers. Most of the country area is classified as snow climate (ET) according to the Köppen–Geiger climate classification for the period 1986–2010 (Rubel and Kottek, 2017). Some regions in southern, southwestern and western Iceland are part of the temperate humid climate zone with cool summers (Cfc) (Rubel and Kottek, 2017). $MAAT$ in the normal period 1981–2010 varied from below -5 °C at the uppermost parts of the ice caps to above 4–5

°C along the southern coast. The distribution of precipitation in Iceland is governed by the prevailing southeasterly winds and topography. Mean annual precipitation in the normal period 1981–2010 is estimated to be above 4 000 mm in the windward mountainous regions in the south, above 1 000 mm in most of the other regions in the south and 500–1 000 mm in the large parts of the northern districts. In the northern part of Iceland, precipitation is generally lower than in the south.

3.2.2 TECTONICS GEOLOGY AND ROCK FORMATIONS

Geologically, Iceland is a young island. Although the earliest rock outcrops are 16 ± 0.3 Ma (Moorbath *et al.*, 1968), Iceland's creation began in the Early Miocene, ~24 Ma (Thordarson and Hoskuldsson, 2002). Iceland was formed by the vigorous volcanic activity of the Iceland hotspot, fed by a buoyant mantle plume (Vink, 1984). The volcanism and tectonism in Iceland are controlled by both the plate-pull at the divergent plate boundaries and the fluid dynamics of the Iceland Mantle Plume (Gudmundsson, 2000). At present, only the neovolcanic zones, which are belts 15–50 km broad, experience volcanic activity and faulting (Thordarson and Höskuldsson, 2008). The exposed rocks in Iceland are primarily igneous, of which most are mafic of basaltic composition. There are multiple sub-horizontal strata of basaltic lava flows in the oldest bedrock succession in Iceland, the Tertiary Basalt Formation (16–3.3 Ma), as well as sporadic sedimentary successions (10–15 % of the Tertiary Formation) and formations linked to extinct central volcanoes (Thordarson and Hoskuldsson, 2002). Since the onset of the Quaternary 2.58 Ma, the character of volcanism has changed to sub-glacial eruptions during the stadials. The Plio-Pleistocene Formation (3.3–0.8 Ma) therefore consists of sub-glacial volcanics, such as pillow lavas and hyaloclastites, together with the fluvio-glacial and glacial deposits, in addition to layers of lava flows and tephra deposits from the interstadials (Thordarson and Hoskuldsson, 2002). Greater amounts of volcanic materials produced during sub-glacial eruptions in the Upper Pleistocene Formation (so-called Palagonite Formation, < 0.8 Ma) than in the Plio-Pleistocene Formation are indicative of the period's more widespread glaciations (Sigmundsson, 2006). Post-glacial lava flows, pyroclastics, glacial and marine deposits, and soil deposited after the deglaciation comprise the youngest Holocene Succession (<11.5 ka BP) (Denk *et al.*, 2011).

3.2.3 QUATERNARY GEOLOGY

More than 20 glaciations are documented in Iceland's stratigraphic records as a result of the lava flows preventing the erosion of the glacial sediments (Wohlfarth *et al.*, 2008). These data show that the island was nearly completely covered by ice sheets during the Quaternary (e.g. Geirsdóttir and Eiríksson, 1994), and the Weichselian ice sheet is even presumed to extend beyond the contemporary coastline onto the continental shelf at the Last Glacial Maximum (~21 ka BP) (Andrews *et al.*, 2000; Hubbard *et al.*, 2006). Iceland had rapid deglaciation that began ~15.4 ka BP, followed by an ice advance that peaked in the YD stadial (Wohlfarth *et al.*, 2008). The fast deglaciation persisted after the YD with modest localised ice re-advances in PB. Prior to 9 ka BP, glaciers likely covered an area comparable to modern glaciers (Björck *et al.*, 1997).

Volcanic eruptions that produced basaltic tephra parent material, active aeolian processes, and cryoturbation have influenced soil development during the Holocene (Arnalds, 2008). The sand-dust material is supplied by the sandy surfaces in the neovolcanic zones and glacio-fluvial floodplains. According to Arnalds (2015), aeolian sand is deposited at rates of < 0.01 mm a^{-1} and > 1 mm a^{-1} in locations away from and near dust sources. Moreover, tephra strata accumulated as a result of the explosive volcanic eruptions during the Holocene (Larsen and Eiríksson, 2008). After the settlement about 874 AD, severe land degradation began, and the rates of soil thickening rose (Arnalds, 2008). Thus, 42 % of Iceland is today covered by barren land, including other sparsely vegetated land areas in the mountains, together with areas subject to volcanic disturbance and catastrophic flooding (Arnalds, 2015). Even though they are frequently referred to as "deserts" in Iceland (e.g. Arnalds, 2000), they do not meet the requirements of the rainfall-based definition. Due to frequent freeze-thaw cycles and frost-susceptible soils, Iceland has particularly active cryoturbation, which is the soil mixing caused by frost action (Arnalds, 2015). Frost activity results in the development of a variety of landforms, including solifluction lobes and terraces on slopes, thufur in flat vegetated regions, patterned ground, and desert pavements on desert surfaces (Arnalds, 2004).

3.2.4 PERMAFROST

Priesnitz and Schunke (1978) presented the first study of permafrost distribution in Iceland, where landforms indicative of sporadic permafrost at an elevation between 460 and 720 m, adjacent to the three largest ice caps in Iceland (Vatnajökull, Langjökull and Hofsjökull), were mapped as the main permafrost areas. On the Circum-Arctic permafrost map (Brown *et al.*, 1997), Icelandic permafrost is mapped only as sporadic or isolated (Figure 3.4). In 1996 and 1997, surveys revealed that permafrost was also present in an area outside of the already known sporadic permafrost zone and that mountain permafrost was common above 800 m and even continuous above 1000 m towards the inland areas (Van Vliet-Lanoë *et al.*, 1998). Later, Etzelmüller *et al.* (2007) modelled permafrost distribution in Iceland based on the interpolated $MAAT$ for the normal period of 1961–1990 and assumed permafrost for areas with MAAT below -3 °C (Figure 3.4). Etzelmüller *et al.*'s (2007) study suggested that permafrost exists outside of the previously mapped sporadic permafrost zone, and that a significant permafrost area is present on the Tröllaskagi peninsula, and between Vatnajökull and Hofsjökull. Permafrost occurs also in the regions close to the Askja volcano and the Smjörfjöll mountains. According to their results, the widespread mountain permafrost area occurs above 800–850 m in the central Tröllaskagi peninsula. The permafrost limit increases further south in Hágöngur to 950–1000 m. Frequently unstable atmospheric conditions and

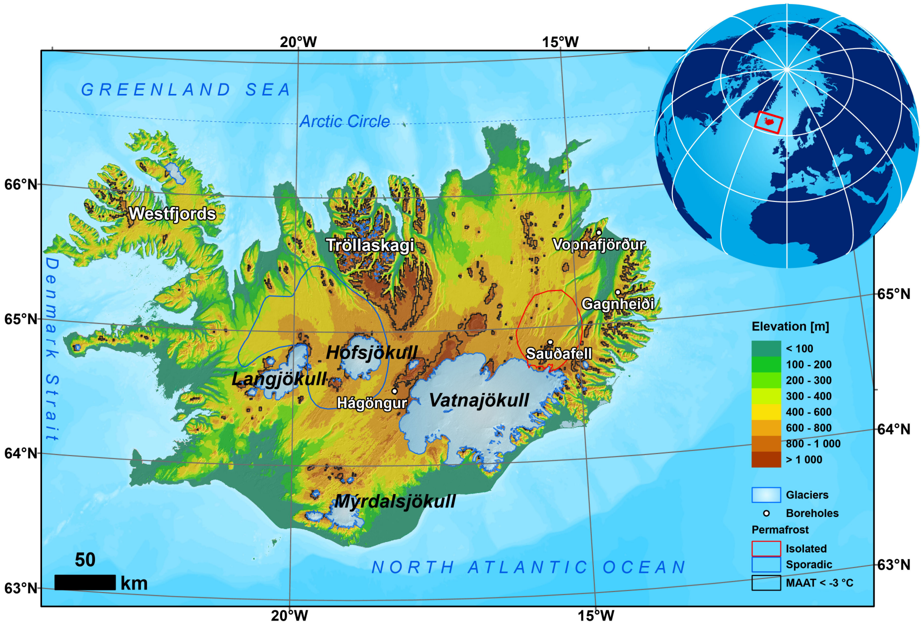

Figure 3.4: Hypsometric map of Iceland, together with permafrost distribution and borehole location. The extent of sporadic and isolated permafrost is from Brown *et al.* (1997), whereas MAAT < -3 °C delineates permafrost areas as modelled by Etzelmüller *et al.* (2007). Map data from the National Land Survey of Iceland.

severe wind-driven snow redistribution influence permafrost dynamics in Iceland (Etzelmüller *et al.*, 2007). Snow cover is believed to be the critical local factor for the permafrost existence in the discontinuous permafrost zone (Williams and Smith, 1989), as it tends to insulate the ground during winter. Moreover, the high geothermal heat flux in Iceland (Hjartarson, 2015) limits permafrost thickness and causes the ground temperatures to be very sensitive to surface temperature variations (Farbrot *et al.*, 2007b). Consequently, the island's permafrost existence is very dynamic due to both maritime climate and the high geothermal heat flow.

Permafrost boreholes – Permafrost monitoring in shallow (< 22 m) vertical boreholes in central and northern Iceland commenced in 2004 (Figure 3.4; Farbrot *et al.*, 2007b). All boreholes are drilled in basaltic bedrock and sparsely vegetated areas.

- **Hágöngur** – The Hágöngur borehole (elevation 899 m; 12 m deep) is located within the volcanic rift zone, in the Icelandic Highlands (Figure 3.5). The borehole had ~5 m deep permafrost at the monitoring onset in 2004 (Farbrot *et al.*, 2007b); however, a talik developed in 2011–2012, and permafrost degraded before 2016.
- **Gagnheiði** – The Gagnheiði borehole (elevation 931 m; 14 m deep) is located in eastern Iceland, outside the volcanic rift zone and within the Tertiary Basalt Formation. Warm permafrost occurs in the area, according to the thermistor measurements.
- **Sauðafell** – The Sauðafell borehole (elevation 906 m; 20 m deep) is located on a hyaloclastite ridge, north of Snæfell and within an intraplate volcanic belt (Figure 3.6). Warm permafrost is present in the borehole.
- **Vopnafjörður** – The Vopnafjörður borehole (elevation 892 m; 22 m deep) is located in eastern Iceland, outside the volcanic rift zone and within the Tertiary Basalt Formation. The borehole has no permafrost recorded, although sorted circles with large radii in the surroundings indicate that permafrost was likely present in the area at some point after deglaciation, perhaps during the LIA.

Rock glaciers in Iceland – Guðmundsson's (2000) first inventory of rock glaciers in Iceland revealed the abundance of these landforms in Tröllaskagi. The first investigations of rock glaciers in the Tröllaskagi region suggested that they originated from glaciers, formed during the LIA, and occurred in non-permafrost environments (e.g. Whalley and Martin, 1994). Subsequent research, by e.g. Farbrot *et al.* (2007a),

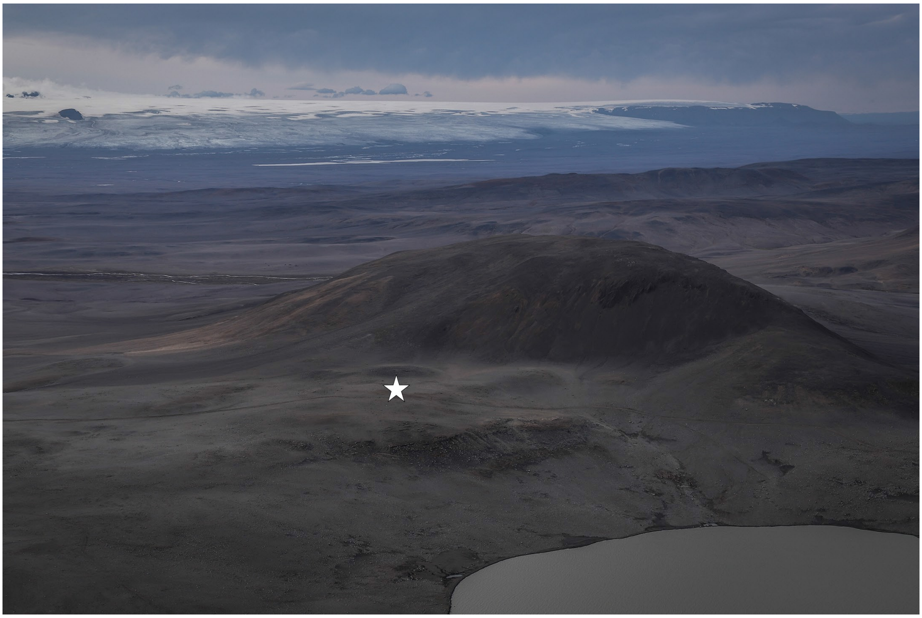

Figure 3.5: The surroundings of the Hágöngur borehole in the Icelandic Highlands. The borehole location is indicated by the white star. The Hofsjökull ice cap is in the background. Photograph by Jaroslav Obu.

Figure 3.6: The surroundings of the Sauðafell borehole in north-eastern Iceland. Photograph by Jaroslav Obu.

demonstrated that these rock glaciers are true permafrost phenomena, and their age was estimated to be a few thousand years old (Kellerer-Pirklbauer *et al.*, 2008). Recently, an inventory of the rock glacier distribution in central and northern Iceland was presented by Lilleøren *et al.* (2013). Due to the region's extensive glaciation, the intact rock glaciers (both active and inactive) are primarily landforms derived from moraines (Lilleøren *et al.*, 2013).

Ice-cored moraines in Iceland – There are ~90 ice-cored moraines in Tröllaskagi, according to Lilleøren *et al.*'s (2013) inventory of the permafrost landforms in the region. These landforms may serve as proxies of permafrost distribution in central north Iceland since they are located at similar elevations as moraine-derived rock glaciers (Lilleøren *et al.*, 2013).

Palsas in Iceland – Palsas occur in the Highlands, particularly in the Þjórsárver area southeast of the Hofsjökull glacier, the Guðlaugstungur area between Langjökull and Hofsjökull glaciers, the Hofsafrétt area north of the Hofsjökull glacier and the highlands of Eastern Iceland (Ottósson *et al.*, 2016). Palsa research has been conducted in the Þjórsárver area (e.g. Thórhallsdóttir, 1994, 1996) and in the Orravatnsrústir area, north of the Hofsjökull glacier (e.g. Hirakawa, 1986; Saemundsson *et al.*, 2012). Icelandic palsas may also be classified as lithalsas, landforms that resemble palsas and are formed in inorganic soils (Pissart, 2002), since they lack typical peat cover due to the steady deposition of aeolian and tephra sediments during volcanic eruptions, which lower the soil organic content (Saemundsson *et al.*, 2012). Climate change caused many Icelandic palsas to disappear between 1930 and 1950 (Thorarinsson, 1951). Later, some palsas aggraded in the 1960s when climate was colder (Friedman *et al.*, 1971). Since then, many palsas in Iceland have decreased in size or vanished (Saemundsson *et al.*, 2012).

4. METHODS AND DATA

4.1 ONE-DIMENSIONAL MODELLING OF PERMAFROST IN ICELAND (PAPER I)

Paper I focuses on regional modelling of GT evolution in Iceland over the last six decades (1960–2016) using the transient permafrost model CryoGrid 2 (Subsection 2.2.1). The methods employed in Paper I are summarised in Figure 4.1.

Surface forcing and boundary conditions – Gridded daily SAT (Crochet and Jóhannesson, 2011) and precipitation data sets (Crochet *et al.*, 2007 and data from the HARMONIE model) were provided by the Icelandic Meteorological Office. A degree-day based algorithm (Saloranta, 2012; "seNorge") is employed to obtain snow water equivalent (SWE). The SWE model is forced by the gridded daily air temperature and precipitation data sets. Minimum and maximum degree-day melt factors are derived from snow depth measurements recorded at the Icelandic weather stations, and are between 4 and 7.5 $\mathrm{mm\,d^{-1}\,°C^{-1}}$, which are relatively high values since snow may have a sand layer on its surface due to aeolian accumulation in Iceland. The modelled snow extent in 2000–2016 was compared with the snow extent visible on optical satellite imagery from Aqua or Terra MODIS. CryoGrid 2 is forced by weekly SAT data and snow depth derived from the SWE algorithm. We used the published heat flow map by Hjartarson (2015) as the lower model boundary at 1 000 m depth.

Ground properties – Subsurface stratigraphy is assigned according to the soil map of Iceland (Arnalds, 2008, 2015). To get an idea of parameter ranges, the model is calibrated against the GT measurements in boreholes (Subsection 3.2.4). The stratigraphy of the remaining soil classes is chosen based on calculated estimates

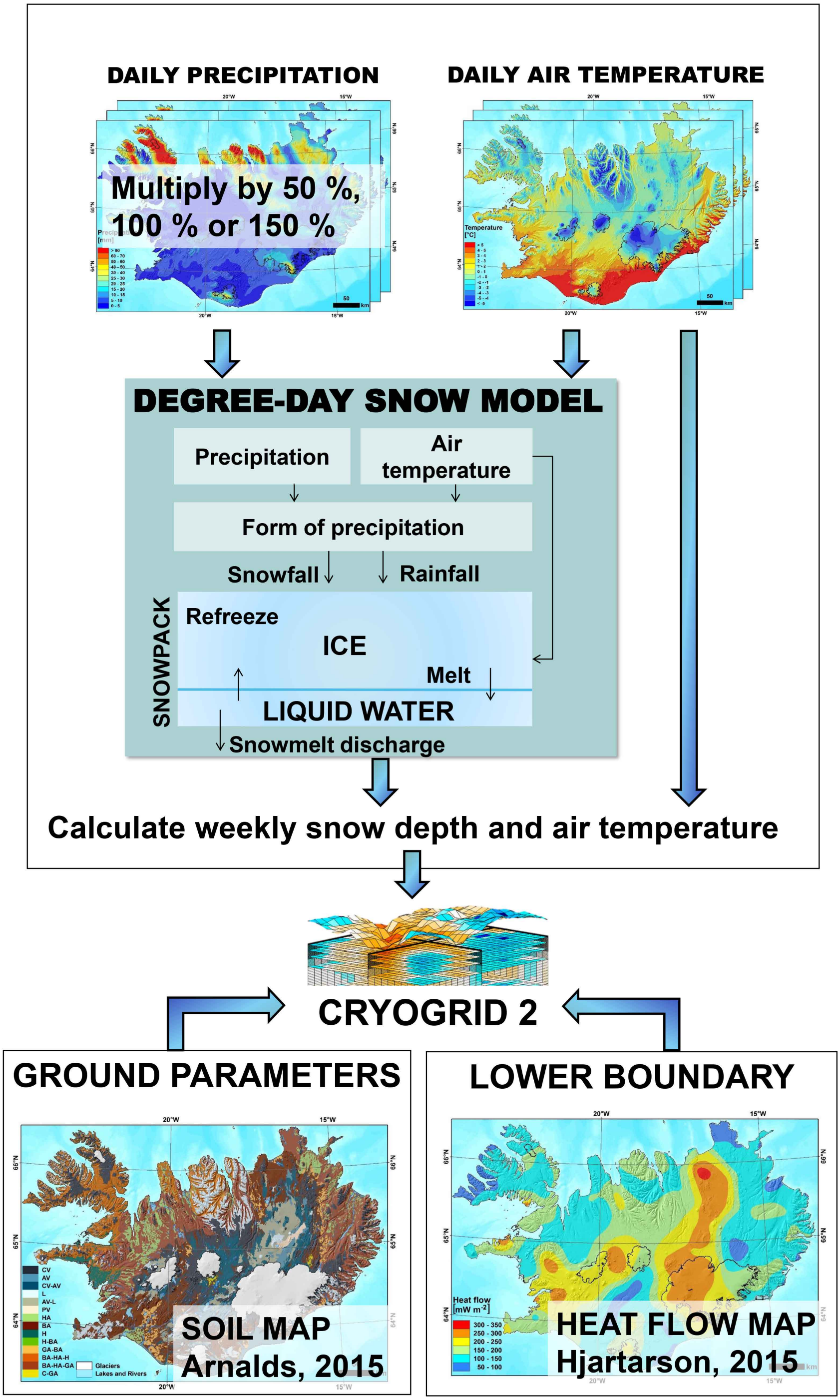

Figure 4.1: Flowchart for transient modelling of permafrost in Iceland (Paper I).

and values that are found in the literature. To estimate the overall depth of unconsolidated sediments in each soil class, we use zonal statistics over the global depth to bedrock data set (Shangguan *et al.*, 2016), and based on the results, we assume a uniform regolith depth of 10 m. A constant bedrock porosity of 8 % is assumed, which represents the average porosity of basaltic lavas in Iceland (Stefánsson *et al.*, 1997).

Model initialisation, implementation and sensitivity – The CryoGrid 2 is implemented for Iceland for the period 01.09.1959–31.12.2016 at a spatial grid resolution of 1 km. The model is initialised using the same procedure as in Westermann *et al.* (2013), based on the first five hydrological years. To account for sub-grid snow variation, we run the model for three snow depth scenarios (50, 100, and 150 % of precipitation). The low-snow-depth scenario (50 % of precipitation), intended to represent the open, unconfined terrain, is run by reducing the snow depth with an average percentage of precipitation calibrated for the boreholes, which are located at windy sites. The second run (100 % precipitation) represents areas where erosion and accumulation of snow roughly balance, whereas the third run (150 % precipitation) is for areas with substantial accumulation of drift snow.

Validation data sets – The simulated GTs are evaluated quantitatively for the borehole sites located at the lower limit of mountain permafrost in Iceland at ~900 m a.s.l. (Etzelmüller *et al.*, 2007). Additionally, the results are validated against the inventory of rock glaciers and ice-cored moraines in central north Iceland (Lilleøren *et al.*, 2013). The modelled permafrost extent is also validated visually based on the extent of palsas, as delineated on the map of habitat types in Iceland from the Icelandic Institute of Natural History (Ottósson *et al.*, 2016).

4.2 TWO-DIMENSIONAL MODELLING OF ROCK WALL PERMAFROST IN NORWAY (PAPER II)

Paper II focuses on the modelling of permafrost distribution in selected rock walls in Norway on an inter-decadal scale over the last 120 years. GT is modelled using the 2D slope-scale transient heat flow model CryoGrid 2D (Subsection 2.2.2) along nine profiles crossing the instrumented rock walls in Norway. The methods employed in Paper II are summarised in Figure 4.2.

Model geometry and ground stratigraphy – The upper boundary for the profiles is extracted from the 0.5–1 m DEMs available from the Norwegian Mapping Authority, whereas the lower boundary extends down to 6000 m below sea level. The constructed meshes have an MTA of 0.05 m^2 between the ground surface and 2 m depth, 0.20 m^2 at depths between 2 and 10 m, 0.50 m^2 at depths between 10 and 20 m, 5.00 m^2 at depths between 20 and 100 m, and 50 m^2 below 100 m depth. The model domains for various profiles consist of 500 000–1 250 000 vertices. A digital map of surface materials is available for all of Norway from the Geological Survey of Norway at 1:250 000 scale. Due to the small scale of the map, we refine the

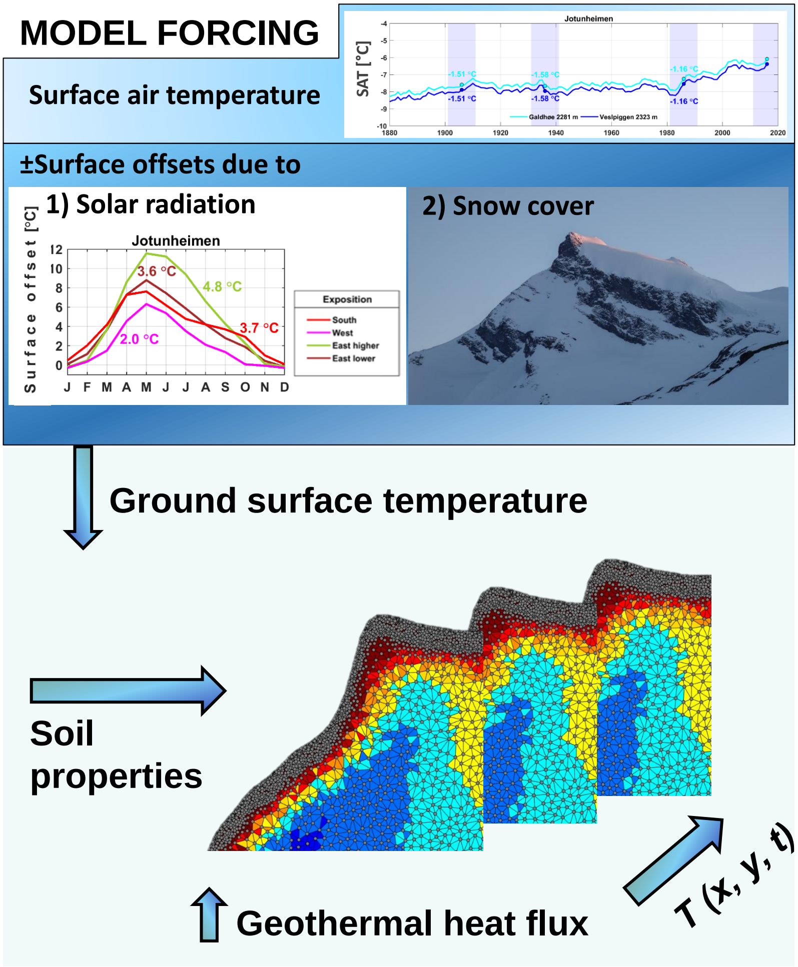

Figure 4.2: Flowchart for modelling of permafrost in steep slopes from Paper II. Photograph of snow cover by Jaroslav Obu.

geomorphological mapping along the profiles based on the available orthophotos from www.norgeibilder.no. Similar volumetric contents and layers for the sediment classes are assumed, as in Westermann *et al.* (2013).

Model forcing – We force the model with the regional monthly data set at 2 km spatial resolution provided by the Norwegian Meteorological Institute (Hanssen-Bauer *et al.*, 2006). This regional model yields robust temporal estimates at a regional scale; however, the data provides rather poor temperature series at local scales. Therefore, we superimpose a local component on the regional data. Regional SAT data sets were provided for valleys at the bottom of each profile. Since we begin to run the model at the end of the LIA in Norway and the regional SAT data sets start in 1900, we reconstruct SAT back in time by using SAT from the long-term meteorological stations. We account for average offsets in the overlapping period between SAT from the long-term meteorological stations and the regional SAT. Subsequently, we adjust regional $SATs$ by subtracting offsets between the regional and local $SATs$ from a nearby meteorological station or seNorge data for valleys, over the last few years. In the next step, we compute the average monthly lapse rate between two meteorological stations, typically one at the bottom of the valley and one at or close to the mountain plateau over the last few years. Finally, we compute monthly SAT along the profiles using monthly lapse rates. The selected last few years used in this analysis are periods when temperature measurements in the rock walls are available. This allows for a comparison of SAT with GST determined from rock wall loggers in months with minimal shortwave radiation, e.g. December, and gives more reliability.

After the generation of the SAT data sets, we account for the nival offsets and SOs arising from the shortwave solar radiation by modifying SAT along the profiles. We follow an easy-to-implement hypothesis that snow thickness and its insulating effect on the GST depend on the slope gradient, and assign various nF-factors (Subsection 2.2.2) according to the slope gradient classes. We assume that steep slopes, i.e. steeper than 60° are snow-free. In the steep slopes, incoming shortwave solar radiation may not necessarily be the largest during June, as expected for a horizontal surface at the latitudes in Norway. Instead of using temperature transfer factors, we add measured average monthly SOs to $SATs$ at the location of rock walls along profiles. Measured monthly SOs are computed as a difference between monthly mean ground surface (GST_{month}) and surface air (SAT_{month}) temperature: $SO_{month} = GST_{month} - SAT_{month}$. We apply the same SOs_{month} to all steep parts of slopes (>60°) along profiles.

Model initialisation, model simulations and sensitivity tests – Model simulations start around the end of the LIA in Norway when the long-term SAT data are available (between 1861 and 1874). In the CryoGrid 2D initialisation, we use the average GST for the first decade of the available data and spin-up of the model at monthly time steps around 50 times, which yields temperature difference between the consecutive simulations on the order of 10^{-4} °C. After the initialisation, the model is run at monthly time steps. A zero heat flux condition is assumed along the vertical boundaries. An average value of geothermal heat flux of 50 mW m^{-2} (Slagstad *et al.*, 2009) is applied at the lower boundary at all sites, except for the Jotunheimen, where we use 33 mW m^{-2} (Isaksen, 2001). We evaluate model sensitivity for all profiles by rerunning the model, including the initialisation steps.

4.3 TWO-DIMENSIONAL FROST CRACKING MODEL FOR ROCK WALLS IN NORWAY (PAPER III)

In Paper III, we extend the previous frost cracking indices to two-dimensional model configurations. We evaluate the spatiotemporal patterns of frost weathering in rock walls, exemplified by those situated in the Jotunheimen Mountains in southern Norway. In contrast to previous studies (Walder and Hallet, 1985; Rempel *et al.*, 2016) that are formulated in terms of a single initial crack size, we account for the population of initial, automatically mapped crack radii in a rock wall by using ensemble-based modelling. We focus on two rock walls below the Veslpiggen Plateau, located in the Galdhøpiggen massif, western Jotunheimen, central southern Norway. We use the same modelling profile as shown in Figure 3.1D.

Frost weathering model in 2D – We derived a two-dimensional version of the model by Rempel *et al.* (2016) (Subsection 2.5.1), using the same underlying equations that satisfy the mass balance. We compute spatiotemporal porosity changes Δn in two dimensions for each node with Cartesian coordinates x and y at time t:

$$\Delta n(x,y,t) = \frac{D\,\Delta T_c^{\alpha-1}}{\alpha}\int_{t_c}^{t}\Delta T(x,y,t)^{-\alpha}\left[\frac{\alpha}{\Delta T(x,y,t)}\big(\nabla T(x,y,t)\big)^2 + \nabla^2 T(x,y,t)\right]dt. \tag{4.1}$$

The accumulated porosity change for one year is defined as:

$$\Delta(x,y) = \frac{D\,\Delta T_c^{\alpha-1}}{\alpha} \int_{\Delta T>\Delta T_c, 1 year} \Delta T(x,y)^{-\alpha} \left[\frac{\alpha}{\Delta T(x,y)} \left(\nabla T(x,y)\right)^2 + \nabla^2 T(x,y) \right] dt. \tag{4.2}$$

We account for latent heat effects, and therefore we keep the second term, although its influence remains minor, because most freezing takes place at higher temperatures and sensible heat changes tend to be more important than latent heat effects in the temperature range where frost cracking occurs.

GT modelling – We run the CryoGrid 2D heat conduction model for four decades: (1) the YD/PB transition (c. 11.5 ka), (2) the HTM (c. 7.5 ka), (3) LIA (around 1750), and (4) the 2010s.

Simulations for the 2010s: We reuse methods for GT modelling presented in Paper II. In the previous simulations, the model was run at monthly time steps, which we consider insufficient for this study. Hence, we rerun the model using the output from the monthly time steps as the initial temperature for the daily runs. We adjust daily SAT from the seNorge data sets (Lussana, 2020) or data from meteorological stations if available, so mean monthly SAT in this study is the same as in Paper II. This procedure minimises the difference in comparison to previous runs and avoids the issues with the lapse rate in the seNorge data sets. Other methods are identical to those in Paper II.

Simulations for the YD/PB, HTM and LIA: As long-term air temperature, we use the TraCE-21ka data set (Liu *et al.*, 2009), filled with NGRIP ice core data (NGRIP, 2004) for the HTM. Mean annual SAT was computed along the profile using the long-term SAT data sets and the 2010s lapse rates. Subsequently, we compute monthly $SATs$ using the 2010s SAT amplitudes. Finally, GST is estimated using slope gradient-dependent nF-factors to account for snow cover and site- and aspect-specific monthly SOs to account for the incoming shortwave solar radiation in rock walls (Paper II). We run the first steady-state simulation for the permafrost model at the local deglaciation onset and assume a warm-based ice sheet with the basal temperature at the ice melting point (T_m). The estimated onset of deglaciation for the highest peaks at the Veslpiggen Plateau occurred around 12 ka, based on data from Hughes *et al.* (2015). We proceed with transient runs at yearly time steps until the YD/PB transition, HTM and LIA. During deglaciation, we use T_m for ice-covered parts along the profile and GST for unglaciated parts. We run the permafrost model at daily steps for one decade at the mentioned end periods using the same SAT amplitudes as for the 2010s, accounting for the SAT offset between the 2010s and YD/PB (-4.7 °C), HTM (+1 °C) or LIA (-3 °C).

Frost weathering modelling – We estimated K_{IC} from the uniaxial compressive strength and applied a uniform mean value of 1.7 MPa $m^{1/2}$. Crystalline bedrock at the study site has low k_0 with an assumed uniform value of 5×10^{-17} m^2 (Nilsen and Thidemann, 1993).

Note that the frost weathering model was formulated to account for homogeneous crack radii as defined in Equation (2.13) to set the upper-temperature limit for frost damage. In reality, a population of cm-scale, mode-I cracks is expected within a single rock wall, and hence a choice must be made for the characteristic crack radius c that is most relevant for the onset of significant frost weathering. In our study, instead of selecting a single value for c, we use the statistical distribution of crack radii that is approximated from the mapped crack lengths observed in a selected rock wall. We employed MATLAB-based software for ridge detection using the complex shearlet transform to detect automatically fractures based on an orthomosaic (Prabhakaran *et al.*, 2019). We conducted fieldwork to collect drone imagery from the 260 m high Kjelen rock wall, created an ultra-high quality dense point cloud in the photogrammetric Agisoft Metashape software using this imagery, and subsequently exported a 10 × 10 m orthomosaic with 1 cm^2 resolution for a section where the drone was closest to the rock wall. The algorithm gave satisfactory results for our rock wall section.

We implemented the frost weathering model according to Equation (4.1) and verified the implementation by comparing it with 1D runs shown by Rempel *et al.* (2016). We note that we do not aim at the application of the frost weathering model in a transient way for longer periods and present the results as annual averages for the four decades around 11.5 ka (YD/PB), 7.5 ka (HTM), 1750 (LIA) and the 2010s. We accumulate porosity change in each vertex in the finite element mesh for each year in each decade using Equation (4.2) and subsequently compute an annual mean. We run the model for the population of crack radii that define ΔT_c. By performing the statistical runs, we assume that there is no interaction between various cracks and that each crack grows independently of others, i.e. each model run for various ΔT_c is run independently.

4.4 ONE-DIMENSIONAL FROST WEATHERING MODEL

I run the 1D version of the frost weathering model (Subsection 2.5.1) for Norway and Iceland. The GT has to be modelled first. The other parameters not described here are the same as in Rempel *et al.* (2016).

4.4.1 GROUND TEMPERATURE MODELLING

I use an analytical solution to model the subsurface temperature $T(z,t)$ for each grid cell:

$$T(z,t) = MAGST - A\ \exp\left(-z\sqrt{\frac{\pi}{\kappa\, P_y}}\right)\cos\left(\frac{2\,\pi\,t}{P_y} - z\sqrt{\frac{\pi}{\kappa\, P_y}}\right), \qquad (4.3)$$

where $MAGST$ denotes the mean annual ground surface temperature, A denotes the amplitude of $MAGST$, P_y denotes the period of 365 days. Thus, the analytical model requires $MAGSTs$ and their amplitudes to be solved. I assume there is no snow, and $MAGST$ equals $MAAT$. Therefore, the model results are valid only for steep slopes where no snow accumulates. GST amplitudes are fitted values using the 2011–2020 SAT data and the following sinusoidal model:

$$SAT = MAAT - A\ \cos\left(\frac{2\,\pi\,(t+\phi)}{P_y}\right), \qquad (4.4)$$

where ϕ is the phase lag at the surface. In addition, κ has to be specified for each grid cell.

SAT for Iceland – I use the output from a 3D, time-integrated ice sheet model (Hubbard, 2006; Patton *et al.*, 2017) to obtain ice extent and spatial $SATs$ for Iceland for 14 and 12 ka at 1 km spatial resolution. Furthermore, I extract the average decadal $SATs$ for the 2011–2020 decade using the same daily $SATs$ as presented in Paper I. Fitted SAT amplitudes using Equation (4.4) are between 4 and 8 °C (mean value 6.2 °C) with the largest amplitudes in the mountainous areas and the smallest amplitudes in the coastal areas.

Thermal parameters for Iceland – The thermal conductivity of the mineral fraction is assumed to be 2 W $\mathrm{m^{-1}\,K^{-1}}$ (Flóvenz and Saemundsson, 1993). For low GTs, when there is little unfrozen liquid water left, and assuming bedrock porosity of 8 %, K is estimated to be 2.02 W $\mathrm{m^{-1}\,K^{-1}}$ from Equation (2.4) and C to be 2.046 MJ $\mathrm{m^{-3}\,K^{-1}}$

from Equation (2.3). Hence, the thermal diffusivity ($\kappa = K/C$) is assumed to be 0.985 $\mathrm{mm}^2\ \mathrm{s}^{-1}$.

SAT for Norway – For Norway, I use the gridded 1-km seNorge SAT data (Lussana, 2020). I extracted $SATs$ for the 2011–2020 decade and computed amplitudes by fitting SAT data to Equation (4.4). Estimated SAT amplitudes are between ~5.5 and 14 °C (mean value 8.7 °C). The largest amplitudes occur in Finnmark, which is an area with the most continental climate in Norway, together with the valleys. For previous periods, I assume uniform offsets in comparison with the 2010s decade: 6 °C lower $SATs$ 12 ka (YD), 1 °C lower $SATs$ over the LIA in Norway (~1750) and 2 °C higher $SATs$ during the HTM.

Thermal parameters for Norway – The same data for the thermal conductivity of the mineral fraction as presented in Westermann *et al.* (2013) are used. The values vary between 2.1 and 4.3 $\mathrm{W\ m^{-1}\ K^{-1}}$ with a mean value of 2.9 $\mathrm{W\ m^{-1}\ K^{-1}}$. Bedrock is assumed to have 5 % porosity and 95 % mineral fraction. K and C are estimated for low GTs from Equations (2.4) and (2.3), respectively. The estimated κ varies between 1 and 2 $\mathrm{mm}^2\ \mathrm{s}^{-1}$, with a mean value of 1.4 $\mathrm{mm}^2\ \mathrm{s}^{-1}$.

4.4.2 MECHANICAL AND HYDRAULIC PROPERTIES OF BEDROCK

Iceland – I assume that the entire Iceland is composed of basalt with K_{IC} of 0.87 MPa $\mathrm{m}^{1/2}$ (value from Atkinson, 1984, for Icelandic tholeiite, a type of basalt) and moderate k_0 equal to 10^{-14} m^2 (value for fractured basalt from Singhal and Gupta, 2010). The c value is assumed to be 5 cm, hence the upper-temperature limit for frost cracking onset is -3 °C and D is 8.7×10^{-5} $\mathrm{mm}^2\ \mathrm{s}^{-1}$.

Norway – There is more variation in bedrock type in Norway than in Iceland; hence, the spatial variation must be accounted for. The k_0 is assigned according to the main rock types: intrusive, extrusive, sedimentary, metasedimentary and metamorphic (Table A.1). K_{IC} is estimated from the uniaxial compressive strength σ_c using an equation from Chang *et al.* (2002):

$$K_{IC} = 4.28 \times 10^{-3}\, \sigma_c + 1.05. \tag{4.5}$$

The σ_c values listed in Table A.1 are from Norwegian studies on rock properties (Hanssen, 1988; Nilsen and Palmström, 2000). ΔT_c for the assumed c of 5 cm is generally higher than in Iceland, between 4.3 and 7.34 °C, meaning that much lower GTs are required for frost cracking onset in Norway than in Iceland.

4.5 ROCKFALL SOURCE DETECTION AND ROCK WALL RETREAT RATES

The term "rockfall" describes a small event (<100 m^3) of rock debris released from a rock wall (Ballantyne, 2018). Here, I estimate short-term (present-day) rock wall retreat rates using the total volume of the recent rockfall events from the Kjelen rock wall (Figures 4.3, 3.1D and 3.2) in the continuous permafrost zone, the Jotunheimen Mountains.

Rock wall retreat rate – Rock wall retreat rate R_r may be estimated using:

$$R_r = \frac{V}{A_r\ t}, \tag{4.6}$$

where V is the total volume of sediments, either from rockfalls for short-term estimation or the volume of sediments in a landform for long-term estimation, and A_r is an area of the contributing rock wall (Ballantyne, 2018). A_r is estimated to be around 187 000 m^2.

Long-term rock wall retreat rate – I also calculate the long-term, i.e. average Holocene, rock wall retreat rate of the same rock wall using the estimated volume of the ice-cored moraine in the Kjelen cirque (Figure 4.3). The latter is a simple volume estimation using a 0.25 m LIDAR-derived DEM from the Norwegian Mapping Authority (www.hoydedata.no/LaserInnsyn2/). A constant base surface of the landform is assumed at an elevation of 1835.51 m that corresponds to the lake level. The ice-cored moraine is assumed to contain 90 % ice by volume (e.g. Costa and Schuster, 1988). The rock wall is assumed to be on average 15 % smaller during the Holocene than at present, and deglaciation is assumed to have occurred 9 ka.

4.5.1 DATA ACQUISITION AND POSTPROCESSING

Terrestrial laser scanning (TLS) was used to acquire point clouds from the Kjelen rock wall 8 June 2021, 17 August 2021 and 31 August 2022. The Riegl VZ-1000 scanner type was used with a measurement program at a range of 950 m (150 kHz). Accuracy and precision for the scanner are listed by the producer as 8 and 5 mm. Scans from two different positions 172 m apart (3D distance) were collected during each field visit. A

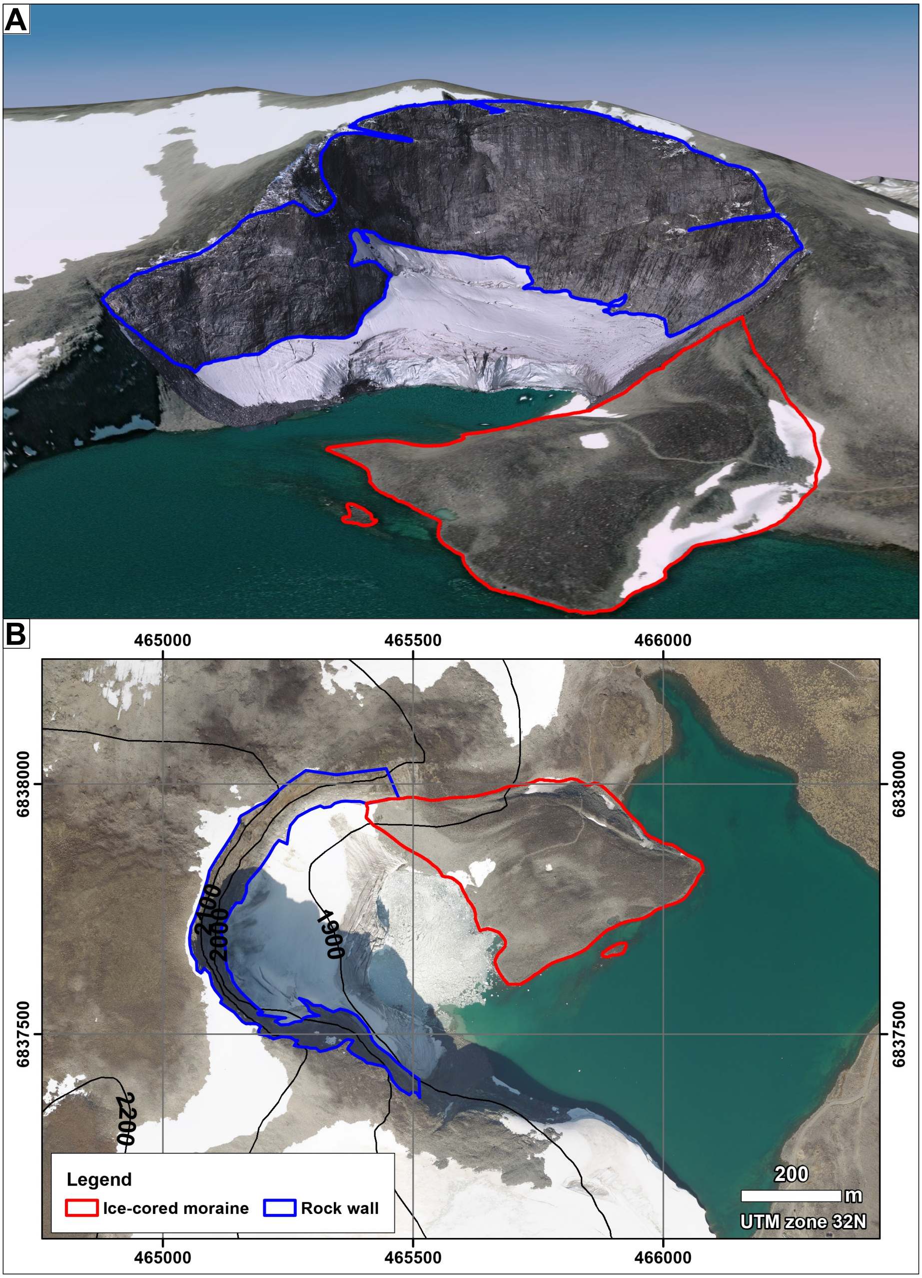

Figure 4.3: Rock wall and ice-cored moraine in the Kjelen cirque, the Juvflye area, southern Norway. **A.** Photogrammetric dense point cloud derived from drone imagery from August 2021 draped over 2.5D background courtesy of ©Mapbox, ©OpenStreetMap, ©Maxar. **B.** Overview map. Orthophoto credits: ©Statens kartverk, Geovekst og kommunene.

measuring program with 10 millidegrees angular spacing was used, with a resulting maximum point spacing (regular grid) of 0.12 m. However, the actual point spacing was usually better than 0.12 m. The precise position of the TLS scanner was measured using Topcon Legacy E+ differential GNSS receivers relative to a GPS base at a nearby survey marker. The data was georeferenced to Universal Transverse Mercator (UTM) coordinates using RiSCAN PRO 2.16.1. A least-squares adjustment was used to align the scans based on the fixed scan positions. Georeferencing errors are on the order of 1–2 cm (standard deviation). Fine coregistration between the point clouds was run in RiSCAN Pro ("Multistation adjustment") using the iterative closest point algorithm.

4.5.2 POINT CLOUD DIFFERENCING

Several methods for computing the distance between two point clouds from a steep rock wall are possible: (1) DEM of difference (DoD) after a suitable coordinate rotation, (2) Cloud-to-cloud (C2C) comparison, (3) Cloud-to-mesh (C2M) distance, (4) Multiscale Model to Model Cloud Comparison (M3C2) (Lague *et al.*, 2013). The differences in the point location and point density between the scans pose difficulties for point cloud comparison. The first three methods are inferior in comparison with the M3C2 algorithm, which proved to be suitable in my study area because the algorithm skips calculation if points are missing in one of the point clouds. Water flows on the rock wall surface; hence, there are many missing data points in the collected point clouds, especially the point cloud from 8 June 2021. For instance, C2C distance yields the largest surface changes where points were missing in one of the clouds. C2M may be possibly as accurate as M3C2; however, it was proved to be a less robust method when it comes to uncertainty estimation (Barnhart and Crosby, 2013).

The M3C2 principles – The M3C2 technique uses "core" points that are sub-sampled points with a specified minimum point distance (Lague *et al.*, 2013). The "core" points shorten the computation time. Note that M3C2 still computes the cloud differences using the full point cloud resolution. The M3C2 algorithm includes two computation steps (Figure 4.4): (1) calculation of surface normals, and (2) distance calculation between the two clouds. Normals $\overrightarrow{N}$ are computed for all points from a chosen point cloud within a radius $D_{M3C2}/2$ around the core point, oriented towards a chosen orientation. Normal scale D_{M3C2} should be chosen according to the application and D_{M3C2} should be generally large enough to minimise the roughness effects. It is recommended that D_{M3C2} is around 25–30 times larger than the roughness;

Table 4.1: The M3C2 parameters for the rockfall estimation.

Parameter	Value
Normal scale diameter D_{M3C2}	1 m
Projection scale diameter d_{M3C2}	0.3 m
Maximum cylinder length	2 m
Core points	Sub-sample cloud #1: 0.1 m

however, this rule does not apply if changes on the metre-size boulders are to be detected and roughness is desirable (Lague *et al.*, 2013). The second step uses a different scale, the so-called projection scale d_{M3C2}. The average positions around the core point at the projection scale are computed for both clouds by projecting a cylinder oriented along the normals computed in the first step. The maximum length of the cylinder is also defined to speed up the computations. The distance between the two average positions within the cylinder is the value that the algorithm assigns as the M3C2 distance. Finally, the algorithm assigns logical values indicating whether the computed distances are statistically significant based on the locally computed level of detection, which requires at least five points in each cloud to be computed (Lague *et al.*, 2013).

The M3C2 application – The M3C2 algorithm is included as a plugin inside the CloudCompare software (EDF R&D, 2023). I run the M3C2 algorithm for all possible combinations of point clouds. The M3C2 parameters that I use are listed in Table 4.1. The projection scale diameter should be as small as possible for rockfall extraction, according to the study by DiFrancesco *et al.* (2020). The latter study used a value of 0.2 m, which resulted in many missing statistical values in my results, hence I used a slightly larger value. The maximum cylinder length is selected after initial runs and chosen to be as small as possible to minimise errors. The non-significant surface changes, as assigned by the M3C2 algorithm, are excluded at this step.

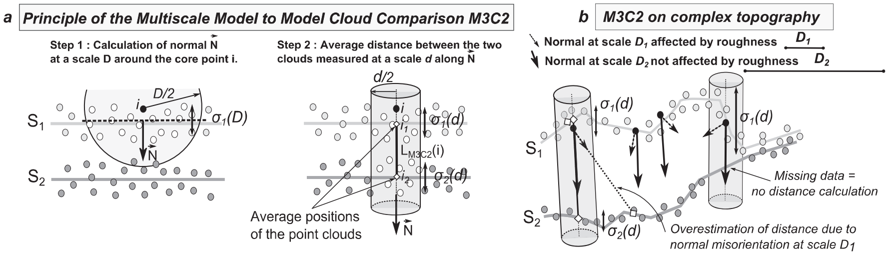

Figure 4.4: The M3C2 technique. Reproduced from Lague *et al.* (2013).

4.5.3 CLUSTERING ROCKFALL SOURCES AND VOLUME ESTIMATION

I extract backs of lost rock volume from the calculations forwards in time, and only values smaller than minus two standard deviations (here -0.0531 m) are kept, following Carrea *et al.* (2021). Similarly, I extracted the fronts of lost rock volume from the calculations backwards in time, and only values larger than two standard deviations are kept (here +0.0531 m). The resulting point clouds with the fronts and backs of lost objects are merged and used in the subsequent steps.

For the clustering of rockfall sources, I use MATLAB Virtual Toolbox for Retrospective Rockfall Source Detection and Volume Estimation presented in Carrea *et al.* (2021), available for download at https://wp.unil.ch/risk/software/PointCloudToolBox. The merged point clouds with the fronts of backs of lost objects also contain noise, and individual rockfall events should be clustered before volume estimation. This step includes a clustering algorithm, which removes noise and clusters data. The density-based clustering algorithm (DBSCAN) is included in the toolbox. DBSCAN clusters data using a chosen circular neighbourhood radius ε (here 0.3 m) and a minimum number of points k_{DBSCAN} (here 12) required within the radius to create a cluster. Furthermore, I filter the events based on the ratio of negative to positive or positive to negative points and set the threshold to three (van Veen *et al.*, 2017), so that a 3D volume object may be successfully reproduced.

To compute the 3D volume of each rockfall event, surface reconstruction is required, i.e. the discrete point cloud of each event must be converted to a mesh, usually a triangulated surface mesh. I employ the iterative alpha-shape algorithm (Bonneau *et al.*, 2019), which allows for the generation of a watertight, manifold surface, i.e. without any surface voids and with each edge connected to only one or two faces (Bonneau *et al.*, 2019).

4.6 MEASURING SOLIFLUCTION USING INSAR

The Juvflye area in the Jotunheimen Mountains, southern Norway (Figure 3.1D) has abundant stone-banked solifluction lobes (Figures 4.5 and 3.3). Solifluction in the area is measured using differential SAR interferometry (Section 2.6). The elevation of the investigated solifluction lobes varies from ~1400 m, the area with no permafrost, to an elevation at ~1800 m, where widespread permafrost occurs. The lobes at the upper elevation move primarily towards the north-west; hence, only the data from the descending track (heading angle ~199°) is used to measure their movement. The lobes at the lower elevation move towards the north-east; hence, only the data from the ascending track is used (heading angle ~-19°).

4.6.1 DATA AND INSAR PAIR PROCESSING USING GAMMA

The openly available C-band (frequency 5.405 GHz; wavelength 5.55 cm) SAR data from the European Space Agency Copernicus Sentinel-1 mission (Sentinel 1-A and 1-B satellites) is used. The L1 SLC data acquired in the Interferometric Wide (IW) mode is downloaded from the Alaska Satellite Facility webpage (search.asf.alaska.edu) for paths 37 (descending) and 44 (ascending). Incidence angles for the descending track are 41.10–41.17° and for the ascending track are 37.97–38.03°. The data sets

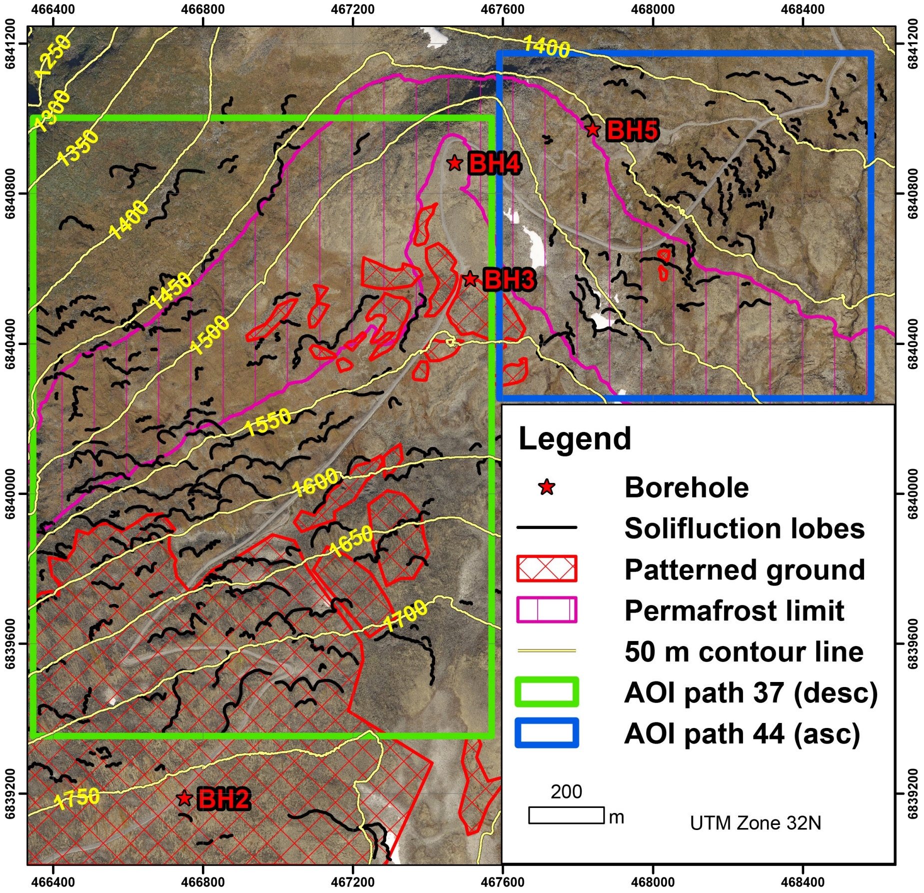

Figure 4.5: Map of solifluction lobes and patterned ground, the Juvflye area, southern Norway. Map background credits: ©Statens kartverk, Geovekst og kommunene. *AOI* - area of interest.

from assumed snow-free periods (1 June–31 October) in years 2017–2022 with a 6- to 12-day revisit period are used.

SLC data is processed in the commercial software developed by GAMMA Remote Sensing (www.gamma-rs.ch) to obtain multiple pairs of interferograms for temporal baselines between 6 and 360 days. No limit on the perpendicular baseline is used since Sentinel-1 baselines rarely exceed critical perpendicular baselines. The data processing follows the standard InSAR methodology described in Section 2.6. The SLC data is coregistered using a 10 m DEM from the Norwegian Mapping Authority (www.hoydedata.no/LaserInnsyn2/) and the contribution of the topographic phase is simulated based on the same DEM. The interferograms are generated using 4 range looks and 1 azimuth look to ensure as fine ground resolution as possible since the investigated landforms are small. The signal-to-noise ratio of the processed interferogram is enhanced using adaptive phase filtering (Goldstein and Werner, 1998). Additionally, areas with a coherence threshold below 0.3 are masked out from the wrapped phase before unwrapping using the Minimum Cost Flow (MCF) algorithm. The ionospheric delay is probably small for the investigated latitudes far away from the geomagnetic equator and C-band (Liang *et al.*, 2019); hence, it is not corrected in this step. However, it may be later removed in InSAR time series analysis using phase deramping. Finally, the data is terrain-corrected and geocoded to a ground resolution of 20 × 20 m.

4.6.2 INSAR TIME SERIES ANALYSIS USING MINTPY

The open-source Miami INsar Time-series software in PYthon ("MintPy"; www.github.com/insarlab/MintPy) by Yunjun *et al.* (2019) is used for InSAR time-series analysis. The MintPy software implements the classic SBAS workflow (Berardino *et al.*, 2002). The georeferenced, unwrapped interferograms and coherence files from GAMMA are used as input to MintPy.

Network inversion for time-series – The network of interferograms is created by a selection of unwrapped interferograms with an average spatial coherence of at least 0.45. The network contains 1368 interferograms for the descending path and 1273 interferograms for the ascending path (Figure 4.6). A pixel with high spatial coherence and located on stable ground is chosen as the reference point, i.e. a common reference pixel for all interferograms to ensure consistent spatial reference. Several reference pixels are tested, and the point with the least noisy results is selected. The network of interferograms is inverted into single-date reference interferograms, i.e. time series, using the weighted least square estimator with the inverse of covariance as weights (Yunjun *et al.*, 2019). The latter method gives more weight to pixels with high coherence than pixels with low coherence (Yunjun *et al.*, 2019), which is especially important here for reducing the impact of snow cover. The MintPy software uses temporal coherence as a measure of the reliability of network inversion (from 0-unreliable to 1-reliable), and a threshold of 0.7 is used for masking out the results. MintPy does not require any assumptions about the linear deformation model; hence, it is suited for measuring nonlinear displacements (Yunjun *et al.*, 2019).

Noise reduction of displacement time-series – MintPy allows for tropospheric delay correction using weather reanalysis model corrections and height correlation. The weather reanalysis model corrections do not seem to improve and even worsen the results for the small area of interest (AOI) used here, which is in agreement with the study of Murray *et al.* (2019) showing that such corrections significantly improve the results for much larger spatial scales (> 75 km). The empirical phase elevation approach is also omitted. Furthermore, a residual long spatial wavelength

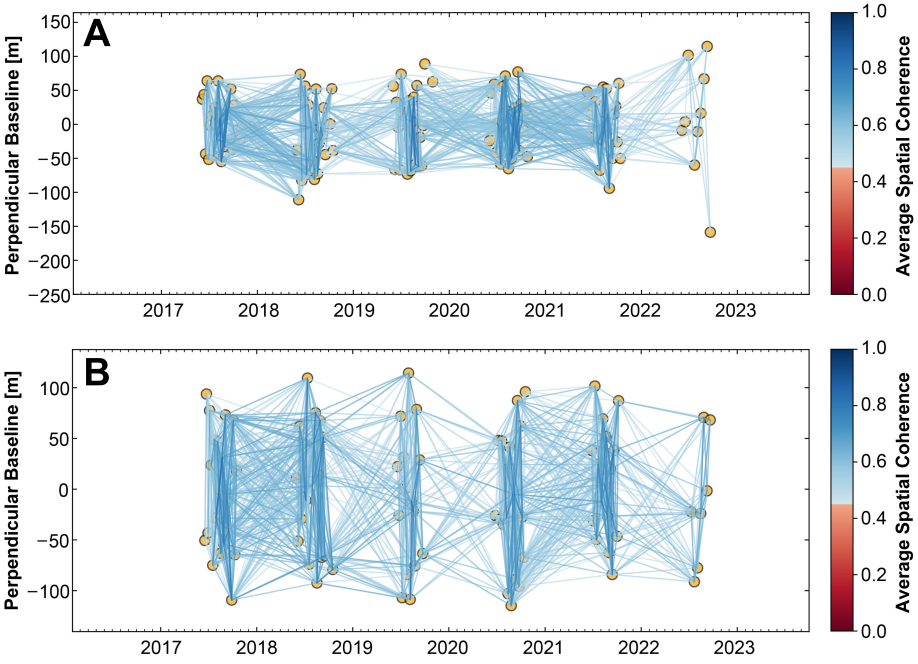

Figure 4.6: Interferogram network for **A.** the descending path 37 and **B.** the ascending path 44.

component, due to e.g. geometry or atmospheric delay, is removed using phase deramping. The topographic residual phase may also be estimated and removed in MintPy, although it introduces more noise and is omitted. After the corrections, noisy acquisitions with a root mean square (RMS) greater than three times the median RMS of the residual phase are removed.

Velocity estimation – The average LOS velocity V_{LOS} for each pixel over 2017–2022 is computed assuming a linear trend. In terms of solifluction movement, it would be preferable to compute vertical, downslope or horizontal velocity, which is more meaningful than the LOS velocity. Solifluction encompasses several displacement vectors, involving frost heave in autumn and winter, and subsequent smaller subsidence during summer with a small horizontal component, resulting in a net movement downslope (Matsuoka, 2001b). Hence, it is challenging to define the predominant displacement direction, whether it is vertical, horizontal or downslope. The vertical vector is assumed here to be larger than the horizontal during summer, also because InSAR is more sensitive to vertical deformation due to the steep incidence angle. Thus, V_{LOS} is projected onto vertical velocity V_z for each pixel, assuming negligible horizontal displacement as follows:

$$V_z = \frac{V_{LOS}}{\cos(\theta_{inc})}, \tag{4.7}$$

where θ_{inc} is the incidence angle.

4.6.3 STATISTICAL MODELLING OF ACTIVITY

The pixels with the LOS velocity <-1.5 mm a^{-1} are defined as active areas (value 1) and all other areas as inactive (value 0). The relationship between activity and environmental variables is modelled using individual models available in the `biomod2` package (version 4.2-4; Thuiller *et al.*, 2009) implemented in the R software environment. The following models are employed: ANN (Artificial Neutral Networks), GBM (Generalised Boosted Regression), GLM (Generalised Linear Model), MARS (Multivariate Adaptive Regression Splines), RF (Random Forest) and XGBoost (eXtreme Gradient Boosting). The sample is divided into calibration (95% data) and validation (5% data) data sets. The models are initially tuned together using the default tuning parameters and subsequently fine-tuned if model under- or overfitting is obvious in the response curves due to outliers. Each model is run twice.

For spatial analysis, rasters are snapped to the same 20 × 20 m pixels as measured by DInSAR. The 10 m DEM from the Norwegian Mapping Authority (www.hoydedata.no/LaserInnsyn2/) is resampled to a resolution of 20 m. Additionally, high-resolution optical imagery from the PlanetScope constellation consisting of around 200 Dove CubeSats (Planet Labs, 2023) is employed. Atmospherically corrected surface reflectance image products at level 3B with 3 m per pixel resolution and four spectral bands (Blue, Green, Red, NIR) are obtained through the Planet's Education and Research Program, which allows non-commercial access to academia. The following environmental variables are used in the statistical modelling of activity:

1. ***Slope.***
2. ***TWI.*** Topographic wetness index (TWI) is a measure of soil wetness considering topographic factors, both the tendency of water to collect at any given location, through specific contributing area (SCA), and how likely that water drains downslope through the use of an approximate hydraulic gradient $\tan(\theta_{slp})$ (Quinn *et al.*, 1991). TWI is defined as:

   $$TWI = \ln \frac{SCA}{\tan(\theta_{slp})}. \tag{4.8}$$

   SCA is calculated in SAGA (Conrad *et al.*, 2015) using the "Flow accumulation" tool and selecting multiple flow direction algorithm (Freeman, 1991; Quinn *et al.*, 1991). In the multiple flow direction algorithm, the flow from a cell is distributed to all adjacent lower cells, and a portion of the catchment is passed to a lower cell according to slope-dependent weights.
3. ***Mean NDVI.*** Normalised difference vegetation index ($NDVI$) is based on the spectral reflectances in the near-infrared (ρ_{NIR}) and red wavelengths (ρ_{Red}) as follows:

   $$NDVI = \frac{\rho_{NIR} - \rho_{Red}}{\rho_{NIR} + \rho_{Red}}. \tag{4.9}$$

   $NDVI$ is computed using the cloud-free PlanetScope imagery from July and August 2017–2022.
4. ***Snow factors.*** Snow-covered area (SCA) is mapped using reflectance values in the blue wavelength (e.g. Thaler *et al.*, 2023) from the cloud-free 3B-level Surface Reflectance PlanetScope scenes (Planet Labs, 2023). Thresholds for a binary classification of "snow" and "non-snow" pixels are assigned manually for each acquisition. The automatic extraction of thresholds, as shown in Thaler *et al.* (2023), was initially attempted; however, it resulted in many

Table 4.2: The CryoGrid 2 parameters.

Parameter [unit]	Value
Thermal conductivity of bedrock $\left[\mathrm{W\,m^{-1}\,K^{-1}}\right]$	2.7
Geothermal heat flux $\left[\mathrm{mW\,m^{-2}}\right]$	33
Snow density $\left[\mathrm{kg\,m^{-3}}\right]$	350
Thermal conductivity of snow $\left[\mathrm{W\,m^{-1}\,K^{-1}}\right]$	0.40

misclassified pixels. The classified images are subsequently resampled to 2 m ground resolution and aggregated to the fractional snow-covered area ($fSCA$, e.g. Salomonson and Appel, 2004), which is a fraction of snow cover in a single image pixel, here 20 × 20 m. 298 acquisitions from 225 various days between 2017 and 2022 are classified. Snow factors, i.e. a ratio of snow depth relative to snow depth from the gridded 1-km seNorge data (Lussana, 2020), are obtained pixel-wise through testing a range of snow factors from 0 to 6 at 0.05 increments. The snow factor that agrees best with the observed snow end date is chosen as the final snow factor for a pixel. The snow end date is chosen as the first date with no snow cover after the observed snow depletion onset, which is the last date with the maximum $fSCA$ for a given melt season.

5. ***GT.*** GT is modelled using CryoGrid 2 (Subsection 2.2.1). The model forcing is computed from SAT measured at the borehole sites BH4 and PACE (Figure 3.1D). SAT data are linearly inter- or extrapolated to the elevation of the grid cells, using the two borehole sites at different elevations as a reference. The average nT-value observed at the borehole sites in the Juvflye area, namely 1.2 is used for sparsely vegetated areas ($NDVI < 0.4$). The data from the BH4 borehole are only available from 2008; hence, it is filled with the seNorge data before 2008. The model is run for 2000–2022 at daily time steps. The initialisation period is the first five years. The chosen model parameters and ground stratigraphy are listed in Tables 4.2 and 4.3. The modelled area includes the boreholes BH2, BH3, BH4 and BH5 (Figure 4.5). To achieve sufficient spatial distribution for 20 m cells, snow depth from the seNorge (Lussana, 2020) is adjusted by using snow cover fractions estimated from the observed depletion onset and snow end dates. For the years before 2018, average observed depletion onset and snow end dates are used. Finally, the average GT over 2018–2022 is computed.

Table 4.3: Ground stratigraphy.

z [m]	$\theta_{mineral}$ [–]	θ_{water} [–]	θ_{air} [–]
Thin till (elevation ≤ 1600 m)			
0.0–1.0	0.70	0.03	0.27
1.0–1.5	0.70	0.02	0.28
>1.5	0.99	0.01	0.00
Blockfields (elevation > 1600 m)			
0.0–2.0	0.50	0.10	0.40
2.0–4.0	0.70	0.30	0.00
>4.0	0.99	0.01	0.00

5. RESULTS

5.1 ONE-DIMENSIONAL MODELLING OF PERMAFROST IN ICELAND (PAPER I)

The 50 % precipitation run indicates that permafrost exists in significant areas of northern and central Iceland (Figure 5.1). Permafrost extent is substantially smaller in the run with average precipitation (100 % precipitation), where permafrost areas are simulated in the Tröllaskagi peninsula and the adjacent southern areas, the western part of Norður-Múlasýsla, and regions north of Langjökull and Vatnajökull. The last run with 150 % precipitation reveals the most limited permafrost occurrence in Iceland, primarily in the Tröllaskagi peninsula. The runs indicate that the Tröllaskagi peninsula and its surroundings have Iceland’s coldest permafrost. The modelled GTs increased in the Tröllaskagi region between the decades of the 1980s and 2000s (Figure 5.1).

Throughout the same decades, the 50 % precipitation run reveals ~3–5 and ~8–15 times more cells with permafrost than the 100 % and 150 % precipitation runs, respectively. The difference in the number of cells with modelled permafrost is less pronounced for 100 % and 150 % precipitation cases, with ~2–3 times more cells in the 100 % precipitation run. The number of modelled permafrost cells decreases over the subsequent periods, with the lowest number of cells with permafrost in the period 2010–2016, when it is reduced by 34 %, 56 % and 49 % for the 50 %, 100 % and 150 % precipitation runs, respectively, in comparison with the period 1980–1989. Assuming equal contribution of each precipitation scenario to a grid cell, the estimated permafrost area over the period 1980–1989 is ~11 495 km^2 (~11 % of Iceland’s land area) and ~6 936 km^2 over the period 2010–2016 (~7 % of Iceland’s land area). This implies a reduction of the permafrost area by ~40 % in Iceland between these two periods.

According to the runs, Iceland has predominantly shallow permafrost, which is likely a consequence of the high geothermal heat flux and generally warm permafrost, as well as the low water content in the soil. The model indicates an increase in the lower limits of permafrost from north to south, where the limits depend on the precipitation assumptions. The lower permafrost limits range from ~600–900 m in the north to ~800–1000 m in the south.

The sensitivity tests show that the following tested parameters influence the modelled *GT* in Iceland the most (in order of importance): (1) the thermal

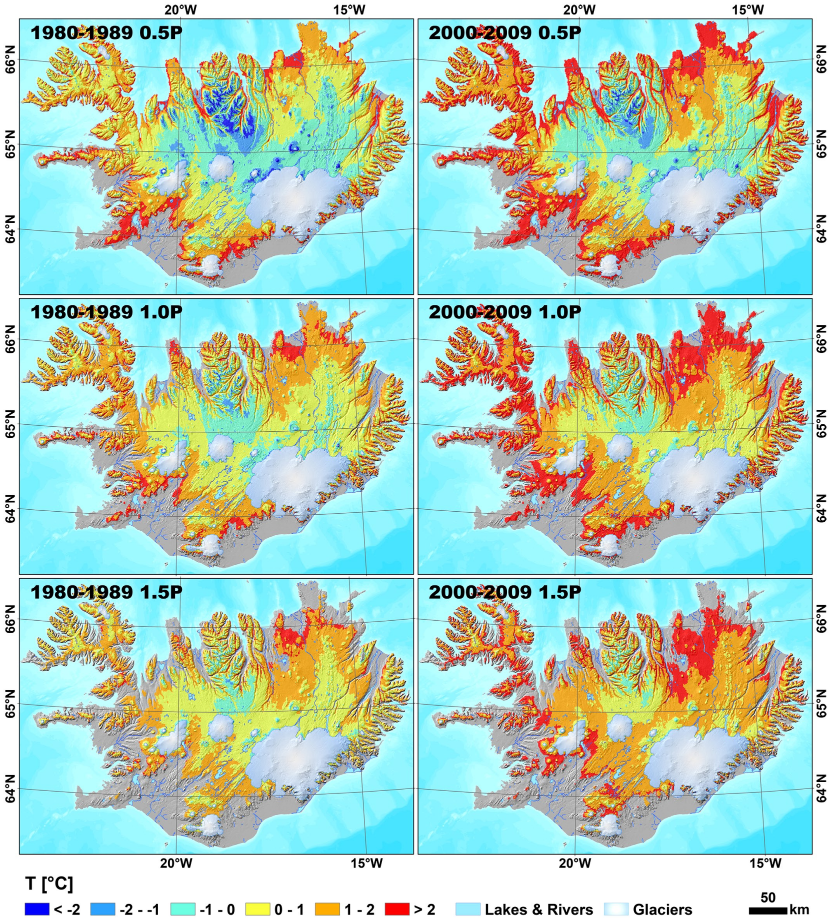

Figure 5.1: Distribution of the simulated average *GT* at 2 m depth in the periods 1980–1989 and 2000–2009 for the three precipitation cases: "0.5P" – 50 % precipitation, "1.0P" – 100 % precipitation, "1.5P" – 150 % precipitation. Permafrost cells are displayed in blue hues. Map data from the National Land Survey of Iceland.

conductivity of the snow, (2) precipitation fraction, (3) water content in the upper layer, (4) snow density, mineral content in the upper layer and the thermal conductivity of the mineral fraction. The validation of the 50 % precipitation run against recorded GTs results in an $RMSE$ of up to 0.54 °C and a mean error of up to 0.52 °C at both 1 and 2 m depths for all boreholes in Iceland. The visual validation of the model against the occurrence of permafrost landforms shows that permafrost is simulated where most of the landforms occur, although some smaller landforms may not be modelled as permafrost owing to the 1 km^2 ground resolution.

5.2 TWO-DIMENSIONAL MODELLING OF ROCK WALL PERMAFROST IN NORWAY (PAPER II)

The main simulations for the mountain peaks in Western Norway below 1400 m (Mannen and Ramnanosi) indicate no permafrost in these mountains after the LIA. The simulations for the higher mountain peaks in Western Norway (Hogrenningsnibba and Kvernhusfjellet) suggest that sporadic to discontinuous permafrost occurs in these mountains, with the simulated lower limits of permafrost ranging from 1300 m for the NNE-facing slope at Hogrenningsnibba to ~1600 m for the W-facing slope at Kvernhusfjellet over the 2010s. The reproduced lower limits of permafrost in Jotunheimen are at ~1530–1950 m over the 2010s. The simulated lower permafrost limits in northern Norway vary between 700 m for the SW-facing slope at Ádjit, 750 m at the NE-facing slope at Gámanjunni, to 900–1000 m at Rombakstøtta over the 2010s.

The dominant ground heat flow direction is often vertical underneath larger plateaus (e.g. Ramnanosi, Mannen, and Galdhøe). The main heat flux direction is more tilted towards colder zones for the mountains with more pronounced differences in GST between opposite mountainsides (e.g. Hogrenningsnibba, Kvernhusfjellet, and Gámanjunni). The tilt between opposite mountainsides may even be horizontal beneath the sharper mountains, where two mountainsides are closer together and there are greater differences in GST between them (e.g. Ádjit, Hogrenningsnibba).

GTs are simulated to be higher beneath the warm-based glaciers at Veslpiggen, with no permafrost present beneath the thickest parts of the glaciers (Figure 5.2a). The primary heat flow direction under the Veslpiggen Plateau changes significantly when glaciers are removed, shifting from the tilted heat flux (between the E-facing slope and the blockfield-covered plateau) to the one-dimensional vertical heat flux in the

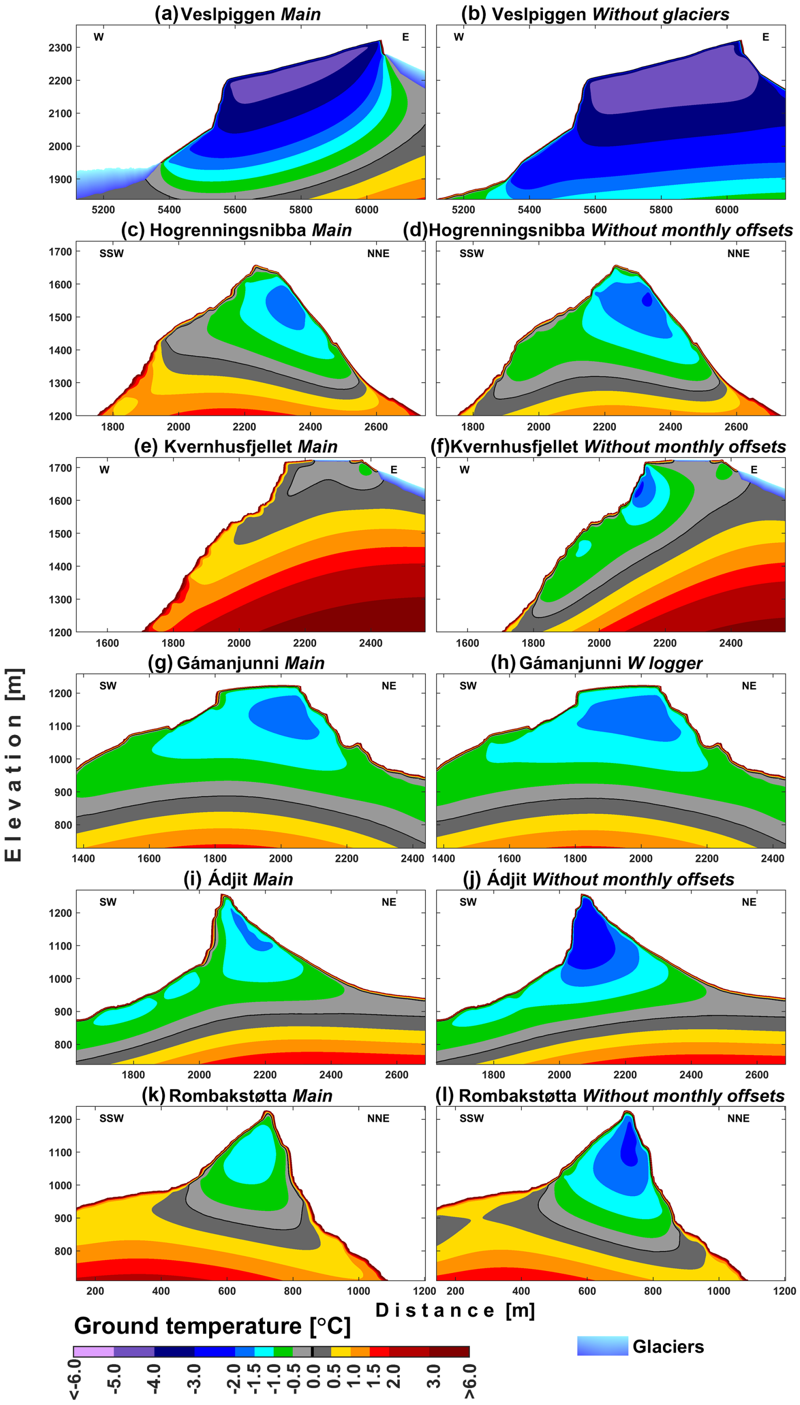

Figure 5.2: Simulated average annual maximum GT over the 2010s for various simulations.

simulation without glaciers (Figure 5.2b). Steepness and the assumed SOs influence the simulated GTs. For instance, ignoring SOs at the steeper Kvernhusfjellet leads to much lower GTs in the whole mountain than when ignoring SOs at the moderately steep Hogrenningsnibba (Figure 5.2c-f). Asymmetric lower permafrost limits at Gámanjunni are not associated with the higher SOs applied to the SW-facing rock wall and are rather caused by the extent of steeper terrain in the profile. The NE-facing slope is rougher and has multiple smaller rock walls, whereas the SW-facing slope consists of one smoother rock wall, less than 50 m in height. The influence of geometry is evident in the “W logger” simulation (Figure 5.2h), where we applied slightly colder forcing to the SW-facing rock walls, and the results still show lower GT in the NE-facing slope. In contrast to the Gámanjunni geometry, the SW-facing rock wall at Ádjit is steeper than the slope facing NE; hence, the SW-facing slope is colder than the NE-facing slope in the simulation without SOs (Figure 5.2j).

We also examine how the distribution of GT varies with elevation for all simulations and profiles at a depth of 20 m in rock walls. Simulations without SOs and with small SOs (annual mean ≤0.5 °C) yield the coldest midsection in a single rock wall. The largest GTs for simulations with large SOs are found in the middle of higher rock walls (> 50 m high, e.g. Veslpiggen). 20 m GT distribution in smaller rock walls (e.g. Gámanjunni, Kvernhusfjellet) is mostly caused by the assumed snow cover, depending on the distribution of the various terrain types in the vicinity of a single rock wall. GT increases with elevation if the terrain above a single rock wall is gentler than the terrain below this single rock wall (i.e. more snow above than below), and the opposite is modelled if the terrain above is steeper than the terrain below (i.e. less snow above than below). Larger rock walls below mountain plateaus (e.g. Rombakstøtta), where GT rises with elevation from a rock wall section’s midpoint, also show the thermal impact of snow cover on the plateau. Due to the strong thermal impact of glaciers, GT decreases with elevation for the uppermost east-facing rock wall at ~2300 m at Veslpiggen (Figure 5.2e), which has glaciers below and blockfields above.

Figure 5.3 shows simulated GT trends since the 1900s. The profiles’ steepest sections respond most strongly to warming and cooling trends in SAT. Nevertheless, because we used a large nF-factor in our simulations, the simulated GT in the Jotunheimen blockfields is also strongly coupled with the SAT. Moreover, at the topmost parts of the sharp mountain peaks (Ádjit, Rombakstøtta), 2D effects substantially affect modelled GT trends. Because the sites in northern Norway had the greatest SAT rise at the start of the 20th century, the simulated GT increase is

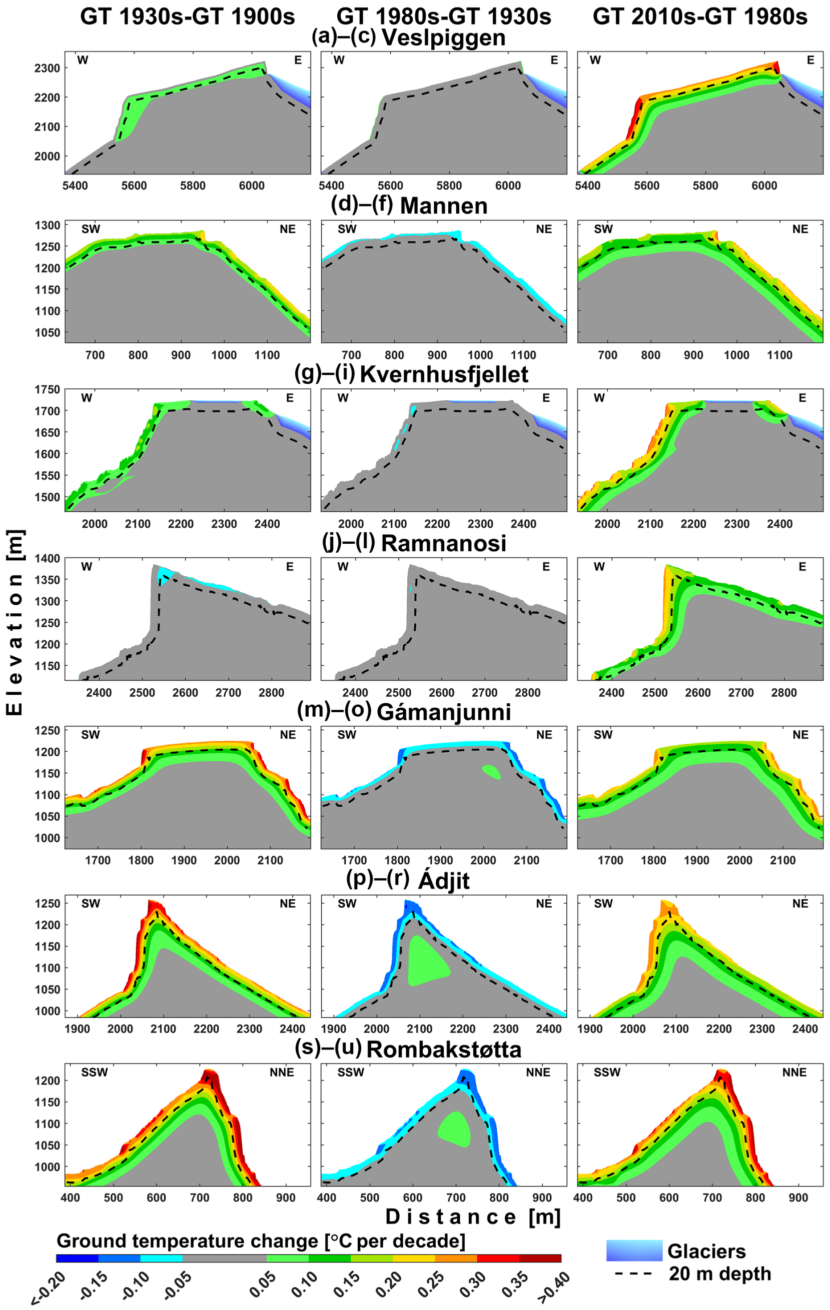

Figure 5.3: Rate of change in simulated decadal mean *GT* for the various profiles between the following decades: (1) the 1900s and 1930s, (2) the 1930s and 1980s, (3) the 1980s and 2010s.

greater between the 1900s and 1930s than between the 1980s and 2010s. All other sites had the greatest GT increase between the 1980s and the 2010s (Figure 5.3). Over the last four decades, GT at 20 m depth increased on average by 0.2 °C per decade in the rock walls. Since we allowed GST at blockfield-covered plateaus to be relatively strongly coupled with SAT, two-dimensional warming is more effective in rock walls below plateaus, and the Jotunheimen region has the greatest simulated mean 20 m GT rise (0.25 °C per decade). Ádjit has larger warming rates than Gámanjunni, especially at higher elevations, demonstrating the increasing relevance of the two-dimensionality because the former has a sharper peak. In general, modelled warming rates seem to increase towards the top of a single rock wall segment. It is expected that the 2D effects increase with elevation in a single rock wall just based on the topography of the study sites since, for a 2D profile, the distance from the surface above a rock wall to a 20 m depth in a rock wall below is shorter than the distance from the surface below a rock wall to a 20 m depth in a rock wall above. Glaciers reduce ground warming in nearby rock walls. In addition, assumed snow conditions have a large influence on simulated warming rates, and any snow accumulation in rock walls leads to lower warming rates.

5.3 TWO-DIMENSIONAL FROST CRACKING MODEL FOR ROCK WALLS IN NORWAY (PAPER III)

The results of the porosity model are presented for two cases: (1) one in which ΔT_c is 6.1 °C for the median crack radius of 4.86 cm (Figure 5.4A), (2) and one in which Δn is computed as a mean of the ensemble-based simulations for the sample of ΔT_c (Figure 5.4B). We also computed the average Δn with depth for the different zones shown in Figure 5.4: blockfields occur in zones 1 and 6, moderately steep slopes occur in zones 2 and 8, rock walls with various expositions occur in zones 3 and 7, parts of rock walls that were or still are just at an elevation of an ice sheet or a glacier occur in zones 4 and 9, and previously or currently glaciated segments of the profile occur in zones 5 and 10. Figure 5.5 shows the average profiles of porosity change Δn with depth in the various zones.

The results for the median crack radius simulations, where the frost cracking may only occur at quite low GTs (< -6.1 °C), suggest that the frost cracking potential was greatest during the coldest YD/PB period. Due to the largest simulated GTs in the HTM, frost cracking was least prevalent in this period, except in profile segments where the present-day glacier was assumed to be absent. The LIA frost weathering potential is modelled to be slightly smaller than the YD/PB frost weathering potential. The 2010s frost weathering potential is smaller than the LIA frost weathering potential and larger than the HTM frost weathering potential. The ensemble simulations allow for frost cracking operating across wider climatic conditions; hence, the computed Δn is always larger and reaches deeper than in the median crack radius simulations. The ensemble simulations' temporal variations in Δn are substantially smaller than

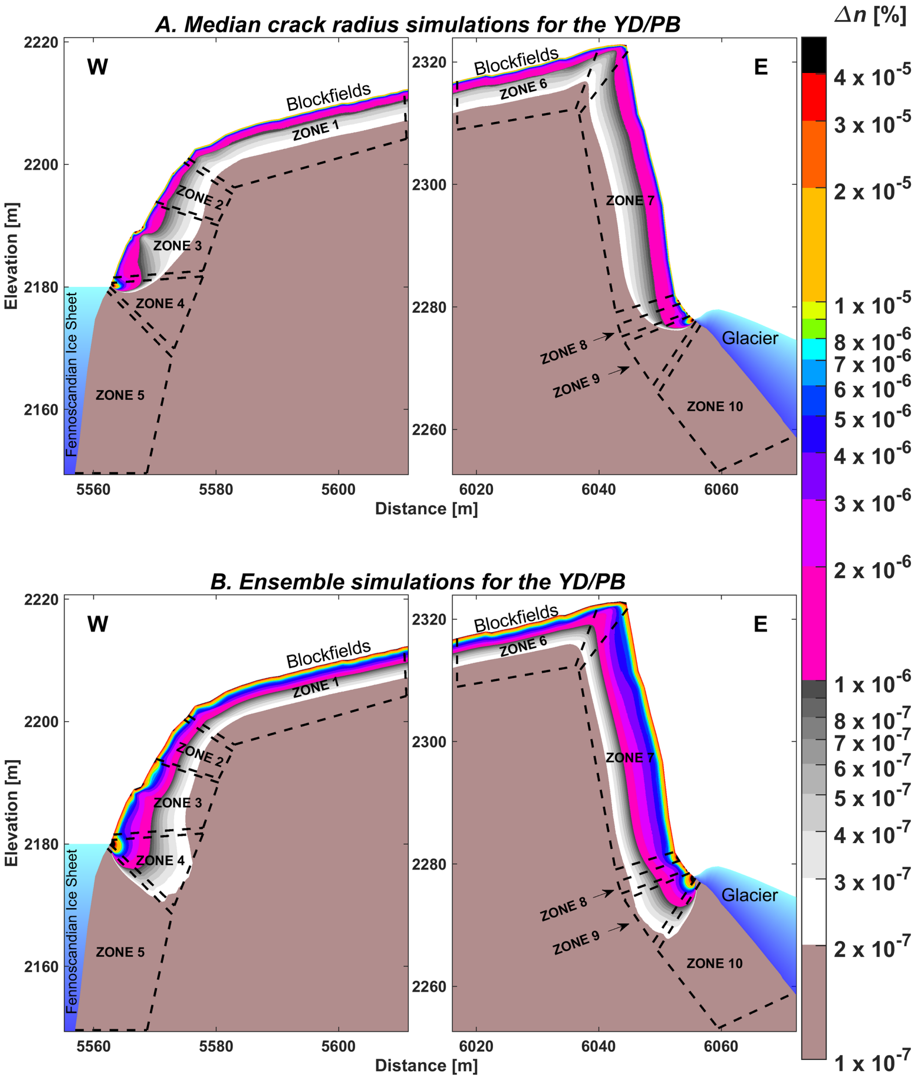
A. Median crack radius simulations for the YD/PB

B. Ensemble simulations for the YD/PB

Figure 5.4: Porosity changes Δn in the Veslpiggen Plateau over the YD/PB from **A**. Median crack radius simulations, and **B**. Ensemble simulations. Note the log scale.

those of simulations with the median crack radius. In contrast to the simulations with the median crack radius, the ensemble simulations indicate that, depending on the zone, the YD/PB is not always the period with the highest potential for frost cracking. In the ensemble simulations, the LIA period also has a significant frost-cracking potential. According to the ensemble runs, the HTM typically has the lowest potential

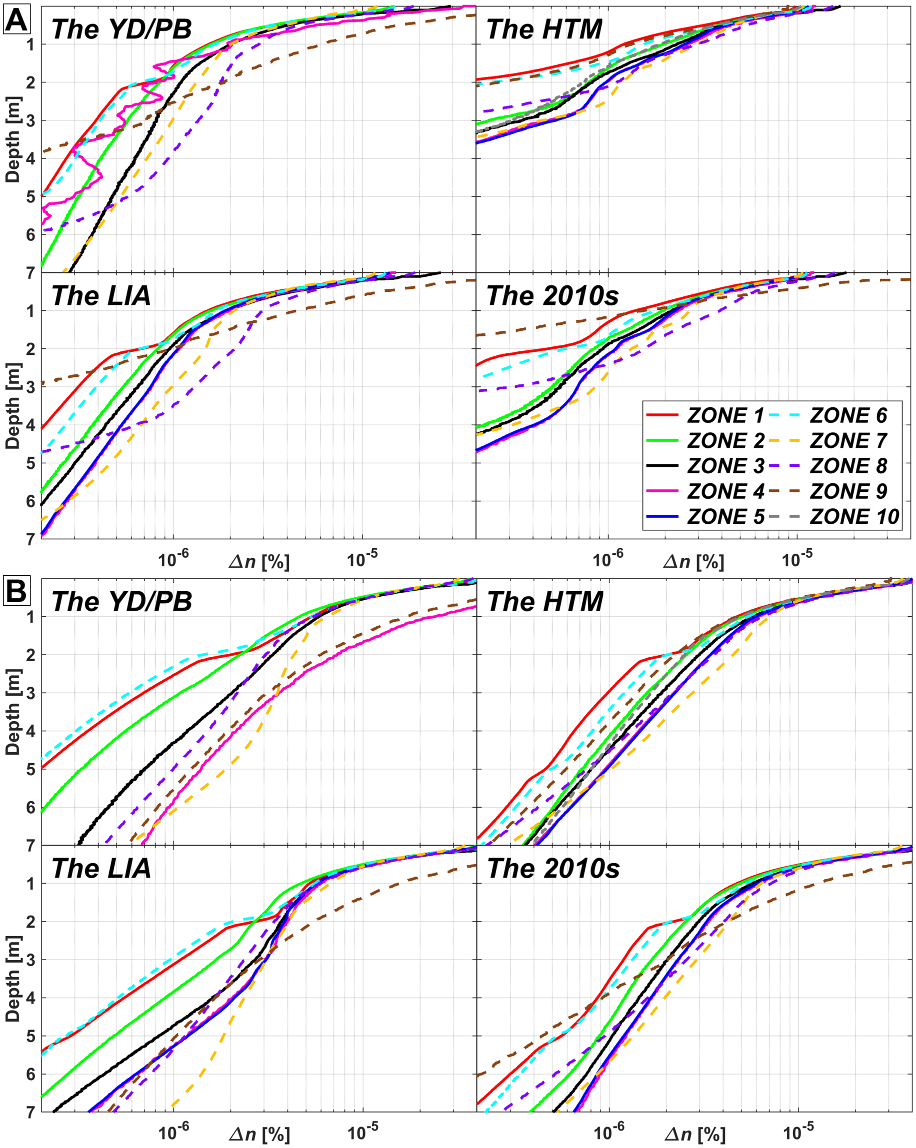

Figure 5.5: Average profiles of porosity change Δn with depth in zones shown in Figure 5.4 for **A**. Median crack radius simulations, and **B**. Ensemble simulations. Note the log scale.

for weathering in the rock walls. The median crack radius simulations show the biggest frost damage potential for colder climate conditions, whereas the ensemble simulations favour slightly warmer climate conditions for the shaded rock walls and colder climate conditions for the sun-exposed rock walls. Ensemble simulations show an average value from 500 simulations with various crack radii, and we evaluated which single crack radius would produce the most similar results to the ensemble simulations. The results suggest that a crack radius of around 8 to 9 cm dominates the mean computed in the ensemble simulations, which is a larger radius than the median crack radius of 4.86 cm.

In the GT modelling, we used the assumption that the slope gradient affects the snow distribution and that rock walls (slope gradient > 60°) are snow-free. We also included SOs caused by incoming shortwave solar radiation in the rock walls. Therefore, rock walls are the areas with the largest GST amplitudes, both in winter and summer. The GST has an amplitude of around 12 °C at the east-facing rock wall, 9 °C at the west-facing rock wall, and 5 °C at the blockfield-covered plateau. The results are influenced by the GT modelling's assumptions, and rock walls generally have the most potential for frost weathering along the profile.

Additionally, the ensemble and median crack radius simulations for different periods and zones produced similar findings, suggesting that the climatic conditions are not a limiting factor for frost cracking in the top 1 m of the subsurface. The variations appear to be more noticeable at depth. Nonetheless, there are some locations where the possibility of frost cracking is significantly higher near the surface than it is elsewhere, even in the top 1 m. These locations include rock walls that were or are currently just at the elevation of an ice sheet or glacier surface. The surface of a melting ice sheet or glacier and any other location where we anticipate an abrupt shift in snow conditions are the important spots for frost cracking, according to all simulations. In these locations, large ground thermal gradients are modelled. The temperature at the glacier bed was assumed to be 0 °C; hence, the areas between the rock walls and the melting ice sheet on the west-facing rock wall (YD/PB) and the glacier on the east-facing rock wall (except HTM) have particularly large ground thermal gradients, resulting in large frost cracking potential. Additionally, our assumption that the slope gradient and snow distribution are related results in a sharp transition in GST in the regions where the slope gradient abruptly changes, creating large thermal gradients in these regions close to the surface, where the majority of frost cracking occurs. The critical zones for enhanced frost weathering are most pronounced in the YD/PB and they become weaker in the later periods.

5.4 ONE-DIMENSIONAL FROST WEATHERING MODEL

5.4.1 ICELAND

The modelled depth-integrated annual increase in porosity λ for northern Iceland is shown in Figure 5.6. The largest frost cracking potential, according to the λ values,

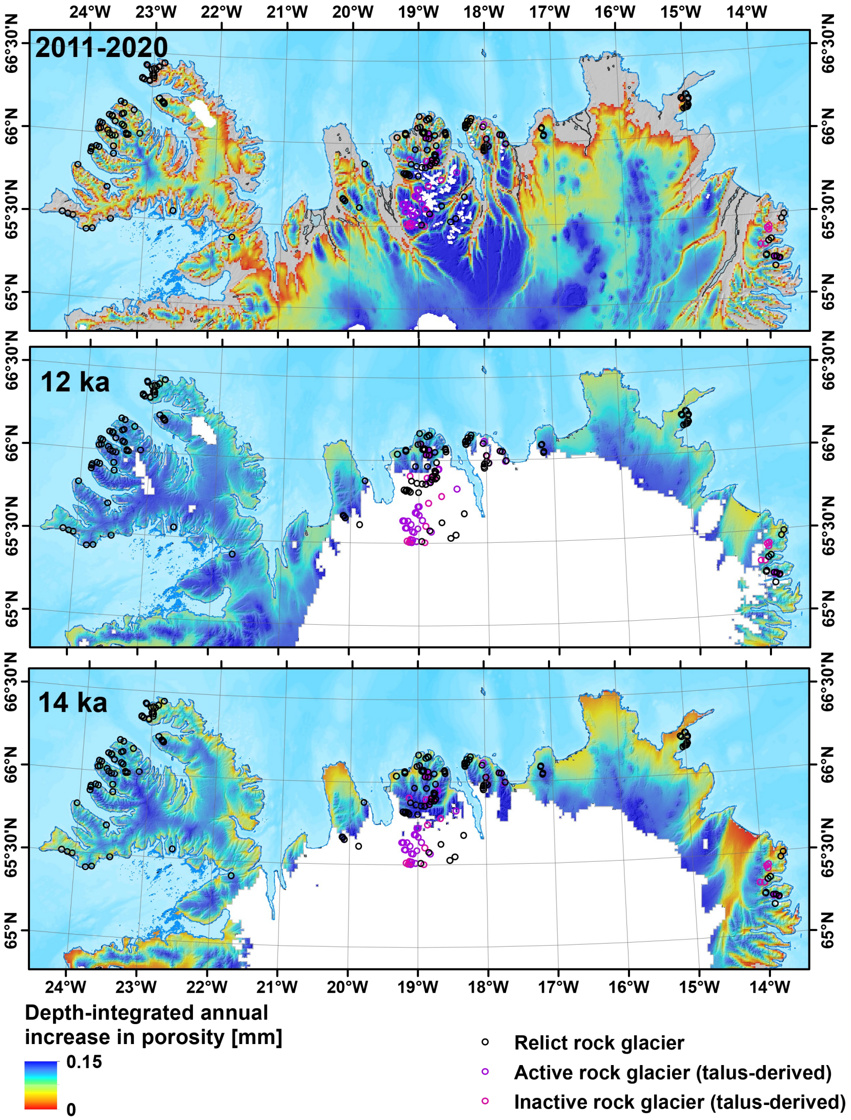

Figure 5.6: The depth-integrated annual increase in porosity for northern Iceland. Rock glacier inventory from Etzelmüller *et al.* (2020). The contemporary rock glacier activity is shown. Map data from the National Land Survey of Iceland.

is generally simulated during the coldest of the modelled periods, namely the YD stadial. *MAGST* was around 2–3 °C lower 14 ka (Bølling-Allerød interstadial) and 4 °C lower 12 ka (YD stadial) with respect to the 2010s. The differences in the frost weathering potential between 14 ka and 12 ka decrease with increasing elevation, and

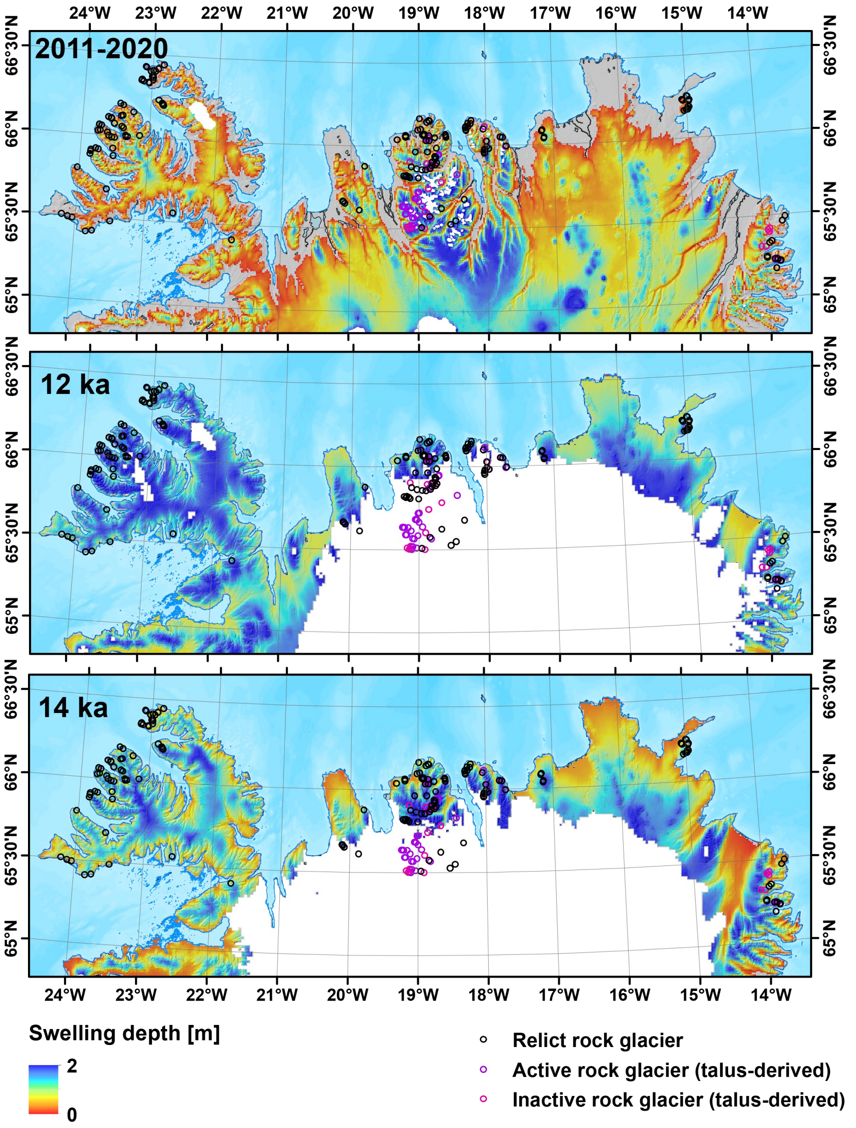

Figure 5.7: The swelling depth for northern Iceland. Rock glacier inventory from Etzelmüller *et al.* (2020). The contemporary rock glacier activity is shown. Map data from the National Land Survey of Iceland.

the areas outside the ice sheet at the highest elevations have very similar λ values, implying that both periods had similar climatic conditions for frost cracking at these elevations. Frost cracking is no longer active in the coastal and low-elevation areas, according to the results for the 2010s. The zone of optimal frost cracking occurs at higher elevations over the 2010s, and the frost cracking potential increases generally with elevation for that period. Figure 5.7 illustrates the modelled swelling depth d for the northern part of Iceland. The frost damage reaches its deepest during the YD stadial, on average 0.4 m deeper than 14 ka and 1.1 m deeper than during the 2010s (Figure 5.8). The differences in the d values between 14 ka and 12 ka are larger at higher elevations than in λ values. The d values increase with elevation for all periods, implying that the coldest areas at higher elevations generally have the deepest frost damage. The relationship between $MAGST$ and frost damage indices is shown in Figure 5.8. In general, there is an increase in frost damage potential with decreasing $MAGST$ for the Icelandic climatic conditions, with $MAGST$ between -5 and 5 °C in all periods. In the YD stadial (12 ka), most of northern Iceland was underlain

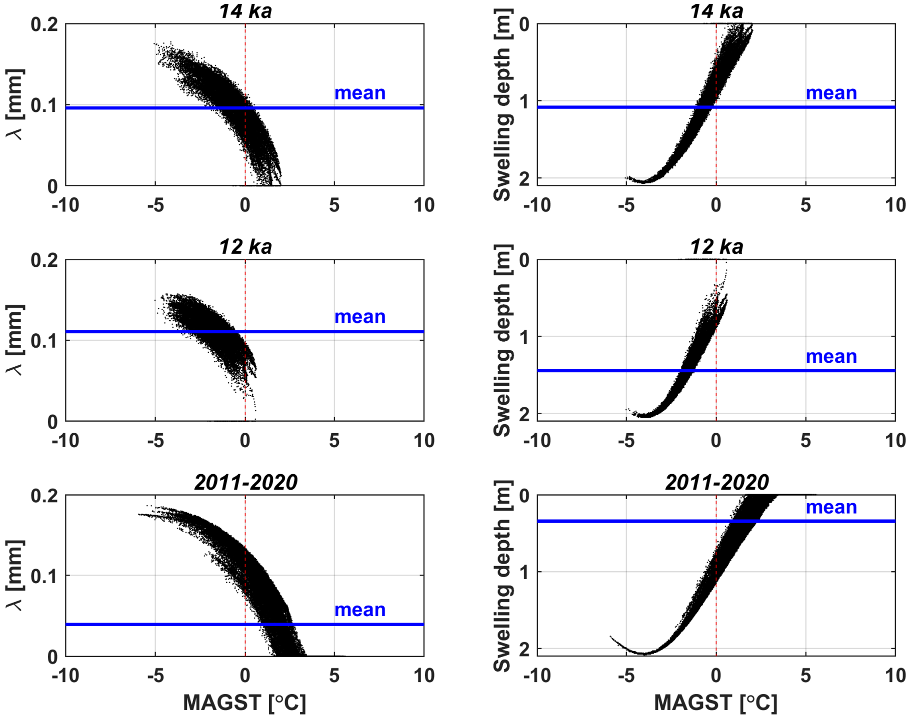

Figure 5.8: $MAGST$ and frost weathering measures for northern Iceland.

by permafrost because there are only a few $MAGST$ values above 0 °C. This is in agreement with the study by Etzelmüller *et al.* (2020), who showed that permafrost was widespread in northern Iceland in that period. The widespread permafrost conditions are connected with extensive frost weathering in Iceland (Figure 5.8).

Since no inventory of active and inactive talus slopes in Iceland exists to be able to relate the results in a similar way as in e.g. Hales and Roering (2009), I relate the frost cracking indices to the distribution of active and inactive talus-derived rock glaciers mapped by Etzelmüller *et al.* (2020). The relation between talus-derived rock glaciers and modelled frost cracking indices may be investigated because talus-derived

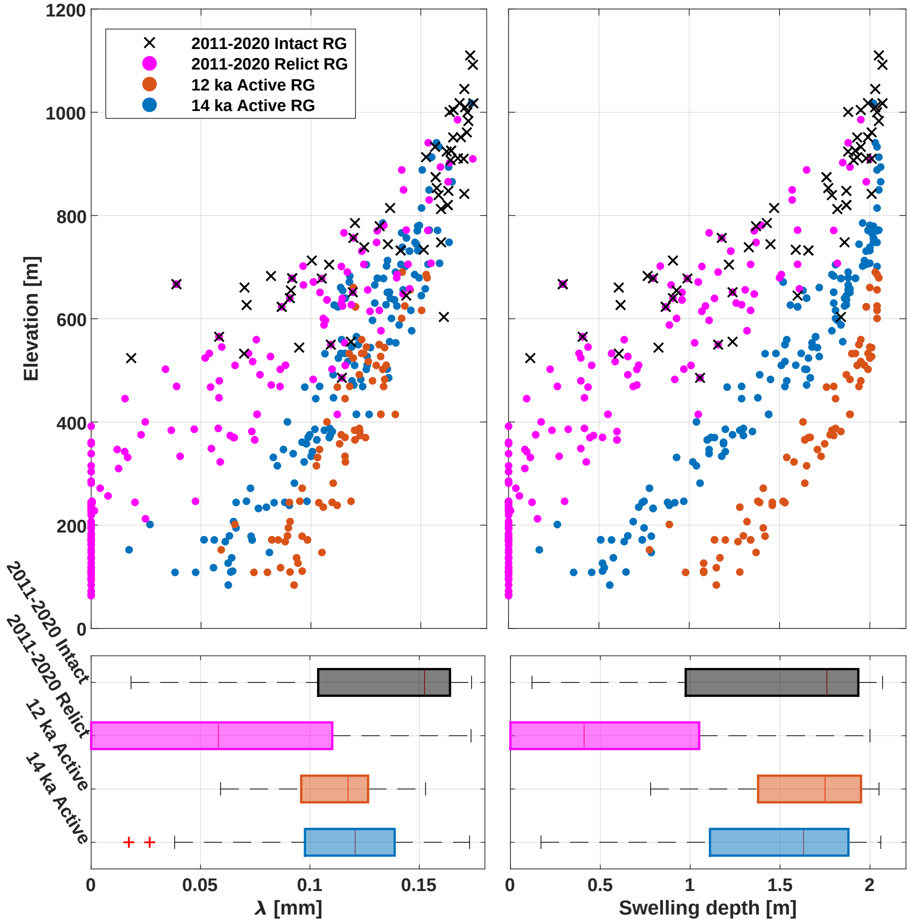

Figure 5.9: The modelled depth-integrated annual increase in porosity λ and swelling depth for the locations of active and relict talus-derived rock glaciers mapped by Etzelmüller *et al.* (2020). All talus-derived rock glaciers are assumed to be active 14 and 12 ka.

landforms may develop from periglacial talus (e.g. Shakesby *et al.*, 1987), which is fed by rockfalls from rock walls where frost cracking occurs. The contemporary relict talus-derived rock glaciers have both the smallest λ and d values, whereas the contemporary intact talus-derived rock glaciers have the largest λ and d values (Figure 5.9). The d and λ values during deglaciation periods are much larger for the majority of contemporary relict rock glaciers. The d values correspond very well to the d values for contemporary intact rock glaciers, whereas the λ values are slightly smaller, although they are still in a similar range.

5.4.2 NORWAY

The modelled λ values in Norway (Figures 5.10 and 5.11) have much larger spatial variations than in Iceland due to the assumed variations in the model parameters. Frost cracking diffusivity parameter particularly influences the order of magnitude in the modelled λ values in Norway. The modelled values are generally smaller in southern Norway than in northern Norway (Figures 5.10 and 5.11), where $MAGST$ is lower. For most areas in southern and northern Norway, λ values are largest during YD (12 ka) for the same pixel, decrease in the LIA, and are even smaller during the 2010s. The smallest values are modelled for the warmest period of the HTM. Ice-free areas at lower elevations in both southern and northern Norway had some potential for frost cracking only during the YD (12 ka). The potential for frost cracking was also large during the LIA, although it was insufficient to reach all areas at the lowest elevations in southern and northern Norway. Figures 5.12 and 5.13 show modelled swelling depths for southern and northern Norway. Spatial variations are much smaller than in the case of λ since swelling depth does not depend on the absolute values of the modelled porosity increases and is only influenced by the relative distribution of λ values with depth. The modelled swelling depth values suggest that frost cracking reaches its deepest during the YD (12 ka), is smallest during the HTM, increases again during the LIA, and decreases over the latest period. The d values for the YD are on average 1.3, 0.7 and 0.9 m larger than for the HTM, LIA and 2010s, respectively (Figure 5.14). Figure 5.14 shows the relationship between $MAGST$ and frost damage measures. For areas with similar diffusivity, frost potential generally increases with decreasing $MAGST$. Mostly negative $MAGST$ values suggest widespread permafrost in the YD, when the modelled frost cracking potential is largest. However, some areas were still ice sheet-covered 12 ka, and therefore they have higher frost weathering potential in the later periods.

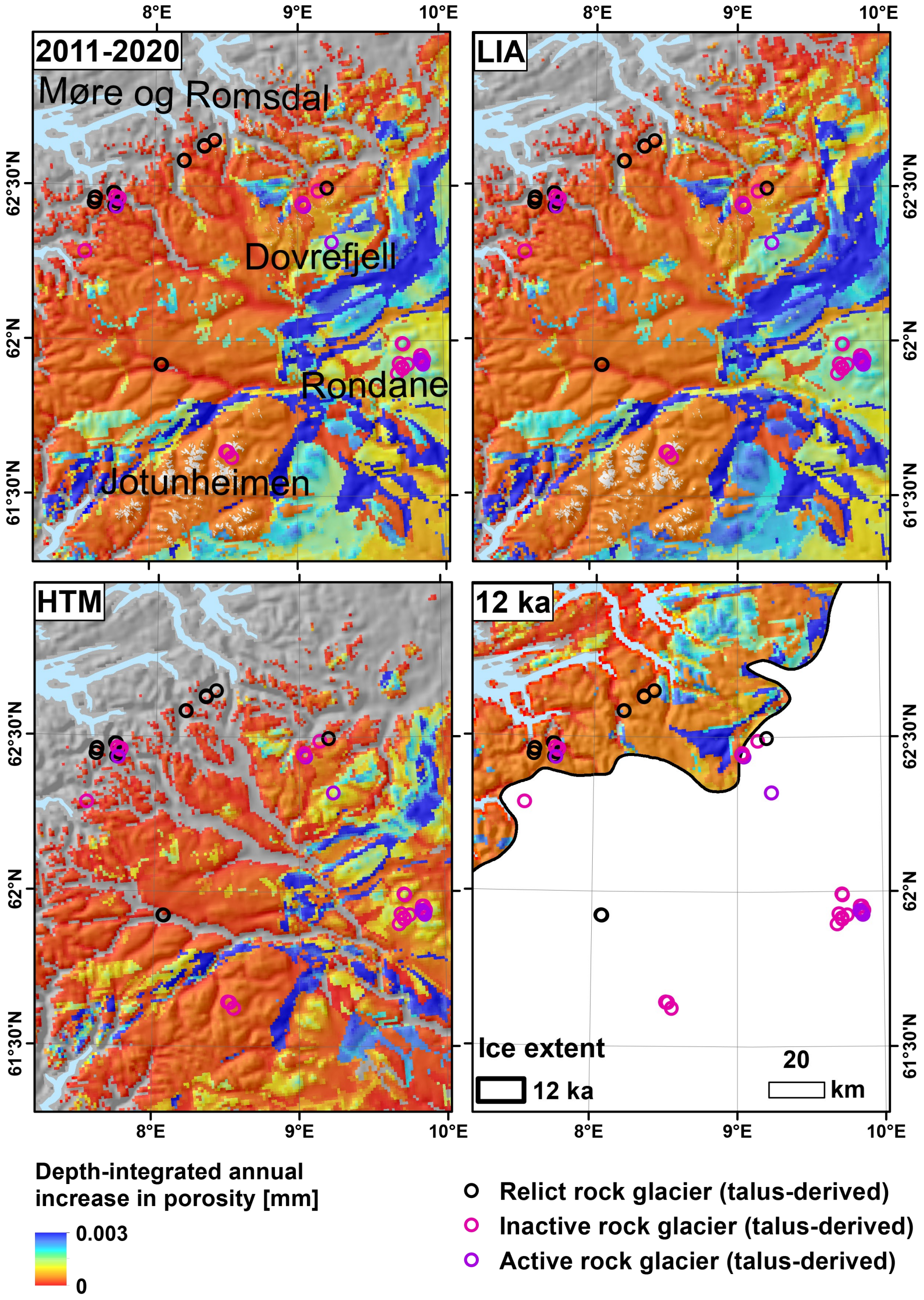

Figure 5.10: The depth-integrated annual increase in porosity for southern Norway. Rock glacier inventory was developed by Lilleøren and Etzelmüller (2011) and later updated by Hestad (2021). The contemporary rock glacier activity is shown. Map data from the Norwegian Mapping Authority.

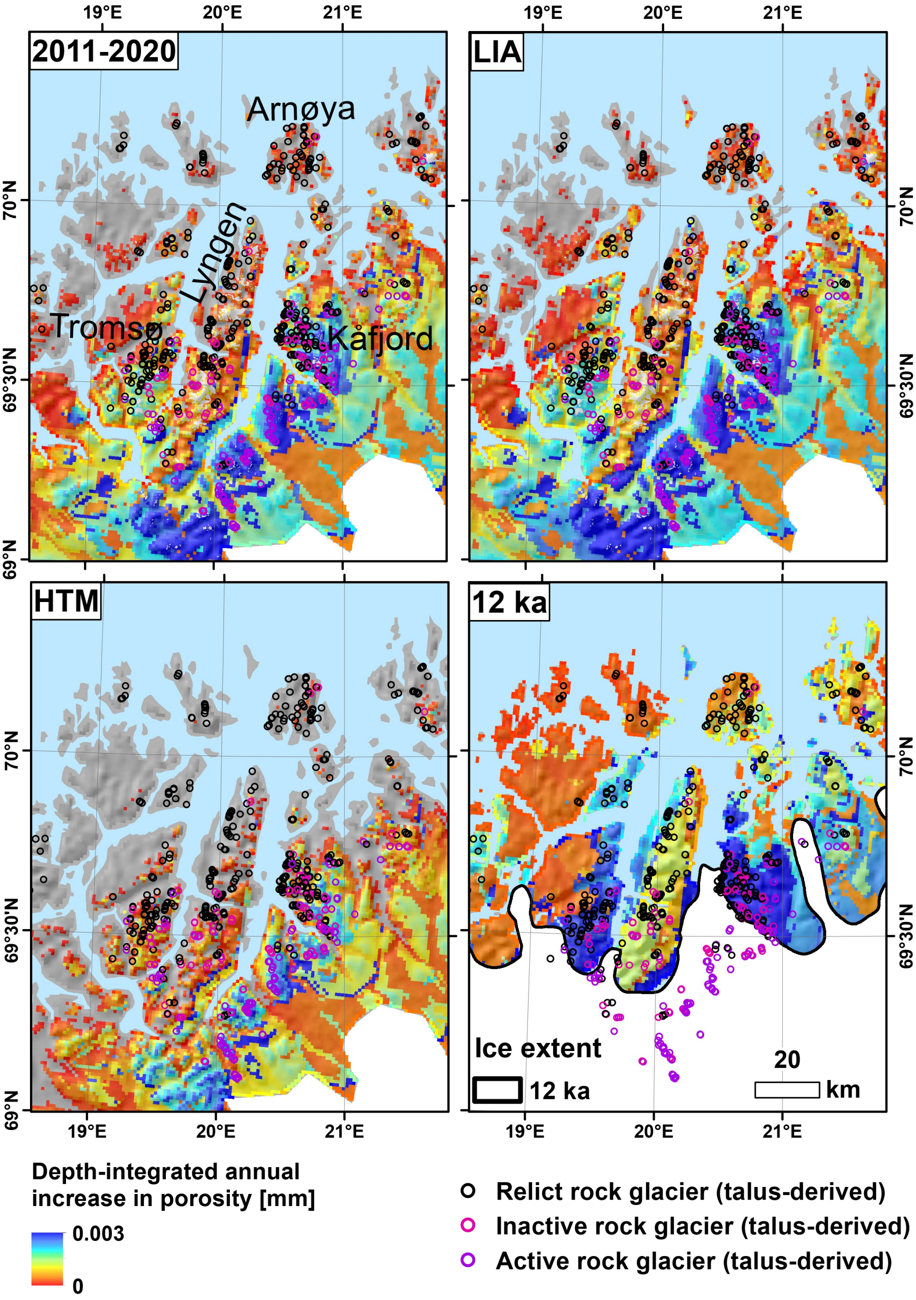

Figure 5.11: The depth-integrated annual increase in porosity for northern Norway. Rock glacier inventory was developed by Lilleøren and Etzelmüller (2011) and later updated by Hestad (2021). The contemporary rock glacier activity is shown. Map data from the Norwegian Mapping Authority.

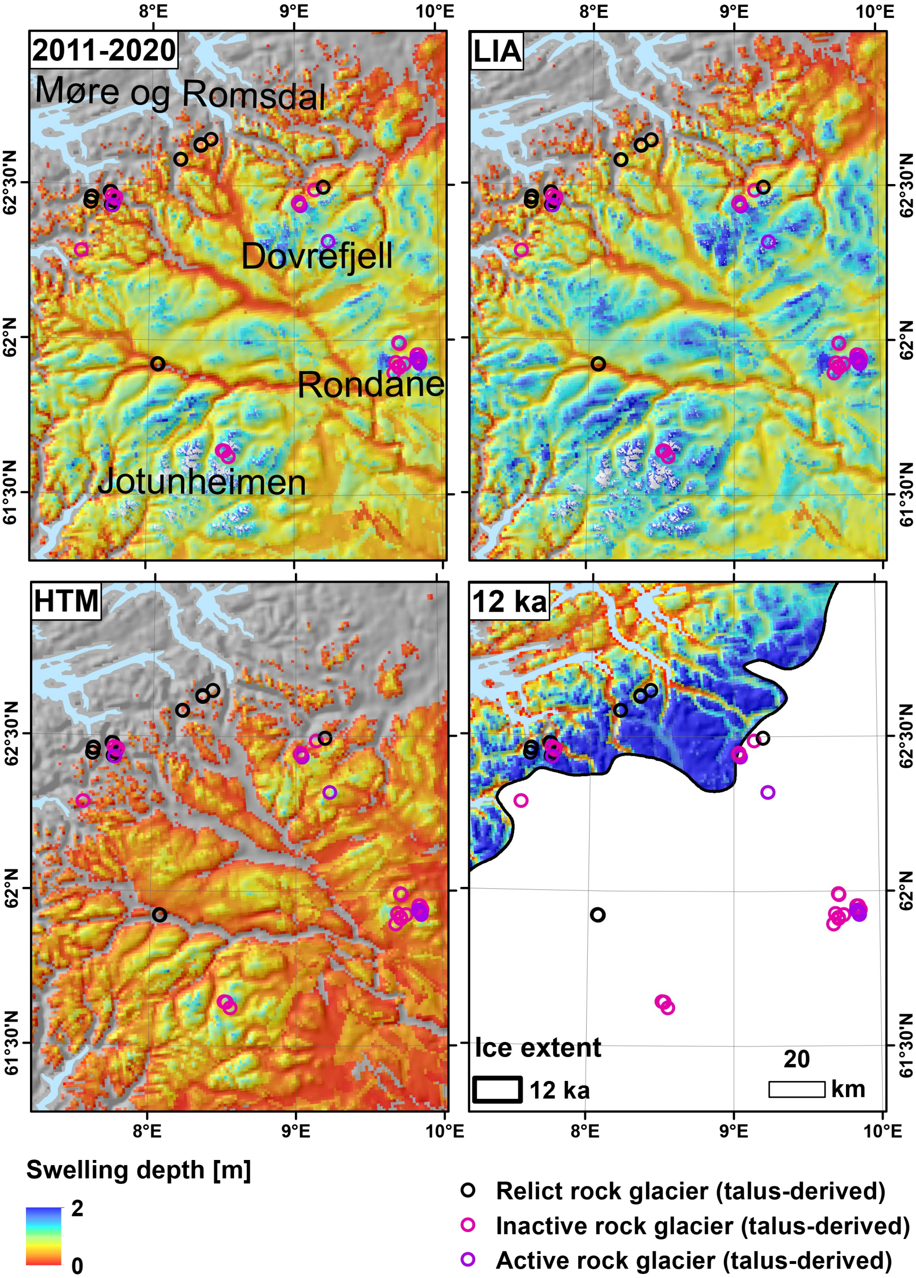

Figure 5.12: The swelling depth for southern Norway. Rock glacier inventory was developed by Lilleøren and Etzelmüller (2011) and later updated by Hestad (2021). The contemporary rock glacier activity is shown. Map data from the Norwegian Mapping Authority.

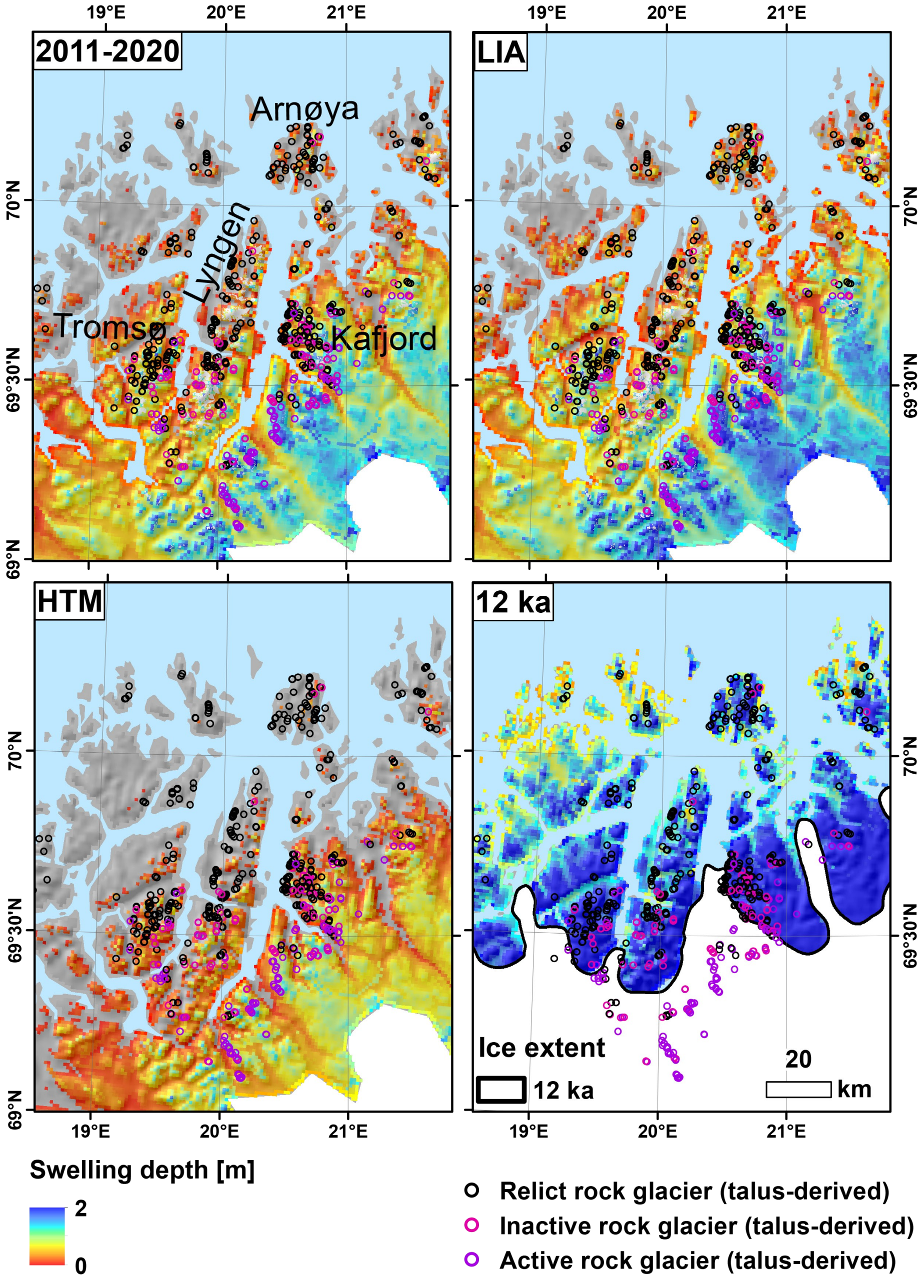

Figure 5.13: The swelling depth for northern Norway. Rock glacier inventory was developed by Lilleøren and Etzelmüller (2011) and later updated by Hestad (2021). The contemporary rock glacier activity is shown. Map data from the Norwegian Mapping Authority.

The modelled frost cracking potential is related to the inventory of talus-derived rock glaciers, as mapped by Lilleøren and Etzelmüller (2011) and later updated by Hestad (2021). There is a clear trend of increasing frost weathering potential with elevation for each period (Figure 5.15), especially for the swelling depth. The λ values are normalised relative to the λ values for the LIA to minimise the influence of the large spatial variations. Talus-derived rock glaciers had the largest and deepest frost

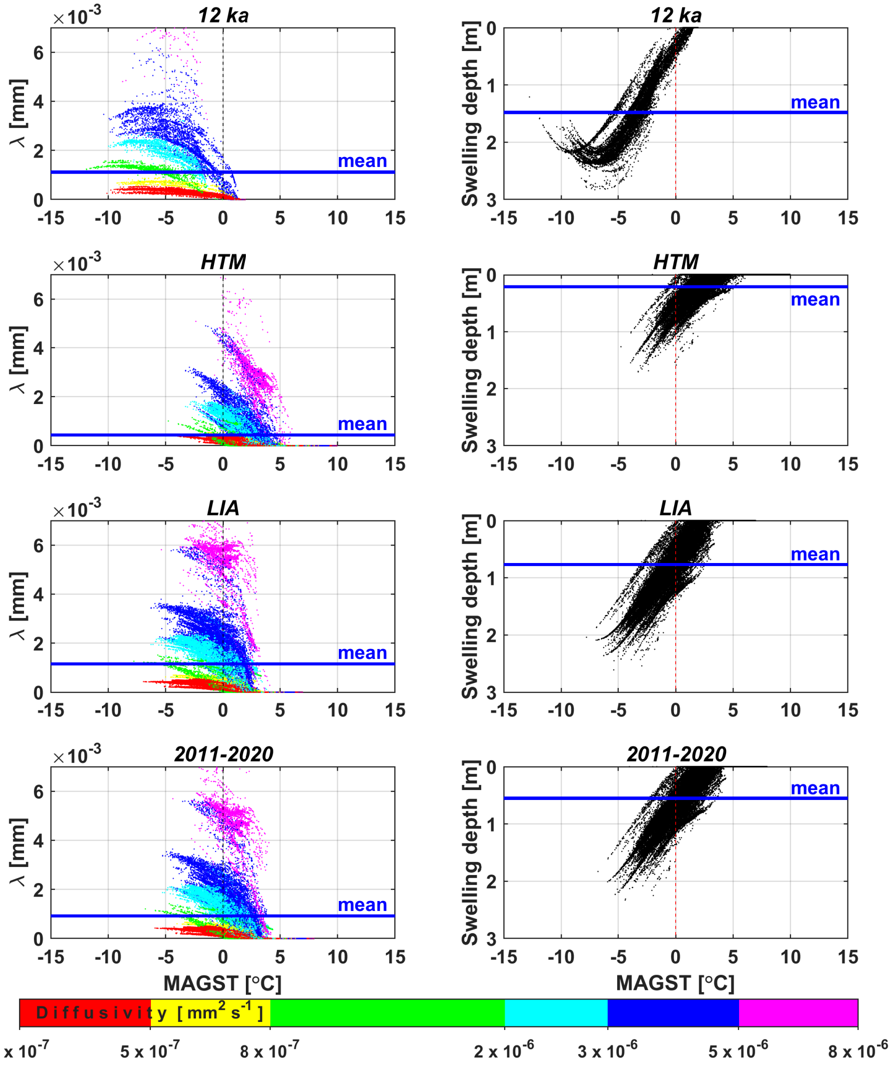

Figure 5.14: *MAGST* and frost damage measures for selected areas in southern and northern Norway shown in Figures 5.10 and 5.11. Note that diffusivity for frost weathering *D* is shown here.

cracking potential over the YD, although this applies only to the rock glaciers outside the YD ice margin. Talus-derived rock glaciers at lower elevations had at least a 50 % decrease in both λ and swelling depth between 12 ka and the 2010s. The currently relict rock glaciers have particularly small swelling depths. The relict rock glaciers occur mostly at lower elevations and in coastal areas outside the YD ice margin. In addition, there is a large difference in frost weathering potential between currently intact and relict rock glaciers.

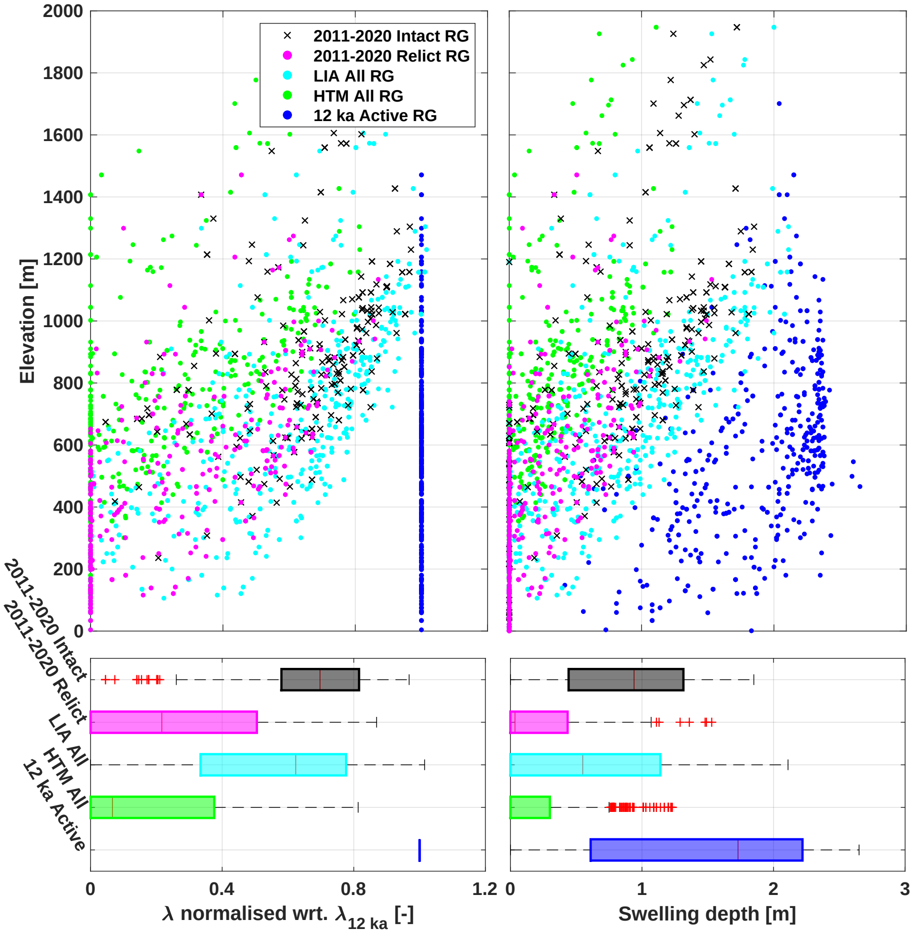

Figure 5.15: The modelled depth-integrated annual increase in porosity λ with respect to λ for 12 ka and swelling depth for the locations of active and relict talus-derived rock glaciers mapped by Lilleøren and Etzelmüller (2011) and later updated by Hestad (2021). All talus-derived rock glaciers are assumed to be active 12 ka.

5.5 ROCKFALL SOURCE DETECTION AND ROCK WALL RETREAT RATES

Long-term rock wall retreat rate – The estimated volume of ice-cored moraine accumulated in the Kjelen cirque is shown in Figure 5.16. The estimated average postglacial rock wall retreat rate is 0.28 mm a^{-1}. The latter rate is in agreement with the long-term rock wall retreat rates estimated for various alpine environments in Europe, which are between 0.02 and 3.97 mm a^{-1} (Ballantyne, 2018).

Rockfall events and short-term rock wall retreat rates – The distribution of volume and number of identified rockfall events are shown in Figure 5.17, the centroids with volume classes are shown in Figure 5.18, and the total volumes and rock wall retreat rates are shown in Figure 5.19.

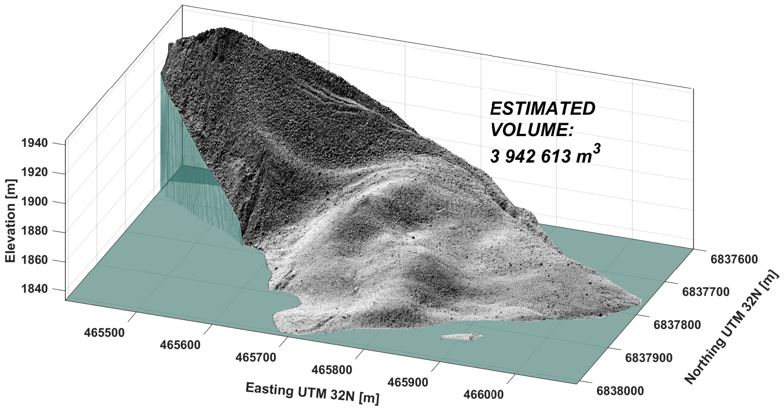

Figure 5.16: Estimated volume of ice-cored moraine above the lake level, which is shown as the teal horizontal surface. Hillshade is computed from a 0.25 m LIDAR-derived DEM from the Norwegian Mapping Authority (www.hoydedata.no/LaserInnsyn2/).

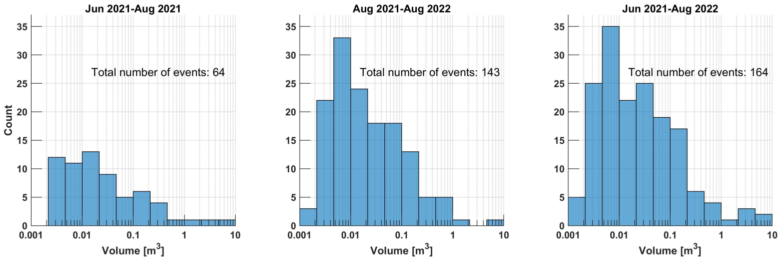

Figure 5.17: Distribution of volume of rockfall events and total number of events.

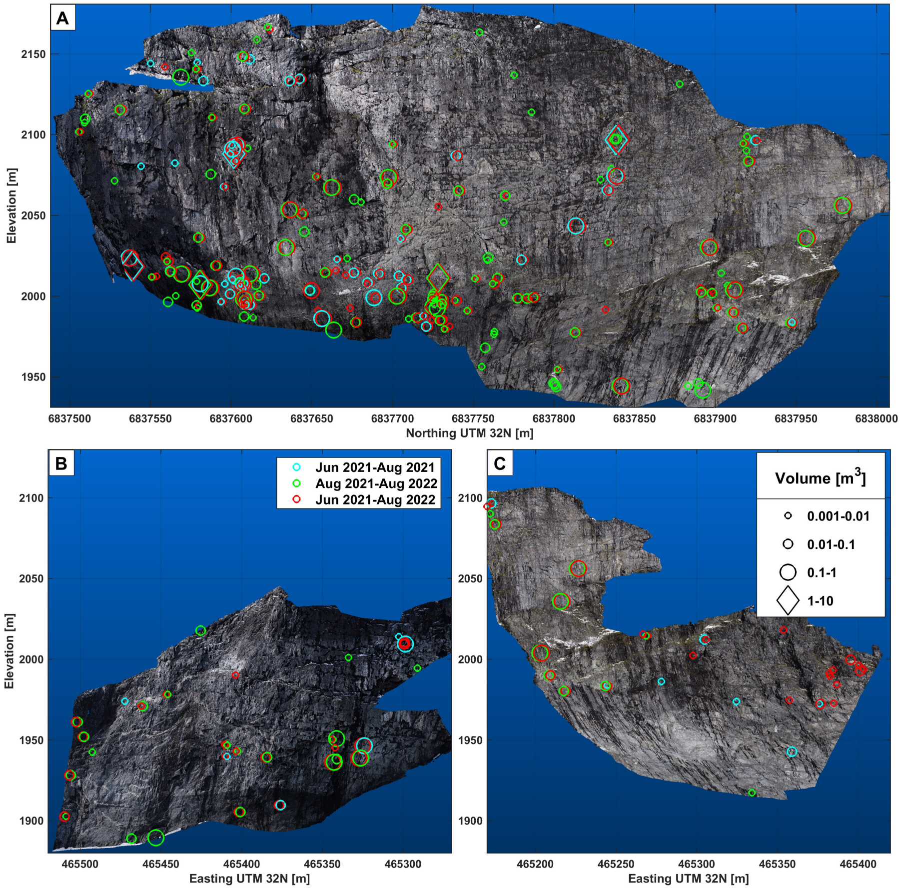

Figure 5.18: Rockfall events and their volume classes. A. The east-facing part of the rock wall. B. The north-facing part of the rock wall. C. The south-facing part of the rock wall. Background: a photogrammetric dense point cloud derived from drone imagery from August 2021.

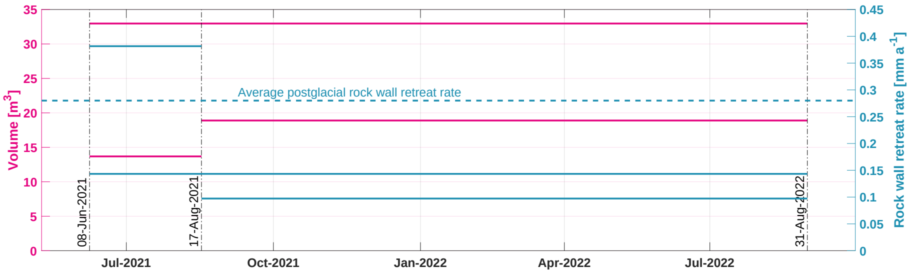

Figure 5.19: Rock wall retreat rates.

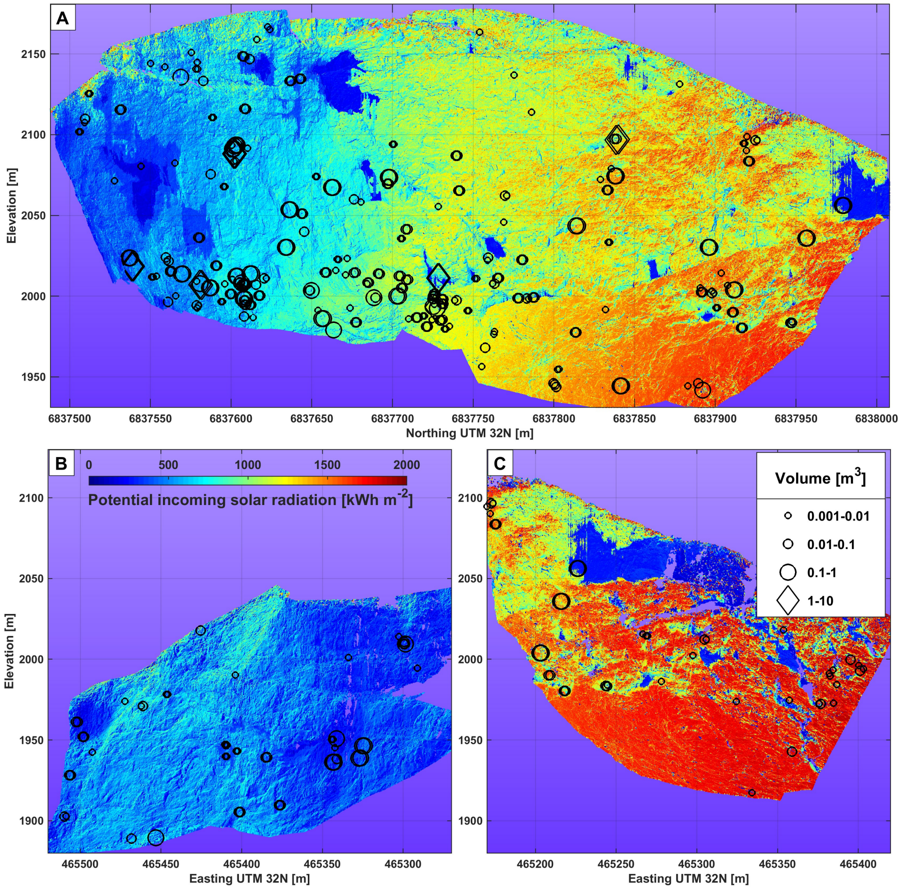

Figure 5.20: Rockfall events and potential incoming solar radiation. A. The east-facing part of the rock wall. B. The north-facing part of the rock wall. C. The south-facing part of the rock wall.

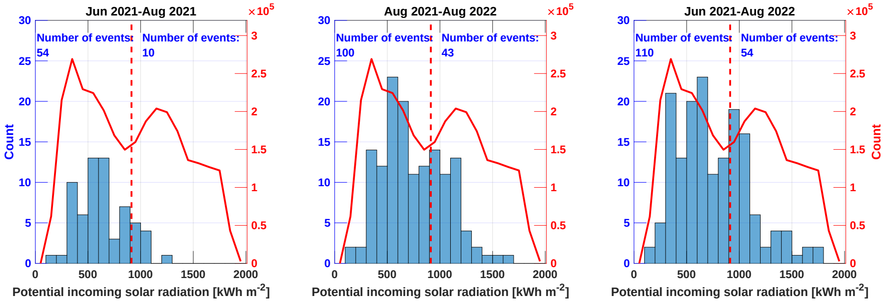

Figure 5.21: Distribution of potential incoming solar radiation for rockfall events (blue histogram). The dashed red line shows the mean value for the whole rock wall, and the red line shows the distribution of all values. A number of events below and above the mean are listed in blue font.

The voids in point clouds led to some differences in the identified rockfall events between the periods, although the sum of total volumes from the first and second periods equals the volume of the longest period, increasing confidence in the estimated rock wall retreat rates (Figure 5.19). The volumes of individual events are quite small, and the largest rockfall event of ~8 m^3 occurred between August 2021 and August 2022. The number of large events above 1 m^3 is low, with only 3 events during June 2021–August 2021, 2 events during August 2021–August 2022 and 6 events during June 2021–August 2022. Despite only a few events with volumes above 1 m^3, they contribute 50–70 % to the total volume for the three periods. The employed method only allows for the detection of rockfalls with a volume of at least 0.001 m^3, and the small magnitude rockfalls are likely underestimated due to point spacing.

Relatively many events occurred over the summer period of June 2021–August 2021 (70 days apart), in comparison with the longer periods (Figure 5.17). The estimated short-term rock wall retreat rate is highest over June 2021–August 2021 and is almost 0.40 mm a^{-1} (Figure 5.19), which is higher than the average postglacial rock wall retreat rate. The longer periods have around three- to fourfold smaller rock wall retreat rates than the shortest period over summer 2021 (Figure 5.19).

The events with the largest rockfall magnitudes (> 1 m^3) only occurred in the east-facing part of the rock wall, which is both higher and wider than the south- and north-facing parts of the rock wall. The lower southern section of the east-facing rock wall is generally an area where most events occurred, including the largest events (> 1 m^3), although one large event also occurred in the upper part of the south-eastern rock wall section. The volume of the latter event was likely underestimated in my calculations due to the missing points. There were many missing points on the rock wall surface in this particular location, most likely due to water flow on the rock wall surface.

Furthermore, I analysed whether the spatial distribution of rockfall events is related to potential incoming solar radiation (Figure 5.20). Potential incoming solar radiation is computed using VOSTOK (the Voxel Octree Solar Toolkit; Bechtold and Höfle, 2020). The algorithm has some issues in several areas, although they are mostly outside the rockfall areas; thus, it is considered that the results are of sufficient quality. The results show that 67–85 % of events occurred in areas with less than average potential incoming solar radiation (Figure 5.21); hence, shadowing seems to play an important role in rockfall distribution.

5.6 MEASURING SOLIFLUCTION USING INSAR

5.6.1 VELOCITY AND DISPLACEMENT

The LOS velocity measured using InSAR is shown in Figure 5.22. The InSAR technique allowed for the measurement of velocity in most of the areas, except for areas with higher and denser vegetation, snow patches and frequently wet areas, where coherence is low. Note that the ground in the vicinity of the solifluction landforms is also active according to the InSAR measurements because the landforms are merely geomorphological manifestations of the solifluction processes taking place at depth (Ridefelt *et al.*, 2010, 2011). The solifluction lobes at the higher elevation above ~1600

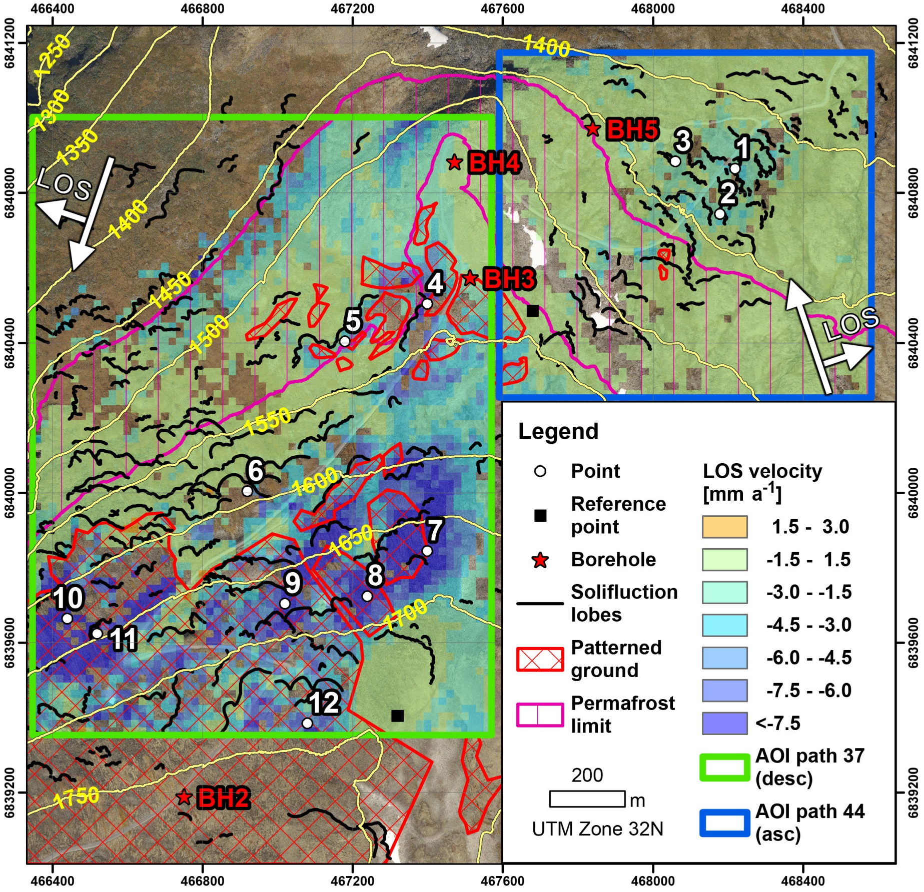

Figure 5.22: The LOS velocity computed based on the displacement between 2017 and 2022. The map contains modified Copernicus Sentinel data (2023).

m move fastest, where a LOS velocity is mostly <-3 mm a^{-1} and in the most active areas even <-7.5 mm a $^{-1}$, with the largest measured LOS velocity of -17.4 mm a $^{-1}$. These are also areas where patterned ground landforms, especially sorted stripes, are abundant. The lobes at the lower AOI move much slower with a LOS velocity between -3 and -1.5 mm a^{-1}.

The results are compared with the InSAR Norway ground deformation portal (NGU, 2023). The PSI results from Sentinel-1 data (5 m east-west resolution and 20 m south-north resolution) may be accessed at http://insar.ngu.no/#llh=8.39402008,61.69865939,2818.03738323&look=-0.07321133,-0.87932000,-0.

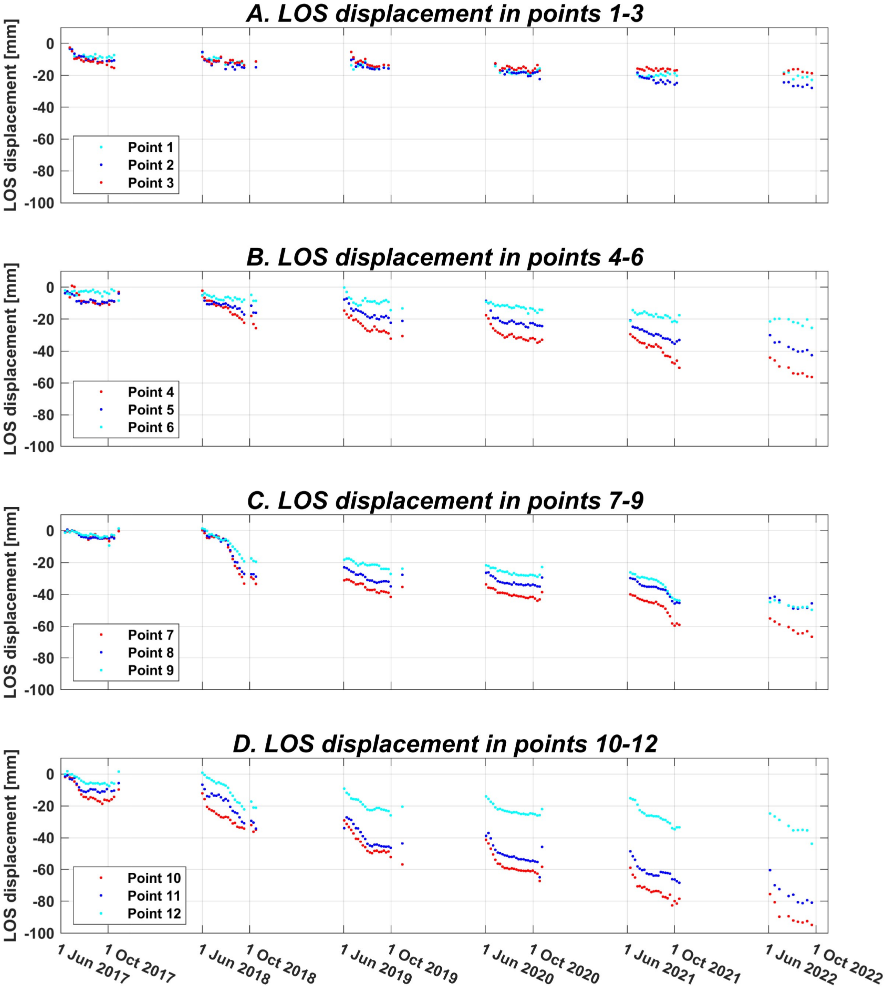

Figure 5.23: The LOS displacement in the selected points shown in Figure 5.22.

47057033&right=0.97003751,0.04681692,-0.23840175&up=-0.23166209,0.47392458,-0.84954586&layers=bluemarble,nib,nma-topo-gray,A2-2-044 for the lower AOI and at http://insar.ngu.no/#llh=8.37802214,61.69137185,3588.99315708&look=-0.07300753,-0.87921573,-0.47079678&right=0.97005595,0.04704317,-0.23828217&up=-0.23164922,0.47409560,-0.84945394&layers=bluemarble,nib,nma-topo-gray,D1-2-037 for the upper AOI. The PSI velocities from NGU (2023) show a similar spatial distribution of active and nonactive areas. The PSI velocity rates are slightly higher than the results shown here, although they agree well if the spatially averaged values from the InSAR Norway portal are used for comparison.

Figure 5.23 shows the LOS displacement in the selected points. For the temporal baselines of minimum 6–12 days, the displacements between individual acquisition

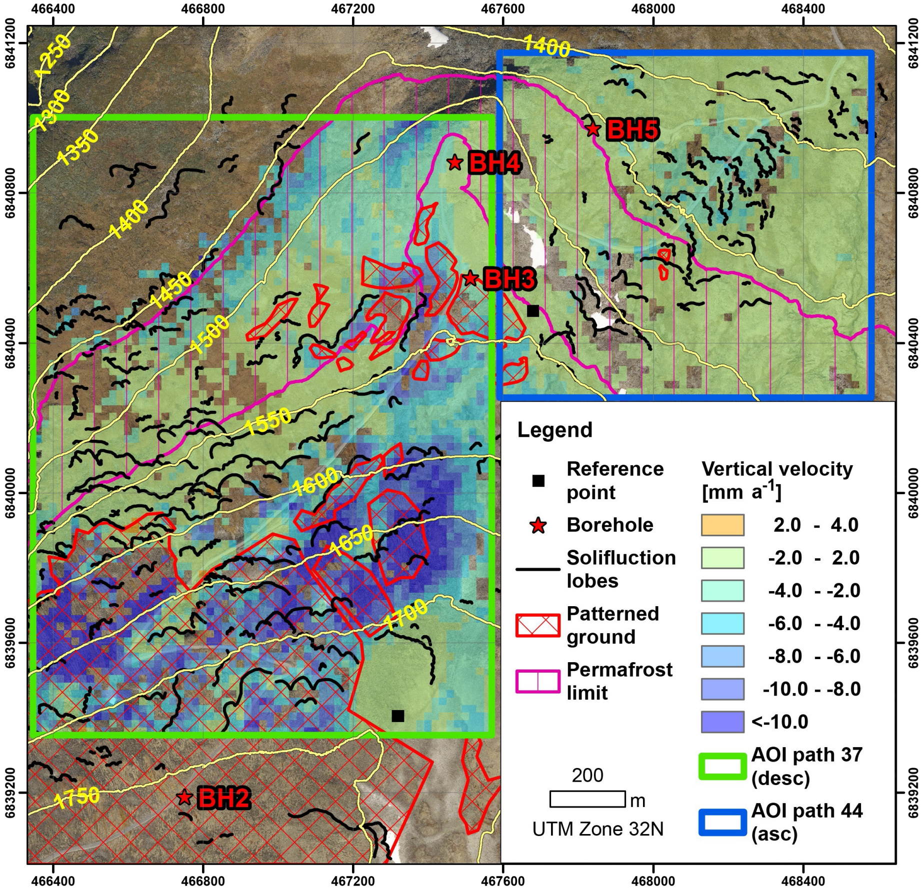

Figure 5.24: The vertical velocity computed from the LOS velocity between 2017 and 2022 (Figure 5.22). The map contains modified Copernicus Sentinel data (2023).

dates are well below half a wavelength, around 2.8 cm for Sentinel-1 data, which is the maximum detectable displacement. The settlement upon thawing is mostly measured in the study area, due to snow in the wintertime and the LOS geometry. The measured LOS displacement is somewhat noisy, although some distinct features in the movement may be observed, e.g. subsidence is especially large in summer 2018 in some points. Furthermore, a slight onset of frost heave is possibly captured at the end of some summers, although this could be noise due to e.g. snowfall. Even though the absolute rates vary, the LOS displacement in the nearby points is quite synchronised.

The vertical velocity computed using Equation 4.7 is shown in Figure 5.24. The vertical velocity distribution is similar to the LOS velocity in most areas. Note that Equation 4.7 may only be applied assuming that there is no horizontal motion. The vertical velocity for the lower AOI is between -4 and -2 mm a^{-1} in areas with subsidence, and it is mostly <-10 mm a^{-1} for the upper AOI, with the largest velocity of -23 mm a^{-1}. Rouyet *et al.* (2021) measured solifluction using InSAR in Troms and Finnmark, northern Norway, an area with sporadic and discontinuous permafrost, and the vertical velocities were between 0 and 7.5 mm a^{-1}, up to 13 mm a^{-1}, which is similar to the velocities measured here.

5.6.2 TEMPORAL VARIATIONS

Temporal variations in the LOS displacement are compared to temporal variations in SAT, GST and thaw depth for lower and upper sites separately (Figures 5.25 and 5.26). Based on the fitted curves for the upper site and the coefficients of determination (r^2), the large proportion of temporal variations in normalised mean displacement may be explained by measured thaw depth in a nearby borehole. For instance, the largest thaw subsidence during 2018 is also related to one of the largest measured thaw depths. However, for the largest LOS displacements < -5 mm, the relationship between thaw depth and the normalised LOS displacement is nearly constant and is not well represented by the quadratic fit. The upward tail for the largest LOS displacements is an artefact of the quadratic fit. Displacement seems to occur throughout the whole thawing period in all years, with average LOS values of seasonal thaw settlement between 2 and 12 mm. Conversion of the LOS to vertical displacement requires division by 0.75 ($= \cos(\theta_{inc})$) for the upper study area; hence, the vertical thaw settlement is slightly higher, between 3 and 16 mm. In some years, e.g. 2017, thaw depth is much shallower, leading to very small displacement, similar

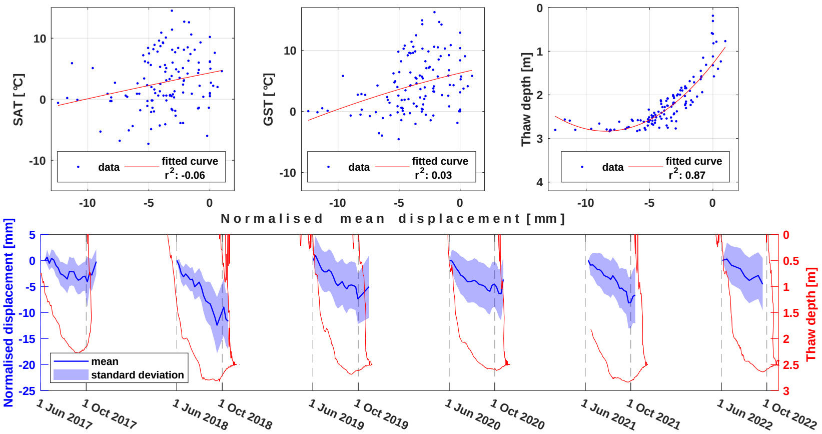

Figure 5.25: Relationship between *SAT*, *GST*, thaw depth measured in the PACE borehole and the normalised LOS displacement for the upper AOI. A quadratic fit curve is shown in the upper row. The depth of the thaw is assumed to be the depth of the 0 °C isotherm. The PACE borehole is located in the continuous permafrost zone with cold permafrost. The LOS displacement is normalised for each year by subtracting the first measurement each year. Only grid cells with the LOS velocity < -1.5 mm a^{-1} are included in the analysis.

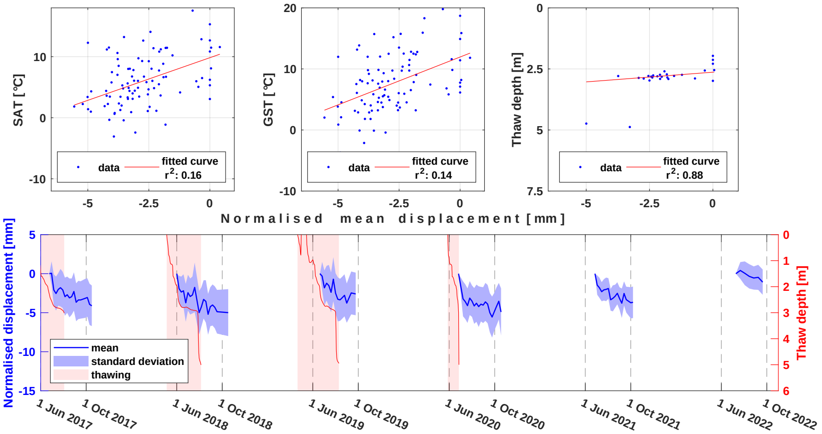

Figure 5.26: Relationship between *SAT*, *GST*, thaw depth measured in the BH5 borehole and the normalised LOS displacement for the lower AOI. A linear fit curve is shown in the upper row. The depth of the thaw is assumed to be the depth of the 0 °C isotherm. The BH5 borehole measurements indicate seasonally frozen ground and no permafrost occurrence; therefore, thawing ceases in the middle of the summer. The LOS displacement is normalised for each year by subtracting the first measurement each year. Only grid cells with the LOS velocity < -1.5 mm a^{-1} are included in the analysis.

to the lower site.

Similarly, thaw depth best explains temporal variations at the lower site, although some data is missing, thaw depth cannot be computed after the seasonally frozen ground thaws during summer, and variations in thaw depth are very small when displacement occurs. Displacement seems to cease at the lower site when seasonal frost thaws completely in the middle of the summer after around 1–5 mm thaw settlement in LOS geometry (Figure 5.26). LOS to vertical thaw settlement requires division by 0.79 for the lower AOI, hence the vertical thaw settlement is 1.3–6.3 mm. Seasonal frost penetrates around 7 m, according to the measurements in BH5.

The InSAR measurements are associated with some uncertainties; however, the high dependency of the displacement on thaw depth increases the confidence that the movement is indeed associated with the active layer or seasonally frozen ground dynamics and that the measurement accuracy is sufficient to detect slow displacements in this area.

5.6.3 SPATIAL VARIATIONS

The spatial distribution of environmental variables is shown in Figure 5.27. The average riser height of the mapped solifluction landforms is estimated to be 2.12 m; hence GT, at 2 m depth was assumed to be the most representative of permafrost occurrence with respect to solifluction processes since the riser height is indicative of the maximum depth of soil movement (Matsuoka, 2001b). The lower AOI has a smaller slope, a larger TWI, a larger $NDVI$, larger snow factors and a higher GT than the upper AOI. Examples of the manual snow classification for the melt season over 2020 are shown in Figures A.1–A.5. Wind redistributes snow from west to east, and wind-exposed locations may be snow-free even in February (Figure A.1). The upper AOI is generally more wind-exposed than the lower AOI, and snow disappears earlier than at the lower AOI. SAT and snow cover are assumed to be the main factors governing GT distribution in the area. The impact of snow on the modelled GT at 2 m depth is complex (Figures 5.27 and A.7). In general, areas with snow factors of around 1 have the highest GT, and areas with snow factors < 1 have a lower GT since the insulating effect of snow cover decreases. Nevertheless, areas with late-lying snow cover, i.e. very large snow factors, also have lower GT, because in that case, a smaller portion of heat penetrates into the ground during summer. Calibration for the GT modelling based on boreholes BH3, BH4 and BH5 is shown in Figure A.6. Good agreement between observed and modelled daily GT at 2 m depth is obtained

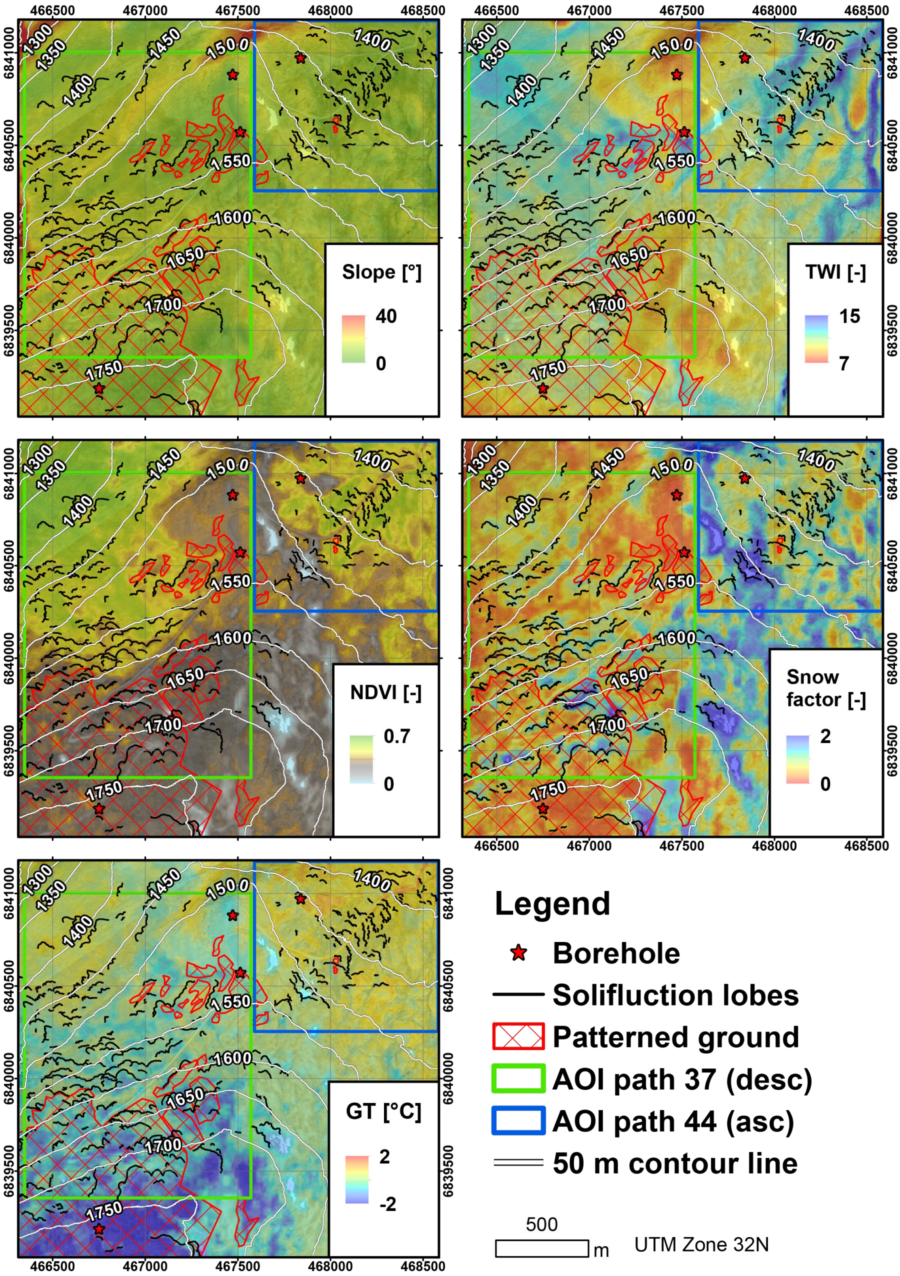

Figure 5.27: Environmental variables for the Juvflye area in the Jotunheimen Mountains. *GT* at 2 m depth is shown.

with $r^2 > 0.8$ and $RMSE < 1.31$ °C. The distribution of GT at 2 m depth agrees well with the expected lower permafrost limit in the area, which is somewhere between boreholes BH4 and BH5.

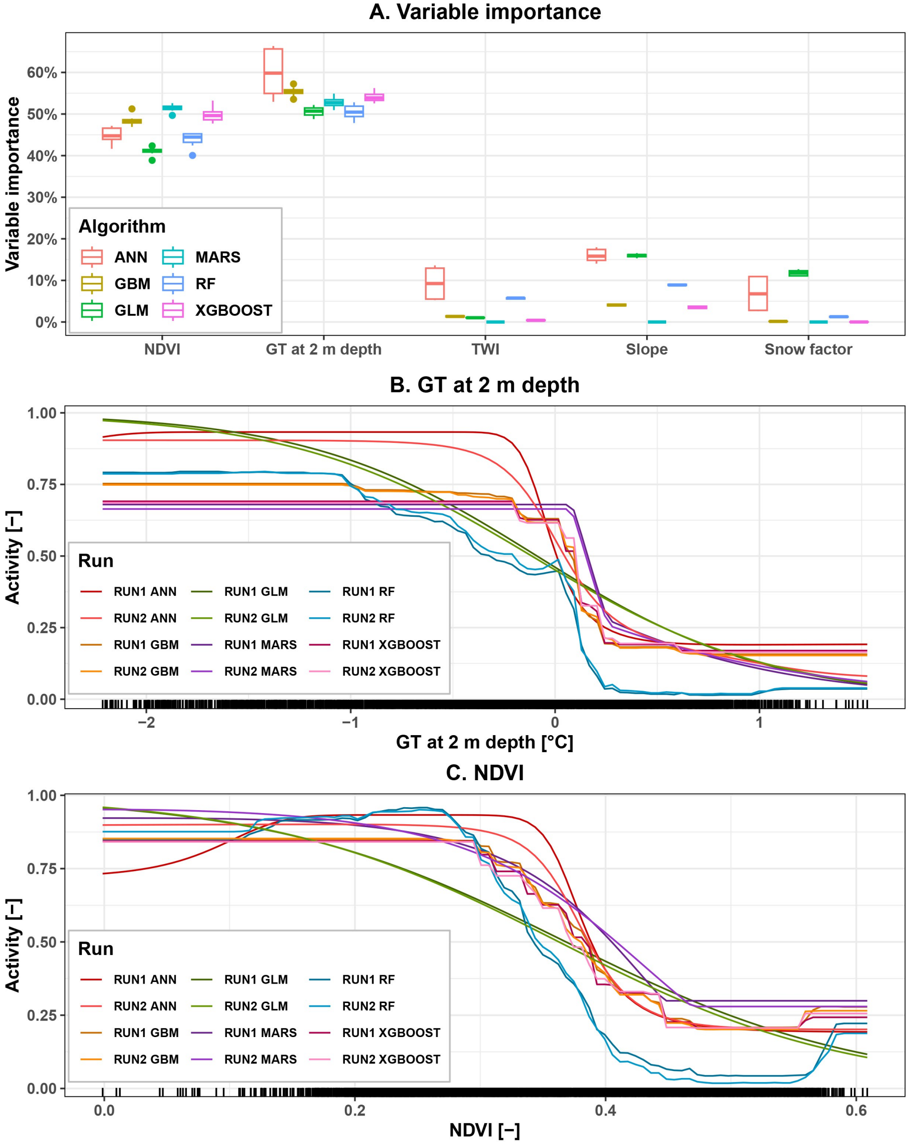

Figure 5.28: A. Variable importance. **B.** Response curves for GT at 2 m depth. **C.** Response curves for $NDVI$. The following models are shown: ANN - Artificial Neutral Networks, GBM - Generalised Boosted Regression, GLM - Generalised Linear Model, MARS - Multivariate Adaptive Regression Splines, RF - Random Forest and XGBoost - eXtreme Gradient Boosting.

The Spearman rank-correlation coefficient between the environmental variables is shown in Figure A.7, and all correlation coefficients are <0.7; hence, all environmental variables are used in the statistical modelling. Evaluation scores for the employed statistical models show sufficient model performance (Figure A.8). The analysis of the relationship between solifluction activity and environmental variables is shown in Figure 5.28. The most important variables explaining the activity in the area are GT at 2 m depth and $NDVI$ (Figure 5.28A). TWI, slope and snow factor are much less important. The response curves for GT at 2 m depth and $NDVI$ show that the most active areas have lower GT and are sparsely vegetated. In this area, sparsely vegetated areas are either bare bedrock, blockfields above 1600 m or till below 1600 m, although there is likely a transition zone with both blockfield and till material at elevations around 1600 m. Bare bedrock is stable in this area, and since movement is largest at the highest elevations, the most active areas are very likely blockfields underlain by permafrost.

6. DISCUSSION

6.1 UNCERTAINTIES AND LIMITATIONS

The uncertainties and limitations of the GT modelling conducted for Iceland and rock walls in Norway are discussed in Paper I and Paper II. In addition, I included spatial modelling of GT at a 20 m scale for the Juvflye area in the Jotunheimen Mountains (Section 5.6). To my best knowledge, 1D spatial modelling of mountain permafrost at such a fine scale, excluding statistical permafrost modelling, has never been attempted. Lack of suitable snow models at such fine scale limited spatial snow modelling to larger scales, usually around 1 km (e.g. Gisnås *et al.*, 2013; Westermann *et al.*, 2013; Obu *et al.*, 2019), even though some of these models include subgrid snow variability. Mapping of snow factors using the PlanetScope data proved to be useful, providing both high spatial and sufficient temporal resolution for the estimation of the key dates during snowmelt. The main limitations of an optical sensor are its inability to penetrate clouds and its poor performance in low-light conditions during winter, potentially resulting in poor temporal resolution. Another challenge is the conversion of the $fSCA$ to actual snow depth. Snow factors are applied as the simplest solution to this problem, although more advanced methods could be used. Nevertheless, the model calibration (Figure A.6) showed that the modelled snow depths allowed for satisfactory model results. Ideally, the presented permafrost map should be validated against the distribution of $MAGST$ or at least the permafrost distribution according to the "Bottom temperature of snow" (BTS). Even though UiO's growing permafrost database contains potential validation data, the rapid warming of near-surface permafrost (here at 2 m depth) during the past few years makes it impossible to validate the modelled GT against the older data.

The uncertainties and limitations of the frost cracking model in two dimensions are discussed in Paper III. In addition, frost weathering is modelled in one dimension for Iceland and Norway (Section 5.4). The 1D frost cracking model requires GT distribution in depth; hence, the uncertainties from the GT modelling are also important. Here, only simple GT modelling is employed, and all pixels are assumed to be snow-free. Hence, the modelled frost weathering measures (the integrated porosity change and swelling depth) may be interpreted as valid only for steep rock walls, which are snow-free or have very thin snow cover. Furthermore, lateral heat fluxes are not considered in this approach. The parameters assumed for frost cracking modelling are uncertain. Frost modelling measures are challenging to validate at larger spatial scales (e.g. 1 km) and were never attempted. In addition, the employed frost cracking measures represent only relative measures and should not be interpreted in terms of absolute values. Nevertheless, they still provide valuable information about the optimal climatic conditions for frost cracking. Note that the modelled frost weathering strongly depends on the chosen frost cracking model. The use of a different frost cracking model would yield different spatial results of frost cracking potential based on the indices presented in Section 2.5, especially Figure 2.6. One of the biggest advantages of the employed model by Rempel *et al.* (2016) is that the lithological component may be included, whereas other frost cracking indices often just assume a FCW of e.g. -8 to -3 °C. For instance, the Hales and Roering's (2007) frost cracking model favours higher frost weathering potential in warmer climates, and the results presented in Savi *et al.* (2015) who applied their model for the eastern Italian Alps, show the largest frost cracking potential in the warmest climate of the Holocene in that area. On the other hand, the study by Marshall *et al.* (2021), which used the Rempel *et al.*'s (2016) model, favoured higher frost weathering potential in colder climates and showed extensive frost weathering during the Last Glacial Maximum in North America.

Furthermore, the average long-term rock wall retreat rate was here computed from a landform, and such an approach may be criticised because the landform could be formed relatively rapidly and not necessarily be representative of the whole postglacial period. The short-term rock wall retreat rates were estimated from point clouds over one year only, and time series over a longer period would result in higher confidence in the estimated rock wall retreat rates. The comparison of two point clouds was more challenging than initially anticipated since the simplest methods of comparison were ineffective for the collected point clouds with many voids. The M3C2 technique worked well, although finding the optimal parameters required many tests. The number of rockfall events and total volume of rockfall debris are likely underestimated due to the accuracy of the employed method, meaning that smaller rockfalls cannot be detected. Granular weathering of the rock wall is included in the long-term rock wall retreat rate, and its contribution may be as much as 30% (Hinchliffe and Ballantyne, 1999), whereas short-term rock wall retreat rates do not include such weathering.

One of the main limitations of the InSAR technique in the selected AOIs (Section 5.6) is temporal decorrelation due to snow, vegetation or surfaces with high water content. InSAR allowed for measuring displacement rates only during summer, although dry-snow winter interferograms, which are usually coherent, could potentially be used. However, thick snow would result in a phase delay of around a half phase (e.g. Liu *et al.*, 2017), which would result in large errors for small displacements, such as solifluction. Dry-snow winter interferograms could be used if the movement is much faster or snow is thinner. In addition, the displacement is measured only one-dimensionally, in LOS. The main movement direction of the lobes in the study area does not allow for the combination of the measurements from the descending and ascending tracks. For the most accurate InSAR results, all components unrelated to displacement must be removed from Equation 2.24, and SAR interferometry requires several processing steps to achieve it, and every processing step is connected to some uncertainties. Nevertheless, the strong relationship of displacement with measured thaw depths, together with the similar pattern of active areas shown at the InSAR Norway mapping service (NGU, 2023), increase confidence in the measured displacements.

6.2 THE GROUND THERMAL REGIME, ICE SEGREGATION AND ROCKFALLS

The importance of frost weathering in evolution and the potential weakening of permafrost-underlain rock walls are emphasised and discussed in Paper III. Frost weathering may also play a role in the development of talus-derived rock glaciers in Iceland and Norway (Section 5.4) since it contributes to the production of the talus material, or in the case of the Kjelen cirque, it may also provide debris for the ice-cored moraine after it is carried through the glacier englacially (Section 5.5).

The 2D approach allowed for the modelling of critical zones of frost weathering in Norway (Paper III); nevertheless, the results using both 1D (Section 5.4) and 2D approaches are in agreement that frost weathering potential was largest in Norway during the YD, frost weathering potential was smallest during the warm period of

HTM, frost weathering potential was larger again during the LIA and dropped again during the contemporary warmer climate; however, not as warm as in the HTM. For Iceland, frost weathering was modelled for the Bølling-Allerød interstadial, YD stadial and the 2010s, and the results also showed that frost cracking potential was largest during the YD stadial. Even though the assumed hydro-mechanical properties of rocks in Iceland and Norway are different, the results agree about the large frost weathering potential during the YD stadial, when permafrost was widespread even in the coastal regions of both Norway and Iceland (Section 5.4; Etzelmüller *et al.*, 2020). However, note that some coastal areas in Iceland were deglaciated long before YD; hence, they possibly experienced intense frost weathering already before the Bølling-Allerød interstadial (Etzelmüller *et al.*, 2020). However, if climate was much colder, frost weathering would be less intense (see e.g. Figure 2.6, where the frost cracking drops in much colder climates). Permafrost distribution in Norway since deglaciation has not been modelled in other studies. The study by Hilger *et al.* (2021) suggests that permafrost distribution was likely at its maximum in Norway in the YD.

In addition, Paper III shows that glaciers may contribute to high subsurface thermal gradients, and their occurrence may have a strong influence on frost cracking rates in rock walls. Studies about post-glacial erosion rates from rock walls usually focus on the debuttressing aspects or increasing frost weathering due to permafrost aggradation when glaciers retreat (e.g. Draebing *et al.*, 2022), whereas the lateral effects across areas with high thermal gradients have not been considered in other studies. Paper III indicates the possibility of significant periglacial weathering in rock walls during deglaciation, particularly in areas where there are large thermal gradients between the rock walls and melting glaciers or ice sheets. The latter also affects deeper areas, not only near-surface areas. The enhanced frost weathering at sites with large thermal gradients could progressively weaken entire rock walls during an ice sheet or glacier retreat. In addition, abundant meltwater would be available from the melting ice sheet or glacier for effective ice segregation, although the water requirements are likely moderate for ice segregation to occur (Rempel *et al.*, 2016). Ongoing glacier retreat already increases rockfalls from newly deglaciated rock wall faces in the European Alps (Fischer *et al.*, 2006), perhaps partly due to the melt-out or warming of ice lenses formed in rock faces adjacent to previous glacier surfaces.

6.2.1 ROCKFALL ACCUMULATIONS

Temporal variations in the modelled frost weathering are discussed here with respect to the knowledge about rockfall accumulations. Note that even though rockfall processes are intensified by frost weathering (Blikra and Nemec, 1998) that leads to generation or widening of rock fractures, the actual rockfall triggering occurs rather due to e.g. deepening of the active layer (Gruber *et al.*, 2004; Ravanel and Deline, 2011), weather factors such as persistent heavy rainfall or snowmelt (Sandersen *et al.*, 1997) or earthquakes e.g. due to seismic activity during glacio-isostatic rebound (Cossart *et al.*, 2014; Bellwald *et al.*, 2019). Segregation ice growth probably mostly generates or extends cracks; hence, it is a preparatory factor for rockfalls (Curry, 2023), which should not be confused with the triggering factors. Rockfall is very common in Iceland, and talus deposits may be found under many steep slopes (Saemundsson *et al.*, 2003). Such a common occurrence of rockfall results from porous bedrock, climate and sometimes also earthquake activity (Saemundsson *et al.*, 2003). It seems that the timing of rockfall activity has not been much investigated in Iceland since deglaciation, and for this area, mostly talus-derived rock glaciers will be discussed.

The majority of the rockfall material in southern Norway accumulated following deglaciation (Matthews and Nesje, 2022) and throughout the climate deterioration over the YD (Blikra and Nemec, 1998). Such timing compares favourably with the large frost cracking modelled for the YD. Hilger (2019) showed also that the accumulation of rock avalanche (volumes > 100 000 m^3) deposits in Norway peaked 12–9 ka, although it is uncertain whether frost weathering processes may be responsible for the larger rock slope failures because ice segregation is mostly active near the surface (up to a few metres; Krautblatter *et al.*, 2013). Nevertheless, frost weathering has been mentioned as a possible destabilising factor for rock avalanches in Norway by Blikra *et al.* (2006), who also mentioned glacial debuttressing (i.e. stress release due to the removal of ice), earthquakes or permafrost thawing as possible triggering mechanisms. In Iceland, post-glacial rebound uplift may be the dominant preparatory factor for landslides in some areas since it generally weakens the internal strength of bedrock through both jointing and faulting (Cossart *et al.*, 2014). The Fennoscandian and Icelandic Ice Sheets melted rapidly following YD due to rapid climate warming in both Iceland and Norway; hence, permafrost likely degraded quickly in many bedrock areas, potentially allowing for high rockfall occurrence. My results are further supported by the analysis of Quaternary deposits in the coastal areas of the Møre-Romsdal district by Blikra and Longva (1995), who proposed that the deposits are the result of highly active frost weathering during the YD climate with deep permafrost. Most of the rockfall sediments studied outside Norway also accumulated early after deglaciation (e.g. Rapp, 1960; Ballantyne and Kirkbride, 1987; Hinchliffe and Ballantyne, 1999), though it may be impossible to identify whether the increased frost weathering or stress release following deglaciation ("debuttressing effects") is responsible for these sediments (Ballantyne and Harris, 1994; Hinchliffe and Ballantyne, 1999; Ballantyne, 2002). Ballantyne and Harris (1994) suggested that the mature talus landforms, i.e. talus slopes that have very little activity at present, in Upland Britain are primarily relict periglacial landforms rather than paraglacial. Nevertheless, there may be a connection between the two processes, so that glacial debuttressing would cause greatly fractured rock walls close to the surface, exposing them to even more effective frost weathering (Ballantyne and Kirkbride, 1987; Hales and Roering, 2009).

According to Blikra and Nemec (1998), the early Holocene and the HTM were likely times of little rockfall activity in Norway, which is consistent with the HTM's lowest estimated frost cracking potential. As a result of climate cooling and therefore likely higher frost weathering activity during colder and perhaps wetter stages of the mid-Holocene (the neoglaciation), rockfall activity rose once again in the second half of the Holocene (Nesje *et al.*, 1994; Blikra and Nemec, 1998; Nesje, 2002). Rockfall accumulation rates in the Jotunheimen region were significantly higher during the coldest phase of the LIA, according to McCarroll *et al.* (2001), suggesting that periglacial weathering and consequently climatic variations are sufficient to explain the origin of talus in this area.

The presented results show the importance of permafrost for effective frost weathering in both Norway and Iceland (Section 5.4); however, the connection with the rockfall distribution has not been established here. The study by Messenzehl *et al.* (2017) showed that permafrost distribution, together with bedrock curvature and valley topography, were the primary rockfall controls in the Turtmann Valley (Swiss Alps), even more important than the debuttressing effects. The authors also discussed that ice segregation is probably the major rock breakdown mechanism in the permafrost-underlain areas. The study by Sass (2010) also found a higher frequency of rockfalls from permafrost-underlain rock walls.

6.2.2 ROCK GLACIERS

Section 5.4 presented a strong relationship between the elevational distribution of talus-derived rock glaciers and frost weathering indices in both Iceland and Norway, implying that frost weathering may be an important factor for the development of talus-derived rock glaciers in these areas. According to the results, relict landforms had much higher frost weathering potential during deglaciation than at present. Part of the variation that is not explained by the relationship between frost weathering measures and elevation is probably associated with (1) aspect variations, which are not considered, (2) "climatically inactive" rock glaciers due to ice melt-out when permafrost thawed, or (3) other processes. Lilleøren and Etzelmüller (2011) mentioned that the activity of modern rock glaciers in Norway is strongly dependent on aspect, whereas relict landforms are less dependent on aspect since permafrost was widespread when they developed. In addition, relict landforms are no longer underlain by permafrost; however, they still may have some frost weathering in rock walls even if $MAGST$ is positive (Section 5.4). Furthermore, some talus-derived glaciers may also develop as secondary creep in postglacial landslides (Lilleøren, 2012). Some talus-derived landforms are clearly continuum landforms having their origins in rockfall talus, as shown by Shakesby *et al.* (1987) for talus-derived rock glaciers in Rondane, southern Norway. Alternatively, talus-derived rock glaciers could develop from other transitional landforms originating from rockfall talus (Matthews *et al.*, 2017). The number of mapped permafrost landforms is much higher in Iceland than in Norway, which Lilleøren (2012) attributed to differences in weathering due to the more prone rock to weathering in Iceland. The average value of the depth-integrated annual increase in porosity for Iceland is around 0.08 mm, whereas for Norway it is around 0.001 mm; hence, it is 80 times less than in Iceland, supporting the idea of less weathering-prone rocks in Norway.

This thesis only shows the modelling of frost weathering for a short time window, whereas rock glaciers require a longer time to develop, usually millennia. Initial deglaciation of coastal areas in both Iceland and Norway had already started millennia before the YD. Permafrost likely developed in both areas already before the YD; hence, contemporary relict rock glaciers should have had sufficient time to develop in the coastal areas at that time. The latter is supported by the study by Paasche *et al.* (2007), who dated a talus-derived rock glacier in Lyngen, northern Norway, to be at least 14 800 years old and active only until the end of the YD when permafrost rapidly thawed in the area. Etzelmüller *et al.* (2020) modelled permafrost distribution in Iceland since deglaciation and discussed that rock glaciers in the coastal areas of northern Iceland had permafrost conditions allowing for rock glacier development between deglaciation onset and the HTM. Relict rock glaciers in both Iceland and Norway have been proposed as paleo-landforms that may be used to help constrain deglaciation history and map paleo-permafrost (Sollid and Sørbel, 1992; Lilleøren and Etzelmüller, 2011; Lilleøren *et al.*, 2013; Etzelmüller *et al.*, 2020).

The importance of enhanced frost weathering for the development of talus-derived rock glaciers in Norway and Iceland is mentioned in other studies (Farbrot *et al.*, 2007a; Lilleøren and Etzelmüller, 2011). Farbrot *et al.* (2007a) computed average minimum retreat rates in rock walls above two talus-derived rock glaciers in Tröllaskagi to be around 0.4–0.6 mm a^{-1}. The authors speculated that the high rock wall retreat rates are due to large thermal gradients between the isothermal snowpack arising from maritime climate and colder permafrost-underlain rock walls. A similar situation is illustrated by the modelling shown in Paper III where a warm-based glacier covers a much colder rock wall. Lilleøren and Etzelmüller (2011) speculated that the former periglacial climate may have led to the formation of relict talus-derived rock glaciers in Norway. The authors mentioned higher weathering and slope activity, perhaps through paraglacial processes or seismic activity due to isostatic rebound. It has also been suggested that enhanced rockfall activity due to frost weathering during the YD contributed to the formation of similar talus-derived landforms in Upland Britain (Ballantyne and Kirkbride, 1987). The results shown here suggest that intense frost weathering occurred during the YD and the periglacial origin may be sufficient to explain rock glacier formation in both Norway or Iceland. Several cool periods have occurred since the onset of deglaciation and were not modelled here, although the YD was the coldest period since deglaciation in Norway and Iceland. The modelled frost weathering showed that the YD climate was particularly favourable for ice segregation. The optimal elevational zone for rock glacier development likely fluctuated after deglaciation. The LIA also had quite a large frost weathering potential (Section 5.4) and this period is also mentioned as important for rock glacier development in Norway (Lilleøren *et al.*, 2022), and it was likely similarly important in Iceland.

As glaciers and permafrost coincide in Tröllaskagi at present, moraine-derived rock glaciers are more common, although periglacial weathering likely provides debris input to these landforms as well. Moraine-derived rock glaciers are not considered here; however, note that they also may develop from rockfall debris that was subsequently transported by a glacier and further becomes a moraine from which a moraine-derived rock glacier develops (Etzelmüller and Frauenfelder, 2009).

6.2.3 THE KJELEN CIRQUE

The short- and long-term rock wall retreat rates were computed for a rock wall in the continuous permafrost zone of Jotunheimen (Section 5.5). The results show that present-day rockfall activity is higher during summer than the average postglacial rock wall retreat rate, although the rock wall retreat rates have likely varied since deglaciation. The average postglacial rock wall retreat rate was only twice as much as the average contemporary rock wall retreat rates. Therefore, it is uncertain whether enhanced rockfall activity after deglaciation, as suggested for many rockfall-derived landforms around the world (Ballantyne and Harris, 1994; Ballantyne, 2002), occurred in this cirque. The rock wall retreat rates during deglaciation computed by Ballantyne and Kirkbride (1987) were two orders of magnitude higher than contemporary rock wall retreat rates, whereas the difference shown here is much smaller. Hence, effective cirque glacial erosion throughout the entire post-glaciation period could have perhaps contributed to the formation of the ice-cored moraine, as long as (1) cirque glacier was present, (2) the glacier had a suitable temperature at the bottom, i.e. it was at least polythermal, and (3) frost weathering in the rock wall was sufficient.

The computed short-term rock wall retreat rates for the Kjelen rock wall (Section 5.5) suggested high rockfall activity over the summer period in June–August, which agrees with other studies showing that peak rockfall activity occurs in summer in permafrost-underlain rock walls (e.g. Ravanel *et al.*, 2010). Thus, it is the active layer and permafrost dynamics that govern rockfall processes in such areas. These results are in contrast to other studies from Norway, showing that peak rockfall activity occurs in March–May, most likely due to snowmelt, and in October–November, probably due to heavy rainfalls during autumn (Sandersen *et al.*, 1997). Specifically, it is the buildup of high water pressure over several days that triggers rockfalls in both seasons. The mentioned rockfall activity has probably not been investigated at elevations as high as the Kjelen cirque. The Kjelen rock wall is unlikely to receive large amounts of rainfall during autumn since solid precipitation is more common at such high elevation at that time of the year. Snow melt could be an alternative explanation for the timing of the Kjelen rockfalls, although the rock wall is high and it is uncertain whether liquid from snowmelt could reach the lower parts of the permafrost-underlain rock wall where most of the rockfalls occurred. The rock wall itself is unlikely to accumulate large amounts of snow. The active layer in the Kjelen rock wall is probably frozen throughout most of the year because (1) the summer season is very short at this particular elevation and (2) the ground thermal regime in rock walls is strongly coupled with air temperature (Paper II). Hence, the rock wall is sealed with ice when it is frozen, and rockfalls cannot occur (Sass, 2005b). Ice segregation is thus active in the frozen active layer during colder months, especially when GT is slightly below the upper temperature limit for frost cracking -ΔT_c (Rempel *et al.*, 2016) and the greatest hydraulic permeability allows for most water migration. During the thawing season, when the active layer thaws to a sufficient depth, rock debris that was detached during winter by ice segregation may fall as a rockfall, as explained by Sass (2005b). $MAGST$ in the east-facing part of the Kjelen rock wall is probably slightly higher than -2 °C for the 2010s, similar to the measurements in the nearby east-facing rock wall (Paper II). The Kjelen rock wall likely experiences GT warming, as modelled in Paper II for the nearby rock walls in Jotunheimen. Further investigations over longer time periods could reveal whether rockfall frequency increases in response to GT warming and subsequent active layer deepening.

Large variations in potential incoming solar radiation in the Kjelen cirque (Section 5.5) suggest that GT variations are perhaps also large within the rock wall. The shaded, more north-facing part of the rock wall is probably colder than the sun-exposed, more south-facing part of the rock wall. The higher rockfall frequency in the shaded rock wall may result from (1) more intense frost weathering in such an aspect and (2) more severe deepening of the active layer in such an aspect. The former is supported by studies showing that north-facing rock walls have lower GTs and sometimes have higher moisture content, leading to more intense frost weathering and higher debris production (Coutard and Francou, 1989; Sass, 2005a). The latter is consistent with observations from the European Alps, where extreme thaw depths in the north-facing rock walls led to higher rockfall activity in such aspects, especially during extremely hot summers (Gruber *et al.*, 2004). Explanations (1) and (2) may also be associated with each other. All of these explanations may be valid for the Kjelen rock wall. Additionally, the debuttressing effects may contribute to rockfalls since the cirque glacier is retreating, although it is doubtful that rockfalls from higher elevations arise from debuttressing effects as a long time has probably passed since their deglaciation.

6.3 THE GROUND THERMAL REGIME AND SLOW MASS MOVEMENTS

6.3.1 CONTRIBUTION OF VARIOUS PROCESSES

Section 5.6 shows velocity measured for the hillslope with abundant stone-banked solifluction lobes at Juvflye. Other processes than solifluction may potentially contribute to the measured displacements. The most important processes are probably: (1) crustal deformation due to primarily glacial isostatic adjustment (Kierulf *et al.*, 2021), (2) cryoturbation because patterned ground is common in the study area, and (3) soil production due to bedrock weathering. Any tectonic component is likely absent due to the relativeness of the InSAR measurements to nearby reference points, which very likely have identical crustal deformation. Schmidt-hammer measurements were performed on the sorted circles (Winkler *et al.*, 2016) and stripes (Winkler *et al.*, 2020) along the same hillslope, and the results suggested that these are relict landforms that stabilised around 6.5–8.5 ka; hence, cryoturbation is no longer active. Soil production would lead to volumetric changes to the parent rock (Anderson and Anderson, 2010), thus the land surface would have positive vertical displacement. However, landscape modelling by Egholm *et al.* (2015) suggests that soil production rates are very slow, and for $MAAT$ at Juvflye, surface rise would be only 20 m Ma^{-1} or 20 μm a^{-1}. In addition, because the main direction of displacement is negative, soil production definitely has a smaller contribution to displacement than other processes that lead to negative displacement. The highest activity measured here is associated with sparsely vegetated areas underlain by permafrost, namely blockfields or more precisely blockslopes since the investigated blockfield material shows movement (Ballantyne, 2018). Ballantyne (2018) mentions that the movement of blockslopes may be explained by the following processes: frost creep, gelifluction, debris flow and even permafrost creep. Debris flow may be excluded because it is a fast-moving type of landslide. Permafrost creep would have continuous downslope displacement with seasonal acceleration, which is not the case here. Hence, solifluction processes are measured here, and the contribution of any other processes should be minimal. Therefore, solifluction is the most widespread denudation process in the study area, and it is balanced by crustal deformation, which is currently around 2–3 mm a^{-1} in this part of Norway (Kierulf *et al.*, 2021).

Even though small solifluction lobes occur in the study area, often on top of the larger solifluction lobes, they are probably not what contributes mainly to the measured displacements, and the dynamics of the large solifluction lobes probably governs the measured displacements. Such lobe morphology is indicative of deeper seasonal frost action (Matsuoka *et al.*, 2005) or active layer dynamics, which is consistent with the seasonal character of the presented displacements. Since the seasonal freeze-thaw cycles are investigated here, only three solifluction components may be considered to explain the measured displacements: (1) annual frost creep, (2) gelifluction, and (3) plug-like flow. Gelifluction is unlikely to be the main solifluction process in the study area because similar displacements over a larger area point to a non-localised movement, whereas gelifluction is characterised by a discrete and localised movement (Kinnard and Lewkowicz, 2005; Hu *et al.*, 2021). Nevertheless, any heterogeneous displacement within the 20 × 20 m cells cannot be detected using InSAR; hence, the contribution of gelifluction is likely minimal at such a scale. Therefore, only annual frost creep and plug-like flow are discussed further. Additional measurements of the frost heave during winter would allow for the computation of potential frost creep (e.g. Matsuoka, 2001b) and displacement measurements of the soil column would help to understand the solifluction processes in the Juvflye area better.

6.3.2 SEASONAL FROST AREA

Rapid thaw settlement upon ground thawing and cessation of movement after seasonal frost disappeared at the lower site is similar as in other areas with seasonal frost in Norway, as shown for solifluction processes at the Dovre Mountains, southern Norway, by Harris *et al.* (2008). The thaw settlement shown by Harris *et al.* (2008) is around 30 cm for an area where seasonal frost is shallow and only 40 cm deep. Seasonal frost in BH5 at the lower AOI reached around 7 m depth in the investigated period, and vertical thaw settlement was only 1.3–6.3 mm. Seasonal frost depth measured in BH5 may not be representative of the lower AOI due to the three-dimensional effects, and it is probably rather around 2 m (Isaksen *et al.*, 2011). In addition, the thickness of sediments at the lower site is only assumed to be 1.5 m; hence, seasonal frost deeper than this cannot contribute to frost creep. Such a large difference in thaw settlement in comparison with the Dovre Mountains could be explained by: (1) spatial scale since InSAR provides average measurements over a larger area, (2) differences in the soil frost-susceptibility, (3) differences in hydrological conditions, (4) differences in slope gradient, (5) gelifluction is unlikely to be detected using InSAR. In addition, the InSAR measurements are delayed with respect to the thawing onset estimated from the borehole; hence, some displacement at the beginning of thawing cannot be measured, although it unlikely explains such large differences. Rouyet *et al.* (2021) also discussed little frost-susceptibility as a possible explanation for the low contribution of surface geology to spatial variations in solifluction movement in northern Norway. Even though the lower site experiences more snow melt and has surface water in some areas, it seems that the lower site may be well drained in other areas because the calibration of modelled GT from boreholes indicated very low water content for the lower AOI. Even though some details about the movement may not be clear at the lower site, the measured displacement is best explained by the annual frost creep component of solifluction, probably with one-sided freezing, which is most common in areas with seasonal frost (e.g. Matsuoka, 2001b).

6.3.3 PERMAFROST-UNDERLAIN AREA

The displacement occurs throughout the whole summer at the upper AOI as ground thawing is progressing. The ground thermal regime at the upper site in the area with the most active solifluction is warm permafrost according to the GT modelling, although due to negative thermal anomalies in blockfields and blockslopes that cannot be modelled using a permafrost model based on conductive heat transfer, cold permafrost could also occur in some places. Rouyet *et al.* (2019) presented the InSAR measurements with thaw displacement associated with solifluction processes occurring in tandem with increasing thaw depth as measured in the Endalen borehole, Svalbard, which also has warm permafrost over the recent years. Annual LOS thaw settlement between 2 and 12 mm measured here is much smaller than 30–50 mm LOS thaw settlement measured at Endalen using InSAR (Rouyet *et al.*, 2019) or 40–80 mm thaw settlement measured at the Endalen solifluction monitoring station (Harris *et al.*, 2011), where frost-susceptible soil occurs. Harris *et al.* (2011) showed that thaw resettlement at Endalen stopped during the ground thawing of ground layers with little excess ice. Such periods cannot be identified here due to temporal resolution. Nevertheless, the nearly constant relationship between the deepest thaw depth and larger displacements could indicate that more ground ice is present in deeper layers at Juvflye and even that small plug-like flow occurs in some years. Plug-like flow involves the movement of an entire active layer. In theory, it only occurs in areas underlain by cold permafrost, although the exact GT threshold between cold and warm permafrost that allows for two-sided freezing is uncertain (Matsuoka, 2001b). The detected thaw resettlement is tiny; hence, it is not necessarily segregated ice that melts, but it could also just be pore ice. Measured GTs in boreholes in southern Norway generally suggest that ice-rich layers are less common in mountainous areas, which are covered by coarse sediments (Farbrot *et al.*, 2011). Ballantyne (2018) mentioned that saturated, non-frost-susceptible soils may also experience frost creep, although because the volumetric expansion is much smaller in this case, frost creep would also be smaller. The presence of widespread permafrost in the upper AOI has probably had a large influence on the hydrological conditions preventing effective drainage; hence, liquid water from e.g. autumn rainfalls or just active layer thawing would refreeze at the bottom of the active layer, possibly forming ice lenses if silt layers are present. In addition, it is possible that a small component of plug-like deformation occurs in some years, especially in 2018, when ground thawing reaches the deeper layers with higher ground ice content towards the end of the summer, similar to the Endalen site (Harris *et al.*, 2011).

6.3.4 SPATIAL VARIATIONS

The ground thermal regime and $NDVI$ were the most important variables dictating solifluction activity in the Juvflye area (Subsection 5.6.3). Other statistical modelling studies of spatial solifluction activity use $MAAT$ or elevation as a proxy for GT. Such studies often find that slope, $MAAT$ or elevation and vegetation are the primary variables explaining solifluction activity (Hjort, 2014; Hjort *et al.*, 2014; Rouyet *et al.*, 2021). The solifluction activity modelled here indicates more activity in areas with lower GT. The solifluction activity increased with lower $MAAT$ in the study by Hjort *et al.* (2014) employing statistical modelling in (sub-)Arctic regions with $MAAT$ ranging from -12 to 4 °C. Other studies also show increasing solifluction activity with decreasing $MAAT$ for a given study area (Rouyet *et al.*, 2021). Slope gradient determines potential frost creep (Matsuoka, 2001b); hence, it has a large contribution when modelling the distribution of active areas (Hjort *et al.*, 2014; Rouyet *et al.*, 2021). However, slope may not be so important for distinguishing between active and inactive solifluction areas, as shown by Hjort (2014), which is in agreement with the modelling conducted here. TWI was also of little importance. TWI fails to account for subsurface drainage conditions arising from various soil types and permafrost versus non-permafrost areas. Snow factors also had a small contribution to solifluction activity, likely because of their complex impact on GT. In addition, snow provides moisture; hence, the lower AOI should be more saturated due to deeper snow in that area. On the other hand, drainage at the lower AOI with only sporadic permafrost and seasonal frost may be more effective than at the upper site with widespread permafrost. Other studies also emphasise the importance of snow for providing additional soil moisture and its influence on GT as important for solifluction activity (Ridefelt *et al.*, 2011; Hjort, 2014). Relatively small solifluction velocities in the study area with such variable snow depths implies that water availability is not the limiting factor in the study area.

Rouyet *et al.* (2021) also found that $NDVI$ was the second most important variable for vertical solifluction velocities in northern Norway, where high velocities occurred on the mountain tops and upper slopes of the mountains. The impact of vegetation on solifluction activity is very complex. While GT is mostly a driver of solifluction, the same is not necessarily valid for $NDVI$, because $NDVI$ may be (1) a complex indicator of optimal conditions for solifluction connected with soil type and its humidity (Ridefelt *et al.*, 2010), vegetation type (Ridefelt *et al.*, 2011), slope, aspect, elevation, snow and even GT, (2) an indicator of solifluction motion itself since motion influences the plant roots and provides fine material (Ridefelt *et al.*, 2010; Hjort *et al.*, 2014), and finally (3) a driver of solifluction by thermal insulating effects of vegetation on GT (Matsuoka, 2001b; Hjort, 2014) or by capturing insulating and moisture-providing snow. In the case explored here, the role of vegetation is unclear and could be associated with lower GTs in sparsely vegetated areas, or perhaps some vegetation types may establish in less active areas (Ridefelt *et al.*, 2011). GT modelling probably failed to account for some site-specific factors influencing GT variations, which could be correlated with $NDVI$. The uncertainties in soil stratigraphy may be especially important. Furthermore, $NDVI$ decreases with elevation in the study area; hence, it may also just be an indicator of elevation. Hence, external conditions such as climate are probably the most important factors for solifluction activity in the study area. This is due to higher amounts of ground ice being accumulated in areas with decreasing GT, with possibly a slight contribution from internal conditions such as the composition of sediment. It is uncertain whether frost heave due to ice lens growth occurs in the area due to such small movements. Soils with low frost susceptibility are perhaps not the limiting factor for solifluction in the study area, similar to northern Norway (Rouyet *et al.*, 2021).

6.4 IMPLICATIONS FOR PERIGLACIAL LANDSCAPE EVOLUTION

6.4.1 POSTGLACIAL LANDSCAPE EVOLUTION

Recent permafrost thawing modelled for Iceland and Norway (Paper I and Paper II) potentially increases rapid mass movements, perhaps leads to an acceleration of rockslides, and may influence landform degradation. Permafrost in both Iceland and Norway is currently experiencing warming and degradation, exemplifying the transition period between permafrost and non-permafrost ground conditions, which has a profound impact on the geomorphological processes. During the transition period, sediment transport is certainly increased, especially by enhanced landsliding due to permafrost degradation (Gruber *et al.*, 2004; Ravanel and Deline, 2011; Saemundsson *et al.*, 2018). Permafrost dynamics may also influence slope destabilisation on much longer timescales. After deglaciation, permafrost stabilised rock slopes in Norway, and later, rockslides destabilised and started their slow movement during periods of intense permafrost degradation in the HTM (Hilger *et al.*, 2021). Periglacial processes may still be active if permafrost disappears, although the disappearance of permafrost could mean that some periglacial processes would be less active and permafrost landforms would change state from active to inactive features. Some areas in Norway and Iceland may serve as active examples of past periglacial landscape evolution elsewhere, e.g. outside the Fennoscandian or Laurentide Ice Sheets, where various relict permafrost features occur in both Europe and North America (French and Millar, 2014; Oliva *et al.*, 2023).

Three recent landslides that occurred in Iceland were likely triggered by decade-scale GT warming and permafrost degradation from the bottom (Saemundsson *et al.*, 2018). GT was modelled for these sites in Paper I. The results supported the idea from Saemundsson *et al.* (2018) that bottom-up, decade-scale GT warming occurred at these sites. In Iceland, mainly shallow and warm permafrost (>-2 °C) is modelled, suggesting that permafrost is very vulnerable under atmospheric warming (Paper I). Furthermore, rock glaciers in northern Iceland seem to have entered a degradation stage, as their main component of movement is currently vertical, implying that subsidence dominates their movement (Tanarro *et al.*, 2019). In addition, palsas in Iceland have decreased in size since the 1960s, and an active layer deepening in these landforms has been measured recently (Saemundsson *et al.*, 2012).

Paper II showed increasing GT warming with elevation when terrain is more exposed to surface warming. Previous research by Noetzli *et al.* (2007) and Noetzli and Gruber (2009) demonstrated the significance of multilateral warming. It showed that surface warming penetrates into narrower and steeper topography from multiple directions, resulting in a faster pace of ground warming than in flatter topography. Even though we only investigated a 2D scenario, our analysis also implies that multilateral warming is significant in Norway. It is unclear how slope stability may be influenced by the variations in GT warming that are simulated in Paper II. Our findings implied that ground warming increases with elevation inside a single rock wall section; hence, this may infer that the probability of instability has a similar pattern. Nonetheless, GT could be highest in the centre portion of the rock wall; as a result, permafrost degradation may be more likely to occur there in the sun-exposed rock walls. Slowly creeping rockslides in warm permafrost environments have recently accelerated in Norway, and this acceleration has been attributed to increasing GT since the LIA (Hilger *et al.*, 2021). In addition, a rock avalanche that occurred in northern Norway in 2008 was likely triggered by thawing permafrost (Frauenfelder *et al.*, 2018). Rock glacier creeping rates in Norway also seem to be influenced by the recent permafrost warming, based on the measurements by Eriksen *et al.* (2018) for Ádjit for the period since the 1950s.

Slow landscape denudation occurs through solifluction processes on the Juvflye hillslope (Section 5.6). Diffusive processes have dominated on the Juvflye hillslope at the upper part of the slope over the past few years. The vertical rate of change of land-surface elevation dz/dt is assumed here to be the difference between the vertical uplift rate U and the vertical erosion rate E due to diffusive processes, especially annual frost creep: $dz/dt = U+E$. The latter equation represents landscape evolution without bedrock channelling and landsliding, which are often included in the landscape evolution models using power laws and nonlinear diffusion (Pelletier, 2008; Refice *et al.*, 2012). In the case of the Juvflye hillslope, it seems that both fluvial erosion and landsliding are of secondary importance due to the high correlation of vertical velocities with thaw depths. For the assumed vertical uplift rate of 2.5 mm a^{-1} (Kierulf *et al.*, 2021), the upper area is dominated by denudation with an average surface lowering of 5 mm a^{-1} and the uplift dominates in the lower area with a surface increase of 1.5 mm a^{-1} on average. Assuming an average vertical rate of land-surface elevation of -8 mm a^{-1} at the upper part of the slope at an elevation of 1700 m and +2 mm a^{-1} at the lower slope at an elevation of 1450 m, the Juvflye hillslope would become uniform at an elevation of 1500 m after only 25 ka. Nevertheless, due to very slow mobile regolith production rates, such landscape evolution is unfeasible over a long time scale. However, these rates still emphasise the potentially large contribution of solifluction to the overall long-term landscape evolution, especially in areas underlain by permafrost and even in areas without frost-susceptible soils.

6.4.2 ROCKFALL "BUZZSAW"

The importance of frost weathering for landscape evolution at larger and longer time scales has been the topic of several studies. Hales and Roering (2007) were perhaps the first authors to use "buzzsaw" in the context of periglacial landscape evolution, inspired by the term "glacial buzzsaw" (Brozovic *et al.*, 1997; Egholm *et al.*, 2009). Glacial and rockfall, also known as periglacial, "buzzsaw" describe the intensification of glacial and periglacial denudation at certain elevations, which would affect the relief and limit mountain elevation (Hales and Roering, 2007). The latter was an implication of frost weathering concentration within a certain elevation range, modelled using FCW, which possibly agrees with peak mountain elevation (Hales and Roering, 2007). Hales and Roering (2007) argued that the elevational zone of segregation ice weathering evolves with climate; hence, global cooling (e.g. during stadials) would intensify segregation ice weathering and facilitate rapid erosion through enhanced rockfall events. Hales and Roering (2009) mapped the distribution of active and inactive talus slopes in the Southern Alps, New Zealand, and identified distinct elevation zones for the occurrence of both classes. The latter coincided with intense periglacial weathering as modelled using FCW; hence, they speculated that periglacial weathering limits peak elevation in the area. Other studies also showed that the frost-cracking potential may peak at certain elevations in the Khumbu Himalaya (Scherler, 2014; Rempel *et al.*, 2016). Delunel *et al.* (2010) showed that denudation rates in the French Western Alps are correlated with elevation and claimed that frost-cracking processes significantly influence landscape evolution in the area. The mentioned studies are also supported by other studies showing the clustering of rockfalls at certain elevations, e.g. in the Swiss Alps (Messenzehl *et al.*, 2017). In the case of Norway and Iceland, the elevational distribution of talus slopes has not been mapped yet. There is a slight clustering of talus-derived rock glaciers according to activity, and active rock glaciers generally occur at higher elevations than inactive. Nevertheless, rock glaciers also require permafrost for existence, and their debris may arise from other non-periglacial processes; hence, mapping of active and inactive talus slopes could be the next step in the investigation of the impact of segregation ice weathering on landscape evolution in Norway and Iceland.

Paper III has implications for backwearing in cirques, which is thought to be a particularly effective mode of landscape smoothing (Oskin and Burbank, 2005; Steer *et al.*, 2012), where denudation is likely driven by a combination of glacial and periglacial processes. Cirque erosion is generally not so well understood; however, it has something to do with glacial erosion at the bed and periglacial processes in the cirque headwall (Sanders *et al.*, 2012). Sanders *et al.* (2012) modelled ice segregation in a rock wall above a cirque glacier and a bergschrund, and their results suggested that ice segregation in both the rock wall and bergschrund is effective in providing debris that is later transported by a cirque glacier. This is illustrated in Paper III in areas with large thermal gradients between rock walls and glaciers, although the modelled thermal gradients depend on the assumed GST in rock walls and bottom temperature in glaciers; hence, this is not representative of the cases where the difference between *GST* in rock walls and bottom temperature in glaciers is small.

6.4.3 LONG-TERM PERIGLACIAL LANDSCAPE EVOLUTION

The periglacial imprint on long-term and large-scale landscape evolution remains debatable. Geomorphological processes in periglacial environments are claimed to be indistinct for their cold climatic conditions by some researchers (André, 2003; French, 2016). The old belief that periglacial areas are rapidly evolving landscapes and the concept of a truly periglacial landscape have been questioned by recent research (French, 2016). For instance, French (2007) wrote: *There is no slope form, or slope assemblage, that may be regarded as uniquely "periglacial" in nature.* In addition, the efficiency of frost weathering contributing to landscape evolution has been shown to be overestimated by others (André, 2003). On the other hand, some researchers explain the long-term evolution of summit flats as resulting from periglacial erosion, which offers an alternative to the criticised conceptual cycle of erosion by Davis or similar cyclic landscape development models (Orme, 2007).

The evolution of the landscape in southern Norway has been much debated over recent years, and periglacial processes are important erosive agents in the alternative hypothesis. The classical model explains the flat summits at higher elevations that form the "paleic surface" in southern Norway as tectonic forms that resulted from the uplift of the initial peneplain. In the Paleogene (66–23.03 Ma), started the post-Cretaceous land uplift of Norway's surface, which was a peneplain in the Cretaceous (145–66 Ma) (Ramberg *et al.*, 2013). The paleic surface, an erosion surface with various Paleozoic, Mesozoic, Paleogene and Neogene landforms and surfaces, is interpreted as an old eroded surface formed before the Quaternary glaciations. Elevation of the paleic surface is reproduced based on e.g. the blockfield distribution, implying that the post-Cretaceous land uplift was uneven and larger in western parts of Norway. During the uplift in the Paleogene and Neogene (23.03–2.6 Ma), rivers started to erode the paleic surface, following the old weakness zones in bedrock (Ramberg *et al.*, 2013). The alternative theory for the formation of flat summits in southern Norway, the so-called ICE (isostasy-climate-erosion) hypothesis (Nielsen *et al.*, 2009; Steer *et al.*, 2012) claims that the peneplanation and the Paleogene-Neogene uplift phases never happened. The ICE hypothesis explains the topography of Norway as formed by rifting processes and erosion since the Caledonian Orogeny. The climatic control since the global cooling in the Eocene–Oligocene through glacial and periglacial buzzsaws is the central part of the hypothesis. Hence, the low-relief, high-elevation surfaces are the results of the buzzsaws, which concentrate around and above the equilibrium-line altitude of glaciers (Steer *et al.*, 2012). The ICE hypothesis has been heavily criticised in several papers by both geologists and geomorphologists (Lidmar-Bergström and Bonow, 2009; Chalmers *et al.*, 2010; Gabrielsen *et al.*, 2010; Hall *et al.*, 2013; Ramberg *et al.*, 2013; Hall and Kleman, 2014; Japsen *et al.*, 2018). I will not discuss the latter studies in depth since they mostly focus on the tectonic and glacial erosion parts of the hypothesis. I will rather focus on the discussion of the long-term landscape evolution model developed to support the ICE hypothesis, presented in Egholm *et al.* (2015).

The periglacial part of the Egholm *et al.*'s (2015) model includes regolith production through segregation ice weathering and slow mass transport through frost creep. They used the Anderson *et al.*'s (2013) model for quantification of segregation ice weathering (see e.g. Figure 2.6) and ran it for various regolith depths in the companion paper (Andersen *et al.*, 2015). Their results show maximum frost-cracking intensity for SATs between -8 and -5 °C, which is similar to my results (Section 5.4), even though the authors used a different frost-cracking model. Soil production rates were not estimated in this dissertation at all, so this part cannot be compared. Egholm *et al.* (2015) modelled 100–300 m vertical periglacial erosion at the summit peaks over 14 Ma in their second experiment. Even though this is a result of transport-limited denudation, the process-limiting factor is soil production rate, which is on average 20 m Ma^{-1} (Egholm *et al.*, 2015).

Egholm *et al.* (2015) claim that sediment transport decreases in the Quaternary because it is too cold for efficient sediment transport. Their sediment transport is most efficient when SAT approaches 0 °C, which disagrees with the velocity rates measured for the Juvflye hillslope, for the northern Norway (Rouyet *et al.*, 2021) and solifluction activity at other sites in the (sub-)Arctic (Hjort *et al.*, 2014). Even though my results do not support the climatic conditions used in the model for the transport processes, they are in agreement that solifluction is the most erosive process on a smaller-scale periglacial hillslope. However, this is likely not sufficient for larger landscape scales in periglacial environments, where both fluvial erosion, landsliding and snow are important. Note also that the original periglacial buzzsaw was inspired by efficient rockfall processes at high elevations, whereas the Egholm *et al.*'s (2015) model is mostly applicable to gentle topography.

The modelling by Egholm *et al.* (2015) does not prove that periglacial processes are responsible for the formation of the high-elevation plateaus in southern Norway.

Topography flattening would be the result of most landscape evolution models over longer time scales if soil creep is used as the only transport process in a landscape evolution model since it is based on the diffusion equation (e.g. Pelletier, 2008). Furthermore, the only flat surfaces recognised from the geomorphological interpretation of periglacial environments are probably step-like terraces, the so-called cryoplanation terraces. The final stage of cryoplanation would result in an almost completely flat surface, although this is an idealised final stage and quite unlikely to occur (Ballantyne, 2018). The other most typical examples of periglacial slope morphology, as classified by French (2007) would not be flat surfaces but rather inclined slopes. Cryoplanation terraces occur in Norway, e.g. in Jotunheimen (Matthews *et al.*, 2019) or below Snøhetta in the Dovre Mountains, southern Norway; however, cryoplanation terraces mostly develop in well-jointed rocks (Ballantyne, 2018), which is not the case in most of southern Norway. Ballantyne (2018) mentions that cryoplanation is perhaps best explained by scarp retreat through nivation at the foot of scarps and slow mass movements operating on terrace treads, such as solifluction and running water. Nivation is an umbrella term for weathering and slope processes intensified by snow patches (Ballantyne, 2018). The 2D frost cracking model (Paper III) could be applied to support such weathering in small scarps. Nivation processes are not represented in Egholm *et al.*'s (2015) periglacial slope evolution model, which explains the development of the high summits rather through vertical lowering and not scarp retreat.

Note that the Egholm *et al.*'s (2015) model is still applicable to the generic landscape evolution in any climatic zone, which is often modelled by progressing weathering front and creep processes (Pelletier, 2008). The model has also the potential to explain the evolution of some periglacial features at shorter time scales. For instance, the model could be applied to explain the evolution of blockfield cover on the summit flats in southern Norway throughout the Quaternary, as illustrated by Ballantyne (2010). The author speculated that blockfields were lowered during the Quaternary, where mass movement was one of his hypotheses for their surface lowering. The movement of blockslopes presented here indirectly supports the assumed lowering of autochthonous (i.e. *in situ*) blockfields presented by Ballantyne (2010) since the blockslopes at Juvflye are likely fed by sediments from the upper flatter area with perhaps autochthonous blockfield, if their movement is insignificant. According to my findings, the presence of permafrost appears to be an important factor in such lowering; hence, climatic conditions for solifluction activity would have to be improved in the model before its application to explain blockfield evolution.

7. CONCLUSIONS

The main conclusions of this work are as follows:

- Permafrost is mainly found in central and northern Iceland, especially in the Tröllaskagi peninsula, where the lowest *GTs* were modelled. The thermal properties of snow and snow depth were identified as the most crucial factors governing the distribution of permafrost in Iceland. Various snow scenarios greatly affected the modelled permafrost extent. Run for the wind-exposed areas with shallow snow depth (50 % precipitation run) had 3–5 and 8–15 times more cells underlain by permafrost than the snow scenarios for areas with average snow depth (100 % precipitation run) and substantial snow accumulation (150 % precipitation run). Predominantly warm and shallow permafrost in Iceland is vulnerable to the atmospheric warming lasting since the 1980s. Throughout time, the proportion of cells with simulated permafrost declined by almost 40 % between 1980–1989 and 2010–2016. Recent permafrost thawing may have implications for slope stability, palsas and rock glacier dynamics in Iceland.

- *GT* modelling for rock walls in Norway suggested no permafrost along some profiles or discontinuous to continuous permafrost above certain elevations at other profiles. The following factors had an impact on the modelled *GT* in rock walls: (1) *SAT* uncertainties, (2) surface offsets arising from the incoming shortwave solar radiation, (3) snow conditions on, above and below rock walls, (4) rock wall geometry and size, (5) adjacent blockfield-covered plateaus and glaciers. Because the 1930s atmospheric warming and the 1970s–80s cooling were more severe in northern Norway, rock walls there had greater variations in *GT* after the LIA than rock walls in southern Norway. During the last three decades, the average warming of Norway's rock walls at a depth of 20 m has been 0.2 °C per decade. Similarly to Iceland, the increasing GTs in permafrost-underlain terrain in Norway may decrease slope stability and also lead to higher creeping rates of rockslides and rock glaciers.

- Two-dimensional modelling of frost cracking potential allowed for the identification of sites with enhanced segregation ice weathering. They are mainly found near the melting ice sheet or glaciers and locations with a sudden transition in the snow conditions, causing significant temperature gradients. According to simulated changes in porosity, bedrock may be progressively weakened by segregation ice weathering during the melting of an ice sheet or glacier, in addition to the glacial debuttressing effects. This may have significance during deglaciation as well as the current retreat of mountain glaciers.
- Climate of the YD stadial was optimal for intensive segregation ice weathering in the coastal areas of Norway and Iceland. Modelled frost weathering for contemporary relict talus-derived rock glaciers was largest during the YD, implying that frost weathering significantly contributed to rock glacier development at that time.
- The frost modelling results using 1D and 2D approaches agree about the largest segregation ice weathering potential in the YD or the YD/PB transition in Norway and Iceland since deglaciation. The large frost weathering at that time is due to climate in the 1D case. On the other hand, the 2D case includes the lateral effect across the critical zones for frost weathering. The modelled increased weathering via frost processes in both 1D and 2D approaches compares favourably with existing research on the timing of rockfall accumulations in Norway.
- The average rates of rock wall retreat since deglaciation were only two times higher than average rates at present, although the investigated period was only one year; hence, there are large uncertainties. The rockfalls were most frequent during the summer period, and most of the material was lost from shaded rock wall sections.
- The solifluction lobes at the higher site with widespread permafrost moved fastest with line-of-sight velocities in the most active areas <-7.5 mm a^{-1}. This translates to vertical velocities <-10 mm a^{-1} in the most active areas. The

lobes at the lower AOI move much slower with line-of-sight velocity between -3 and -1.5 mm a^{-1}, which is equivalent to vertical velocities between -4 and -2 mm a^{-1}. The temporal variations in displacement measured by InSAR are correlated with the thaw depth measured in nearby boreholes, increasing the confidence that the measured displacement is associated with the active layer or seasonal frost dynamics and thus solifluction processes. The measured displacements at the lower study area with the seasonal frost are best explained by the annual frost creep component of solifluction with one-sided freezing, since the movement stops after the complete thawing of seasonal frost. The displacement occurs throughout the whole summer at the upper study area as ground thawing progresses, and activity in this area results from annual frost creep, possibly with plug-like flow over some summers. GT at 2 m depth and $NDVI$ were the most important variables governing the distribution of the active solifluction areas, although the influence of $NDVI$ is unclear.

Segregation ice weathering producing debris, together with the subsequent rapid and slow mass movements, slowly contribute to the overall long-term landscape denudation in the periglacial environments of Norway and Iceland. The presence of ground ice, especially permanently frozen ground, has a profound impact on geomorphological processes. Nevertheless, the contribution of the periglacial processes to the formation of the high-elevation, low-relief surfaces in southern Norway is quite uncertain.

REFERENCES

Andersen, J. L., Egholm, D. L., Knudsen, M. F., Jansen, J. D., and Nielsen, S. B. (2015). The periglacial engine of mountain erosion – Part 1: Rates of frost cracking and frost creep. *Earth Surface Dynamics*, *3*(4), 447–462. doi: 10.5194/esurf-3-447-2015.

Anderson, R. S. (1998). Near-surface thermal profiles in alpine bedrock: Implications for the frost weathering of rock. *Arctic and Alpine Research*, *30*(4), 362–372. doi: 10.2307/1552008.

Anderson, R. S. and Anderson, S. P. (2010). *Geomorphology: the mechanics and chemistry of landscapes.* Cambridge, UK: Cambridge University Press, 637 pp.

Anderson, R. S., Anderson, S. P., and Tucker, G. E. (2013). Rock damage and regolith transport by frost: an example of climate modulation of the geomorphology of the critical zone. *Earth Surface Processes and Landforms*, *38*(3), 299–316. doi: 10.1002/esp.3330.

Andrews, J. T., Hardardóttir, J., Helgadóttir, G., Jennings, A. E., Geirsdóttir, Á., Sveinbjörnsdóttir, Á. E., Schoolfield, S., Kristjánsdóttir, G. B., Smith, L. M., Thors, K., and Syvitski, J. P. (2000). The N and W Iceland Shelf: insights into Last Glacial Maximum ice extent and deglaciation based on acoustic stratigraphy and basal radiocarbon AMS dates. *Quaternary Science Reviews*, *19*(7), 619–631. doi: 10.1016/S0277-3791(99)00036-0.

André, M.-F. (2003). Do periglacial landscapes evolve under periglacial conditions? *Geomorphology*, *52*(1–2), 149–164. doi: 10.1016/s0169-555x(02)00255-6.

Arnalds, Ó. (2000). Desertification: an appeal for a broader perspective. In Arnalds, Ó. and Archer, S. (Eds.), *Rangeland Desertification*, Dordrecht, The Netherlands: Kluwer Academic Publishers, pp. 5–15. doi: 10.1007/978-94-015-9602-2_2.

Arnalds, Ó. (2004). Volcanic soils of Iceland. *Catena*, *56*(1), 3–20. doi: 10.1016/j.catena.2003.10.002.

Arnalds, Ó. (2008). Soils of Iceland. *Jökull*, *58*, 409–421.

Arnalds, Ó. (2015). *The Soils of Iceland.* Dordrecht, The Netherlands: World Soils Book Series, Springer, 183 pp. doi: 10.1007/978-94-017-9621-7.

Associate Committee on Geotechnical Research (1988). *Glossary of permafrost and related ground-ice terms.* National Research Council of Canada, Ottawa, Permafrost Subcommittee, Technical memorandum 142, 156 pp.

Atkinson, B. K. (1984). Subcritical crack growth in geological materials. *Journal of Geophysical Research: Solid Earth*, *89*(B6), 4077–4114. doi: 10.1029/JB089iB06p04077.

Ballantyne, C. K. (2002). Paraglacial geomorphology. *Quaternary Science Reviews*, *21*(18), 1935–2017. doi: 10.1016/S0277-3791(02)00005-7.

Ballantyne, C. K. (2010). A general model of autochthonous blockfield evolution. *Permafrost and Periglacial Processes*, *21*(4), 289–300. doi: 10.1002/ppp.700.

Ballantyne, C. K. (2018). *Periglacial geomorphology.* Chichester, UK: Wiley-Blackwell, 454 pp.

Ballantyne, C. K. and Harris, C. (1994). *The periglaciation of Great Britain.* Cambridge, UK: Cambridge University Press, 330 pp.

Ballantyne, C. K. and Kirkbride, M. P. (1987). Rockfall Activity in Upland Britain during the Loch Lomond Stadial. *The Geographical Journal*, *153*(1), 86–92.

Barboux, C., Delaloye, R., and Lambiel, C. (2014). Inventorying slope movements in an Alpine environment using DInSAR. *Earth Surface Processes and Landforms*, *39*(15), 2087–2099. doi: 10.1002/esp.3603.

Barnhart, T. B. and Crosby, B. T. (2013). Comparing Two Methods of Surface Change Detection on an Evolving Thermokarst Using High-Temporal-Frequency Terrestrial Laser Scanning, Selawik River, Alaska. *Remote Sensing*, *5*(6), 2813–2837. doi: 10.3390/rs5062813.

Barsch, D. (1996). *Rockglaciers: indicators for the present and former geoecology in high mountain environments.* Heidelberg, Germany: Springer Verlag, 331 pp.

Bechtold, S. and Höfle, B. (2020). *VOSTOK - The Voxel Octree Solar Toolkit.* heiDATA. doi: 10.11588/data/QNA02B.

Bellwald, B., Hjelstuen, B., Sejrup, H., Stokowy, T., and Kuvås, J. (2019). Holocene mass movements in west and mid-Norwegian fjords and lakes. *Marine Geology*, *407*, 192–212. doi: 10.1016/j.margeo.2018.11.007.

Berardino, P., Fornaro, G., Lanari, R., and Sansosti, E. (2002). A new algorithm for surface deformation monitoring based on small baseline differential SAR interferograms. *IEEE Transactions* *on Geoscience and Remote Sensing*, *40*(11), 2375–2383. doi: 10.1109/TGRS.2002.803792.

Berthling, I. and Etzelmüller, B. (2011). The concept of cryo-conditioning in landscape evolution. *Quaternary Research*, *75*(2), 378–384. doi: 10.1016/j.yqres.2010.12.011.

Björck, S., Rundgren, M., Ingolfsson, O., and Funder, S. (1997). The Preboreal oscillation around the Nordic Seas: terrestrial and lacustrine responses. *Journal of Quaternary Science*, *12*(6), 455–465. doi: 10.1002/(SICI)1099-1417(199711/12)12:6<455::AID-JQS316>3.0.CO;2-S.

Blikra, L. H. and Longva, O. (1995). Frost-shattered debris facies of Younger Dryas age in the coastal sedimentary successions in western Norway: palaeoenvironmental implications. *Palaeogeography, Palaeoclimatology, Palaeoecology*, *118*(1), 89–110. doi: 10.1016/0031-0182(94)00141-T.

Blikra, L. H., Longva, O., Braathen, A., Anda, E., Dehls, J., and Stalsberg, K. (2006). Rock slope failures in Norwegian fjord areas: examples, spatial distribution and temporal pattern. In Evans, S., Mugnozza, G., Strom, A., and Hermanns, R. (Eds.), *Landslides from massive rock slope failure*, Dordrecht, The Netherlands: Springer, *NATO Science Series*, vol. 49, pp. 475–496.

Blikra, L. H. and Nemec, W. (1998). Postglacial colluvium in western Norway: depositional processes, facies and palaeoclimatic record. *Sedimentology*, *45*(5), 909–959. doi: 10.1046/j.1365-3091.1998.00200.x.

Bonneau, D., DiFrancesco, P.-M., and Hutchinson, D. J. (2019). Surface Reconstruction for Three-Dimensional Rockfall Volumetric Analysis. *ISPRS International Journal of Geo-Information*, *8*(12). doi: 10.3390/ijgi8120548.

Brown, J., Ferrians Jr, O. J., Heginbottom, J. A., and Melnikov, E. S. (1997). *Circum-Arctic map of permafrost and ground-ice conditions.* National Snow and Ice Data Center, Boulder, CO. Digital media.

Brozovic, N., Burbank, D. W., and Meigs, A. J. (1997). Climatic limits on landscape development in the northwestern Himalaya. *Science*, *276*(5312), 571–574. doi: 10.1126/science.276.5312.571.

Böhme, M., Bunkholt, H. S. S., Dehls, J. F., Oppikofer, T., Hermanns, R., Dalsegg, E., Kristensen, L., Lauknes, T. R., and Eriksen, H. Ø. (2016). *Geologisk modell og fare-og risikoklassifisering av det ustabile fjellpartiet Gamanjunni 3 i Manndalen, Troms.* Report 64, Geological Survey of Norway, Trondheim, Norway. Retrieved from https://www.ngu.no/upload/Publikasjoner/Rapporter/2016/2016_031.pdf.

Böhme, M., Hermanns, R. L., Fischer, L., Oppikofer, T., Bunkholt, H., Derron, M. H., Carrea, D., Jaboyedoff, M., and Eiken, T. (2012). Detailed assessment of the deep-seated gravitational deformation at Stampa above Flåm, Norway. *Landslides and Engineered Slopes: Protecting Society through Improved Understanding, Taylor & Francis Group, London*, pp. 647–652.

Böhme, M., Hermanns, R. L., Gosse, J., Hilger, P., Eiken, T., Lauknes, T. R., and Dehls, J. F. (2019). Comparison of monitoring data with paleo-slip rates: Cosmogenic nuclide dating detects acceleration of a rockslide. *Geology*, *47*(4), 339–342. doi: 10.1130/G45684.1.

Böhme, M., Hermanns, R. L., Oppikofer, T., Fischer, L., Bunkholt, H. S. S., Eiken, T., Pedrazzini, A., Derron, M.-H., Jaboyedoff, M., Blikra, L. H., and Nilsen, B. (2013). Analyzing complex rock slope deformation at Stampa, western Norway, by integrating geomorphology, kinematics and numerical modeling. *Engineering Geology*, *154*, 116–130. doi: 10.1016/j.enggeo.2012.11.016.

Carrea, D., Abellan, A., Derron, M.-H., Gauvin, N., and Jaboyedoff, M. (2021). MATLAB virtual toolbox for retrospective rockfall source detection and volume estimation using 3D point clouds: A case study of a subalpine Molasse Cliff. *Geosciences*, *11*(2), 75. doi: 10.3390/geosciences11020075.

Carslaw, H. S. and Jaeger, J. C. (1959). *Conduction of heat in solids.* Oxford, Great Britain: Oxford University Press, 2nd ed., 520 pp.

Chalmers, J., Green, P., Japsen, P., and Rasmussen, E. (2010). The Scandinavian mountains have not persisted since the Caledonian orogeny. A comment on Nielsen et al. (2009a). *Journal of Geodynamics*, *50*(2), 94–101. doi: 10.1016/j.jog.2010.02.001.

Chang, S.-H., Lee, C.-I., and Jeon, S. (2002). Measurement of rock fracture toughness under modes I and II and mixed-mode conditions by using disc-type specimens. *Engineering Geology*, *66*(1), 79–97. doi: 10.1016/S0013-7952(02)00033-9.

Christiansen, H. H., Etzelmüller, B., Isaksen, K., Juliussen, H., Farbrot, H., Humlum, O., Johansson, M., Ingeman-Nielsen, T., Kristensen, L., Hjort, J., Holmlund, P., Sannel, A. B. K., Sigsgaard, C., Åkerman, H. J., Foged, N., Blikra, L. H., Pernosky, M. A., and Ødegård, R. S. (2010). The thermal state of permafrost in the Nordic area during the international polar year 2007–2009. *Permafrost and Periglacial Processes*, *21*(2), 156–181. doi: 10.1002/ppp.687.

Conrad, O., Bechtel, B., Bock, M., Dietrich, H., Fischer, E., Gerlitz, L., Wehberg, J., Wichmann, V., and Böhner, J. (2015). System for Automated Geoscientific Analyses (SAGA) v. 2.1.4. *Geoscientific Model Development*, *8*(7), 1991–2007. doi: 10.5194/gmd-8-1991-2015.

Cosenza, P., Guérin, R., and Tabbagh, A. (2003). Relationship between thermal conductivity and water content of soils using numerical modelling. *European Journal of Soil Science*, *54*(3), 581–588. doi: 10.1046/j.1365-2389.2003.00539.x.

Cossart, E., Mercier, D., Decaulne, A., Feuillet, T., Jónsson, H. P., and Sæmundsson, (2014). Impacts of post-glacial rebound on landslide spatial distribution at a regional scale in northern Iceland (Skagafjörður). *Earth Surface Processes and Landforms*, *39*(3), 336–350. doi: 10.1002/esp.3450.

Costa, J. E. and Schuster, R. L. (1988). The formation and failure of natural dams. *Geological Society of America Bulletin*, *100*(7), 1054–1068. doi: 10.1130/0016-7606(1988)100<1054:TFAFON>2.3.CO;2.

Coutard, J.-P. and Francou, B. (1989). Rock temperature measurements in two alpine environments: implications for frost shattering. *Arc-*

tic and Alpine Research, *21*(4), 399–416. doi: 10.2307/1551649.

Crochet, P., Jóhannesson, T., Jónsson, T., Sigurðsson, O., Björnsson, H., Pálsson, F., and Barstad, I. (2007). Estimating the spatial distribution of precipitation in Iceland using a linear model of orographic precipitation. *Journal of Hydrometeorology*, *8*(6), 1285–1306. doi: 10.1175/2007JHM795.1.

Crochet, P. and Jóhannesson, T. (2011). A data set of gridded daily temperature in Iceland, 1949-2010. *Jokull*, *61*, 1–18.

Curry, A. M. (2023). Talus slopes. In *Reference Module in Earth Systems and Environmental Sciences*, Elsevier. doi: 10.1016/B978-0-323-99931-1.00047-7.

Dabrowski, M., Krotkiewski, M., and Schmid, D. W. (2008). MILAMIN: MATLAB-based finite element method solver for large problems. *Geochemistry Geophysics Geosystems*, *9*. doi: 10.1029/2007gc001719.

Dall'Amico, M., Endrizzi, S., Gruber, S., and Rigon, R. (2011). A robust and energy-conserving model of freezing variably-saturated soil. *The Cryosphere*, *5*(2), 469–484. doi: 10.5194/tc-5-469-2011.

Dash, J. G., Rempel, A. W., and Wettlaufer, J. S. (2006). The physics of premelted ice and its geophysical consequences. *Reviews of Modern Physics*, *78*(3), 695–741. doi: 10.1103/RevModPhys.78.695.

Delunel, R., van der Beek, P. A., Carcaillet, J., Bourlès, D. L., and Valla, P. G. (2010). Frost-cracking control on catchment denudation rates: Insights from in situ produced ^{10}Be concentrations in stream sediments (Ecrins–Pelvoux massif, French Western Alps). *Earth and Planetary Science Letters*, *293*(1), 72–83. doi: 10.1016/j.epsl.2010.02.020.

Denk, T., Grímsson, F., Zetter, R., and Símonarson, L. A. (2011). Introduction to the nature and geology of Iceland. In *Late Cainozoic floras of Iceland: 15 million years of vegetation and climate history in the northern North Atlantic*, Dordrecht: Springer Netherlands, pp. 1–29. doi: 10.1007/978-94-007-0372-8_1.

DiFrancesco, P.-M., Bonneau, D., and Hutchinson, D. J. (2020). The implications of M3C2 projection diameter on 3D semi-automated rockfall extraction from sequential terrestrial laser scanning point clouds. *Remote Sensing*, *12*(11), 1885. doi: 10.3390/rs12111885.

Draebing, D., Mayer, T., Jacobs, B., and McColl, S. T. (2022). Alpine rockwall erosion patterns follow elevation-dependent climate trajectories. *Communications Earth & Environment*, *3*(1), 21. doi: 10.1038/s43247-022-00348-2.

Dramis, F., Govi, M., Guglielmin, M., and Mortara, G. (1995). Mountain permafrost and slope instability in the Italian Alps: the Val Pola landslide. *Permafrost and Periglacial Processes*, *6*(1), 73–81. doi: 10.1002/ppp.3430060108.

Duca, S., Occhiena, C., Mattone, M., Sambuelli, L., and Scavia, C. (2014). Feasibility of ice segregation location by acoustic emission detection: A laboratory test in gneiss. *Permafrost and Periglacial Processes*, *25*(3), 208–219. doi: 10.1002/ppp.1814.

EDF R&D (2023). CloudCompare (version 2.12.4). Retrieved from http://www.danielgm.net/cc/.

Egholm, D. L., Andersen, J. L., Knudsen, M. F., Jansen, J. D., and Nielsen, S. B. (2015). The periglacial engine of mountain erosion – Part 2: Modelling large-scale landscape evolution. *Earth Surface Dynamics*, *3*(4), 463–482. doi: 10.5194/esurf-3-463-2015.

Egholm, D. L., Nielsen, S., Pedersen, V. K., and Lesemann, J.-E. (2009). Glacial effects limiting mountain height. *Nature*, *460*(7257), 884–887. doi: 10.1038/nature08263.

Einarsson, M. Á. (1984). Climate of Iceland. In Van Loon, H. (Ed.), *World survey of climatology*, Amsterdam: Elsevier, vol. 15, pp. 673–697.

Elachi, C. and Van Zyl, J. J. (2006). *Introduction to the physics and techniques of remote sensing*, vol. 28. Hoboken, New Jersey: John Wiley & Sons.

Eriksen, H. Ø. (2018). *Instrumentation and temperature data (2014–2017) for the Ádjet Mountain in Skibotn, Troms.* Data set. doi: 10.6084/m9.figshare.6225056.v3.

Eriksen, H. Ø., Rouyet, L., Lauknes, T. R., Berthling, I., Isaksen, K., Hindberg, H., Larsen, Y., and Corner, G. D. (2018). Recent acceleration of a rock glacier complex, Ádjet, Norway, documented by 62 years of remote sensing observations. *Geophysical Research Letters*, *45*(16), 8314–8323. doi: 10.1029/2018GL077605.

Etzelmüller, B. (2013). Recent advances in mountain permafrost research. *Permafrost and Periglacial Processes*, *24*(2), 99–107. doi: 10.1002/ppp.1772.

Etzelmüller, B., Farbrot, H., Guðmundsson, Á., Humlum, O., Tveito, O. E., and Björnsson, H. (2007). The regional distribution of mountain permafrost in Iceland. *Permafrost and Periglacial Processes*, *18*(2), 185–199. doi: 10.1002/ppp.583.

Etzelmüller, B. and Hagen, J. O. (2005). Glacier-permafrost interaction in Arctic and alpine mountain environments with examples from southern Norway and Svalbard. *Geological Society, London, Special Publications*, *242*(1), 11–27. doi: 10.1144/GSL.SP.2005.242.01.02.

Etzelmüller, B., Berthling, I., and Sollid, J. L. (2003). Aspects and concepts on the geomorphological significance of Holocene permafrost in southern Norway. *Geomorphology*, *52*(1), 87–104. doi: 10.1016/S0169-555X(02)00250-7.

Etzelmüller, B., Czekirda, J., Magnin, F., Duvillard, P. A., Ravanel, L., Malet, E., Aspaas, A., Kristensen, L., Skrede, I., Majala, G. D., Jacobs, B., Leinauer, J., Hauck, C., Hilbich, C., Böhme, M., Hermanns, R., Eriksen, H. Ø., Lauknes, T. R., Krautblatter, M., and Westermann, S. (2022). Permafrost in monitored unstable rock slopes in Norway – new insights from temperature and surface velocity measurements, geophysical surveying, and ground temperature modelling. *Earth Surface Dynamics*, *10*(1), 97–129. doi: 10.5194/esurf-10-97-2022.

Etzelmüller, B. and Frauenfelder, R. (2009). Factors controlling the distribution of mountain permafrost in the Northern Hemisphere and their influence on sediment transfer. *Arctic, Antarctic, and Alpine Research*, *41*(1), 48–58. doi:

10.1657/1523-0430-41.1.48.

Etzelmüller, B., Patton, H., Schomacker, A., Czekirda, J., Girod, L., Hubbard, A., Lilleøren, K. S., and Westermann, S. (2020). Icelandic permafrost dynamics since the Last Glacial Maximum – model results and geomorphological implications. *Quaternary Science Reviews, 233*, 106236. doi: 10.1016/j.quascirev.2020.106236.

Farbrot, H., Etzelmüller, B., Guðmundsson, Á., Humlum, O., Kellerer-Pirklbauer, A., Eiken, T., and Wangensteen, B. (2007a). Rock glaciers and permafrost in Tröllaskagi, northern Iceland. *Zeitschrift für Geomorphologie, Supplementary Issues, 51*(2), 1–16. doi: 10.1127/0372-8854/2007/0051S2-0001.

Farbrot, H., Etzelmüller, B., Schuler, T. V., Guðmundsson, Á., Eiken, T., Humlum, O., and Björnsson, H. (2007b). Thermal characteristics and impact of climate change on mountain permafrost in Iceland. *Journal of Geophysical Research: Earth Surface, 112*(F3). doi: 10.1029/2006JF000541.

Farbrot, H., Hipp, T. F., Etzelmüller, B., Isaksen, K., Ødegård, R. S., Schuler, T. V., and Humlum, O. (2011). Air and ground temperature variations observed along elevation and continentality gradients in Southern Norway. *Permafrost and Periglacial Processes, 22*(4), 343–360. doi: 10.1002/ppp.733.

Farbrot, H., Isaksen, K., and Etzelmüller, B. (2008). Present and past distribution of mountain permafrost in Gaissane Mountains, Northern Norway. In *Proceedings of the 9th International Conference on Permafrost, Fairbanks, AK, USA, 29 June-3 July 2008*. pp. 427–432.

Farbrot, H., Isaksen, K., Etzelmüller, B., and Gisnås, K. (2013). Ground thermal regime and permafrost distribution under a changing climate in northern Norway. *Permafrost and Periglacial Processes, 24*(1), 20–38. doi: 10.1002/ppp.1763.

Ferretti, A., Prati, C., and Rocca, F. (2001). Permanent scatterers in SAR interferometry. *IEEE Transactions on Geoscience and Remote Sensing, 39*(1), 8–20. doi: 10.1109/36.898661.

Fischer, L., Kääb, A., Huggel, C., and Noetzli, J. (2006). Geology, glacier retreat and permafrost degradation as controlling factors of slope instabilities in a high-mountain rock wall: the Monte Rosa east face. *Natural Hazards and Earth System Sciences, 6*(5), 761–772. doi: 10.5194/nhess-6-761-2006.

Fischer, L., Purves, R. S., Huggel, C., Noetzli, J., and Haeberli, W. (2012). On the influence of topographic, geological and cryospheric factors on rock avalanches and rockfalls in high-mountain areas. *Natural Hazards and Earth System Sciences, 12*(1), 241–254. doi: 10.5194/nhess-12-241-2012.

Flóvenz, Ó. G. and Saemundsson, K. (1993). Heat flow and geothermal processes in Iceland. *Tectonophysics, 225*(1), 123–138. doi: 10.1016/0040-1951(93)90253-G.

Frauenfelder, R., Haeberli, W., and Hoelzle, M. (2003). Rockglacier occurrence and related terrain parameters in a study area of the Eastern Swiss Alps. In Phillips, M., Springman, S. M., and Arenson, L. U. (Eds.), *Proceedings of the Eighth International Conference on Permafrost*, vol. 1, pp. 253–258.

Frauenfelder, R., Isaksen, K., Lato, M. J., and Noetzli, J. (2018). Ground thermal and geomechanical conditions in a permafrost-affected high-latitude rock avalanche site (Polvartinden, northern Norway). *The Cryosphere, 12*(4), 1531–1550. doi: 10.5194/tc-12-1531-2018.

Fredin, O., Bergstrøm, B., Eilertsen, R., Hansen, L., Longva, O., Nesje, A., and Sveian, H. (2013). Glacial landforms and Quaternary landscape development in Norway. In Olsen, L., Fredin, O., and Olesen, O. (Eds.), *Quaternary Geology of Norway. Geological Survey of Norway Special Publication*, Trondheim, Norway: Geological Survey of Norway, vol. 13, pp. 5–25.

Freeman, T. (1991). Calculating catchment area with divergent flow based on a regular grid. *Computers Geosciences, 17*(3), 413–422. doi: 10.1016/0098-3004(91)90048-I.

French, H. M. (2007). *The periglacial environment*. Chichester, UK: John Wiley & Sons, Ltd, 3rd ed., 480 pp.

French, H. M. (2016). Do periglacial landscapes exist? A discussion of the upland landscapes of northern interior Yukon, Canada. *Permafrost and Periglacial Processes, 27*(2), 219–228. doi: 10.1002/ppp.1866.

French, H. M. and Millar, S. W. S. (2014). Permafrost at the time of the Last Glacial Maximum (LGM) in North America. *Boreas, 43*(3), 667–677. doi: 10.1111/bor.12036.

Friedman, J. D., Johansson, C. E., Oskarsson, N., Svensson, H., Thorarinsson, S., and Williams, R. S. (1971). Observations on Icelandic polygon surfaces and palsa areas. Photo interpretation and field studies. *Geografiska Annaler. Series A, Physical Geography, 53*(3/4), 115–145. doi: 10.2307/520785.

Gabrielsen, R. H., Faleide, J. I., Pascal, C., Braathen, A., Nystuen, J. P., Etzelmuller, B., and O'Donnell, S. (2010). Reply to discussion of Gabrielsen et al. (2010) by Nielsen et al. (this volume): Latest Caledonian to present tectonomorphological development of southern Norway. *Marine and Petroleum Geology, 27*(6), 1290–1295. doi: 10.1016/j.marpetgeo.2010.02.003.

Gauer, P., Kristensen, K., Ragulina, G., Frauenfelder, R., and Jaedicke, C. (2016). *Skredfarekartlegging i Narvik kommune*. Report 20–2016, The Norwegian Water Resources and Energy Directorate, Oslo, Norway, 176 pp. Retrieved from https://publikasjoner.nve.no/rapport/2016/rapport2016_20.pdf.

Geirsdóttir, Á. and Eiríksson, J. (1994). Growth of an intermittent ice sheet in Iceland during the late Pliocene and early Pleistocene. *Quaternary Research, 42*(2), 115–130. doi: 10.1006/qres.1994.1061.

Gisnås, K. (2016). *Permafrost modelling over different scales in arctic and high-mountain environments*. Ph.D. thesis, University of Oslo, Oslo, Norway. Retrieved from http://urn.nb.no/URN:NBN:no-54520.

Gisnås, K., Etzelmuller, B., Lussana, C., Hjort, J., Sannel, A. B. K., Isaksen, K., Westermann, S., Kuhry, P., Christiansen, H. H., Frampton, A., and Akerman, J. (2017). Permafrost map for Norway, Sweden and Finland. *Permafrost and Periglacial Processes*, *28*(2), 359–378. doi: 10.1002/ppp.1922.

Gisnås, K., Etzelmüller, B., Farbrot, H., Schuler, T. V., and Westermann, S. (2013). CryoGRID 1.0: Permafrost distribution in Norway estimated by a spatial numerical model. *Permafrost and Periglacial Processes*, *24*(1), 2–19. doi: 10.1002/ppp.1765.

Goehring, B. M., Brook, E. J., Linge, H., Raisbeck, G. M., and Yiou, F. (2008). Beryllium-10 exposure ages of erratic boulders in southern Norway and implications for the history of the Fennoscandian Ice Sheet. *Quaternary Science Reviews*, *27*(3), 320–336. doi: 10.1016/j.quascirev.2007.11.004.

Goldstein, R. M. and Werner, C. L. (1998). Radar interferogram filtering for geophysical applications. *Geophysical Research Letters*, *25*(21), 4035–4038. doi: 10.1029/1998GL900033.

Gruber, S. (2012). Derivation and analysis of a high-resolution estimate of global permafrost zonation. *The Cryosphere*, *6*(1), 221–233. doi: 10.5194/tc-6-221-2012.

Gruber, S. and Haeberli, W. (2007). Permafrost in steep bedrock slopes and its temperature-related destabilization following climate change. *Journal of Geophysical Research: Earth Surface*, *112*(F2). doi: 10.1029/2006JF000547.

Gruber, S., Hoelzle, M., and Haeberli, W. (2004). Permafrost thaw and destabilization of Alpine rock walls in the hot summer of 2003. *Geophysical Research Letters*, *31*(13). doi: 10.1029/2004gl020051.

Gudmundsson, A. (2000). Dynamics of volcanic systems in Iceland: example of tectonism and volcanism at juxtaposed hot spot and mid-ocean ridge systems. *Annual Review of Earth and Planetary Sciences*, *28*(1), 107–140. doi: 10.1146/annurev.earth.28.1.107.

Guðmundsson, A. (2000). *Frerafjöll, urðarbingir á Tröllaskaga*. Master's thesis, University of Iceland, Reykjavík, Iceland.

Hales, T. and Roering, J. J. (2007). Climatic controls on frost cracking and implications for the evolution of bedrock landscapes. *Journal of Geophysical Research: Earth Surface*, *112*(F2). doi: 10.1029/2006JF000616.

Hales, T. C. and Roering, J. J. (2009). A frost "buzzsaw" mechanism for erosion of the eastern Southern Alps, New Zealand. *Geomorphology*, *107*(3), 241–253. doi: 10.1016/j.geomorph.2008.12.012.

Hall, A. M., Ebert, K., Kleman, J., Nesje, A., and Ottesen, D. (2013). Selective glacial erosion on the Norwegian passive margin. *Geology*, *41*(12), 1203–1206. doi: 10.1130/G34806.1.

Hall, A. M. and Kleman, J. (2014). Glacial and periglacial buzzsaws: fitting mechanisms to metaphors. *Quaternary Research*, *81*(2), 189–192. doi: 10.1016/j.yqres.2013.10.007.

Hallet, B., Walder, J. S., and Stubbs, C. W. (1991). Weathering by segregation ice growth in microcracks at sustained subzero temperatures: Verification from an experimental study using acoustic emissions. *Permafrost and Periglacial Processes*, *2*(4), 283–300. doi: 10.1002/ppp.3430020404.

Hanssen, R. F. (2001). *Radar interferometry: data interpretation and error analysis*, vol. 2. Dordrecht, The Netherlands: Kluwer Academic Publishers.

Hanssen, T. H. (1988). Rock properties. In *Norwegian Tunnelling Today*, Trondheim, Norway: Tapir Publishers, University of Trondheim, vol. 5, pp. 41–44.

Hanssen-Bauer, I., Tveito, O., and Szewczyk-Bartnicka, H. (2006). *Comparison of grid-based and station-based regional temperature and precipitation series*. Report 4/2006, Norwegian Meteorological Institute, Oslo, Norway, 26 pp. Retrieved from https://www.met.no/publikasjoner/met-report/met-report-2006/_/attachment/download/dd9d9481-5986-4790-9154-54dd5a4ceae7:4b95bfe33dcc6651f34bed4e1e36399cb19bbdef/MET-report-04-2006.pdf.

Harris, C., Davies, M. C. R., and Rea, B. R. (2003). Gelifluction: viscous flow or plastic creep? *Earth Surface Processes and Landforms*, *28*(12), 1289–1301. doi: 10.1002/esp.543.

Harris, C., Haeberli, W., Vonder Mühll, D., and King, L. (2001). Permafrost monitoring in the high mountains of Europe: the PACE Project in its global context. *Permafrost and Periglacial Processes*, *12*(1), 3–11. doi: 10.1002/ppp.377.

Harris, C., Kern-Luetschg, M., Christiansen, H. H., and Smith, F. (2011). The role of interannual climate variability in controlling solifluction processes, Endalen, Svalbard. *Permafrost and Periglacial Processes*, *22*(3), 239–253. doi: 10.1002/ppp.727.

Harris, C., Kern-Luetschg, M., Smith, F., and Isaksen, K. (2008). Solifluction processes in an area of seasonal ground freezing, Dovrefjell, Norway. *Permafrost and Periglacial Processes*, *19*(1), 31–47. doi: 10.1002/ppp.609.

Harris, S. A., Brouchkov, A., and Goudong, C. (2018). *Geocryology: Characteristics and Use of Frozen Ground and Permafrost Landforms*. London, UK: CRC Press, 810 pp.

Heggem, E. S. F., Juliussen, H., and Etzelmüller, B. (2005). Mountain permafrost in Central-Eastern Norway. *Norsk Geografisk Tidsskrift - Norwegian Journal of Geography*, *59*(2), 94–108. doi: 10.1080/00291950510038377.

Henry, K. and Smith, M. (2001). A model-based map of ground temperatures for the permafrost regions of Canada. *Permafrost and Periglacial Processes*, *12*(4), 389–398. doi: 10.1002/ppp.399.

Hestad, H. W. (2021). *Statistisk prediksjonsmodellering av steinbreer i Norge*. Master's thesis, University of Oslo, Oslo, Norway. Retrieved from https://www.duo.uio.no/handle/10852/88983.

Hilger, P. (2019). *Rock-slope failures in Norway-temporal development and climatic conditioning*. Ph.D. thesis, University of Oslo, Norway, Oslo, Norway. Retrieved from https://www.duo.uio.no/handle/10852/70806.

Hilger, P., Hermanns, R. L., Czekirda, J., Myhra, K. S., Gosse, J. C., and Etzelmüller, B. (2021). Permafrost as a first order control on long-term rock-slope deformation in (Sub-)Arctic Norway. *Quaternary Science Reviews*, *251*, 106718. doi:

10.1016/j.quascirev.2020.106718.

Hinchliffe, S. and Ballantyne, C. K. (1999). Talus accumulation and rockwall retreat, Trotternish, Isle of Skye, Scotland. *Scottish Geographical Journal*, *115*(1), 53–70. doi: 10.1080/00369229918737057.

Hindmarsh, A. C., Brown, P. N., Grant, K. E., Lee, S. L., Serban, R., Shumaker, D. E., and Woodward, C. S. (2005). SUNDIALS: Suite of nonlinear and differential/algebraic equation solvers. *ACM Transactions on Mathematical Software*, *31*(3), 363–396. doi: 10.1145/1089014.1089020.

Hinzman, L. D., Goering, D. J., and Kane, D. L. (1998). A distributed thermal model for calculating soil temperature profiles and depth of thaw in permafrost regions. *Journal of Geophysical Research*, *103*(D22), 28975–28991. doi: 10.1029/98JD01731.

Hipp, T., Etzelmüller, B., and Westermann, S. (2014). Permafrost in alpine rock faces from Jotunheimen and Hurrungane, southern Norway. *Permafrost and Periglacial Processes*, *25*(1), 1–13. doi: 10.1002/ppp.1799.

Hirakawa, K. (1986). Development of palsa bog in central highland, Iceland. *Geographical Reports of Tokyo Metropolitan University*, *21*, 111–122.

Hjartarson, Á. (2015). Heat flow in Iceland. In *Proceedings World Geothermal Congress 2015, Melbourne, Australia, 19–25 April 2015*.

Hjort, J. (2014). Which environmental factors determine recent cryoturbation and solifluction activity in a subarctic landscape? A comparison between active and inactive features. *Permafrost and Periglacial Processes*, *25*(2), 136–143. doi: 10.1002/ppp.1808.

Hjort, J., Ujanen, J., Parviainen, M., Tolgensbakk, J., and Etzelmüller, B. (2014). Transferability of geomorphological distribution models: Evaluation using solifluction features in subarctic and Arctic regions. *Geomorphology*, *204*, 165–176. doi: 10.1016/j.geomorph.2013.08.002.

Hu, Y., Liu, L., Wang, X., Zhao, L., Wu, T., Cai, J., Zhu, X., and Hao, J. (2021). Quantification of permafrost creep provides kinematic evidence for classifying a puzzling periglacial landform. *Earth Surface Processes and Landforms*, *46*(2), 465–477. doi: 10.1002/esp.5039.

Hubbard, A. (2006). The validation and sensitivity of a model of the Icelandic ice sheet. *Quaternary Science Reviews*, *25*(17), 2297–2313. doi: 10.1016/j.quascirev.2006.04.005.

Hubbard, A., Sugden, D., Dugmore, A., Norddahl, H., and Pétursson, H. G. (2006). A modelling insight into the Icelandic Last Glacial Maximum ice sheet. *Quaternary Science Reviews*, *25*(17), 2283–2296. doi: 10.1016/j.quascirev.2006.04.001.

Hughes, A. L. C., Gyllencreutz, R., Lohne, O. S., Mangerud, J., and Svendsen, J. I. (2016). The last Eurasian ice sheets – a chronological database and time-slice reconstruction, DATED-1. *Boreas*, *45*(1), 1–45. doi: 10.1111/bor.12142.

Hughes, A. L. C., Gyllencreutz, R., Lohne, S., Mangerud, J., and Svendsen, J.-I. (2015). *DATED-1: compilation of dates and time-slice reconstruction of the build-up and retreat of the last Eurasian (British-Irish, Scandinavian, Svalbard-Barents-Kara Seas) Ice Sheets 40-10 ka*. Data set, PANGAEA. doi: 10.1594/PANGAEA.848117.

IPCC (2019). *IPCC special report on the ocean and cryosphere in a changing climate*. Cambridge, UK and New York, NY, USA: Cambridge University Press, 755 pp. doi: 10.1017/9781009157964.

Isaksen, K. (2001). *Past and present ground thermal regime, distribution and creep of permafrost: Case studies in Svalbard, Sweden and Norway*. Ph.D. thesis, University of Oslo, Oslo, Norway.

Isaksen, K., Farbrot, H., Blikra, L. H., Johansen, B., Sollid, J. L., and Eiken, T. (2008). Five year ground surface temperature measurements in Finnmark, Northern Norway. In *Proceedings of the 9th International Conference on Permafrost, Fairbanks, AK, USA, 29 June-3 July 2008*. pp. 789–794.

Isaksen, K., Ødegård, R. S., Etzelmüller, B., Hilbich, C., Hauck, C., Farbrot, H., Eiken, T., Hygen, H. O., and Hipp, T. F. (2011). Degrading mountain permafrost in southern Norway: spatial and temporal variability of mean ground temperatures, 1999–2009. *Permafrost and Periglacial Processes*, *22*(4), 361–377. doi: 10.1002/ppp.728.

Jafarov, E. E., Marchenko, S. S., and Romanovsky, V. E. (2012). Numerical modeling of permafrost dynamics in Alaska using a high spatial resolution dataset. *The Cryosphere*, *6*(3), 613–624. doi: 10.5194/tc-6-613-2012.

Japsen, P., Green, P. F., Chalmers, J. A., and Bonow, J. M. (2018). Mountains of southernmost Norway: uplifted Miocene peneplains and re-exposed Mesozoic surfaces. *Journal of the Geological Society*, *175*(5), 721–741. doi: 10.1144/jgs2017-157.

Juliussen, H. and Humlum, O. (2007). Preservation of block fields beneath Pleistocene ice sheets on Sølen and Elgåhogna, central-eastern Norway. *Zeitschrift für Geomorphologie*, *51*(2), 113–138. doi: 10.1127/0372-8854/2007/0051S2-0113.

Kellerer-Pirklbauer, A., Wangensteen, B., Farbrot, H., and Etzelmüller, B. (2008). Relative surface age-dating of rock glacier systems near Hólar in Hjaltadalur, northern Iceland. *Journal of Quaternary Science*, *23*(2), 137–151. doi: 10.1002/jqs.1117.

Kierulf, H. P., Steffen, H., Barletta, V. R., Lidberg, M., Johansson, J., Kristiansen, O., and Tarasov, L. (2021). A GNSS velocity field for geophysical applications in Fennoscandia. *Journal of Geodynamics*, *146*, 101845. doi: 10.1016/j.jog.2021.101845.

King, L. (1986). Zonation and ecology of high mountain permafrost in Scandinavia. *Geografiska Annaler. Series A, Physical Geography*, *68*(3), 131–139. doi: 10.2307/521452.

Kinnard, C. and Lewkowicz, A. G. (2005). Movement, moisture and thermal conditions at a turf-banked solifluction lobe, Kluane Range, Yukon Territory, Canada. *Permafrost and Periglacial Processes*, *16*(3), 261–275. doi: 10.1002/ppp.530.

Kleman, J., Stroeven, A. P., and Lundqvist, J. (2008). Patterns of Quaternary ice sheet erosion and deposition in Fennoscandia and a theoretical framework for explanation. *Geomorphology*, *97*(1), 73–90. doi: 10.1016/j.geomorph.2007.02.049.

Krautblatter, M., Funk, D., and Günzel, F. K. (2013). Why permafrost rocks become unstable: a rock-ice-mechanical model in time and space. *Earth Surface Processes and Landforms, 38*(8), 876–887. doi: 10.1002/esp.3374.

Kristensen, L., Czekirda, J., Penna, I., Etzelmüller, B., Nicolet, P., Pullarello, J. S., Blikra, L. H., Skrede, I., Oldani, S., and Abellan, A. (2021). Movements, failure and climatic control of the Veslemannen rockslide, Western Norway. *Landslides*, pp. 1–18. doi: 10.1007/s10346-020-01609-x.

Krüger, J. and Kjær, K. H. (2000). De-icing progression of ice-cored moraines in a humid, subpolar climate, Kötlujökull, Iceland. *The Holocene, 10*(6), 737–747. doi: 10.1191/09596830094980.

Lachenbruch, A. H. and Marshall, B. V. (1986). Changing climate: geothermal evidence from permafrost in the Alaskan Arctic. *Science, 234*(4777), 689–696. doi: 10.1126/science.234.4777.689.

Lague, D., Brodu, N., and Leroux, J. (2013). Accurate 3D comparison of complex topography with terrestrial laser scanner: Application to the Rangitikei canyon (N-Z). *ISPRS Journal of Photogrammetry and Remote Sensing, 82*, 10–26. doi: 10.1016/j.isprsjprs.2013.04.009.

Larsen, G. and Eiríksson, J. (2008). Late Quaternary terrestrial tephrochronology of Iceland—frequency of explosive eruptions, type and volume of tephra deposits. *Journal of Quaternary Science, 23*(2), 109–120. doi: 10.1002/jqs.1129.

Lee, H., Schuur, E. A. G., and Vogel, J. G. (2010). Soil CO_2 production in upland tundra where permafrost is thawing. *Journal of Geophysical Research: Biogeosciences, 115*(G1). doi: 10.1029/2008JG000906.

Liang, C., Agram, P., Simons, M., and Fielding, E. J. (2019). Ionospheric Correction of InSAR Time Series Analysis of C-band Sentinel-1 TOPS Data. *IEEE Transactions on Geoscience and Remote Sensing, 57*(9), 6755–6773. doi: 10.1109/TGRS.2019.2908494.

Lidmar-Bergström, K. and Bonow, J. M. (2009). Hypotheses and observations on the origin of the landscape of southern Norway—A comment regarding the isostasy-climate-erosion hypothesis by Nielsen et al. 2008. *Journal of Geodynamics, 48*(2), 95–100. doi: 10.1016/j.jog.2009.06.003.

Lilleøren, K. S. and Etzelmüller, B. (2011). A regional inventory of rock glaciers and ice-cored moraines in Norway. *Geografiska Annaler: Series A, Physical Geography, 93*(3), 175–191. doi: 10.1111/j.1468-0459.2011.00430.x.

Lilleøren, K., Etzelmuller, B., and Hestad, H. (2022). Prediction modelling of rock glacier distribution in Norway. In *Book of Abstracts, EUCOP 6, Puigcerdà, 18–22 June 2022*, pp. 286–286. doi: 10.52381/EUCOP6.abstracts.1.

Lilleøren, K. S. (2012). *Late-Pleistocene and Holocene mountain permafrost geomorphology of Norway and Iceland.* Ph.D. thesis, Department of Geosciences, University of Oslo, Oslo, Norway. Retrieved from http://urn.nb.no/URN:NBN:no-32579.

Lilleøren, K. S., Etzelmüller, B., Gärtner-Roer, I., Kääb, A., Westermann, S., and Guðmundsson, A. (2013). The distribution, thermal characteristics and dynamics of permafrost in Tröllaskagi, northern Iceland, as inferred from the distribution of rock glaciers and ice-cored moraines. *Permafrost and Periglacial Processes, 24*(4), 322–335. doi: 10.1002/ppp.1792.

Liu, Y., Li, L., Yang, J., Chen, X., and Hao, J. (2017). Estimating snow depth using multi-source data fusion based on the D-InSAR method and 3DVAR fusion algorithm. *Remote Sensing, 9*(11). doi: 10.3390/rs9111195.

Liu, Z., Otto-Bliesner, B. L., He, F., Brady, E. C., Tomas, R., Clark, P. U., Carlson, A. E., Lynch-Stieglitz, J., Curry, W., Brook, E., Erickson, D., Jacob, R., Kutzbach, J., and Cheng, J. (2009). Transient simulation of last deglaciation with a new mechanism for Bølling – Allerød warming. *Science, 325*(5938), 310–314. doi: doi:10.1126/science.1171041.

Lunardini, V. J. (1981). *Heat transfer in cold climates.* New York, USA: Van Nostrand Reinhold Company, 731 pp.

Lussana, C. (2018). *seNorge_2018 daily total precipitation amount 1957-2017, version 18.12.* Data set. doi: 10.5281/zenodo.2082320.

Lussana, C. (2020). *seNorge observational gridded datasets. seNorge_2018, version 20.05.* Data set. doi: 10.48550/arXiv.2008.02021.

Magnin, F., Etzelmüller, B., Westermann, S., Isaksen, K., Hilger, P., and Hermanns, R. L. (2019). Permafrost distribution in steep rock slopes in Norway: measurements, statistical modelling and implications for geomorphological processes. *Earth Surface Dynamics, 7*(4), 1019–1040. doi: 10.5194/esurf-7-1019-2019.

Magnin, F., Josnin, J. Y., Ravanel, L., Pergaud, J., Pohl, B., and Deline, P. (2017). Modelling rock wall permafrost degradation in the Mont Blanc massif from the LIA to the end of the 21st century. *The Cryosphere, 11*(4), 1813–1834. doi: 10.5194/tc-11-1813-2017.

Marshall, J. A., Roering, J. J., Rempel, A. W., Shafer, S. L., and Bartlein, P. J. (2021). Extensive frost weathering across unglaciated North America during the Last Glacial Maximum. *Geophysical Research Letters, 48*(5). doi: 10.1029/2020GL090305.

Marushchak, M. E., A, P., Koponen, H., Biasi, C., Seppälä, M., and Martikainen, P. J. (2011). Hot spots for nitrous oxide emissions found in different types of permafrost peatlands. *Global Change Biology, 17*(8), 2601–2614. doi: 10.1111/j.1365-2486.2011.02442.x.

Matsuoka, N. (1990). Mechanisms of rock breakdown by frost action: An experimental approach. *Cold Regions Science and Technology, 17*(3), 253–270. doi: 10.1016/S0165-232X(05)80005-9.

Matsuoka, N. (2001a). Microgelivation versus macrogelivation: towards bridging the gap between laboratory and field frost weathering. *Permafrost and Periglacial Processes, 12*(3), 299–313. doi: 10.1002/ppp.393.

Matsuoka, N. (2001b). Solifluction rates, processes and landforms: a global review. *Earth-Science Reviews, 55*(1), 107–134. doi: 10.1016/S0012-8252(01)00057-5.

Matsuoka, N., Ikeda, A., and Date, T. (2005). Morphometric analysis of solifluction lobes and rock glaciers in the Swiss Alps. *Permafrost and Periglacial Processes*, *16*(1), 99–113. doi: 10.1002/ppp.517.

Matsuoka, N. and Murton, J. (2008). Frost weathering: recent advances and future directions. *Permafrost and Periglacial Processes*, *19*(2), 195–210. doi: 10.1002/ppp.620.

Matthews, J. A. and Nesje, A. (2022). Scandinavia. In Oliva, M., Nývlt, D., and Fernández-Fernández, J. M. (Eds.), *Periglacial Landscapes of Europe*, Cham: Springer, pp. 365–426. doi: 10.1007/978-3-031-14895-8_14.

Matthews, J. A., Wilson, P., and Mourne, R. W. (2017). Landform transitions from pronival ramparts to moraines and rock glaciers: a case study from the Smørbotn cirque, Romsdalsalpane, southern Norway. *Geografiska Annaler: Series A, Physical Geography*, *99*(1), 15–37. doi: 10.1080/04353676.2016.1256582.

Matthews, J. A., Wilson, P., Winkler, S., Mourne, R. W., Hill, J. L., Owen, G., Hiemstra, J. F., Hallang, H., and Geary, A. P. (2019). Age and development of active cryoplanation terraces in the alpine permafrost zone at Svartkampan, Jotunheimen, southern Norway. *Quaternary Research*, *92*(3), 641–664. doi: 10.1017/qua.2019.41.

McCarroll, D., Shakesby, R. A., and Matthews, J. A. (2001). Enhanced rockfall activity during the Little Ice Age: further lichenometric evidence from a Norwegian talus. *Permafrost and Periglacial Processes*, *12*(2), 157–164. doi: 10.1002/ppp.359.

McGreevy, J. P. and Whalley, W. B. (1982). The geomorphic significance of rock temperature variations in cold environments: a discussion. *Arctic and Alpine Research*, *14*(2), 157–162. doi: 10.2307/1551114.

Messenzehl, K., Meyer, H., Otto, J.-C., Hoffmann, T., and Dikau, R. (2017). Regional-scale controls on the spatial activity of rockfalls (Turtmann Valley, Swiss Alps) — A multivariate modeling approach. *Geomorphology*, *287*, 29–45. doi: 10.1016/j.geomorph.2016.01.008.

Moorbath, S., Sigurdsson, H., and Goodwin, R. (1968). KAr ages of the oldest exposed rocks in Iceland. *Earth and Planetary Science Letters*, *4*(3), 197–205. doi: 10.1016/0012-821X(68)90035-6.

Morken, O. A. (2017). *Integrated analysis of past, and potential future rock slope failures of various size from Rombakstøtta, Nordland*. Master's thesis, NTNU, Norway, Trondheim, Norway. Retrieved from http://hdl.handle.net/11250/2444279.

Murray, K. D., Bekaert, D. P., and Lohman, R. B. (2019). Tropospheric corrections for InSAR: Statistical assessments and applications to the Central United States and Mexico. *Remote Sensing of Environment*, *232*, 111326. doi: 10.1016/j.rse.2019.111326.

Murton, J. B., Peterson, R., and Ozouf, J.-C. (2006). Bedrock fracture by ice segregation in cold regions. *Science*, *314*(5802), 1127–1129. doi: 10.1126/science.1132127.

Myhra, K. S. (2016). *Modelling permafrost conditions in steep mountain environments*. Ph.D. thesis, University of Oslo, Norway, Oslo, Norway.

Myhra, K. S., Westermann, S., and Etzelmüller, B. (2017). Modelled distribution and temporal evolution of permafrost in steep rock walls along a latitudinal transect in Norway by CryoGrid 2D. *Permafrost and Periglacial Processes*, *28*(1), 172–182. doi: 10.1002/ppp.1884.

Myhra, K. S., Westermann, S., and Etzelmüller, B. (2019). Modeling conductive heat flow between steep rock walls and talus slopes – thermal processes and geomorphological implications. *Frontiers in Earth Science*, *7*(192). doi: 10.3389/feart.2019.00192.

Nesje, A. (2002). A large rockfall avalanche in Oldedalen, inner Nordfiord, western Norway, dated by means of a sub-avalanche Salix sp. tree trunk. *Norwegian Journal of Geology - Norsk Geologisk Forening*, *82*(1).

Nesje, A., Bakke, J., Dahl, S. O., Lie, Ø., and Matthews, J. A. (2008). Norwegian mountain glaciers in the past, present and future. *Global and Planetary Change*, *60*(1), 10–27. doi: 10.1016/j.gloplacha.2006.08.004.

Nesje, A., Blikra, L. H., and Anda, E. (1994). Dating rockfall-avalanche deposits from degree of rock-surface weathering by Schmidt-hammer tests: a study from Norangsdalen, Sunnmøre, Norway. *Norsk Geologisk Tidsskrift*, *74*(2), 108–113.

NGRIP (North Greenland Ice Core Project Members) (2004). *North Greenland Ice Core Project Oxygen Isotope Data*. Data set.

NGU (2023). Map over subsidence and unstable rock slopes (InSAR Norway). Retrieved from http://insar.ngu.no/.

Nicolsky, D. J., Romanovsky, V. E., Panda, S. K., Marchenko, S. S., and Muskett, R. R. (2017). Applicability of the ecosystem type approach to model permafrost dynamics across the Alaska North Slope. *Journal of Geophysical Research: Earth Surface*, *122*, 50–75. doi: 10.1002/2016JF003852.

Nielsen, S. B., Gallagher, K., Leighton, C., Balling, N., Svenningsen, L., Jacobsen, B. H., Thomsen, E., Nielsen, O. B., Heilmann-Clausen, C., Egholm, D. L., Summerfield, M. A., Clausen, O. R., Piotrowski, J. A., Thorsen, M. R., Huuse, M., Abrahamsen, N., King, C., and Lykke-Andersen, H. (2009). The evolution of western Scandinavian topography: A review of Neogene uplift versus the ICE (isostasy–climate–erosion) hypothesis. *Journal of Geodynamics*, *47*(2), 72–95. doi: 10.1016/j.jog.2008.09.001.

Nilsen, B. and Palmström, A. (2000). *Engineering geology and rock engineering*. Oslo, Norway: Norwegian soil and rock engineering association, 251 pp. Retrieved from https://bergmekanikk.no/wp-content/uploads/2021/12/Handbook-No-2.pdf.

Nilsen, B. and Thidemann, A. (1993). *Rock engineering*. Trondheim, Norway: Norwegian Institute of Technology, Department of Hydraulic Engineering, 156 pp.

Noetzli, J. and Gruber, S. (2009). Transient thermal effects in Alpine permafrost. *The Cryosphere*, *3*(1), 85–99. doi: 10.5194/tc-3-85-2009.

Noetzli, J., Gruber, S., Kohl, T., Salzmann, N., and Haeberli, W. (2007). Three-dimensional distribution and evolution of permafrost temperatures in idealized high-mountain topography. *Journal* *of Geophysical Research: Earth Surface*, *112*(F2). doi: 10.1029/2006jf000545.

Nopper, H. (2015). *Geomorphological study of the rock-slope failure at Adjet, Storfjord, Troms.* Master's thesis, UiT, Norway, Tromsø, Norway. Retrieved from https://hdl.handle.net/10037/7758.

Obu, J., Westermann, S., Bartsch, A., Berdnikov, N., Christiansen, H. H., Dashtseren, A., Delaloye, R., Elberling, B., Etzelmüller, B., Kholodov, A., Khomutov, A., Kääb, A., Leibman, M. O., Lewkowicz, A. G., Panda, S. K., Romanovsky, V., Way, R. G., Westergaard-Nielsen, A., Wu, T., Yamkhin, J., and Zou, D. (2019). Northern Hemisphere permafrost map based on TTOP modelling for 2000–2016 at 1 km^2 scale. *Earth-Science Reviews*, *193*, 299–316. doi: 10.1016/j.earscirev.2019.04.023.

Odegård, R. S., Sollid, J. L., and Liestøl, O. (1992). Ground temperature measurements in mountain permafrost, Jotunheimen, southern Norway. *Permafrost and Periglacial Processes*, *3*(3), 231–234. doi: 10.1002/ppp.3430030310.

Oliva, M., Nývlt, D., and Fernández-Fernández, J. M. (2023). *Periglacial landscapes of Europe.* Cham, Switzerland: Springer Nature, 523 pp. doi: 10.1007/978-3-031-14895-8.

Orme, A. R. (2007). The Rise and Fall of the Davisian Cycle of Erosion: Prelude, Fugue, Coda, and Sequel. *Physical Geography*, *28*(6), 474–506. doi: 10.2747/0272-3646.28.6.474.

Oskin, M. and Burbank, D. W. (2005). Alpine landscape evolution dominated by cirque retreat. *Geology*, *33*(12), 933–936. doi: 10.1130/g21957.1.

Ottósson, J. G., Sveinsdóttir, A., and Harðardóttir, M. (2016). *Vistgerðir á Íslandi.* Report 54, Fjölrit Náttúrufræðistofnunar, Garðabær, Iceland, 299 pp. Retrieved from http://utgafa.ni.is/fjolrit/Fjolrit_54.pdf.

Paasche, , Dahl, S. O., Løvlie, R., Bakke, J., and Nesje, A. (2007). Rockglacier activity during the Last Glacial–Interglacial transition and Holocene spring snowmelting. *Quaternary Science Reviews*, *26*(5), 793–807. doi: 10.1016/j.quascirev.2006.11.017.

Patton, H., Hubbard, A., Bradwell, T., and Schomacker, A. (2017). The configuration, sensitivity and rapid retreat of the Late Weichselian Icelandic ice sheet. *Earth-Science Reviews*, *166*, 223–245. doi: 10.1016/j.earscirev.2017.02.001.

Pelletier, J. D. (2008). *Quantitative modeling of earth surface processes.* New York, USA: Cambridge University Press, 295 pp.

Pissart, A. (2002). Palsas, lithalsas and remnants of these periglacial mounds. A progress report. *Progress in Physical Geography*, *26*(4), 605–621. doi: 10.1191/0309133302pp354ra.

Planet Labs (2023). *Planet application program interface: In space for life on earth.* Planet. Retrieved from https://api.planet.com.

Prabhakaran, R., Bruna, P.-O., Bertotti, G., and Smeulders, D. (2019). An automated fracture trace detection technique using the complex shearlet transform. *Solid Earth*, *10*(6), 2137–2166. doi: 10.5194/se-10-2137-2019.

Priesnitz, K. and Schunke, E. (1978). An approach to the ecology of permafrost in central Iceland. In *Third International Conference on Permafrost*, National Research Council of Canada, Ottawa, p. 474–479.

Quinn, P., Beven, K., Chevallier, P., and Planchon, O. (1991). The prediction of hillslope flow paths for distributed hydrological modelling using digital terrain models. *Hydrological Processes*, *5*(1), 59–79. doi: 10.1002/hyp.3360050106.

Ramberg, I., Bryhni, I., Nøttvedt, A., and K., R. (2013). *Landet blir til - Norges geologi.* Trondheim, Norway: Norsk Geologisk Forening, 2nd ed., 656 pp.

Rapp, A. (1960). Recent development of mountain slopes in Kärkevagge and surroundings, northern Scandinavia. *Geografiska Annaler*, *42*(2/3), 65–200. doi: 10.2307/520126.

Ravanel, L., Allignol, F., Deline, P., Gruber, S., and Ravello, M. (2010). Rock falls in the Mont Blanc Massif in 2007 and 2008. *Landslides*, *7*(4), 493–501. doi: 10.1007/s10346-010-0206-z.

Ravanel, L. and Deline, P. (2011). Climate influence on rockfalls in high-Alpine steep rockwalls: The north side of the Aiguilles de Chamonix (Mont Blanc massif) since the end of the 'Little Ice Age'. *The Holocene*, *21*(2), 357–365. doi: 10.1177/0959683610374887.

Ravanel, L., Magnin, F., and Deline, P. (2017). Impacts of the 2003 and 2015 summer heatwaves on permafrost-affected rockwalls in the Mont Blanc massif. *Science of The Total Environment*, *609*, 132–143. doi: 10.1016/j.scitotenv.2017.07.055.

Refice, A., Giachetta, E., and Capolongo, D. (2012). SIGNUM: A Matlab, TIN-based landscape evolution model. *Computers Geosciences*, *45*, 293–303. doi: 10.1016/j.cageo.2011.11.013.

Rempel, A. W., Marshall, J. A., and Roering, J. J. (2016). Modeling relative frost weathering rates at geomorphic scales. *Earth and Planetary Science Letters*, *453*, 87–95. doi: 10.1016/j.epsl.2016.08.019.

Rempel, A. W., Wettlaufer, J. S., and Worster, M. G. (2001). Interfacial premelting and the thermomolecular force: thermodynamic buoyancy. *Physical Review Letters*, *87*, 088501. doi: 10.1103/PhysRevLett.87.088501.

RGIK (2023). *Guidelines for inventorying rock glaciers: baseline and practical concepts (version 1.0).* IPA Action Group Rock glacier inventories and kinematics, 25 pp. doi: 10.51363/unifr.srr.2023.002.

Ridefelt, H., Boelhouwers, J., and Etzelmüller, B. (2011). Local variations of solifluction activity and environment in the Abisko Mountains, Northern Sweden. *Earth Surface Processes and Landforms*, *36*(15), 2042–2053. doi: 10.1002/esp.2225.

Ridefelt, H., Etzelmüller, B., and Boelhouwers, J. (2010). Spatial analysis of solifluction landforms and process rates in the Abisko Mountains, northern Sweden. *Permafrost and Periglacial Processes*, *21*(3), 241–255. doi: 10.1002/ppp.681.

Riseborough, D., Shiklomanov, N., Etzelmüller, B., Gruber, S., and Marchenko, S. (2008). Recent advances in permafrost modelling. *Permafrost and Periglacial Processes*, *19*(2), 137–156. doi: 10.1002/ppp.615.

Rosen, P., Hensley, S., Joughin, I., Li, F., Madsen, S., Rodriguez, E., and Goldstein, R. (2000). Synthetic aperture radar interferometry. *Proceedings of the IEEE*, *88*(3), 333–382. doi: 10.1109/5.838084.

Rossmanith, H.-P. (1983). *Rock fracture mechanics*, vol. 275. New York, USA: Springer-Verlag Wien, 484 pp.

Rott, H. (2009). Advances in interferometric synthetic aperture radar (InSAR) in earth system science. *Progress in Physical Geography: Earth and Environment*, *33*(6), 769–791. doi: 10.1177/0309133309350263.

Rouyet, L., Karjalainen, O., Niittynen, P., Aalto, J., Luoto, M., Lauknes, T. R., Larsen, Y., and Hjort, J. (2021). Environmental controls of InSAR-based periglacial ground dynamics in a sub-Arctic landscape. *Journal of Geophysical Research: Earth Surface*, *126*(7), e2021JF006175. doi: 10.1029/2021JF006175.

Rouyet, L., Lauknes, T. R., Christiansen, H. H., Strand, S. M., and Larsen, Y. (2019). Seasonal dynamics of a permafrost landscape, Adventdalen, Svalbard, investigated by InSAR. *Remote Sensing of Environment*, *231*, 111236. doi: 10.1016/j.rse.2019.111236.

Rubel, F. and Kottek, M. (2017). *Köppen-Geiger climate classification 1986–2010*. Digital media. Available online at http://koeppen-geiger.vu-wien.ac.at/present.htm.

Saemundsson, T., Arnalds, Ó., Kneisel, C., Jonsson, H. P., and Decaulne, A. (2012). The Orravatnsrustir palsa site in Central Iceland–Palsas in an aeolian sedimentation environment. *Geomorphology*, *167*, 13–20. doi: 10.1016/j.geomorph.2012.03.014.

Saemundsson, T., Morino, C., Helgason, J. K., Conway, S. J., and Petursson, H. G. (2018). The triggering factors of the Moafellshyrna debris slide in northern Iceland: Intense precipitation, earthquake activity and thawing of mountain permafrost. *Science of The Total Environment*, *621*, 1163–1175. doi: 10.1016/j.scitotenv.2017.10.111.

Saemundsson, T., Pétursson, H. G., and Decaulne, A. (2003). Triggering factors for rapid mass movements in Iceland. In Rickenmann, D. and Chen, C. (Eds.), *Debris-Flow Hazards Mitigation: Mechanics, Prediction, and Assessment. Proceedings of the Third International Conference on Debris-Flow Hazards Mitigation, Davos, Switzerland, 10-12 September 2003*. Mill Press: Rotterdam, vol. 1, pp. 167–178.

Salomonson, V. and Appel, I. (2004). Estimating fractional snow cover from MODIS using the normalized difference snow index. *Remote Sensing of Environment*, *89*(3), 351–360. doi: 10.1016/j.rse.2003.10.016.

Saloranta, T. M. (2012). Simulating snow maps for Norway: description and statistical evaluation of the seNorge snow model. *The Cryosphere*, *6*(6), 1323–1337. doi: 10.5194/tc-6-1323-2012.

Sanders, J. W., Cuffey, K. M., Moore, J. R., MacGregor, K. R., and Kavanaugh, J. L. (2012). Periglacial weathering and headwall erosion in cirque glacier bergschrunds. *Geology*, *40*(9), 779–782. doi: 10.1130/g33330.1.

Sandersen, F., Bakkehøi, S., Hestnes, E., and Lied, K. (1997). The influence of meteorological factors on the initiation of debris flows, rockfalls, rockslides and rockmass stability. In Senneset, K. (Ed.), *Landslides*, Rotterdam / Brookfield: A. A. Balkema, vol. 201, pp. 97–114.

Sass, O. (2005a). Rock moisture measurements: techniques, results, and implications for weathering. *Earth Surface Processes and Landforms*, *30*(3), 359–374. doi: 10.1002/esp.1214.

Sass, O. (2005b). Temporal variability of rockfall in the Bavarian Alps, Germany. *Arctic, Antarctic, and Alpine Research*, *37*(4), 564–573. doi: 10.1657/1523-0430(2005)037[0564:TVORIT]2.0.CO;2.

Sass, O. (2010). Spatial and temporal patterns of talus activity – a lichenometric approach in the Stubaier Alps, Austria. *Geografiska Annaler. Series A, Physical Geography*, *92*(3), 375–391.

Savi, S., Delunel, R., and Schlunegger, F. (2015). Efficiency of frost-cracking processes through space and time: An example from the eastern Italian Alps. *Geomorphology*, *232*, 248–260. doi: 10.1016/j.geomorph.2015.01.009.

Schaefer, K., Zhang, T., Bruhwiler, L., and Barrett, A. P. (2011). Amount and timing of permafrost carbon release in response to climate warming. *Tellus B*, *63*(2), 165–180. doi: 10.1111/j.1600-0889.2011.00527.x.

Scherler, D. (2014). Climatic limits to headwall retreat in the Khumbu Himalaya, eastern Nepal. *Geology*, *42*(11), 1019–1022. doi: 10.1130/g35975.1.

Schiesser, W. E. (1991). *The numerical method of lines: integration of partial differential equations*. San Diego, USA: Academic Press, 326 pp.

Schneevoigt, N. J., Sund, M., Bogren, W., Kääb, A., and Weydahl, D. J. (2012). Glacier displacement on Comfortlessbreen, Svalbard, using 2-pass differential SAR interferometry (DInSAR) with a digital elevation model. *Polar Record*, *48*(1), 17–25. doi: 10.1017/S0032247411000453.

Schuur, E. A. G., Bockheim, J., Canadell, J. G., Euskirchen, E., Field, C. B., Goryachkin, S. V., Hagemann, S., Kuhry, P., Lafleur, P. M., Lee, H., Mazhitova, G., Nelson, F. E., Rinke, A., Romanovsky, V. E., Shiklomanov, N., Tarnocai, C., Venevsky, S., Vogel, J. G., and Zimov, S. A. (2008). Vulnerability of permafrost carbon to climate change: Implications for the global carbon cycle. *BioScience*, *58*(8), 701–714. doi: 10.1641/B580807.

Schuur, E. A. G., Vogel, J. G., Crummer, K. G., Lee, H., Sickman, J. O., and Osterkamp, T. E. (2009). The effect of permafrost thaw on old carbon release and net carbon exchange from tundra. *Nature*, *459*(7246), 556–559. doi: 10.1038/nature08031.

Seppälä, M. and Kujala, K. (2009). The role of buoyancy in palsa formation. *Geological Society, London, Special Publications*, *320*(1), 51–56. doi: 10.1144/SP320.4.

Shakesby, R. A., Dawson, A. G., and Matthews, J. A. (1987). Rock glaciers, protalus ramparts and related phenomena, Rondane, Norway: a continuum of large-scale talus-derived landforms. *Boreas*, *16*(3), 305–317. doi: 10.1111/j.1502-3885.1987.tb00099.x.

Shangguan, W., Hengl, T., Mendes de Jesus, J., Yuan, H., and Dai, Y. (2016). Mapping the global depth to bedrock for land surface modeling. *Journal of Advances in Modeling Earth Systems*, *9*. doi: 10.1002/2016MS000686.

Shewchuk, J. R. (1996). Triangle: Engineering a 2D quality mesh generator and Delaunay triangulator. In Lin, M. C. and Manocha, D. (Eds.), *Applied Computational Geometry Towards Geometric Engineering*. Berlin, Heidelberg: Springer Berlin Heidelberg, pp. 203–222.

Sigmundsson, F. (2006). *Iceland geodynamics: crustal deformation and divergent plate tectonics*. Chichester, UK: Springer Berlin, Heidelberg, 214 pp. doi: 10.1007/3-540-37666-6.

Singhal, B. B. S. and Gupta, R. P. (2010). *Applied hydrogeology of fractured rocks*. Springer Science & Business Media, 2 ed., 408 pp. doi: 10.1007/978-90-481-8799-7.

Slagstad, T., Balling, N., Elvebakk, H., Midttømme, K., Olesen, O., Olsen, L., and Pascal, C. (2009). Component parts of the World Heat Flow Data Collection. *PANGAEA*. doi: 10.1594/PANGAEA.805921.

Smith, M. W. and Riseborough, D. W. (1996). Permafrost monitoring and detection of climate change. *Permafrost and Periglacial Processes*, *7*(4), 301–309. doi: 10.1002/(SICI)1099-1530(199610)7:4<301::AID-PPP231>3.0.CO;2-R.

Smith, M. W. and Riseborough, D. W. (2002). Climate and the limits of permafrost: a zonal analysis. *Permafrost and Periglacial Processes*, *13*(1), 1–15. doi: 10.1002/ppp.410.

Smith, S. L., O'Neill, H. B., Isaksen, K., Noetzli, J., and Romanovsky, V. E. (2022). The changing thermal state of permafrost. *Nature Reviews Earth & Environment*, *3*(1), 10–23. doi: 10.1038/s43017-021-00240-1.

Sollid, J. L., Isaksen, K., Eiken, T., and Ødegård, R. S. (2003). The transition zone of mountain permafrost on Dovrefjell, southern Norway. In *the Eighth International Conference on Permafrost, Zürich, Switzerland, 21-25 July 2003*. vol. 2, pp. 1085–1090.

Sollid, J. L. and Sørbel, L. (1992). Rock glaciers in Svalbard and Norway. *Permafrost and Periglacial Processes*, *3*(3), 215–220. doi: 10.1002/ppp.3430030307.

Steer, P., Huismans, R. S., Valla, P. G., Gac, S., and Herman, F. (2012). Bimodal Plio–Quaternary glacial erosion of fjords and low-relief surfaces in Scandinavia. *Nature Geoscience*, *5*(9), 635–639. doi: 10.1038/ngeo1549.

Stefánsson, V., Sigurðsson, Ó., Guðmundsson, Á., Franzson, H., Ó., F. G., and Tulinius, H. (1997). Core measurements and geothermal modelling. In *Second Nordic Symposium on Petrophysics*. Fractured reservoirs. Nordic Petroleum Technology Series One, pp. 199–220.

Steiger, C., Etzelmüller, B., Westermann, S., and Myhra, K. S. (2016). Modelling the permafrost distribution in steep rock walls in Norway. *Norwegian Journal of Geology*, *96*(4). doi: 10.17850/njg96-4-04.

Tanarro, L. M., Palacios, D., Andrés, N., Fernández-Fernández, J. M., Zamorano, J. J., Sæmundsson, , and Brynjólfsson, S. (2019). Unchanged surface morphology in debris-covered glaciers and rock glaciers in Tröllaskagi peninsula (northern Iceland). *Science of The Total Environment*, *648*, 218–235. doi: 10.1016/j.scitotenv.2018.07.460.

Thaler, E. A., Crumley, R. L., and Bennett, K. E. (2023). Estimating snow cover from high-resolution satellite imagery by thresholding blue wavelengths. *Remote Sensing of Environment*, *285*, 113403. doi: 10.1016/j.rse.2022.113403.

Thorarinsson, S. (1951). Notes on patterned ground in Iceland, with particular reference to the Icelandic "flás". *Geografiska Annaler*, *33*(3–4), 144–156. doi: 10.1080/20014422.1951.11880839.

Thordarson, T. and Hoskuldsson, A. (2002). *Iceland. Classic Geology in Europe 3*. Hertfordshire, England: Terra Publishing, 200 pp.

Thordarson, T. and Höskuldsson, Á. (2008). Postglacial volcanism in Iceland. *Jökull*, *58*(198).

Thórhallsdóttir, T. E. (1994). Effects of changes in groundwater level on palsas in central Iceland. *Geografiska Annaler. Series A. Physical Geography*, pp. 161–167. doi: 10.2307/521035.

Thórhallsdóttir, T. E. (1996). Seasonal and annual dynamics of frozen ground in the central highland of Iceland. *Arctic and Alpine Research*, *28*(2), 237. doi: 10.2307/1551765.

Thuiller, W., Lafourcade, B., Engler, R., and Araújo, M. B. (2009). BIOMOD – a platform for ensemble forecasting of species distributions. *Ecography*, *32*(3), 369–373. doi: 10.1111/j.1600-0587.2008.05742.x.

Van Genuchten, M. T. (1980). A closed-form equation for predicting the hydraulic conductivity of unsaturated soils. *Soil Science Society of America Journal*, *44*(5), 892–898. doi: 10.2136/sssaj1980.03615995004400050002x.

van Veen, M., Hutchinson, D. J., Kromer, R., Lato, M., and Edwards, T. (2017). Effects of sampling interval on the frequency-magnitude relationship of rockfalls detected from terrestrial laser scanning using semi-automated methods. *Landslides*, *14*, 1579–1592. doi: 10.1007/s10346-017-0801-3.

Van Vliet-Lanoë, B., Bourgeois, O., and Dauteuil, O. (1998). Thufur formation in northern Iceland and its relation to Holocene climate change. *Permafrost and Periglacial Processes*, *9*(4), 347–365. doi: 10.1002/(SICI)1099-1530(199810/12)9:4<347::AID-PPP299>3.0.CO;2-4.

Vaughan, D. G., Comiso, J. C., Allison, I., Carrasco, J., Kaser, G., Kwok, R., Mote, P., Murray, T., Paul, F., Ren, J., and Zhang, T. (2013). Observations: Cryosphere. In Stocker, T., Qin, D., Plattner, G.-K., Tignor, M., Allen, S., Boschung, J., Nauels, A., Xia, Y., Bex, V., and Midgley, P. (Eds.), *Climate change 2013: The Physical Science Basis Contribution of working Group I to the Fifth Assessment Report of the Intergovernmental Panel on Climate Change*, Cambridge, United Kingdom and New York, NY, USA: Cambridge University Press, vol. 2103, chap. 4, pp. 317–382.

Vink, G. E. (1984). A hotspot model for Iceland and the Vøring Plateau. *Journal of Geophysical Research: Solid Earth*, *89*(B12), 9949–9959. doi: 10.1029/JB089iB12p09949.

Walder, J. and Hallet, B. (1985). A theoretical model of the fracture of rock during freezing. *Geological Society of America Bulletin*, *96*(3), 336–346. doi: 10.1130/0016-7606(1985)96<336:Atmotf>2.0.Co;2.

Walder, J. S. and Hallet, B. (1986). The physical basis of frost weathering: toward a more fundamental and unified perspective. *Arctic and Alpine Research*, *18*(1), 27–32. doi: 10.2307/1551211.

Washburn, A. L. (1967). Instrumental observations of mass wasting in the Mesters Vig District, Northeast Greenland. *Meddelelser om Grønland*, *166*, 1–297.

Westermann, S., Elberling, B., Højlund Pedersen, S., Stendel, M., Hansen, B. U., and Liston, G. E. (2015a). Future permafrost conditions along environmental gradients in Zackenberg, Greenland. *The Cryosphere*, *9*(2), 719–735. doi: 10.5194/tc-9-719-2015.

Westermann, S., Østby, T. I., Gisnås, K., Schuler, T. V., and Etzelmüller, B. (2015b). A ground temperature map of the North Atlantic permafrost region based on remote sensing and reanalysis data. *The Cryosphere*, *9*(3), 1303–1319. doi: 10.5194/tc-9-1303-2015.

Westermann, S., Peter, M., Langer, M., Schwamborn, G., Schirrmeister, L., Etzelmüller, B., and Boike, J. (2017). Transient modeling of the ground thermal conditions using satellite data in the Lena River delta, Siberia. *The Cryosphere*, *11*(3), 1441–1463. doi: 10.5194/tc-11-1441-2017.

Westermann, S., Schuler, T. V., Gisnås, K., and Etzelmüller, B. (2013). Transient thermal modeling of permafrost conditions in Southern Norway. *The Cryosphere*, *7*(2), 719–739. doi: 10.5194/tc-7-719-2013.

Wettlaufer, J. and Worster, M. G. (2006). Premelting dynamics. *Annual Review of Fluid Mechanics*, *38*(1), 427–452. doi: 10.1146/annurev.fluid.37.061903.175758.

Weydahl, D. (2001). Analysis of ERS Tandem SAR coherence from glaciers, valleys, and fjord ice on Svalbard. *IEEE Transactions on Geoscience and Remote Sensing*, *39*(9), 2029–2039. doi: 10.1109/36.951093.

Whalley, B. and Martin, H. (1994). Rock glaciers in Tröllaskagi: Their origin and climatic significance. *Münchener Geographische Arbeiten*, *12*, 289–308.

Williams, P. J. and Smith, M. W. (1989). *The frozen earth: fundamentals of geocryology*, vol. 306. Cambridge, UK: Cambridge University Press, 306 pp. doi: 10.1017/CBO9780511564437.

Winkler, S., Matthews, J. A., Haselberger, S., Hill, J. L., Mourne, R. W., Owen, G., and Wilson, P. (2020). Schmidt-hammer exposure-age dating (SHD) of sorted stripes on Juvflye, Jotunheimen (central South Norway): Morphodynamic and palaeoclimatic implications. *Geomorphology*, *353*, 107014. doi: 10.1016/j.geomorph.2019.107014.

Winkler, S., Matthews, J. A., Mourne, R. W., and Wilson, P. (2016). Schmidt-hammer exposure ages from periglacial patterned ground (sorted circles) in Jotunheimen, Norway, and their interpretative problems. *Geografiska Annaler: Series A, Physical Geography*, *98*(3), 265–285. doi: 10.1111/geoa.12134.

Wohlfarth, B., Bjorck, S., Funder, S., Houmark-Nielsen, M., Ingólfsson, Ó., Lunkka, J.-P., Mangerud, J., Saarnisto, M., and Vorren, T. (2008). Quaternary of Norden. *Episodes*, *31*(1), 73–81. doi: 10.18814/epiiugs/2008/v31i1/011.

Woodhouse, I. H. (2006). *Introduction to microwave remote sensing*. Boca Raton, Florida, USA: CRC press.

Yen, Y.-C. (1981). *Review of thermal properties of snow, ice and sea ice*. Report 81–10, U.S. Army Cold Regions Research and Engineering Laboratory, Hanover, New Hampshire, USA, 27 pp.

Yershow, E. D. (2004). *General Geocryology*. Cambridge, UK: Cambridge University Press, 580 pp.

Yunjun, Z., Fattahi, H., and Amelung, F. (2019). Small baseline InSAR time series analysis: Unwrapping error correction and noise reduction. *Computers Geosciences*, *133*, 104331. doi: 10.1016/j.cageo.2019.104331.

Zhang, Y., Chen, W., and Cihlar, J. (2003). A process-based model for quantifying the impact of climate change on permafrost thermal regimes. *Journal of Geophysical Research*, *108*(D22). doi: 10.1029/2002jd003354.

Zhang, Y., Chen, W., and Riseborough, D. W. (2006). Temporal and spatial changes of permafrost in Canada since the end of the Little Ice Age. *Journal of Geophysical Research: Atmospheres*, *111*(D22). doi: 10.1029/2006JD007284.

Zimov, S. A., Schuur, E. A. G., and Chapin, F. S. (2006). Permafrost and the global carbon budget. *Science*, *312*(5780), 1612–1613. doi: 10.1126/science.1128908.

Zuidhoff, F. S. and Kolstrup, E. (2000). Changes in palsa distribution in relation to climate change in Laivadalen, northern Sweden, especially 1960–1997. *Permafrost and Periglacial Processes*, *11*(1), 55–69. doi: 10.1002/(SICI)1099-1530(200001/03)11:1<55::AID-PPP338>3.0.CO;2-T.

II

PAPERS

PAPER I

Transient modelling of permafrost distribution in Iceland

Justyna Czekirda, Sebastian Westermann, Bernd Etzelmüller and Tómas Jóhannesson

Published in *Frontiers in Earth Science*, Vol. 7, 2019.
doi: 10.3389/feart.2019.00130

frontiers in Earth Science

ORIGINAL RESEARCH
published: 04 June 2019
doi: 10.3389/feart.2019.00130

Transient Modelling of Permafrost Distribution in Iceland

Justyna Czekirda[1]*, *Sebastian Westermann*[1], *Bernd Etzelmüller*[1] and
Tómas Jóhannesson[2]

[1] Department of Geosciences, University of Oslo, Oslo, Norway, [2] Icelandic Meteorological Office, Reykjavík, Iceland

Warming and degradation of permafrost during the ongoing climate change is of growing concern. Recently, permafrost thawing has been recognized as a new factor triggering landslides in Iceland. Therefore, there is an increased need for a more thorough understanding of permafrost distribution and the temporal evolution of the ground thermal regime in this region. This study focuses on regional modelling of ground temperature evolution in Iceland for the last six decades (1960–2016) by employing the transient permafrost model CryoGrid 2 at 1-km spatial resolution. To account for the strong wind redistribution of snow in Iceland, we ran three realizations of the model, by forcing the embodied snow water equivalent model with 50, 100, and 150% of gridded precipitation. The modelled permafrost extent strongly depends on snow depth, with around 3–15 times more cells indicating permafrost in the halved-precipitation run in comparison to the other two precipitation runs. A three- to four-decade-long warming trend has led to warming or degradation of permafrost in some areas of Iceland. We roughly estimate that ∼11 and 7% of the land area of Iceland was underlain by permafrost during the periods 1980–1989 and 2010–2016, respectively. Model validation with ground temperature measurements and the distribution of permafrost-related landforms, such as active rock glaciers and stable ice-cored moraines, together with palsas and peat plateaus, shows good agreement. The simulation results may be further used as a baseline for modelling of future permafrost evolution at a regional scale or for identification of landslide-susceptible areas in Iceland.

Keywords: permafrost, Iceland, transient permafrost modelling, maritime permafrost, permafrost dynamics

Edited by:
Benjamin M. Jones,
University of Alaska Fairbanks,
United States

Reviewed by:
Elchin Jafarov,
Los Alamos National Laboratory
(DOE), United States
Noriaki Ohara,
University of Wyoming, United States

***Correspondence:**
Justyna Czekirda
justyna.czekirda@geo.uio.no

Specialty section:
This article was submitted to
Cryospheric Sciences,
a section of the journal
Frontiers in Earth Science

Received: *23 January 2019*
Accepted: *13 May 2019*
Published: *04 June 2019*

Citation:
Czekirda J, Westermann S,
Etzelmüller B and Jóhannesson T
(2019) Transient Modelling of
Permafrost Distribution in Iceland.
Front. Earth Sci. 7:130.
doi: 10.3389/feart.2019.00130

INTRODUCTION

Permafrost temperature is a sensitive climate indicator, providing a filtered signal of surface temperature variations, from annual-scale surface temperature variations at depths of a few meters to century-scale climate change at depths of several 100 m (Lachenbruch and Marshall, 1986). Substantial permafrost warming trends have been observed in most permafrost regions of the Earth during the last decades (e.g., Romanovsky et al., 2010). Because of likely continuation of climate warming and seasonal snow cover changes, future projections indicate shrinkage of the near-surface permafrost extent (e.g., Collins et al., 2013). Enhanced thaw of ice-rich permafrost has the potential to alter the landscape, tundra ecosystems, and associated hydrological processes (e.g., Smith et al., 2005; Jorgenson et al., 2006; White et al., 2007). Furthermore, permafrost thaw affects infrastructure in the Arctic (Hjort et al., 2018; Yumashev et al., 2019) and in high mountains. There, permafrost degradation is considered to be an important factor for geotechnical slope stability, contributing to triggering rockfalls, rock avalanches, or landslides (Gruber and Haeberli, 2007; Ravanel et al., 2010; Krautblatter et al., 2012). In addition, permafrost is one of the largest vulnerable carbon pools, storing two times more organic carbon than the entire atmosphere (Schuur et al., 2008), which may contribute to enhanced greenhouse gas emissions if permafrost thaws. According to recent studies (e.g., Schuster et al., 2018) permafrost contains also a large amount of buried mercury, a release of which may potentially threaten human health. During the ongoing warming, the knowledge of the spatial and temporal evolution of permafrost is thus essential for the assessment of permafrost vulnerability, and plausible impacts of permafrost degradation on the environment.

In the North-Atlantic region, permafrost is widespread and highly diverse, ranging from mountain discontinuous permafrost in Scandinavia (Gisnås et al., 2017), via warm continuous permafrost on Svalbard (e.g., Humlum et al., 2003) to cold continuous permafrost at the east coast in Greenland (Christiansen et al., 2008; Westermann et al., 2015a). Iceland is situated in the transition between mountain permafrost in Norway and continuous permafrost in Greenland and is dominated by both mountain permafrost above c. 800 m a.s.l. in deep regolith-dominated slopes and mountain plateaus, along with sporadic permafrost in palsas and peat plateaus (e.g., Etzelmüller et al., 2007; Farbrot et al., 2007b; Saemundsson et al., 2012). Ground temperatures have been monitored in four shallow boreholes since 2004 (Farbrot et al., 2007b), and show near-surface permafrost temperatures between -1°C to close to 0°C between 800 and 900 m a.s.l. in eastern and central Iceland.

Snow cover and redistribution of snow by strong wind is one of the major factors governing permafrost distribution locally due to maritime climate conditions (Etzelmüller et al., 2007), with frequent low-pressure systems developing around Iceland during all seasons. Moreover, the volcanic activity in Iceland leads to high geothermal heat flux (Hjartarson, 2015), which restricts permafrost thickness and causes the ground temperatures to be very sensitive to the changes in surface temperature (Farbrot et al., 2007b). Thus, permafrost existence is assumed very dynamic in Iceland. This has become obvious recently through three events where ice-cemented debris was observed within landslide deposits (Sæmundsson et al., 2018; **Figure 1**). The importance of permafrost thaw for slope processes in Iceland has therefore became a focal point of interest over the past few years, where e.g., Sæmundsson et al. (2018) urge that the mentioned landslides "have highlighted the need for a more detailed understanding of the distribution and condition of mountain permafrost within perched talus deposits." These previous events occurred in unsettled areas; however, a similar type of landslides may occur in the future in other regions of the country, thus increasing hazard risk for infrastructure and inhabitants.

To address these issues, knowledge about permafrost distribution, dynamics, and sensitivity to climate change is needed. Earlier, the potential permafrost extent in Iceland was simply delineated based on the mean annual air temperature for the normal period of 1961–1990 (Etzelmüller et al., 2007; **Figure 1**), where threshold values for permafrost presence were derived using ground surface temperature data. Later, equilibrium approaches were presented for the entire North Atlantic region, where the semi-empirical TTOP-model (Smith and Riseborough, 2002; Riseborough et al., 2008) was forced by land surface temperate obtained by satellites (Westermann et al., 2015b). In these approaches, the effects of the snow cover on the ground thermal regime (nival offsets) and the thermal offsets within the active layer were neither addressed nor handled through simplified empirical relationships. Transient behaviour of ground temperatures was not considered.

The overall objective of this study was to model regional permafrost distribution in Iceland transiently for the period 1960–2016. To achieve this task, we implemented a temperature-index snow model for Iceland (Saloranta, 2012) and established a permafrost model using the transient permafrost model CryoGrid 2 (Westermann et al., 2013), with a ground resolution of 1 km. To address sub-grid variability due to snow depth heterogeneity, the permafrost model was run with three precipitation scenarios. The snow and permafrost models were forced by gridded data sets of air temperature and precipitation provided by the Icelandic Meteorological Office (IMO). This paper presents the main results of this study, together with model sensitivity, and discusses the ability to distinguish regions of high interest for probable future landslide hazards due to permafrost thaw.

GEOLOGY AND CLIMATE

Iceland is a geologically young island that is located in the northern part of the North Atlantic ridge, stretching between 63 and 66°N. Currently, the volcanic activity and faulting take place almost exclusively within the neo-volcanic zones, which are 15–50 km-wide belts (Thordarson and Höskuldsson, 2008). Iceland is dominated by basaltic rock, partly highly fractured, and easily weathered.

Iceland has a maritime climate, with mild winters and cool summers. Mean annual air temperature (MAAT) in the normal period 1981–2010 varied from below -5°C at the uppermost parts of the ice caps to above 4–5°C along the southern coast (Crochet and Jóhannesson, 2011). Mean annual precipitation (MAP) during the same normal period is estimated to be above 4,000 mm in the windward mountainous regions in the south, above 1,000 mm in most of the other regions in the south and 500–1,000 mm in the large parts of the northern Iceland (Crochet et al., 2007). The climate has substantially varied since the start of instrumental observations in the nineteenth century. A warm period during the 1930s was followed by a cold period until the early 1990s (Hanna et al., 2004; **Figure 2**). Since then, air temperature has increased.

Regional distribution and thicknesses of the surficial sediments are generally unclear in Iceland. Soil development throughout the Holocene has been shaped by volcanic eruptions, active aeolian processes and cryoturbation (Arnalds, 2008). Sandy surfaces in the neo-volcanic zones and glacio-fluvial floodplains supply sand-dust material, which is deposited with rates of <0.01 mm yr^{-1} and >1 mm yr^{-1} in the areas away

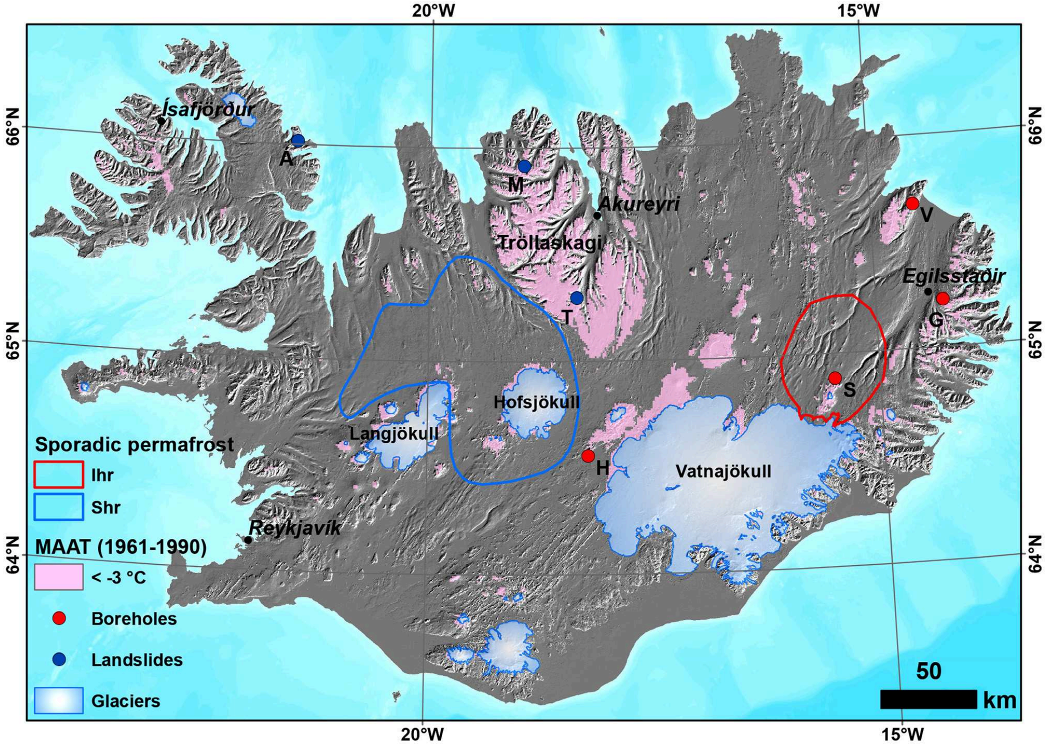

FIGURE 1 | Sporadic permafrost from Brown et al. (1997): Ihr, Isolated patches of permafrost extent with high ground ice content and thin overburden and exposed bedrock; Shr, Sporadic permafrost extent with high ground ice content and thin overburden and exposed bedrock. MAAT < −3°C indicates areas of widespread permafrost as modelled in Etzelmüller et al. (2007). Boreholes: G, Gagnheiði; H, Hágöngur; S, Sauðafell; V, Vopnafjörður. Landslides with ice-cemented deposits: M, Móafellshyrna Mountain; T, Torfufell Mountain; Á, Árnesfjall Mountain. Map data from the National Land Survey of Iceland (NLSI; License: http://www.lmi.is/wp-content/uploads/2013/10/licenceNLSI.pdf).

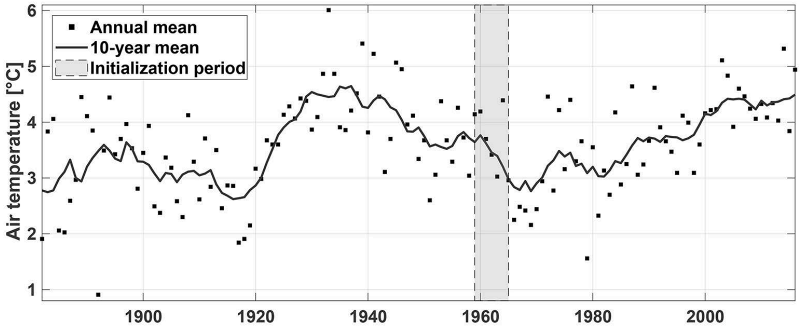

FIGURE 2 | Mean annual air temperature with a 10-year running mean in Akureyri in the period 1882–2016. Initialization period of the transient permafrost model is also shown. Data from the Icelandic Meteorological Office.

from and close to the dust sources, respectively (Arnalds, 2015). In addition, the soil thickening rates increased after the settlement ("Landnám," around 874 AD), when an extensive land degradation started (Arnalds, 2008). The resulting barren land together with the other poorly vegetated land areas, which occur in the mountains and in areas subjected to volcanic disturbance and catastrophic flooding, currently cover ∼42% of Iceland (Arnalds, 2015).

FORCING DATA AND MODELLING APPROACH

The CryoGrid 2 Model

CryoGrid 2 is a numerical permafrost model, where the evolution of the temperature profile is computed both in the soil and snowpack (when present), by forcing the model with sets of air/surface temperature and snow depth. The model physics is similar to the other transient permafrost models, e.g., GIPL2 (Jafarov et al., 2012; Nicolsky et al., 2017). The detailed description of the equations implemented in the CryoGrid 2 model, together with the numerical solvers, can be found in Westermann et al. (2013). The mathematical basis of the model is one-dimensional transient heat conduction equation that additionally accounts for the latent heat effects due to ice-water phase changes:

$$c_{eff}\left(z,T\right)\frac{\partial T}{\partial t}-\frac{\partial}{\partial z}\left(k\left(z,T\right)\frac{\partial T}{\partial z}\right)=0, \tag{1}$$

where $c_{eff}(z,T)$ [J m^{-3} K^{-1}], $k(z,T)$ [W m^{-1} K^{-1}], z, T, t denote the effective volumetric heat capacity, thermal conductivity, depth, temperature and time, respectively. Equation (1) can be applied for spatially distributed permafrost modelling by calculating it for each grid cell, i.e., there is no interaction between the neighbouring cells and the lateral heat flux is thus overlooked in the model. Thermal properties of the subsurface layers are estimated as functions of the thermal properties of the individual soil constituents, such as water, ice, organic matter, mineral content, air, and their respective volumetric fractions. The liquid water and ice contents are obtained in CryoGrid 2 from the functions by Dall'Amico et al. (2011), which link liquid water content, temperature and soil saturation degree. Variations in soil water content depend exclusively on freezing and thawing processes, i.e., water or water vapour movement in the soil, along with additional external water inputs (meltwater, rain), and their impact on the ground temperature are neglected in the model.

A snowpack layer has constant thermal properties in space and time, which are estimated as functions of a uniform snow density. In this study, the thermal conductivity of snow k_{snow} [W m^{-1} K^{-1}] was estimated from an equation derived by Yen (1981):

$$k_{snow}=k_{ice}\left(\frac{\rho_{snow}}{\rho_{water}}\right)^{1.885}, \tag{2}$$

where k_{ice}, ρ_{snow}, ρ_{water} denote the thermal conductivity of ice and the densities of snow and water, respectively. The same snow density is used to convert snow water equivalent (SWE), provided as the forcing data, to snow depth. Influence of processes in the snow cover, such as water infiltration, snow melting or refreezing of melt- or rainwater, on the ground temperature is excluded.

Surface Forcing and Boundary Conditions

Gridded Air Temperature Data Set

Gridded air temperature data set was provided by the Icelandic Meteorological Office (IMO). The IMO data set of gridded daily temperature has a 1 km^2 resolution and is described in detail in Crochet and Jóhannesson (2011). The data set is in principle based on lapse rate adjustment and interpolation based on meteorological stations on Iceland. The model verification of the mean monthly temperatures for the 1961–1990 period indicated that the modelled temperatures are unbiased in average within ±1°C. The evaluation of the gridded daily temperatures in 1995–2010 estimated 60–80% and 90–95% of the errors to be within ±1 and ±2°C, respectively (Crochet and Jóhannesson, 2011).

Gridded Precipitation Data Sets

Two gridded precipitation data sets from IMO were derived from the large-scale atmospheric conditions based on reanalysis data from the European Centre for Medium-Range Weather Forecasts (ECMWF). The first precipitation data set for the period 1958–2002 has a 1-km resolution (Crochet et al., 2007), and was calculated from a physically-based linear theory model of orographic precipitation (henceforth LT model) developed by Smith and Barstad (2004), where airflow over the orography is estimated using linear mountain-wave theory and a linear cloud physics representation is used to estimate the resulting precipitation field. The second precipitation data set at a 2.5-km resolution for the period between 1980 and 2016 was created using the non-hydrostatic convection-permitting numerical weather prediction (NWP) model HARMONIE (Bengtsson et al., 2017). The gridded precipitation data for Iceland derived with the HARMONIE model were created based on ERA-Interim reanalysis (T255 resolution, ∼79 km) data and from ECMWF operational reanalysis in the recent period.

Snow Water Equivalent (SWE) Model

A degree-day based algorithm from Saloranta (2012) was employed to obtain snow water equivalent (SWE). This approach, so-called "*seNorge,*" is operationally used in Norway to produce daily maps of snow distribution and depth. The SWE model is run for each grid cell separately and is forced by daily mean air temperature and daily sum of precipitation. The model includes the accumulation of snowfall and liquid water content (snowmelt or rainfall) in the snowpack. Precipitation is categorized as liquid or solid based on an air temperature threshold. Snow always accumulates in the snowpack, whereas addition of liquid water cannot exceed a given liquid water-retention capacity parameter that depends on ice content in the snowpack. When air temperature is above a chosen temperature threshold for melting/refreezing, the available ice content melts, otherwise, the available liquid content refreezes to ice. Potential melting and refreezing are quantified based on seasonally varying degree-day factors for melting and refreezing. The detailed description of the equations used in the seNorge model for snowpack water balance can be found in Saloranta (2012).

The SWE model was forced by the gridded daily air temperature and precipitation data sets. The HARMONIE data set was linearly interpolated to 1-km^2 cells for exactly the same central grid coordinates as used in the permafrost model. The data set from the HARMONIE was given the higher priority than the results of the LT model since it should be more reliable, according to the validation studies conducted at IMO (Nawri et al., 2017). Therefore, between 1.9.1959 and 31.12.1979 precipitation data set derived from the LT model was used, and in the remaining period, the data set from the HARMONIE model was employed.

Most of the SWE-model parameters for Iceland were assumed or based on the values found in the literature. Correction factors for input precipitation as snow or rain were set to unity. Threshold air temperature for rain/snow was set to 1°C, following different studies from Icelandic glaciers (Jóhannesson et al., 1995; Jóhannesson, 1997; Aðalgeirsdóttir et al., 2006), while we used the base temperature of 0°C as a threshold for melting/refreezing (e.g., DeWalle and Rango, 2008). The degree-day factor for refreezing followed Saloranta (2012), yielding values between 0.32 and 0.6 mm d^{-1} °C^{-1} for Iceland, which are within the ranges of the minimum and maximum degree-day refreezing factors found in the literature (Kokkonen et al., 2006; Saloranta, 2012). The snowpack could retain liquid water of maximum 10% of its ice content.

Minimum and maximum degree-day melt factors were derived from snow depth measurements recorded at Icelandic weather stations, located above 150 m a.s.l. with snow cover remaining for at least a few months during winter were analysed. The analysis encompassed only chosen years, where relatively deep snow cover was present during melting season. SWE was calculated from the observed snow depth, assuming snow density of 350 kg m^{-3} that is an approximate mean value of snow densities in Sigurðsson and Jóhannesson (2014). The same snow density was assumed in the CryoGrid 2 permafrost model to convert SWE to snow depth and to calculate thermal conductivity of snow. The accumulated melt depth M_{acc}[mm] was derived for every chosen melt season between the date of maximum snow depth and modelled snow-free day, i.e., when M_{acc} equals maximum SWE. M_{acc} is given by:

$$\mathrm{M_{acc}} = \Delta \mathrm{t} \sum\nolimits_{\mathrm{i}=1}^{\mathrm{n}} \mathrm{C_M} \left(\mathrm{T_{air}} - \mathrm{T_M}\right) \text{ for } \mathrm{T_{air}} > \mathrm{T_M}, \tag{3}$$

where T_{air} is air temperature, T_M is threshold air temperature for melting (0°C) and t is time interval (1 day). Various combinations of the minimum and maximum degree-day melting factors were tested in order to determine the best possible snow-free date. The initial guess values of the melt factors for snow were assumed to be similar to the melt factors used in the degree-day glacier mass-balance models applied to the Icelandic glaciers: 4.45–5.6 mm d^{-1} °C^{-1} (Jóhannesson et al., 1995; Jóhannesson, 1997; Aðalgeirsdóttir et al., 2006). These parameters are higher than the melt factors used in the SWE model for Norway, where minimum degree-day melting factor of 2 mm d^{-1} °C^{-1} and maximum degree-day factor of 3–4 mm d^{-1} °C^{-1} is used (Saloranta, 2012). In Iceland, snow may have a sand layer on top due to aeolian accumulation, leading to higher melt factors for snow than in Norway. Additionally, maximum degree-day melting factors vary in the SWE model for Norway depending on the latitude and forest cover; however, it was assumed that this approach was unnecessary for Iceland, considering that the forest cover is sparse and its latitudinal extent is much less than Norway's.

The modelled snow extent in periods of 2000 to 2016 was visually compared with the snow extent visible on satellite imagery. An archive of low-resolution optical satellite imagery from Aqua/Terra MODIS is available for Iceland from 2000 until present on NASA Worldview application (https://worldview.earthdata.nasa.gov/) operated by the NASA/Goddard Space Flight Center Earth Science Data and Information System (ESDIS) project. The False Colour Composites (FCCs) 721 were utilized, where shortwave infrared (SWIR; Band 7), near-infrared (NIR; band 2), and visible band (VIS; band 1) are used as red, green and blue components, respectively, of the RGB composite. Snow and ice are in most cases easily distinguishable from clouds in FCC 721 (NASA, 2018).

Surface Forcing and Lower Boundary Conditions

CryoGrid 2 was forced by weekly averaged surface air temperature data and snow depth data derived from the SWE algorithm. As the lower model boundary at 1,000 m depth, we used the published heat flow map by Hjartarson (2015), assuming constant heat flux in time. The heat flux is generally high in Iceland, between 40 to over 300 mW m^{-2}, with the largest values occurring in or near the active volcanic zones. The applied thermal conductivity values varied regionally between 1.6 W m^{-1} K^{-1} for the young volcanic rocks, 1.7–1.8 W m^{-1} K^{-1} for the intermediate-aged rocks and 1.9 W m^{-1} K^{-1} for the oldest volcanic rocks. The influence of paleoclimatic changes, such as glaciations, was assumed to be erased by the high geothermal heat flux and was not accounted for in the heat flow map (Hjartarson, 2015).

Ground Properties

Sediment Cover

Thermal conductivity of the rock matrix or mineral fraction was set to 2 W m^{-1} K^{-1} (Flóvenz and Saemundsson, 1993). For each subsurface layer volumetric contents of water (θ_w), mineral component (θ_m), organic matter (θ_o), and air (θ_a) were defined as means for the whole modelling period. The seasonal variations in the water content or depth to the saturated zone are neglected.

As there is no nationwide map of surficial sediments, subsurface stratigraphy was assigned according to the soil map of Iceland (Arnalds, 2008, 2015). The main soil types in Iceland are Histosols, Histic Andosols, Gleyic Andosols, Brown Andosols, Vitrisols, Leptosols, and Cryosols (Arnalds, 2015). Some grids on the soil map are soil complexes, composed of two or more soil types, because of the small scale of this map. To get an idea of parameter ranges, the model was calibrated against the ground temperature measurements at depths of 1 and 2 m acquired in four shallow boreholes in central and eastern Iceland (Farbrot et al., 2007b). The boreholes are located in the same soil class (Cambic Vitrisol), thus their subsurface parameters (subsurface layers, volumetric contents, and type of the freeze curve) were assumed to be equal. To account for the snow depth heterogeneity within a grid cell, we additionally adjusted snow depth at each borehole site by forcing the seNorge SWE model with precipitation reduced by the most suitable fraction parameter (percentage of precipitation). For the borehole locations, we varied precipitation fraction for each site and conducted multiple tests in order to find the most optimal subsurface parameters. Stratigraphy of the remaining soil classes was chosen based on estimates and values that were found in the literature. **Table 1** contains the subsurface parameters for each main soil classes. Subsurface stratigraphy of the soil complexes was calculated as a mean of the single soil classes assuming the equal contribution of these classes to a cell, and in case when the freezing curve was between silt and sand, the latter was applied.

TABLE 1 | Assumed depths of subsurface layers, along with volumetric fractions of the soil constituents and type of freeze curve (FC) for each layer: 1, sand and 2, silt.

z [m]	θ_w [-]	θ_m [-]	θ_o [-]	θ_a [-]	FC
Cambic Vitrisol					
0.0–4.0	0.04	0.60	0.00	0.36	1
4.0–10.0	0.20	0.80	0.00	0.00	1
>10.0	0.08	0.92	0.00	0.00	1
Arenic Vitrisol					
0.0–4.0	0.04	0.60	0.00	0.36	1
4.0–10.0	0.40	0.60	0.00	0.00	1
>10.0	0.08	0.92	0.00	0.00	1
Pumice Vitrisol					
0.0–0.1	0.20	0.20	0.00	0.60	1
0.1–4.0	0.04	0.60	0.00	0.36	1
4.0–10.0	0.20	0.80	0.00	0.00	1
>10.0	0.08	0.92	0.00	0.00	1
Leptosol					
0.0–1.0	0.10	0.60	0.00	0.30	1
1.0–10.0	0.40	0.60	0.00	0.00	1
>10.0	0.08	0.92	0.00	0.00	1
Brown Andosol					
0.0–1.0	0.25	0.22	0.03	0.50	2
1.0–1.5	0.75	0.22	0.03	0.00	2
1.5–10.0	0.40	0.60	0.00	0.00	1
>10.0	0.08	0.92	0.00	0.00	1
Gleyic Andosol					
0.0–0.5	0.30	0.14	0.06	0.50	2
0.5–1.5	0.80	0.14	0.06	0.00	2
1.5–10.0	0.40	0.60	0.00	0.00	1
>10.0	0.08	0.92	0.00	0.00	1
Histic Andosol					
0.0–0.5	0.40	0.08	0.12	0.40	2
0.5–2.0	0.80	0.11	0.09	0.00	2
2.0–10.0	0.40	0.60	0.00	0.00	1
>10.0	0.08	0.92	0.00	0.00	1
Histosol					
0.0–0.5	0.60	0.06	0.14	0.20	2
0.5–2.0	0.80	0.08	0.12	0.00	2
2.0–10.0	0.40	0.60	0.00	0.00	1
>10.0	0.08	0.92	0.00	0.00	1
Cryosol					
0.0–0.5	0.30	0.12	0.08	0.50	2
0.5–2.0	0.80	0.16	0.04	0.00	2
2.0–10.0	0.40	0.60	0.00	0.00	1
>10.0	0.08	0.92	0.00	0.00	1

θ_w, volumetric content of water; θ_m, volumetric mineral content; θ_o, volumetric content of organic matter; θ_a, volumetric air content; z, depth.

Vitrisols and Leptosols

Vitrisols ("vitr" is Latin for "glass") are soils of the poorly vegetated and barren land areas, i.e., "deserts" (e.g., Arnalds, 2000, 2015). In these areas, very dry conditions prevail owing to: (1) sand-dominated sediments with low water holding capacity and rapid hydraulic conductivity, (2) rapid evaporation during sunny spells in summer, when the dark surfaces heat up, and (3) limited infiltration during winter as a result of impermeable ice formation (Arnalds, 2015). Moreover, snow is removed by wind in the poorly vegetated areas. Hence, only one third to one half of the precipitation infiltrates into the ground (Arnalds, 2015). In absence of measurements for near-surface water contents, a value of 4% vol. water was chosen for Vitrisols, which yielded a satisfactory fit for the borehole locations. However, higher water contents are likely at least periodically, and the effect of near-surface water contents in Vitrisols should be investigated further. Sand fraction dominates in Vitrisols and organic content is low (<1% C) (Arnalds and Kimble, 2001; Arnalds, 2008, 2015). Therefore, the upper layer in Vitrisols was parametrized as sand with 40% porosity and no organic matter. On the soil map there are three subclasses of Vitrisols: (1) Cambic Vitrisols, shallow soils with cambic horizon, often underlain by glacial till, (2) Sandy (Arenic) Vitrisols, which are underlain by lava or till, (3) Pumice Vitrisols, with pumice layer in the top of the soil (Arnalds, 2015). Pumice has very high porosity, hence it was assumed that it could retain water in the pores (20% vol. water). This material can presumably lead to permafrost aggradation, because of its low thermal conductivity ($<0.5\ \mathrm{W\ m^{-1}}$) (Farbrot, 2007). Leptosols encompass lava surfaces and scree slopes, where we assumed dry conditions in the near-surface layer (10% vol. water).

Histosols, Andosols, and Cryosols

Icelandic soils under vegetation have andic (volcanic) and/or histic (organic) properties (Arnalds, 2008). Depending on the rates of eolian and tephra deposition and drainage class, these soils are divided into: Histosols (>20% C average in the top 30 cm; wet), Histic Andosols (12–20% C average in the top 30 cm; poorly drained), Gleyic Andosols (<12% C average in the top 30 cm; poorly drained) and Brown Andosols (<12% C average in the top 30 cm; freely drained). In general, the further away from the active volcanic zones and sources of eolian materials, the wetter and more organic soil exists in the area (Arnalds, 2008). Soils of the wetlands are aquic soils with low organic carbon content (Gleyic Andosols and Histic Andosols) and true peat soils with higher carbon content (Histosols). Vegetated drylands are underlain by Brown Andosols. Histosols and Andosols have low bulk densities ($<0.9\,\mathrm{g\ cm^{-3}}$) and contain large water amounts with a wilting point often >60% water per dry weight of soil (Arnalds, 2015). Cryosols are permafrost soils, related to Gleyic Andosols, and occurring mostly in palsa areas (Arnalds, 2004).

The two uppermost layers for Andosol, Histosol, and Cryosol classes in **Table 1** represent the true soils (so-called solum; A and B soil horizons). Total depths of Andosols were rounded values from Óskarsson et al. (2004). Soil textures of Andosols are mostly silt loams (Arnalds, 2015), thus the freeze curve for these soils was parametrized as silt. We estimated the total porosity ϕ of Andosols and Histosols from the average bulk density ρ_b [g cm^{-3}] and density of the soil particles ρ_{soil} [g cm^{-3}]:

$$\phi = 1 - \frac{\rho_b}{\rho_{soil}} \tag{4}$$

(e.g., Hillel, 2004). Values of ρ_b for Andosols were also from Óskarsson et al. (2004), whereas ρ_{soil} for Andosols were determined based on the empirical relationship between ρ_{soil} and the organic carbon content C [–]:

$$\rho_{soil} = -4\,C + 2.678, \tag{5}$$

as obtained by Poulenard et al. (2003). For Histosols, we assumed ρ_b of 0.3 g cm^{-3} (e.g., Arnalds, 2004) and ρ_{soil} of 1.55 g cm^{-3}, which is an average value for Histosols in Redding and Devito (2006). The calculated values of the porosity for Histosols and Andosols are in general high (>70%).

Volumetric water contents θ_w of Histosols and Andosols were computed from mass wetness w [–] in Arnalds (2015) and ρ_b, using the following equation:

$$\theta_w = w\frac{\rho_b}{\rho_w} \tag{6}$$

(e.g., Hillel, 2004). The lower range of the field capacity (0.3 bar) was assumed the most likely representation of the yearly means of water content.

Volumetric organic content θ_o was determined based on values of average organic carbon content, mentioned in Arnalds (2004, 2015) and Óskarsson et al. (2004), and value for Cryosols was from Ottósson et al. (2016). These gravimetric values were converted to the gravimetric soil organic matter (SOM_g [–]), assuming the conversion factor of 2, i.e., the organic matter contains 50% of organic carbon, following Pribyl (2010). θ_o was finally calculated from the gravimetric organic matter content, using the equation:

$$\theta_o = SOM_g\frac{\rho_b}{\rho_o}, \tag{7}$$

where ρ_o is the density of the organic matter, assumed 1.3 g cm^{-3} (Farouki, 1981).

Bedrock

To estimate the overall depth of unconsolidated sediments in each soil class, we used zonal statistics over the global depth to bedrock data set (Shangguan et al., 2016), and based on the results we assumed a uniform regolith depth of 10 m to be an adequate approximation for all the soil classes. The global depth to bedrock data set of Shangguan et al. (2016) has large uncertainties, and therefore it was not applied spatially. Porosity of Icelandic basalt decreases in general horizontally with the distance from the spreading zone and vertically with depth (Flóvenz and Saemundsson, 1993). However, owing to the unavailability of such measurements spatially for Iceland, constant bedrock porosity of 8% was assumed, which represents average porosity of basaltic lavas in Iceland (Stefánsson et al., 1997).

Model Initialization, Implementation, and Sensitivity

The model was initialized using the same procedure as described in Westermann et al. (2013). The first five hydrological years (1960–1964) were used to derive the initial temperature profile. Some uncertainties are connected with the initial temperature profile since, i.e., the derivation of the initial profile is based on the equilibrium permafrost model and TTOP is set as surface temperature. Nevertheless, the initial temperature profile impacts primarily the beginning period of the main run (Westermann et al., 2013).

The CryoGrid 2 was implemented for Iceland for the period 01.09.1959–31.12.2016 at a spatial grid resolution of 1 km. In the windy climate of Iceland, snow drift tends to preferentially accumulate snow in gullies, depressions and other small-scale irregularities in the landscape. The effect of this redistribution is clearly seen in satellite images and MODIS images from the spring where the open landscape becomes snow-free long before areas where drift snow tends to accumulate. To account for sub-grid snow variation we ran the model for three snow depth scenarios (50, 100, and 150% of modelled precipitation). The low-snow-depth scenario, which is intended to represent the open, unconfined terrain, was run by reducing the snow depth with an average percentage of precipitation calibrated for the boreholes, which are located at windy sites, i.e., 50% of precipitation. The second run, which represents areas where erosion and accumulation of snow roughly balance, was processed for an average precipitation for a grid cell (100% precipitation), whereas the third run with 150% precipitation is intended to represent areas with substantial accumulation of drift snow, such as relatively gentle leeside slopes, as well as creeks and depressions near the paths of rivers and brooks. Value of 150% precipitation was chosen in order to satisfy conservation of mass within each grid cell, i.e., snow removed from the areas represented by the 50% precipitation scenario is deposited in the areas represented by the 150% precipitation run.

Model sensitivity was conducted by changing the site-specific parameters for the borehole sites. In the model parameters, snow thermal conductivity is a function of snow density. In order to separate its contribution to the model uncertainty, it was tested independently of snow density and vice versa. The range of thermal conductivity for snow density of 300–450 kg m^{-3} mentioned in Sturm et al. (1997) was applied in the tests.

Validation Data Sets

Ground Temperature Measurements

The simulated ground temperatures were evaluated quantitatively for the borehole sites, located at the previously presumed lower limit of mountain permafrost in Iceland at ∼900 m a.s.l. (Etzelmüller et al., 2007). The measurement accuracies vary between 0.01°C and 0.2°C. Boreholes are located on flat and open sites with almost no vegetation. More detailed information about the boreholes can be found in Farbrot et al. (2007b).

Inventories of Permafrost Landforms

Research about landforms indicative of permafrost in Iceland, can be grouped into two quite distinct branches, focusing on different geographical areas: (1) studies about landforms in the widespread mountain permafrost area, represented by active rock glaciers and stable ice-cored moraines, and (2) investigations about isolated and sporadic permafrost landforms, i.e., palsas.

Active rock glaciers are "the visible expression of steady-state creep of ice-supersaturated mountain permafrost bodies in unconsolidated materials" (Barsch, 1996). The distribution of rock glaciers in central north Iceland (Tröllaskagi) was inventoried by Lilleøren et al. (2013) and Guðmundsson (2000). The intact (active and inactive) rock-glaciers are dominated by moraine-derived landforms, caused by the extensive local glaciation in this region (Lilleøren et al., 2013). Stable ice-cored moraines have been defined as permafrost landform, based on discussions in e.g., Etzelmüller and Hagen (2005). The permafrost landform inventory (Lilleøren et al., 2013) indicated that 87 ice-cored moraines exist in the Tröllaskagi area. These landforms are situated at the same elevations as talus and moraine-derived rock glaciers, and therefore they can be used as reliable permafrost indicators in central north Iceland (Lilleøren et al., 2013).

Palsas are peaty mounds with a permafrost nucleus, composed of frozen peat and mineral soil, and dimensions of up to >100 m in width and >10 m in height (Seppälä and Kujala, 2009). In Iceland, palsas are mainly found in the central parts of the Highlands southeast and north of the Hofsjökull glacier, between Langjökull and Hofsjökull glaciers, and in the highlands of Eastern Iceland (Ottósson et al., 2016). The modelled permafrost extent was validated visually based on the extent of palsas as delineated on the map of habitat types in Iceland (scale 1:25 000) from the Icelandic Institute of Natural History (Ottósson et al., 2016). The map was prepared based on data collected after 1999. According to the map, palsas in Iceland cover an area of c. 93 km^2.

RESULTS

Model Validation

Validation of Snow Distribution and Depth

For most years and stations, the timing, and measured snow depth is similar to the simulated values in one of the precipitation scenarios. Four examples out of analysed 126 combinations of stations and years are shown in **Figure 3**. Over- and underestimation errors are apparent in some cases, where the deviations between measurements and simulations can be as large as 1 m.

The temporal pattern of the modelled snow extent agrees well with the observed snow extent (**Figure 4**; **Supplementary Video 1**). Nevertheless, the SWE (*seNorge*) model has sometimes demonstrated a tendency to: (1) overestimate SWE in west Iceland in April–May, (2) underestimate SWE in eastern Iceland in April–June, and (3) underestimate SWE in the Tröllaskagi peninsula and its vicinity, along with north-western Iceland in June–July.

Permafrost Temperatures

Comparison of the modelled mean annual ground temperature at depths of 1 and 2 m with the ground temperature measurements is shown in **Figure 5**. We use the results from the 50% precipitation run, which is the closest precipitation fraction to the site-specific precipitation fractions used in the model calibration. The results indicate an RMSE of maximum 0.54°C and a mean error of maximum 0.52°C at both 1 and 2 m depths for all the boreholes.

Permafrost Landforms

Figure 6 illustrates visual validation of the modelled permafrost extent and palsa distribution in Iceland. In general, there is a good agreement between the reproduced permafrost and palsa occurrence both in west-central and eastern Iceland. However, some palsa areas south and west of Hofsjökull are not modelled as permafrost. In these regions, however, palsas and peat plateaus are often smaller than a 1-km^2 grid cell.

Most of the active glacier- and talus-derived rock glaciers, together with the ice-cored moraines are reproduced as permafrost areas (**Figure 7**); however, some of the landforms in the northern Tröllaskagi, especially ice-cored moraines, are not within the modelled permafrost cells. The comparison indicates that many of the active permafrost landforms are related to areas where permafrost may form even when 150% precipitation is applied in the CryoGrid 2 model, which results from the relatively cold climate in the Tröllaskagi area.

Permafrost Distribution and Temperatures

According to the 50% precipitation run, permafrost occurs in large parts of northern and central Iceland, such as Norður-Múlasýsla in the Eastern Region, together with the Northwestern and Northeastern Regions of Iceland (**Figure 8**; **Supplementary Videos 2–4**). In the run with the average precipitation, permafrost extent is substantially reduced. Permafrost areas are modelled in the Tröllaskagi peninsula and the adjacent southern areas, the western part of Norður-Múlasýsla, and regions north of Langjökull and Vatnajökull. The last run with 150% precipitation shows the most limited permafrost occurrence in Iceland, primarily in the Tröllaskagi peninsula and other high-mountain areas on the island. According to the runs, the coldest permafrost

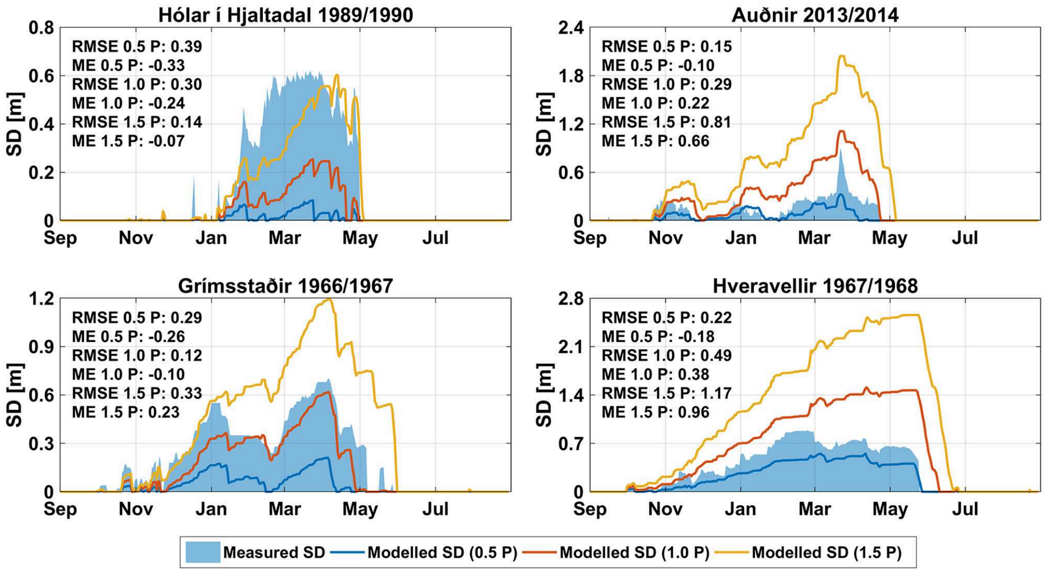

FIGURE 3 | Examples of measured and modelled daily SD (snow depth) for the three precipitation scenarios: 0.5P-50% precipitation, 1.0P-100% precipitation, 1.5P-150% precipitation. SD was obtained using the *seNorge* SWE sub-model (Saloranta, 2012) and snow density of 350 kg m^{-3}. RMSE-root mean square error, ME-mean error.

in Iceland can be found in the Tröllaskagi peninsula and its vicinity. The modelled ground temperatures increased in this region between the decades of the 1980s and 2000s (**Figure 8**).

Mean temperature at the top of permafrost (TTOP) was calculated for every snow depth case (**Supplementary Videos 5–7**) and based on the areas with TTOP at or below 0°C we present modelled permafrost extent for the three snow depth cases in **Figure 9** and **Supplementary Video 8**. The model outcome shows the largest permafrost extent in the period 1980–1989 in the 50 and 100% precipitation runs and in the 1970–1979 in the 150% precipitation run (**Figure 9**), presumably as a result of the climate deterioration in Iceland until 1980s (e.g., Hanna et al., 2004). In these periods permafrost aggraded up to depths of 1–5 m. These findings are in accordance with the observations by Priesnitz and Schunke (1978) between 1970 and 1976 who expected permafrost aggradation in palsa areas in Iceland.

The 50% precipitation run indicates ~3–5 and 8–15 times more cells with permafrost in comparison to the 100 and 150% precipitation runs, respectively, within the same decades (**Table 2**). The difference in the number of cells with modelled permafrost is less pronounced for 100 and 150% precipitation cases, with ~2–3 times more cells in the 100% precipitation run. The number of modelled permafrost cells decreases in the subsequent time periods, with the lowest number of cells with permafrost in the period 2010–2016, when it is reduced by 34, 56, and 49% for the 50, 100, and 150% precipitation runs, respectively, in comparison to the period 1980–1989 (**Table 2**).

Assuming equal contribution of each precipitation scenario to a grid cell, the estimated permafrost area for the period 1980–1989 is c. 11 495 km^2 (~11% of Iceland's land area), and c. 6 936 km^2 for the period 2010–2016 (~7% of Iceland's land area). This implies a reduction of the permafrost area of c. 40% in Iceland between these two periods. We note, however, that the snow distributions within grid cells are unknown, and these numbers are only very rough estimates of the permafrost area in Iceland.

Table 2 presents the statistics for the bare, vegetated and all soil types, with the total number of cells modelled as permafrost, as well as average and standard deviation of TTOP and average elevation for the same cells. The reproduced permafrost underlies predominantly Vitrisols and Leptosols, with ~1,000–3,500 more cells indicating permafrost than for Histosols, Andosols, and Cryosols for all the runs and periods. This is probably related to the fact that the bare soil classes tend to occur at higher elevation (mean c. 580 m a.s.l.) than the vegetated classes (mean c. 300 m a.s.l.). Mean elevation of the permafrost area for the two classes also varies accordingly, where permafrost cells with Vitrisols and Leptosols have ~250–350 m higher mean elevation than cells with the vegetated soil types. The modelled average temperatures at the top of permafrost are relatively high, with all the values above ~−0.9°C after the first 10 years of simulations.

Figure 10 shows the modelled permafrost distribution at 10 m depth, where the number of cells that show permafrost

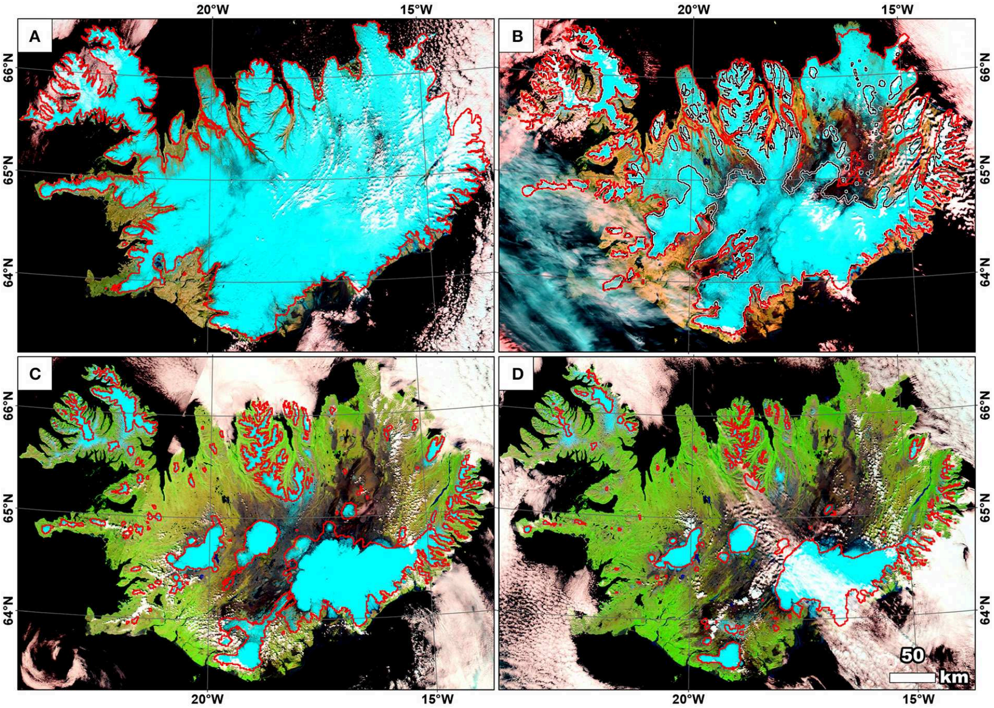

FIGURE 4 | Validation of snow extent in the year 2000: **(A)** 12.04.2000; **(B)**. Red line: 19.05.2000, Black line with a white border: 26.05.2000; **(C)** 23.06.2000; **(D)** 10.07.2000. Backgrounds: MODIS Aqua/Terra FCCs 721 from the same dates as the red lines. Image courtesy of NASA Worldview. For days when there was large disagreement between observed and modelled snow extent (red lines), a black line with a white border was added for a week before or after if the correspondence between modelled and observed snow extent improved.

is substantially reduced in comparison to the permafrost reproduced at 2 m depth (**Figure 8**) or TTOP (**Figure 9**). Thus, the CryoGrid 2 model indicates mostly shallow permafrost in Iceland, which is likely a consequence of the high geothermal heat flux and generally warm permafrost, along with probably too little water content for the soil/bedrock. Only minor variations in reproduced permafrost can be observed through time at 10 m depth (**Figure 10**). We note, however, that the long-term climate signals, e.g., the cooling during the Little Ice Age, are not captured in our simulations; hence, the model likely overestimates deep ground temperatures.

Lower limits of permafrost (LLP) in the northern part of Iceland along a chosen transect are illustrated in **Figure 11**. The model produces an increase of the LLP from north to south, where absolute values depend on the precipitation assumptions (**Figure 11**). They increase from around 600–900 m in the north to around 800–1,000 m a.s.l. in the south.

Sensitivity Tests for Borehole Locations

Sensitivity of the model to uncertainties in the thermal properties of snow and subsurface for the borehole sites is shown in **Table 3**. Volumetric mineral and water content in the middle layer, depth to bedrock, and bedrock porosity have minor importance (≤ 0.1°C) for the near-surface ground temperatures. Increase in mineral content in the upper layer or thermal conductivity of the mineral fraction allows for greater heat penetration in summer, resulting in higher mean ground temperatures, even up to 0.3°C higher than the default parameters. Higher water contents lead to longer zero curtain effect, leading to ground temperature being modelled up to 1.3°C warmer for 30% vol. water in comparison to 1% vol. water. Snow density influences both snow depth and specific effective volumetric heat capacity of snow, and its increase yields up to 0.8°C colder ground temperatures. Larger snow thermal conductivity causes more effective heat loss during winter, which results in much lower ground temperatures. The differences in the modelled average ground temperatures between the runs with the lowest and highest values of the thermal conductivity of snow are ~2°C. The impact of the precipitation fraction on the modelled ground temperatures is somehow more complicated, because apart from snow depth, also snow timing is involved. Ground temperatures often increase for larger precipitation fraction, e.g., at Sauðafell and Hágöngur;

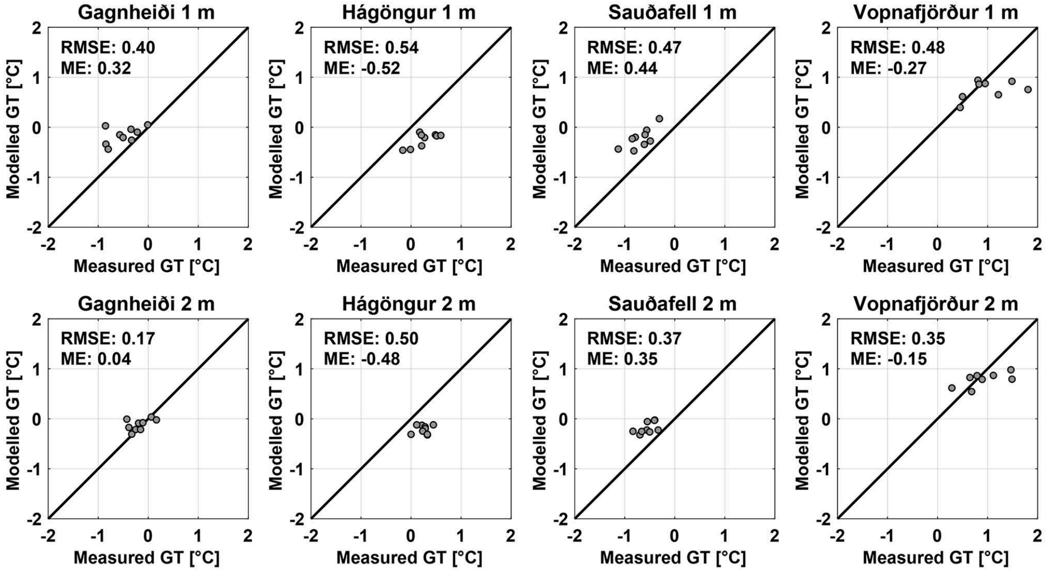

FIGURE 5 | Yearly validation of the modelled ground temperature (GT) at 1 and 2 m depth for the borehole locations. In these simulations, precipitation fraction of 50% was used. RMSE-root mean square error, ME-mean error.

however, prolonged snow cover leads sometimes to colder ground temperature, e.g., at Gagnheiði and Vopnafjörður when comparing 100 and 150% precipitation cases. The deviations in the simulated ground temperature between the lowest and highest precipitation runs are up to ∼1.6°C. The sensitivity tests indicate thus the following tested parameters to be the major factors (sorted by their importance) influencing the modelled ground temperature: (1) thermal conductivity of the snow, (2) precipitation fraction, (3) water content in the upper layer, (4) snow density, mineral content in the upper layer and thermal conductivity of the mineral fraction.

DISCUSSION

Uncertainties and Limitations

Spatial modelling over larger areas and over longer periods always will lead to uncertainties related to the chosen spatial and temporal resolution, affecting forcing data and thus the results. The chosen 1 km^2 resolution is fine in relation to most climate models; however, it is too coarse to address processes related to: (1) topography (e.g., detailed assessment of permafrost in slopes, e.g., Noetzli et al., 2007; Magnin et al., 2017); (2) convective heat transfer in volcanic rift zones (Flóvenz and Saemundsson, 1993), (3) convective heat transfer in block ground material (Juliussen and Humlum, 2008; Wicky and Hauck, 2017) or (4) temporal and spatial variations in soil water content (Marmy et al., 2013; Scherler et al., 2013). Some uncertainties of this study are, however, related to site-specific conditions, problems with input data sets or model limitations, and are therefore discussed in a closer context. In general, probability of permafrost occurrence is relatively high in grid cells where permafrost is modelled in the scenario with the deepest snow cover (150% precipitation fraction), especially because less than average snow depths (<100% precipitation fraction in our study) likely dominate in mountain areas (e.g., Gisnås et al., 2014).

Boundary Conditions

The CryoGrid 2 model was forced with a weekly-averaged data set of gridded daily temperature in Iceland derived by interpolating data from sparse stations, which are mainly located along the coast (Crochet and Jóhannesson, 2011). The quality of the data set is thus best at lower elevations where the stations are denser; however, the establishment of the automatic stations in the early 1990s and deployment of stations to higher elevations in the 2000s improved the data set. The gridded data set captures spatial air temperature variations exclusively due to elevation and neglects other factors such as e.g., distance to the coast or temperature inversions (Crochet and Jóhannesson, 2011). Apart from the effect of elevation, the mean summer temperature increases towards the interior of Iceland, whereas the mean winter temperature decreases with increasing distance to the shore (Einarsson, 1984).

Precipitation and Snow Depth

Snow depth was derived from a degree–day SWE model using two precipitation data sets and constant snow density. Between

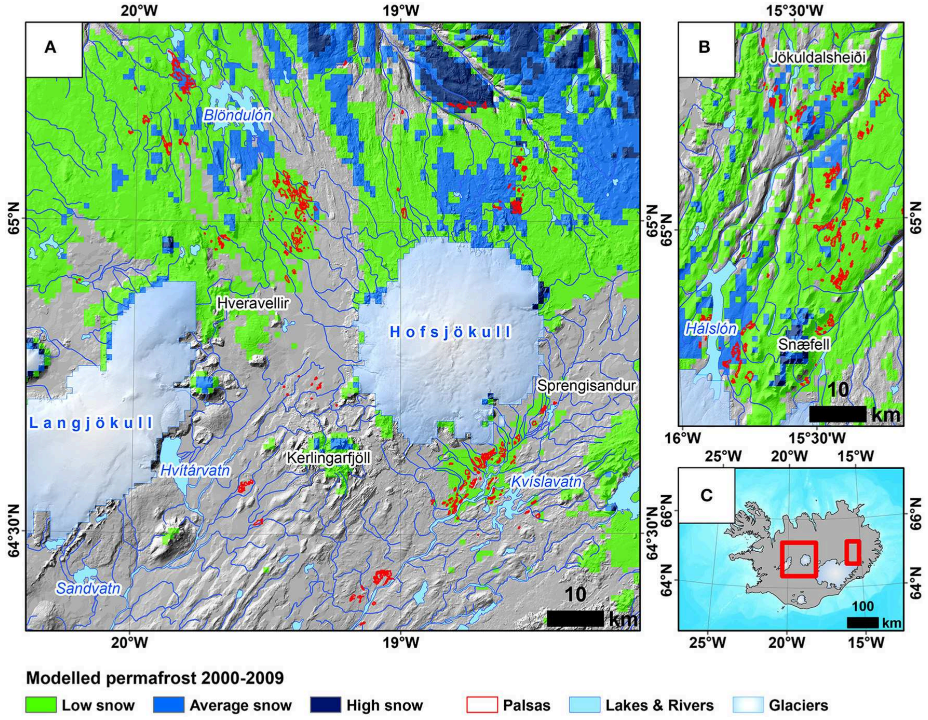

FIGURE 6 | Validation of the permafrost model simulations for the period 2000–2009 based on the palsa distribution in **(A)** west-central Iceland, **(B)** eastern Iceland. **(C)** Inset map showing the location of the west-central **(A)** and eastern **(B)** palsa areas. Modelled permafrost based on TTOP is shown (see **Figure 9** for details). Palsa distribution data from the Icelandic Institute of Natural History. Map data from NLSI.

9/1959 and 12/1979, we used precipitation data set derived from the linear theory model (LT-model) of orographic precipitation described in Crochet and Jóhannesson (2011). Evaluation of daily precipitation simulated by LT-model indicated that this model has flaws related to a misidentification of the wet and dry regions, errors in the model parameters, and large-scale wind field, yielding over- or underestimated daily precipitation, especially severe on the windward side of the mountains (Crochet et al., 2007). In 1980–2016, the *SWE* model was forced with precipitation data set created using the HARMONIE–AROME model. Validation showed that the model produced more accurate precipitation estimates than the LT-model (Nawri et al., 2017). However, the HARMONIE–AROME model tended to underestimate daily precipitation during winter (DJF) due to underestimation of extreme precipitation events and showed a frequent overestimation of daily precipitation (Nawri et al., 2017). Furthermore, the HARMONIE–AROME model has a resolution of 2.5 km, hence it may fail to predict weather extremes smaller than that scale, and precipitation was linearly interpolated to a 1 km grid, introducing possible errors. The inconsistencies between the two data sets (**Supplementary Figure 1**) could have affected the modelled ground temperatures during the 1980s and possibly 1990s.

Snow depth data was obtained from a degree-day model using spatially and temporally constant parameters, except for degree–day melt and refreezing factors, which varied seasonally. The employed single-layer snow scheme is simple, and thus its ability to account for internal snow processes and the energy balance components is limited. The more physically-based approaches to snow modelling with multiple snow layers would likely yield more accurate snow-depth estimates (e.g., the detailed snowpack scheme Crocus; Vionnet et al., 2012); however, they are often impractical. The merits of the applied algorithm are therefore its simplicity, fast runtime and low data requirements, with the disadvantages of errors due to the simple formulation (e.g., Hock, 2003; Kokkonen et al., 2006). One major factor is that we applied a constant snow density of 350 kg m^{-3}, even though snow densities of up to 400–450 kg m^{-3} were measured in north Iceland for a stable mid-winter snow cover (Haraldsdóttir et al., 2001), and varies elsewhere (Sigurðsson and Jóhannesson, 2014). The seNorge model includes also a second submodule that yields snow depth and snowpack density (Saloranta, 2012).

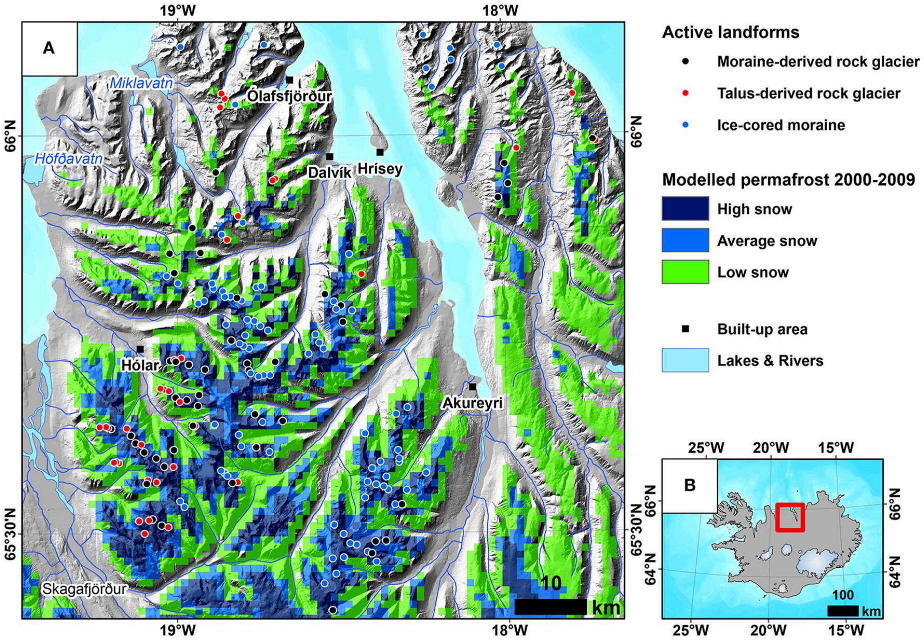

FIGURE 7 | (A) Outcome of the permafrost model simulations for the period 2000–2009 in comparison to the distribution of the active permafrost landforms, such as active moraine- and talus-derived rock glaciers, along with ice-cored moraines, as inventoried by Lilleøren et al. (2013). **(B)** Inset map. Modelled permafrost based on TTOP is shown (see **Figure 9** for details). Map data from NLSI.

However, this submodule was not applied in this study since it considers snow compaction only as a result of the snow weight, overlooking snow compaction resulting from wind drift, which is probably the main cause for snow compaction in environments like Iceland. The snow depth measurements conducted at permafrost monitoring sites in southern Norway (Westermann et al., 2013) showed that snow density did not increase significantly from the snowpack surface to the snowpack base, likely because the wind compaction dominates. Similarly, in case of Iceland, the existing measurements of snow density do not necessarily indicate an increase towards the snowpack bottom (Sigurðsson and Jóhannesson, 2014). Other processes, such as e.g., sublimation were neglected in the snow model. It is emphasised earlier that the employment of a more sophisticated snow model does not guarantee better results in Iceland, since the main limitation is the lack of accurate snow observations in this region (Haraldsdóttir et al., 2001).

Furthermore, snow redistribution by wind is difficult to account for in a regional model, since there is a substantial sub-grid variability in snow depths within a 1-km spatial grid. This issue has been addressed earlier in a more simple modelling approach using statistical distributions of snow depths within grid cells, so the ensemble approach with many model realizations could be implemented (Westermann et al., 2015b; Gisnås et al., 2017). Such procedures could potentially be implemented in a transient permafrost model. The validation data would, however, require the measurements of the snow depths within grid cells, and such data is unavailable for Iceland. The representativity of the chosen precipitation factors for a grid cell is thus challenging to quantify without the mentioned data. Therefore, only a simple weighting using factors of 1/3 for each scenario was applied to calculate the total permafrost area in Iceland.

Model Parameters

Thermal *properties of subsurface materials* were calculated according to volumetric fractions of soil constituents assigned based on the soil map of Iceland (Arnalds, 2008, 2015). It is obvious that the map is a representation of major soil types in Iceland, and soil or sediment heterogeneity on a sub-pixel scale is neglected, along with the lack of detailed knowledge of sediment thicknesses. Surficial geologic maps are often used in transient permafrost models (e.g., Jafarov et al., 2012; Westermann et al., 2013) to specify the subsurface layers, which is a more suitable representation of the variation in stratigraphy of the deeper ground layers. Unfortunately, no geomorphological map of Iceland has been published, hence only the soil map could be employed. The sensitivity test also showed that variations in

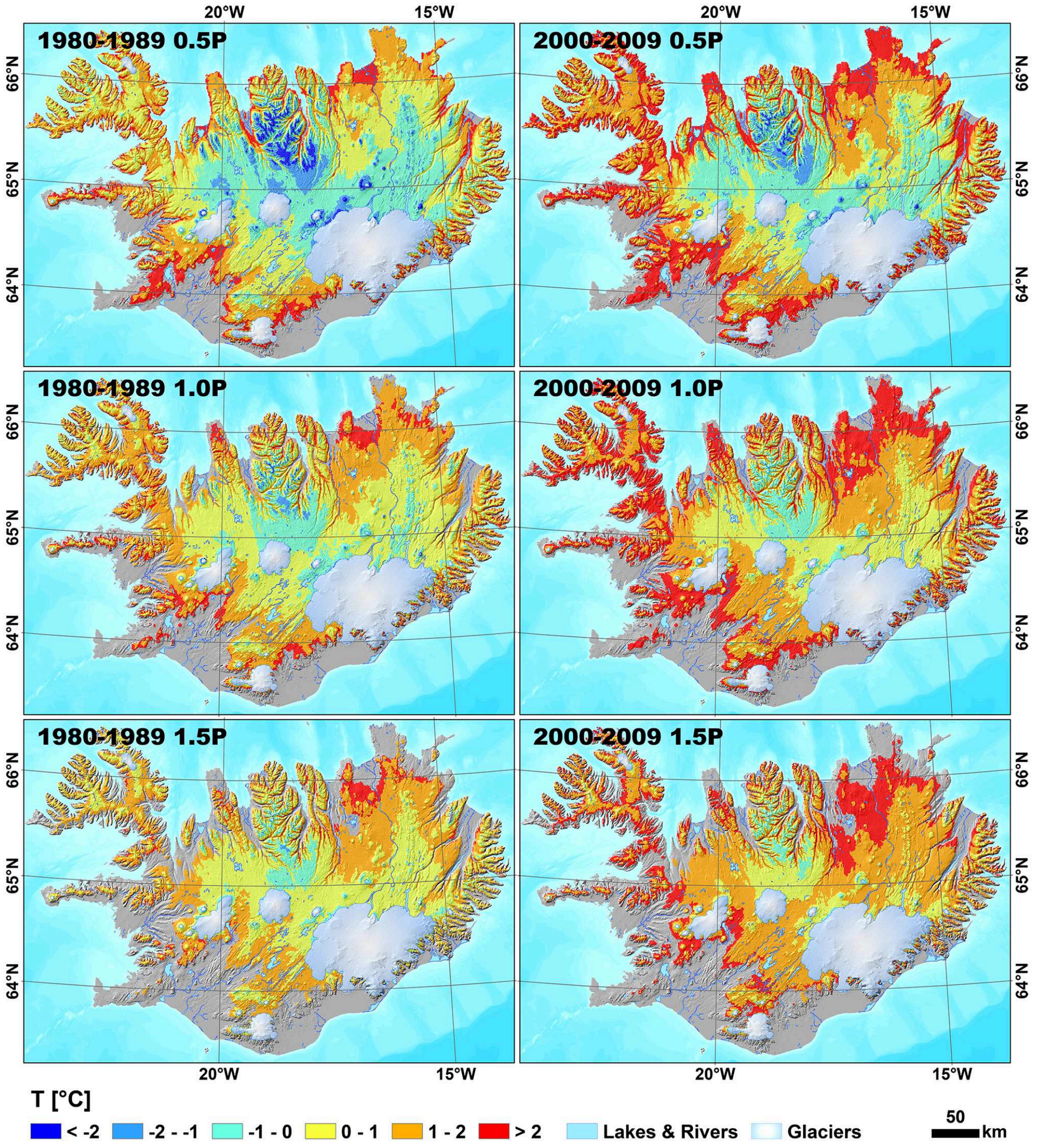

FIGURE 8 | Distribution of the simulated average ground temperature (T) at 2 m depth in the periods 1980–1989 and 2000–2009 for the three precipitation cases: 0.5P-50% precipitation, 1.0P-100% precipitation, 1.5P-150% precipitation. Permafrost cells are displayed in blue hues. Map data from NLSI.

ground properties are less important than other factors, e.g., in relation to snow. There are also some uncertainties connected with the bedrock porosity, depth to bedrock, and bedrock conductivity. We used constant values for thermal conductivity and porosity of the basaltic rock (Pálmason et al., 1979; Flóvenz and Saemundsson, 1993; Hjartarson, 2015), knowing that the influence of bedrock porosity and depth to bedrock has only marginal impact on the 1 and 2 m ground temperatures for the borehole locations. Nevertheless, these variables have presumably more pronounced effect on the deeper ground temperatures

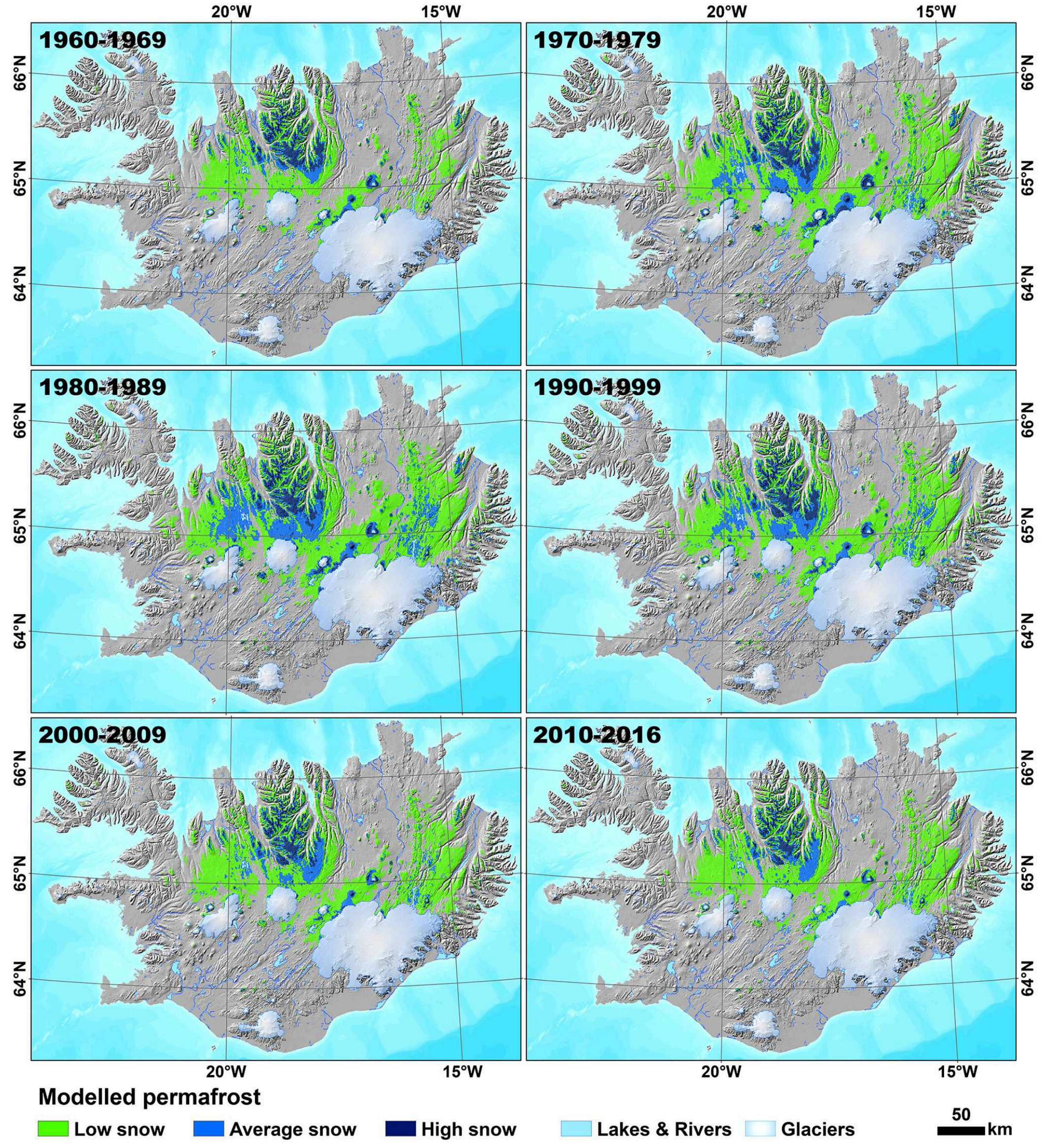

FIGURE 9 | Spatio-temporal evolution of the modelled permafrost extent based on TTOP at or below 0°C in 10 consecutive years for the three snow depth scenarios: "Low snow" represents permafrost reproduced in 50% precipitation scenario, "Average snow" represents permafrost reproduced in 50 and 100% precipitation scenarios, and "High snow" represents permafrost reproduced in all precipitation scenarios. Map data from NLSI.

or within areas of exposed bedrock. There is no typical bedrock class in the classes of the ground stratigraphy used in this study.

Small topographic features and vegetation both influence snow redistribution, acting as snow traps (Pomeroy et al., 2006; Jafarov et al., 2018). The role of vegetation is, however, limited

TABLE 2 | Total number of cells with temperature at the top of permafrost (TTOP) <0°C for every precipitation case, average TTOP and its standard deviation (STD), together with average elevation (Z) and its standard deviation of cells with TTOP < 0°C.

Soil classes	Period	Number of grid cells			Mean ± STD TTOP [°C]			Mean ± STD Z [m a.s.l.]		
		0.5P	1.0P	1.5P	0.5P	1.0P	1.5P	0.5P	1.0P	1.5P
Vitrisols and Leptosols	1960–1969	7,633	2,770	1,483	−1.33 ± 0.85	−1.07 ± 0.61	−0.80 ± 0.48	905 ± 132	1027 ± 104	1067 ± 86
	1970–1979	12,179	4,546	2,296	−0.83 ± 0.72	−0.63 ± 0.49	−0.51 ± 0.35	848 ± 140	970 ± 122	1033 ± 97
	1980–1989	14,013	4,914	1,944	−0.87 ± 0.72	−0.66 ± 0.49	−0.57 ± 0.40	817 ± 155	945 ± 139	1038 ± 102
	1990–1999	11,900	4,026	1,709	−0.77 ± 0.65	−0.54 ± 0.39	−0.40 ± 0.24	846 ± 145	970 ± 133	1043 ± 99
	2000–2009	9,918	2,963	1,136	−0.58 ± 0.58	−0.38 ± 0.35	−0.32 ± 0.28	874 ± 136	1007 ± 120	1079 ± 87
	2010–2016	8,695	2,489	961	−0.50 ± 0.54	−0.30 ± 0.32	−0.26 ± 0.29	890 ± 135	1028 ± 110	1092 ± 82
Histosols, Andosols, and Cryosols	1960–1969	6,084	771	139	−0.65 ± 0.45	−0.48 ± 0.37	−0.34 ± 0.24	592 ± 123	688 ± 139	825 ± 86
	1970–1979	9,866	1,636	204	−0.37 ± 0.35	−0.18 ± 0.21	−0.17 ± 0.13	564 ± 129	663 ± 126	799 ± 106
	1980–1989	10,672	2,724	217	−0.52 ± 0.45	−0.21 ± 0.25	−0.26 ± 0.20	548 ± 135	602 ± 126	758 ± 113
	1990–1999	9,406	2,037	226	−0.40 ± 0.35	−0.17 ± 0.20	−0.17 ± 0.13	566 ± 128	631 ± 124	772 ± 111
	2000–2009	8,372	1,140	172	−0.28 ± 0.27	−0.17 ± 0.20	−0.16 ± 0.13	580 ± 121	673 ± 125	767 ± 108
	2010–2016	7,694	834	136	−0.20 ± 0.23	−0.12 ± 0.15	−0.09 ± 0.05	588 ± 118	694 ± 123	773 ± 102
All	1960–1969	13,717	3,541	1,622	−1.03 ± 0.78	−0.94 ± 0.62	−0.76 ± 0.48	766 ± 202	953 ± 180	1047 ± 109
	1970–1979	22,045	6,182	2,500	−0.62 ± 0.63	−0.51 ± 0.47	−0.49 ± 0.35	721 ± 196	889 ± 183	1014 ± 117
	1980–1989	24,685	7,638	2,161	−0.72 ± 0.64	−0.50 ± 0.47	−0.54 ± 0.40	701 ± 198	822 ± 213	1010 ± 133
	1990–1999	21,306	6,063	1,935	−0.61 ± 0.57	−0.41 ± 0.38	−0.37 ± 0.24	722 ± 196	856 ± 206	1011 ± 133
	2000–2009	18,290	4,103	1,308	−0.44 ± 0.48	−0.33 ± 0.33	−0.30 ± 0.27	739 ± 196	914 ± 193	1038 ± 139
	2010–2016	16,389	3,323	1,097	−0.36 ± 0.45	−0.25 ± 0.30	−0.24 ± 0.28	748 ± 197	944 ± 184	1053 ± 135

We note that in the period 1960–1969 the results seem to be strongly influenced by the model behaviour in its initialization period.

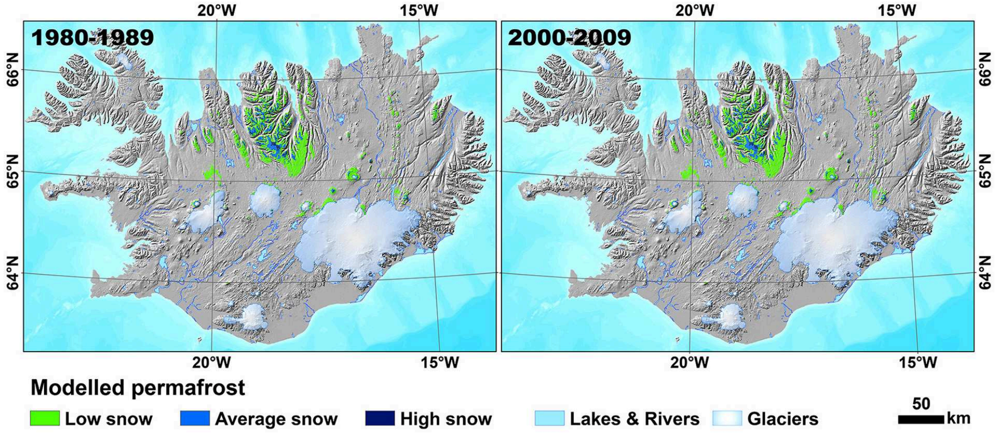

FIGURE 10 | Permafrost extent over the periods 1980–1989 and 2000–2009 based on cells that indicated ground temperature at 10 m depth at or below 0°C in 10 consecutive years for the three snow depth scenarios: "Low snow" represents permafrost reproduced in 50% precipitation scenario, "Average snow" represents permafrost reproduced in 50 and 100% precipitation scenarios, and "High snow" represents permafrost reproduced in all precipitation scenarios. Results for the other periods reveal similar permafrost extent at this depth. Map data from NLSI.

in Iceland, since areas at higher elevations are commonly barren or half vegetated (Ottósson et al., 2016). The heterogeneous snow cover affect furthermore the soil moisture and thus the ground thermal regime. The model simulations could be further improved by running multiple model realizations taking into consideration sub-grid variability in the surface topography and the subsurface stratigraphy, as proposed by Westermann et al. (2017).

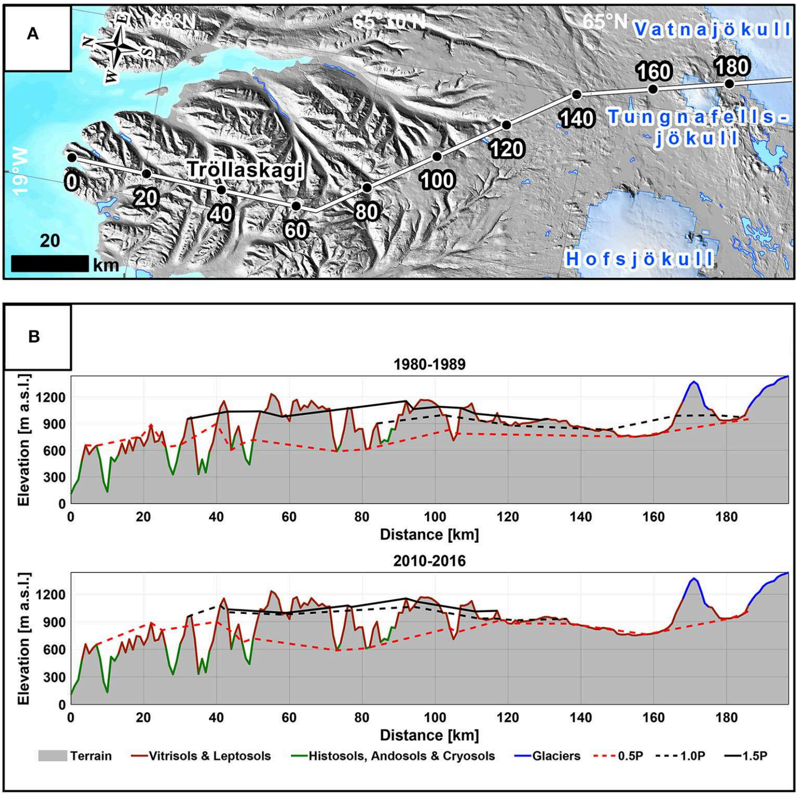

FIGURE 11 | **(A)** Transect from the northern part of Tröllaskagi to the north of Vatnajökull, similar to the transect in Etzelmüller et al. (2007). Numbers indicate distance along the transect in km. Map data from NLSI. **(B)** Lower limits of permafrost along the transect shown in A for the three precipitation scenarios: 0.5P-50% precipitation, 1.0P-100% precipitation, 1.5P-150% precipitation, in the periods 1980–1989 and 2010–2016.

Model Performance

Validation

The validation indicated quite good results with maximum RMSE of 0.54°C and a mean error of maximum 0.52°C for all the borehole locations. The model performance is similar to the performance reported in other studies employing spatially distributed transient permafrost models (Jafarov et al., 2012; Westermann et al., 2013, 2017). Most palsas are modelled as permafrost areas according to the CryoGrid 2 runs (**Figure 6**); however, the consistency between the modelled permafrost distribution and palsas does not necessarily indicate that the palsa areas are reproduced as permafrost related specifically to these landforms. The uncertainties are mainly connected with the chosen ground stratigraphy and the precipitation fractions, with the latter having presumably the largest influence. Previous investigations of palsas in Iceland indicate that their organic content is relatively low due to the accumulation of wind-transported sediments (Saemundsson et al., 2012) and peat cover is generally thin (Friedman et al., 1971). Thermal offsets might, therefore, not be the most crucial factor for palsa formation in Iceland. Snow removal by wind from the tops of palsas has been previously recognized as an important factor for growth and maintenance of palsas (e.g., Seppälä, 1982). It is uncertain whether the 50% precipitation run is sufficient to account for the limited snow cover in these areas. The precipitation fraction should be probably further reduced to properly reproduce palsa areas. However, short and relatively cold summers might also contribute to the existence of palsas in Iceland (Friedman et al., 1971; Saemundsson et al., 2012). Furthermore, we note that there is a scale mismatch between 1-km^2 model cells and the landforms that are local features, usually covering an area of <1 km^2. Nevertheless, we emphasize that it is feasible to reproduce palsa permafrost even in a simple one-dimensional model at 1 km^2 scale,

TABLE 3 | Sensitivity of the modelled mean ground temperature at depths of 1 and 2 m to uncertainties in the chosen subsurface and snow parameters in the period 1.09.2004–31.08.2006.

Measured/modelled parameters	**Average ground temperature [°C]**							
	Gagnheiði		**Sauðafell**		**Hágöngur**		**Vopnafjörður**	
	1 m	**2 m**	**1 m**	**2 m**	**1 m**	**2 m**	**1 m**	**2 m**
Measured	−0.58	−0.33	−0.78	−0.68	0.14	0.12	0.89	0.96
VOLUMETRIC MINERAL CONTENT IN THE UPPER LAYER								
0.50	−0.25	−0.19	−0.46	−0.28	−0.43	−0.26	0.69	0.67
0.60 (D)	−0.15	−0.12	−0.40	−0.26	−0.37	−0.24	0.86	0.84
0.70	−0.05	−0.07	−0.35	−0.24	−0.32	−0.22	1.00	0.98
VOLUMETRIC WATER CONTENT IN THE UPPER LAYER								
0.01	−0.50	−0.45	−0.62	−0.49	−0.60	−0.45	0.23	0.13
0.04 (D)	−0.15	−0.12	−0.40	−0.26	−0.37	−0.24	0.86	0.84
0.30	0.71	0.74	0.06	0.19	0.01	−0.05	1.39	1.40
VOLUMETRIC MINERAL (θ_m) AND WATER CONTENTS (θ_W) IN THE MIDDLE LAYER								
θ_m= 0.50 & $\theta_W = 0.50$	−0.15	−0.12	−0.40	−0.25	−0.37	−0.24	0.87	0.84
θ_m= 0.60 & $\theta_W = 0.40$	−0.15	−0.12	−0.40	−0.25	−0.37	−0.24	0.87	0.84
θ_m= 0.80 & $\theta_W = 0.20$ (D)	−0.15	−0.12	−0.40	−0.26	−0.37	−0.24	0.86	0.84
DEPTH TO BEDROCK								
5 m	−0.15	−0.13	−0.40	−0.27	−0.38	−0.25	0.86	0.83
10 m (D)	−0.15	−0.12	−0.40	−0.26	−0.37	−0.24	0.86	0.84
15 m	−0.15	−0.12	−0.40	−0.26	−0.38	−0.25	0.86	0.84
BEDROCK POROSITY								
0.08 (D)	−0.15	−0.12	−0.40	−0.26	−0.37	−0.24	0.86	0.84
0.15	−0.15	−0.12	−0.40	−0.26	−0.38	−0.25	0.87	0.84
0.30	−0.15	−0.12	−0.40	−0.26	−0.37	−0.25	0.86	0.84
BEDROCK THERMAL CONDUCTIVITY								
2 W m^{-1} K^{-1} (D)	−0.15	−0.12	−0.40	−0.26	−0.37	−0.24	0.86	0.84
3 W m^{-1} K^{-1}	−0.02	−0.04	−0.33	−0.23	−0.29	−0.20	1.01	0.99
4 W m^{-1} K^{-1}	0.07	0.02	−0.28	−0.20	−0.23	−0.17	1.11	1.08
SNOW DENSITY								
300 kg m^{-3}	−0.04	−0.05	−0.33	−0.21	−0.29	−0.19	1.01	0.99
350 kg m^{-3} (D)	−0.15	−0.12	−0.40	−0.26	−0.37	−0.24	0.86	0.84
450 kg m^{-3}	−0.36	−0.32	−0.53	−0.37	−0.50	−0.34	0.38	0.20
SNOW THERMAL CONDUCTIVITY								
0.05 W m^{-1} K^{-1}	1.25	1.33	0.88	1.02	1.11	1.34	2.03	2.03
0.31 W m^{-1} K^{-1} (D)	−0.15	−0.12	−0.40	−0.26	−0.37	−0.24	0.86	0.84
0.50 W m^{-1} K^{-1}	−0.55	−0.49	−0.63	−0.47	−0.59	−0.41	0.21	0.08
PRECIPITATION FRACTION								
0.30	−0.81	−0.68	−0.79	−0.62	−0.67	−0.48	0.17	0.06
0.50 (D)	−0.15	−0.12	−0.40	−0.26	−0.37	−0.24	0.86	0.84
0.70	0.32	0.28	−0.09	−0.08	−0.22	−0.08	1.12	1.10
1.00	0.72	0.73	0.42	0.46	0.12	0.34	1.04	1.07
1.50	0.63	0.65	0.84	0.87	0.52	0.73	0.90	0.94

Measured mean ground temperature is also listed. D, default.

provided that the ground stratigraphy and snow forcing are tuned specifically for these landforms. Such approach has limitations, particularly it cannot yield a total area of permafrost in palsas or capture the true processes and factors for thermal stability of palsas that are more complex (Aas et al., 2019; Martin et al., 2019).

Active rock glaciers are reliable permafrost indicators (Barsch, 1996; Farbrot et al., 2007a; Berthling, 2011; Lilleøren et al., 2013). Comparison of the modelled permafrost extent with the distribution of the active permafrost landforms in the Tröllaskagi peninsula showed good agreement (**Figure 7**); nevertheless, some landforms in the north were outside of the modelled permafrost area. The disagreement may be explained by the location of these landforms at the northern-facing slopes receiving less direct solar radiation and having lower surface temperature than the gridded temperature used in the permafrost model. Lilleøren et al. (2013)

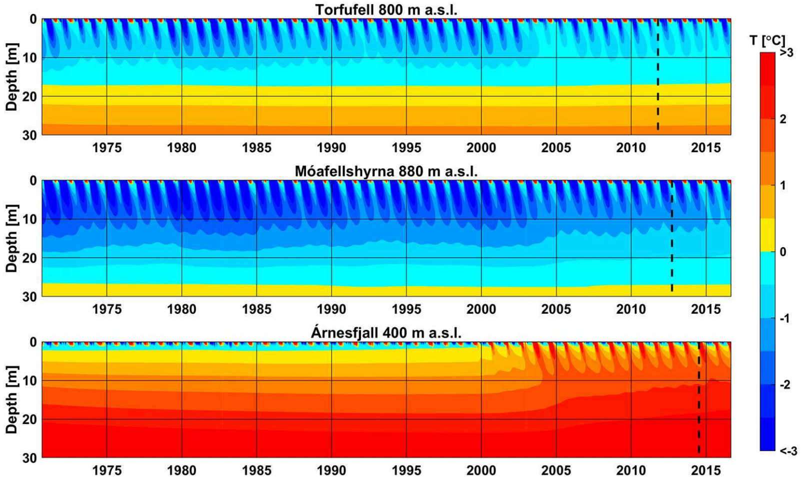

FIGURE 12 | Evolution of ground temperature for the source areas of the landslides with ice-cemented debris in the period 1970–2016. Lapse rate of 0.0065°C m^{-1} was used to correct for elevation differences between the elevation of the source areas and elevation of the gridded air temperature [following recommendations in Crochet and Jóhannesson (2011)]. To account for that the source areas are steep (45–60°) and do not accumulate much snow, precipitation fraction of 0.1 was applied in the modelling. Ground stratigraphy of Leptosols (see **Table 1**) was assumed. The dashed lines indicate dates of the landslides. Torfufell Mountain in north Iceland (14.10.2011) with a source area at an elevation of ∼800 m a.s.l., (2) Móafellshyrna Mountain in the Tröllaskagi area (20.09.2012) with a source area at an elevation of ∼880 m a.s.l., and (3) Árnesfjall Mountain in Westfjords (10.07.2014).

mentions also that the active permafrost-related landforms in the northern part of Tröllaskagi (∼400 m a.s.l.) occur at lower elevation than the landforms in the south (above 800–900 m a.s.l.), where aspect is recognized as one of the possible factors for the permafrost occurrence in the northern area. It is, however, also possible that the modelling period is too short to reproduce permafrost at lower elevations close to the coast and should be extended to e.g., the Little Ice Age, when the climate was colder.

Therefore, in general we find that the model results satisfactorily describe the distribution and thermal regime of permafrost in Iceland, given the shortcomings related to the 1 km^2 resolution. Permafrost extent was larger than permafrost reproduced in Etzelmüller et al. (2007). The model reproduced also the general characteristics of permafrost in Iceland, i.e., it indicated warm and mostly shallow permafrost, which is in accordance with previous conclusions by Farbrot et al. (2007b) on the dynamics of permafrost in Iceland. The Tröllaskagi area is the area with the highest likelihood of widespread permafrost in Iceland according to the runs, where permafrost was reproduced even in the snow-rich scenario. Permafrost was almost absent in south Iceland, with exception of e.g., high mountain ridges near Hekla and Torfajökull. Permafrost occurrence at Hekla has been previously reported by Farbrot (2007) and Kellerer-Pirklbauer et al. (2007), and CryoGrid 2 indicates permafrost in this area.

The multiple model realizations for the various snow depths within grid cells in the equilibrium permafrost models (e.g., Gisnås et al., 2017) allowed for the calculation of permafrost percentage and classification of each grid cell into a permafrost zone, such as continuous, discontinuous and sporadic permafrost. This required, however, e.g., 100 model realizations per grid cell and additional assumptions about the statistical snow distribution within grid cells. In our study, the number of runs per grid cell had to be reduced because of the large computational requirements in a transient permafrost model. The interpretation of our results with respect to the classic permafrost zonations is thus more difficult. Study on small-scale snow variability of Gisnås et al. (2014) was conducted in similar permafrost environments of southern Norway, and demonstrated that most of the snow heights within 1 km x 1 km area were less than average snow depth. The 100% precipitation run in our study corresponds to the average snow depth, hence the halved-precipitation run could be considered as the most frequent within a 1-km^2 grid cell. Furthermore, based on the right-skewed distributions of snow depth in wind-exposed mountains (See e.g., Gisnås et al., 2014, 2016), the frequency is lower for the average snow depth (100% precipitation run) and lowest for the 150% precipitation run. Therefore, most of the reproduced permafrost cells in Iceland is likely sporadic to maybe even discontinuous. Permafrost cells modelled in the 150% precipitation run can possibly represent the continuous permafrost zone.

Model Application

Regional permafrost models can have wide application and help discussions of topics within basic and applied science. Three examples are given below:

(1) Ground temperature is an important factor for understanding geomorphological processes, as emphasized in e.g., Berthling and Etzelmüller (2011) for periglacial geomorphology, or Etzelmüller and Hagen (2005), and Haeberli (2005) for the interaction of permafrost and glaciers.

(2) In steep mountain areas, permafrost influences slope stability (e.g., Gruber and Haeberli, 2007; Krautblatter et al., 2012). Even if the model is not designed to model high topographic heterogeneity, the transient changes in mountain areas can be resolved. In three landslides that occurred at in Iceland, ice-cemented blocks were observed within the deposits (Sæmundsson et al., 2014, 2018). Permafrost was still present at the time of the landslides, since the landslide deposits that were observed contained ice at the time of the slides. For instance, at Móafellshyrna site, blocks with pore-filling ice of size up to 12 m wide and 10 m high were found (Sæmundsson et al., 2018). To test the evolution of the ground thermal regime at the landslide sites we run our model using site-specific parameters (**Figure 12**). All the locations have or had permafrost according to the CryoGrid 2 runs; nevertheless, the Árnesfjall site had only very shallow permafrost of ∼1 m until 2000. Since the slopes of the source areas face north, the amount of direct solar radiation they receive is likely small, and it should have probably been accounted for. Furthermore, the modelling period might be too short to reproduce permafrost at Árnesfjall. The modelled ground temperatures illustrated in **Figure 12** show substantial overall ground temperature warming for the source locations of the landslides, especially since 2000–2005. At Torfufell and Móafellshyrna, the CryoGrid 2 model indicates a slight decrease in the depth of permafrost base around the dates of these landslides, whereas maximum thaw depths are relatively stable throughout the entire modelling period. Considering the model uncertainties, the decrease in the depth of permafrost base could be even more severe. Sæmundsson et al. (2018) argue that the most likely triggering factor of the slide at Móafellshyrna was thawing of the deeper permafrost, implying that the longer-term (decade-scale) ground temperature warming was responsible for this event. The authors additionally discussed the base-up permafrost thawing as a probable reason for this slide, contributing among other things to lubrication of the base of the colluvium and lowering cohesion. Three-dimensional effects could also play a role, e.g., warming of bedrock at the southern side and propagation of the thermal wave to the northern side, together with warmer water input from the southern side (Sæmundsson et al., 2018). The CryoGrid 2 simulations confirm the previous interpretations of the landslide at Móafellshyrna, both the long-term warming of permafrost and the permafrost degradation at the bottom.

(3) The CryoGrid 2 runs indicated that the permafrost temperatures are relatively high in Iceland, with most of the average ground temperatures above −2°C. As a consequence, permafrost in Iceland is certainly highly vulnerable to current and future atmospheric warming. Our modelling indicates that the number of modelled permafrost cells already has decreased considerably in 2010–2016 in comparison to earlier decades. Moreover, as noted by Farbrot et al. (2007b) permafrost at Hágöngur site (at that time 5–6 m thick) would be very sensitive to any changes in temperature or snow depth, and between 2012 and 2015 permafrost degraded completely at that site, exemplifying permafrost sensitivity in Iceland. Projected climate warming will likely lead to further permafrost degradation in Iceland, especially in case of shallower permafrost. Deeper permafrost will probably need more time to disappear completely. To assess future climate impacts on permafrost in Iceland, the modelled permafrost profiles at the end of the simulations could be used as initial conditions for modelling future permafrost evolution by forcing the CryoGrid 2 model with projected climate scenarios. Such approach would combine and improve the previous modelling methods [e.g., sub-grid snow depth and equilibrium model in Gisnås et al. (2017), or no sub-grid snow depth and transient model in Westermann et al. (2013)] by both considering the sub-grid variability in snow depths and additionally being able to capture the ground thermal response to changing atmospheric forcing and precipitation.

CONCLUSIONS

From this study, the following conclusions can be drawn:

- Snow is the most crucial factor for permafrost simulation. Snow depth, distribution, and duration were satisfactorily simulated during our study, with some deviations. The permafrost model was most sensitive to (1) thermal conductivity of the snow, (2) precipitation fractions, (3) water content in the upper layer, and (4) snow density, volumetric mineral content in the upper layer, and thermal conductivity of the mineral fraction.
- CryoGrid2 modelled ground temperatures well, with an accuracy of ∼0.5°C for mean annual near-surface ground temperatures. Spatially, the model runs indicated permafrost in most of the palsa areas with an exception of small palsas near Hofsjökull. In addition, most stable-ice cored moraines and active rock-glaciers were within the modelled permafrost cells.
- Permafrost occurs mainly in central and north Iceland, particularly in the Tröllaskagi peninsula, where the simulated permafrost temperatures are generally lowest and permafrost is deepest. For the period of 2010–2016, lower permafrost limits in the Tröllaskagi area are modelled at 600–900 m a.s.l. at windy sites and at 1,000–1,150 m a.s.l. in snow-rich areas.
- Substantial differences in permafrost extent were observed when forcing the model with the different precipitation fractions. The 50% precipitation run indicated ∼3–5 and 8–15 times more cells with permafrost in comparison with the 100 and 150% precipitation runs, whilst 100% precipitation run reproduced ∼2–3 times more permafrost cells than 150% precipitation run.
- Icelandic permafrost is predominantly warm and probably quite shallow. Such conditions make it especially vulnerable to climate warming.
- The three- to four-decade-long warming trend in Iceland has led to the recent permafrost warming or degradation, according to the model output. This was especially evident

for the period between 2010 and 2016, when the number of the modelled permafrost cells was reduced by 34, 56, and 49% for the 50, 100, and 150% precipitation runs, respectively, in comparison to the period 1980–1989.

Projected climate warming will likely lead to further warming or degradation of permafrost in Iceland, thus the frequency of the permafrost-induced landslides might potentially increase in Iceland. The model results yield a realistic picture of permafrost distribution at a regional scale, hence future permafrost evolution in Iceland could be modelled transiently at such scale using the ground temperature profiles reproduced in this study. Nevertheless, the simulation results should be carefully used to identification of areas susceptible to permafrost-related hazards. The simulated ground temperatures presented in this study might be overestimated in steep and north-facing slopes; hence, it should be considered that the modelled ground temperatures are representative mostly at a regional scale.

AUTHOR CONTRIBUTIONS

JC, SW, and BE contributed to the conception and design of the study. JC performed snow and permafrost modelling. TJ provided the data and contributed to snow modelling. BE provided validation data from Iceland. JC wrote the first drafts of the manuscript, with various additions by BE. All authors contributed to manuscript revisions, and approved the submitted version.

FUNDING

Field visits in Iceland have been financed by the University of Oslo and Jarðfræðistofan ehf. (Ágúst Guðmundsson).

ACKNOWLEDGMENTS

This work is partly based on a MSc thesis submitted to the Department of Geosciences, University of Oslo. Help in field was provided by Kjetil Skarsvåg Ovesen. The simulations were performed on the Abel Cluster, owned by the University of Oslo and Uninett/Sigma2, and operated by the Department for Research Computing at USIT, the University of Oslo IT-department. In addition, we acknowledge the editor and reviewers for providing valuable comments that greatly improved the manuscript. We want to thank all mentioned individuals and institutions.

SUPPLEMENTARY MATERIAL

The Supplementary Material for this article can be found online at: https://www.frontiersin.org/articles/10.3389/feart.2019.00130/full#supplementary-material

REFERENCES

Aðalgeirsdóttir, G., Jóhannesson, T., Björnsson, H., Pálsson, F., and Sigurðsson, O. (2006). Response of Hofsjökull and southern Vatnajökull, Iceland, to climate change. *J. Geophys. Res.* 111:F03001. doi: 10.1029/2005JF000388

Aas, K. S., Martin, L., Nitzbon, J., Langer, M., Boike, J., Lee, et al. (2019). Thaw processes in ice-rich permafrost landscapes represented with laterally coupled tiles in a land surface model. *Cryosphere* 13, 591–609. doi: 10.5194/tc-13-591-2019

Arnalds, O. (2000). "Desertification: an appeal for a broader perspective," in *Rangeland Desertification*, eds O. Arnalds and S. Archer (Dordrecht: Kluwer Academic Publishers), 5–15. doi: 10.1007/978-94-015-9602-2

Arnalds, O. (2004). Volcanic soils of Iceland. *Catena* 56, 3–20. doi: 10.1016/j.catena.2003.10.002

Arnalds, Ó. (2008). Soils of Iceland. *Jökull* 58, 409–421. doi: 10.1007/978-94-017-9621-7

Arnalds, Ó. (2015). *The Soils of Iceland. World Soils Book Series.* Dordrecht: Springer.

Arnalds, O., and Kimble, J. (2001). Andisols of deserts in Iceland. *Soil Sci. Soc. Am. J.* 65, 1778–1786. doi: 10.2136/sssaj2001.1778

Barsch, D. (1996). *Rockglaciers: Indicators for the Present and Former Geoecology in High Mountain Environments*. Heidelberg: Springer Verlag.

Bengtsson, L., Andrae, U., Aspelien, T., Batrak, Y., Calvo, J., de Rooy, W., et al. (2017). The HARMONIE–AROME model configuration in the ALADIN–HIRLAM NWP System. *Monthly Weather Rev.* 145, 1919–1935. doi: 10.1175/MWR-D-16-0417.1

Berthling, I. (2011). Beyond confusion: rock glaciers as cryo-conditioned landforms. *Geomorphology* 131, 98–106. doi: 10.1016/j.geomorph.2011.05.002

Berthling, I., and Etzelmüller, B. (2011). The concept of cryo-conditioning in landscape evolution. *Quat. Res.* 75, 378–384. doi: 10.1016/j.yqres.2010.12.011

Brown, J., Ferrians, O. J. Jr., Heginbottom, J. A., and Melnikov, E. S. (1997). *Circum-Arctic Map of Permafrost and Ground-Ice Conditions*. Reston, VA: U.S. Geological Survey.

Christiansen, H. H., Sigsgaard, C., Humlum, O., Rasch, M., and Hansen, B. U. (2008). Permafrost and periglacial geomorphology at Zackenberg. *Adv. Ecol. Res.* 40, 151–174. doi: 10.1016/S0065-2504(07)00007-4

Collins, M., Knutti, R., Arblaster, J., Dufresne, J.-L., Fichefet, T., Friedlingstein, P., et al. (2013). "Long-term climate change: projections, commitments and irreversibility," in *Climate Change 2013: The Physical Science Basis Contribution of Working Group I to the Fifth Assessment Report of the Intergovernmental Panel on Climate Change*, eds T. Stocker, D. Qin, G.-K. Plattner, M. Tignor, S. Allen, J. Boschung, et al. (Cambridge; New York, NY: Cambridge University Press), 1029–1136.

Crochet, P., and Jóhannesson, T. (2011). A data set of gridded daily temperature in Iceland, 1949–2010. *Jökull* 61, 1–17.

Crochet, P., Jóhannesson, T., Jónsson, T., Sigurðsson, O., Björnsson, H., Pálsson, F., et al. (2007). Estimating the spatial distribution of precipitation in Iceland using a linear model of orographic precipitation. *J. Hydrometeorol.* 8, 1285–1306. doi: 10.1175/2007JHM795.1

Dall'Amico, M., Endrizzi, S., Gruber, S., and Rigon, R. (2011). A robust and energy-conserving model of freezing variably-saturated soil. *Cryosphere* 5, 469–484. doi: 10.5194/tc-5-469-2011

DeWalle, D. R., and Rango, A. (2008). *Principles of Snow Hydrology*. Cambridge: Cambridge University Press. doi: 10.1017/CBO9780511535673

Einarsson, M. Á. (1984). *Climate of Iceland*, Vol. 15. Amsterdam: Elsevier, 673–697.

Etzelmüller, B., Farbrot, H., Guðmundsson, Á., Humlum, O., Tveito, O. E., and Björnsson, H. (2007). The regional distribution of mountain permafrost in Iceland. *Permafrost and Periglacial Processes* 18, 185–199. doi: 10.1002/ppp.583

Etzelmüller, B., and Hagen, J. O. (2005). Glacier-permafrost interaction in Arctic and alpine mountain environments with examples from southern Norway and Svalbard. *Geol. Soc. Lond. Spec. Publ.* 242, 11–27. doi: 10.1144/GSL.SP.2005.242.01.02

Farbrot, H. (2007). *Distribution, Thermal Regime and Geomorphic Significance of Mountain Permafrost in Northern Europe–Examples from Iceland, Northern*

Norway and Svalbard (Ph.D. thesis). Department of Geosciences, University of Oslo.

Farbrot, H., Etzelmüller, B., Guðmundsson, Á., Humlum, O., Kellerer-Pirklbauer, A., Eiken, T., et al. (2007a). Rock glaciers and permafrost in Tröllaskagi, northern Iceland. *Zeitschrift für Geomorphol. Suppl. Issues* 51, 1–16. doi: 10.1127/0372-8854/2007/0051S2-0001

Farbrot, H., Etzelmüller, B., Schuler, T. V., Guðmundsson, Á., Eiken, T., Humlum, O., et al. (2007b). Thermal characteristics and impact of climate change on mountain permafrost in Iceland. *J. Geophys. Res.* 112:F03S90. doi: 10.1029/2006JF000541

Farouki, O. T. (1981). *Thermal Properties of Soils*. Hanover: Cold Regions Research and Engineering Laboratory. doi: 10.21236/ADA111734

Flóvenz, Ó. G., and Saemundsson, K. (1993). Heat flow and geothermal processes in Iceland. *Tectonophysics* 225, 123–138. doi: 10.1016/0040-1951(93)90253-G

Friedman, J. D., Johansson, C. E., Oskarsson, N., Svensson, H., Thorarinsson, S., and Williams, R. S. (1971). Observations on Icelandic polygon surfaces and palsa areas. Photo interpretation and field studies. *Geografiska Annaler. Ser. Phys. Geogr.* 53, 115–145. doi: 10.2307/520785

Gisnås, K., Etzelmüller, B., Lussana, C., Hjort, J., Sannel, A. B. K., Isaksen, K., et al. (2017). Permafrost map for Norway, Sweden and Finland. *Permafrost and Periglacial Processes* 28, 359–378. doi: 10.1002/ppp.1922

Gisnås, K., Westermann, S., Schuler, T. V., Litherland, T., Isaksen, K., Boike, J., et al. (2014). A statistical approach to represent small-scale variability of permafrost temperatures due to snow cover. *Cryosphere* 8, 2063–2074. doi: 10.5194/tc-8-2063-2014

Gisnås, K., Westermann, S., Schuler, T. V., Melvold, K., and Etzelmüller, B. (2016). Small-scale variation of snow in a regional permafrost model. *Cryosphere* 10, 1201–1215. doi: 10.5194/tc-10-1201-2016

Gruber, S., and Haeberli, W. (2007). Permafrost in steep bedrock slopes and its temperature-related destabilization following climate change. *J. Geophys. Res.* 112:F02S18. doi: 10.1029/2006JF000547

Guðmundsson, A. (2000). *Frerafjöll, Urðarbingir á Tröllaskaga* (Master's thesis). University of Iceland, Reykjavík. In Icelandic.

Haeberli, W. (2005). Investigating glacier-permafrost relationships in high-mountain areas: historical background, selected examples and research needs. *Geol. Soc. Lond. Spec. Publ.* 242, 29–37. doi: 10.1144/GSL.SP.2005.242.01.03

Hanna, E., Jónsson, T., and Box, J. E. (2004). An analysis of Icelandic climate since the nineteenth century. *Int. J. Climatol.* 24, 1193–1210. doi: 10.1002/joc.1051

Haraldsdóttir, S. H., Ólafsson, H., Durand, Y., Mérindol, L., and Giraud, G. (2001). SAFRAN- Crocus snow simulations in an unstable and windy climate. *Ann. Glaciol.* 32, 339–344. doi: 10.3189/172756401781819120

Hillel, D. (2004). *Introduction to Environmental Soil Physics*. Amsterdam: Elsevier Academic Press.

Hjartarson, Á. (2015). "Heat flow in Iceland," in *Proceedings World Geothermal Congress 2015* (Melbourne, VIC).

Hjort, J., Karjalainen, O., Aalto, J., Westermann, S., Romanovsky, V. E., Nelson, F. E., et al. (2018). Degrading permafrost puts Arctic infrastructure at risk by mid-century. *Nat. Commun.* 9:5147. doi: 10.1038/s41467-018-07557-4

Hock, R. (2003). Temperature index melt modelling in mountain areas. *J. Hydrol.* 282, 104–115. doi: 10.1016/S0022-1694(03)00257-9

Humlum, O., Instanes, A., and Sollid, J. L. (2003). Permafrost in Svalbard: a review of research history, climatic background and engineering challenges. *Polar Res.* 22, 191–215. doi: 10.1111/j.1751-8369.2003.tb00107.x

Jafarov, E. E., Coon, E. T., Harp, D. R., Wilson, C. J., Painter, S. L., Atchley, A. L., et al. (2018). Modeling the role of preferential snow accumulation in through talik development and hillslope groundwater flow in a transitional permafrost landscape. *Environ. Res. Lett.* 13:105006. doi: 10.1088/1748-9326/aadd30

Jafarov, E. E., Marchenko, S. S., and Romanovsky, V. E. (2012). Numerical modeling of permafrost dynamics in Alaska using a high spatial resolution dataset. *Cryosphere* 6, 613–624. doi: 10.5194/tc-6-613-2012

Jóhannesson, T. (1997). The response of two Icelandic glaciers to climatic warming computed with a degree-day glacier mass-balance model coupled to a dynamic glacier model. *J. Glaciol.* 43, 321–327. doi: 10.1017/S0022143000003270

Jóhannesson, T., Sigurdsson, O., Laumann, T., and Kennett, M. (1995). Degree-day glacier mass-balance modelling with applications to glaciers in Iceland, Norway and Greenland. *J. Glaciol.* 41, 345–358. doi: 10.1017/S0022143000016221

Jorgenson, M. T., Shur, Y. L., and Pullman, E. R. (2006). Abrupt increase in permafrost degradation in Arctic Alaska. *Geophys. Res. Lett.* 33:L02503. doi: 10.1029/2005GL024960

Juliussen, H., and Humlum, O. (2008). Thermal regime of openwork block fields on the mountains Elgåhogna and Sølen, central-eastern Norway. *Permafrost and Periglacial Processes* 19, 1–18. doi: 10.1002/ppp.607

Kellerer-Pirklbauer, A., Farbrot, H., and Etzelmüller, B. (2007). Permafrost aggradation caused by tephra accumulation over snow-covered surfaces: examples from the Hekla-2000 eruption in Iceland. *Permafrost and Periglacial Processes* 18, 269–284. doi: 10.1002/ppp.596

Kokkonen, T., Koivusalo, H., Jakeman, A., and Norton, J. (2006). "Construction of a degree-day snow model in the light of the ten iterative steps in model development," in *Proceedings of the iEMSs Third Biennial Meeting: "Summit on Environmental Modelling and Software". International Environmental Modelling and Software Society* (Burlington, VT).

Krautblatter, M., Moser, M., Schrott, L., Wolf, J., and Morche, D. (2012). Significance of rockfall magnitude and solute transport for rock slope erosion and geomorphic work in an Alpine trough valley (Reintal, German Alps). *Geomorphology* 167, 21–34. doi: 10.1016/j.geomorph.2012.04.007

Lachenbruch, A. H., and Marshall, B. V. (1986). Changing climate: geothermal evidence from permafrost in the Alaskan Arctic. *Science* 234, 689–696. doi: 10.1126/science.234.4777.689

Lilleøren, K. S., Etzelmüller, B., Gärtner-Roer, I., Kääb, A., Westermann, S., and Guðmundsson, A. (2013). The distribution, thermal characteristics and dynamics of permafrost in Tröllaskagi, Northern Iceland, as inferred from the distribution of rock glaciers and ice-cored moraines. *Permafrost and Periglacial Processes* 24, 322–335. doi: 10.1002/ppp.1792

Magnin, F., Westermann, S., Pogliotti, P., Ravanel, L., Deline, P., and Malet, E. (2017). Snow control on active layer thickness in steep alpine rock walls (Aiguille du Midi, 3842 m asl, Mont Blanc massif). *Catena* 149, 648–662. doi: 10.1016/j.catena.2016.06.006

Marmy, A., Salzmann, N., Scherler, M., and Hauck, C. (2013). Permafrost model sensitivity to seasonal climatic changes and extreme events in mountainous regions. *Environ. Res. Lett.* 8:035048. doi: 10.1088/1748-9326/8/3/035048

Martin, L. C. P., Nitzbon, J., Aas, K. S., Etzelmüller, B., Kristiansen, H., and Westermann, S. (2019). Stability conditions of peat plateaus and palsas in northern Norway. *J. Geophys. Res.* 124, 705–719. doi: 10.1029/2018JF004945

NASA (2018). *NASA Worldview*. Available online at: https://worldview.earthdata.nasa.gov/ (accessed May 26, 2018).

Nawri, N., Pálmason, B., Petersen, G. N., Björnsson, H., and Þ*orsteinsson, S. (2017). *The ICRA Atmospheric Reanalysis Project for Iceland*. Icelandic Meteorological Office, Technical Report 2017–005.

Nicolsky, D. J., Romanovsky, V. E., Panda, S. K., Marchenko, S. S., and Muskett, R. R. (2017). Applicability of the ecosystem type approach to model permafrost dynamics across the Alaska North Slope. *J. Geophys. Res.* 122, 50–75. doi: 10.1002/2016JF003852

Noetzli, J., Gruber, S., Kohl, T., Salzmann, N., and Haeberli, W. (2007). Three-dimensional distribution and evolution of permafrost temperatures in idealized high-mountain topography. *J. Geophys. Res.* 112:F02S13. doi: 10.1029/2006JF000545

Óskarsson, H., Arnalds, Ó., Gudmundsson, J., and Gudbergsson, G. (2004). Organic carbon in Icelandic Andosols: geographical variation and impact of erosion. *Catena* 56, 225–238. doi: 10.1016/j.catena.2003.10.013

Ottósson, J. G., Sveinsdóttir, A., and Harðardóttir, M. (eds.) (2016). Vistgerðir á Íslandi, Fjölrit Náttúrufræðistofnunar 54. Garðabær: Náttúrufræðistofnun Íslands (Icelandic Institute of Natural History). In Icelandic with English summary.

Pálmason, G., Arnórsson, S., Fridleifsson, I. B., Kristmannsdóttir, H., Saemundsson, K., Stefánsson, V., et al. (1979). "The Iceland crust: evidence from drillhole data on structure and processes," in *Deep Drilling Results in the Atlantic Ocean: Ocean Crust*, eds M. Talwani, C. G. Harrison and D. E. Hayes (Washington, DC: American Geophysical Union), Maurice Ewing Series 2, 43–65.

Pomeroy, J. W., Bewley, D. S., Essery, R. L. H., Hedstrom, N. R., Link, T., Granger, R. J., et al. (2006). Shrub tundra snowmelt. *Hydrol. Processes Int. J.* 20, 923–941. doi: 10.1002/hyp.6124

Poulenard, J., Podwojewski, P., and Herbillon, A. J. (2003). Characteristics of non-allophanic Andisols with hydric properties from the Ecuadorian páramos. *Geoderma* 117, 267–281. doi: 10.1016/S0016-7061(03)00128-9

Pribyl, D. W. (2010). A critical review of the conventional SOC to SOM conversion factor. *Geoderma* 156, 75–83. doi: 10.1016/j.geoderma.2010.02.003

Priesnitz, K., and Schunke, E. (1978). "An approach to the ecology of permafrost in Central Iceland,"in *Third International Conference on Permafrost, Edmonton, Canada* (Ottawa, ON: National Research Council of Canada), 474–479.

Ravanel, L., Allignol, F., Deline, P., Gruber, S., and Ravello, M. (2010). Rock falls in the Mont Blanc Massif in 2007 and 2008. *Landslides* 7, 493–501. doi: 10.1007/s10346-010-0206-z

Redding, T. E., and Devito, K. J. (2006). Particle densities of wetland soils in northern Alberta, Canada. *Can. J. Soil Sci.* 86, 57–60. doi: 10.4141/S05-061

Riseborough, D., Shiklomanov, N., Etzelmüller, B., Gruber, S., and Marchenko, S. (2008). Recent advances in permafrost modelling. *Permafrost and Periglacial Processes* 19, 137–156. doi: 10.1002/ppp.615

Romanovsky, V. E., Smith, S. L., and Christiansen, H. H. (2010). Permafrost thermal state in the Polar Northern Hemisphere during the international polar year 2007–2009: a synthesis. *Permafrost and Periglacial Processes* 21, 106–116. doi: 10.1002/ppp.689

Sæmundsson, Þ., Helgason, J. K., and Pétursson, H. P. (2014). "Decline of mountain permafrost and the occurrence of recent large debris slides in Iceland," in *European Geosciences Union, General Assembly 2014* (Vienna).

Sæmundsson, Þ., Morino, C., Helgason, J. K., Conway, S. J., and Pétursson, H. G. (2018). The triggering factors of the Móafellshyrna debris slide in northern Iceland: intense precipitation, earthquake activity and thawing of mountain permafrost. *Sci. Total Environ.* 621, 1163–1175. doi: 10.1016/j.scitotenv.2017.10.111

Saemundsson, T., Arnalds, O., Kneisel, C., Jonsson, H. P., and Decaulne, A. (2012). The Orravatnsrustir palsa site in Central Iceland–Palsas in an aeolian sedimentation environment. *Geomorphology* 167, 13–20. doi: 10.1016/j.geomorph.2012.03.014

Saloranta, T. M. (2012). Simulating snow maps for Norway: description and statistical evaluation of the seNorge snow model. *Cryosphere* 6, 1323–1337. doi: 10.5194/tc-6-1323-2012

Scherler, M., Hauck, C., Hoelzle, M., and Salzmann, N. (2013). Modeled sensitivity of two alpine permafrost sites to RCM-based climate scenarios. *J. Geophys. Res.* 118, 780–794. doi: 10.1002/jgrf.20069

Schuster, P. F., Schaefer, K. M., Aiken, G. R., Antweiler, R. C., Dewild, J. F., Gryziec, J. D., et al. (2018). Permafrost stores a globally significant amount of mercury. *Geophys. Res. Lett.* 45, 1463–1471. doi: 10.1002/2017GL075571

Schuur, E. A. G., Bockheim, J., Canadell, J. G., Euskirchen, E., Field, C. B., Goryachkin, S. V., et al. (2008). Vulnerability of permafrost carbon to climate change: implications for the global carbon cycle. *BioScience* 58, 701–714. doi: 10.1641/B580807

Seppälä, M. (1982). "An experimental study of the formation of palsas," in *Proceedings Fourth Canadian Permafrost Conference* (Ottawa, ON: National Research Council of Canada), 36–42.

Seppälä, M., and Kujala, K. (2009). The role of buoyancy in palsa formation. *Geol. Soc. Lond. Spec. Publ.* 320, 51–56. doi: 10.1144/SP320.4

Shangguan, W., Hengl, T., Mendes de Jesus, J., Yuan, H., and Dai, Y. (2016). Mapping the global depth to bedrock for land surface modeling. *J. Adv. Model.* 9, 65–88. doi: 10.1002/2016MS000686

Sigurðsson, O., and Jóhannesson, T. (2014). *Samantekt um Snjómælingar á Hálendi Íslands*. Icelandic Meteorological Office. (In Icelandic).

Smith, L. C., Sheng, Y., MacDonald, G. M., and Hinzman, L. D. (2005). Disappearing Arctic Lakes. *Science* 308, 1429–1429. doi: 10.1126/science.1108142

Smith, M. W., and Riseborough, D. W. (2002). Climate and the limits of permafrost: a zonal analysis. *Permafrost and Periglacial Processes* 13, 1–15. doi: 10.1002/ppp.410

Smith, R. B., and Barstad, I. (2004). A linear theory of orographic precipitation. *J. Atmos. Sci.* 61, 1377–1391. doi: 10.1175/1520-0469(2004)061<1377:ALTOOP>2.0.CO;2

Stefánsson, V., Sigurðsson, Ó., Guðmundsson, Á., Franzson, H., Friðleifsson, G. Ó., and Tulinius, H. (1997). "Core measurements and geothermal modelling," in *Second Nordic Symposium on Petrophysics: Fractured reservoirs*. Nordic Petroleum Technology Series (Göteborg, Sweden), 199–220.

Sturm, M., Holmgren, J., König, M., and Morris, K. (1997). The thermal conductivity of seasonal snow. *J. Glaciol.* 43, 26–41. doi: 10.1017/S0022143000002781

Thordarson, T., and Höskuldsson, Á. (2008). Postglacial volcanism in Iceland. *Jökull* 58, 197–228.

Vionnet, V., Brun, E., Morin, S., Boone, A., Faroux, S., Moigne, P. L., et al. (2012). The detailed snowpack scheme Crocus and its implementation in SURFEX v7.2. *Geosci. Model Dev.* 5, 773–791. doi: 10.5194/gmd-5-773-2012

Westermann, S., Elberling, B., Højlund Pedersen, S., Stendel, M., Hansen, B. U., and Liston, G. E. (2015a). Future permafrost conditions along environmental gradients in Zackenberg, Greenland. *Cryosphere* 9, 719–735. doi: 10.5194/tc-9-719-2015

Westermann, S., Østby, T. I., Gisnås, K., Schuler, T. V., and Etzelmüller, B. (2015b). A ground temperature map of the North Atlantic permafrost region based on remote sensing and reanalysis data. *Cryosphere* 9, 1303–1319. doi: 10.5194/tc-9-1303-2015

Westermann, S., Peter, M., Langer, M., Schwamborn, G., Schirrmeister, L., Etzelmüller, B., et al. (2017). Transient modeling of the ground thermal conditions using satellite data in the Lena River delta, Siberia. *Cryosphere* 11, 1441–1463. doi: 10.5194/tc-11-1441-2017

Westermann, S., Schuler, T. V., Gisnås, K., and Etzelmüller, B. (2013). Transient thermal modeling of permafrost conditions in Southern Norway. *Cryosphere* 7, 719–739. doi: 10.5194/tc-7-719-2013

White, D., Hinzman, L., Alessa, L., Cassano, J., Chambers, M., Falkner, K., et al. (2007). The arctic freshwater system: changes and impacts. *J. Geophys. Res.* 112:G04S54. doi: 10.1029/2006JG000353

Wicky, J., and Hauck, C. (2017). Numerical modelling of convective heat transport by air flow in permafrost talus slopes. *Cryosphere* 11, 1311–1325. doi: 10.5194/tc-11-1311-2017

Yen, Y.-C. (1981). *Review of Thermal Properties of Snow, Ice and Sea Ice*. Hanover: Technical report, Cold Regions Research and Engineering Laboratory.

Yumashev, D., Hope, C., Schaefer, K., Riemann-Campe, K., Iglesias-Suarez, F., Jafarov, E., et al. (2019). Climate policy implications of nonlinear decline of Arctic land permafrost and other cryosphere elements. *Nat. Commun.* 10:1900. doi: 10.1038/s41467-019-09863-x

Conflict of Interest Statement: The authors declare that the research was conducted in the absence of any commercial or financial relationships that could be construed as a potential conflict of interest.

PAPER II

Post-Little Ice Age rock wall permafrost evolution in Norway

Justyna Czekirda, Bernd Etzelmüller, Sebastian Westermann, Ketil Isaksen, Florence Magnin

Published in *The Cryosphere*, Vol. 17, 2725–2754, 2023.
doi: 10.5194/tc-17-2725-2023

The Cryosphere, 17, 2725–2754, 2023
https://doi.org/10.5194/tc-17-2725-2023

The Cryosphere
Open Access

Post-Little Ice Age rock wall permafrost evolution in Norway

Justyna Czekirda[1], **Bernd Etzelmüller**[1], **Sebastian Westermann**[1], **Ketil Isaksen**[2], **and Florence Magnin**[3]

[1]Department of Geosciences, University of Oslo, 0316 Oslo, Norway
[2]Department of Research and Development, Norwegian Meteorological Institute, 0313 Oslo, Norway
[3]EDYTEM, Université Savoie Mont Blanc, CNRS, 73000 Chambery, France

Correspondence: Justyna Czekirda (justyna.czekirda@geo.uio.no)

Received: 4 January 2022 – Discussion started: 17 March 2022
Revised: 6 June 2023 – Accepted: 7 June 2023 – Published: 13 July 2023

Abstract. The ground thermal regime and permafrost development have an important influence on geomorphological processes in periglacial regions and ultimately landscape development. About 10 % of unstable rock slopes in Norway are potentially underlain by widespread permafrost. Permafrost thaw and degradation may play a role in slope destabilisation, and more knowledge about rock wall permafrost in Norway is needed to investigate possible links between the ground thermal regime, geomorphological activity and natural hazards. We assess spatio-temporal permafrost variations in selected rock walls in Norway over the last 120 years. Ground temperature is modelled using the two-dimensional ground heat flux model CryoGrid 2D along nine profiles crossing instrumented rock walls in Norway. The simulation results show the distribution of permafrost is sporadic to continuous along the modelled profiles. Results suggest that ground temperature at 20 m depth in steep rock faces increased by 0.2 °C per decade on average since the 1980s, and rates of change increase with elevation within a single rock wall section. Heat flow direction is primarily vertical within mountains in Norway. Nevertheless, narrow ridges may still be sensitive to even small differences in ground surface temperature and may have horizontal heat fluxes. This study further demonstrates how rock wall temperature increase rates and rock wall permafrost distribution are influenced by factors such as surface air temperature uncertainties; surface offsets arising from the incoming shortwave solar radiation; snow conditions on, above and below rock walls; and rock wall geometry and size together with adjacent blockfield-covered plateaus or glaciers.

1 Introduction

Permafrost thaw has decreased the stability of the world's cold mountain slopes (Hock et al. 2019). Numerous studies infer that thawing permafrost induced rapid mass movement events around the world, e.g. in the European Alps, the New Zealand Southern Alps, Alaska and the Caucasus (Dramis et al., 1995; Haeberli et al., 2004; Fischer et al., 2006; Allen et al., 2009; Huggel et al., 2010; Ravanel et al., 2010). Inventories from the European Alps document an enhanced frequency of rockfalls from permafrost rock walls since the 1990s, especially at the lower permafrost limit, in response to accelerated global warming (Ravanel and Deline, 2011; Fischer et al., 2012). An example of a fast response was the exceptional rockfall activity reported during the extremely hot summers of 2003 and 2015 in the European Alps, likely due to permafrost degradation (Gruber et al., 2004; Ravanel et al., 2017). Deep permafrost requires longer timescales to degrade, and its warming or degradation may have influenced the activation of slowly creeping rock masses in the warmer period of the Holocene thermal maximum, thousands of years after local deglaciation (Lebrouc et al., 2013; Böhme et al., 2019; Hilger et al., 2021). The stability of rock faces underlain by permafrost with the consequent hazards, such as rockfalls and rock avalanches, is of growing concern considering global surface warming projections. Rock wall permafrost is highly susceptible to atmospheric warming because (1) small latent heat effects and high thermal conductivity cause more rapid ground temperature (GT) increase (Gruber and Haeberli, 2007), (2) the three-dimensional nature of heat flow leads to faster degradation of deeper permafrost in some locations than would be the case in flatter terrain (Noetzli et al., 2007) and (3) thermal conditions in

Published by Copernicus Publications on behalf of the European Geosciences Union.

steep bedrock and the atmosphere are strongly coupled since steep slopes typically have shallow snow or surface material, if any (e.g. Boeckli et al., 2012; Myhra et al., 2017).

Permafrost degradation is suggested to have had an impact on the dynamics of recent rock slope instabilities at a few sites in Norway, e.g. the unstable rock slope Gámanjunni 3 in northern Norway that accelerated recently (Böhme et al., 2019; Etzelmüller et al., 2022), the Polvartinden rock avalanche in northern Norway that occurred in 2008 (Frauenfelder et al., 2018) or possibly the north-facing Veslemannen in southern Norway that fell in 2019, where at least seasonal freezing controlled the rock stability (Kristensen et al., 2021). Moreover, Blikra et al. (2006) proposed permafrost thawing as a possible triggering mechanism for rock slope failures that have occurred since the deglaciation of Norway. Hilger et al. (2021) modelled permafrost distribution in the Holocene and suggested that permafrost likely had a stabilising effect on some rock slopes in Norway for several millennia after deglaciation. Magnin et al. (2019) estimated that 11 % of potentially unstable slopes in Norway are currently underlain by at least discontinuous permafrost.

Numerous studies concerning permafrost in the flatter parts of the Scandinavian Mountains have been published since the 1980s, attributing variations in mountain permafrost occurrence to mean annual air temperature (Etzelmüller et al., 1998), elevation (Sollid et al., 2003; Heggem et al., 2005), snow cover (Farbrot et al., 2008, 2011; Isaksen et al., 2011; Gisnås et al., 2017), blockfield cover or surface materials (Farbrot et al., 2011; Gisnås et al., 2017), and vegetation cover (Farbrot et al., 2013; Gisnås et al., 2017). Studies indicate that recent atmospheric warming has led to the degradation of mountain permafrost in flatter terrain in Norway, especially since the 1990s (Isaksen et al., 2007; Hipp et al., 2012; Westermann et al., 2013; Etzelmüller et al., 2020).

The earliest rock wall permafrost studies in Norway provided (1) the first rock wall temperature measurements from rock faces in the Jotunheimen Mountains, central southern Norway (Hipp et al., 2014), and from small rock cliffs in Troms, northern Norway (Frauenfelder et al., 2018); (2) a first-order rock wall permafrost map for mainland Norway based on a statistical permafrost model relating permafrost distribution to both elevation and potential incoming shortwave radiation (Steiger et al., 2016); and (3) the first 2D modelling for three north-facing rock walls in Norway based on the interpolated air temperature, variable snow cover and presence of glaciers (Myhra et al., 2017). Systematic field observations were taken at selected sites in the Jotunheimen Mountains (Hipp et al., 2014). From 2015 through 2017, other sites across southern and northern Norway were also logged (Magnin et al., 2019), allowing for the improvement of earlier approaches by Hipp et al. (2014) and Steiger et al. (2016). The acquired data helped to calibrate a near-surface thermal regime model for rock wall permafrost in Norway by using mean annual air temperature (MAAT) and potential incoming solar radiation as explanatory variables instead of elevation.

The aim of this study is to improve knowledge about the spatio-temporal variations in ground temperature in steep rock walls in Norway on the inter-decadal scale. We employ the 2D slope-scale transient heat flow model CryoGrid 2D (Myhra et al., 2017) to simulate the thermal evolution of mountain permafrost since 1900 along nine transects crossing the instrumented rock walls in mainland Norway. We advance the methods presented in the study by Myhra et al. (2017) by utilising an observation-constrained model for ground surface temperature (GST), i.e. including the field observations from rock walls in various expositions. All sites considered in this study have at least one rock wall logger in a vertical rock face for temperature monitoring, and displacement at three unstable sites is monitored by the Norwegian Water Resources and Energy Directorate (NVE). Thus, this study aims to establish an important baseline for the development of the ground thermal regime in potentially unstable mountain terrain.

2 Study areas and field installations

2.1 Western Norway

Western Norway is characterised by alpine mountains, deep glacial valleys and fjords, which were formed after multiple mountain and full-sized Fennoscandian ice sheets linearly eroded the pre-existing fluvially eroded valleys (Kleman et al., 2008). The region's climate is maritime, with annual total precipitation of more than 2000 mm (Lussana, 2018). Normal mean annual air temperature (the normal period 1971–2000) varies between −5 and −4 °C at the highest mountain peaks to between 6 and 8 °C in the coastal areas (Lussana, 2020), and the annual range of mean monthly air temperature is less than 18 °C (Tveito et al., 2000). The permafrost limit is higher in this part of Norway, as high-elevation areas are often occupied by glaciers or deeper winter snow, which insulates the ground (Etzelmüller et al., 2003). During 2015–2017, nine *GEOprecision, M-Log 5W Rock* loggers with at least 0.1 °C at 0 °C accuracy were installed at selected rock walls to measure surface temperature in western Norway (Magnin et al., 2019). The lower rock wall permafrost limits in the area at present can be expected at 1300–1400 m elevation in north-facing slopes (Magnin et al., 2019). We chose four profiles in western Norway for this study: (1) Mannen (Fig. 1g), (2) Hogrenningsnibba (Fig. 1b), (3) Kvernhusfjellet (Fig. 1b) and (4) Ramnanosi (Fig. 1c). The name Mannen is used for both a mountain peak at 1294 m elevation and a large active rockslide. Over the last few years, the Mannen instability has been moving with a velocity of more than 20 mm a^{-1} in the upper part of the slope above about 1000 m elevation (Etzelmüller et al., 2022). Hogrenningsnibba (1670 m) and Kvernhusfjel-

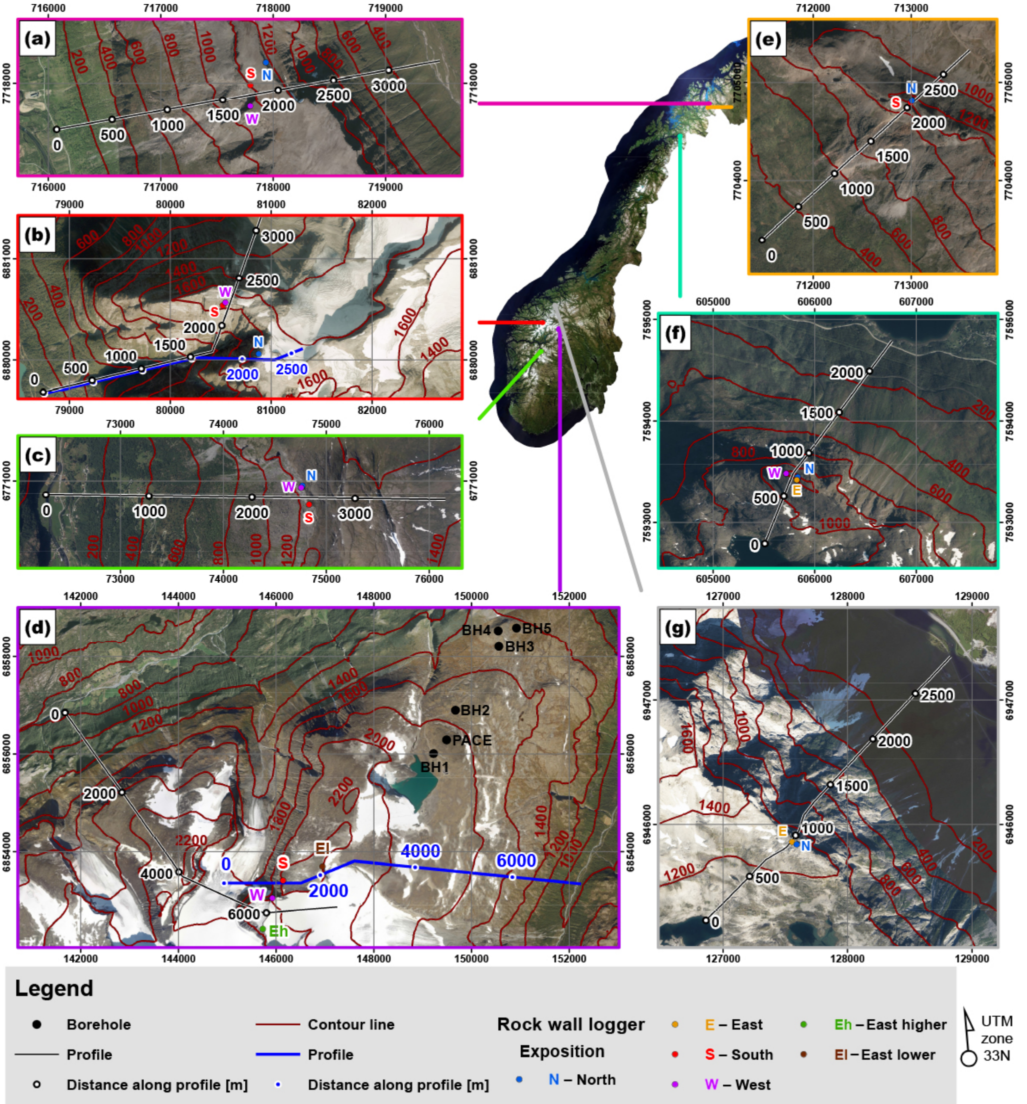

Figure 1. Transects for the two-dimensional modelling: **(a)** Gámanjunni 3, Kåfjord; **(b)** Hogrenningsnibba (the northernmost profile or the black line) and Kvernhusfjellet (the southernmost profile or the blue line), Stryn; **(c)** Ramnanosi, Aurland; **(d)** Veslpiggen (the southernmost profile or the black line) and Galdhøe (the northernmost profile or the blue line), the Jotunheimen Mountains; **(e)** Ádjit, Storfjord; **(f)** Rombakstøtta, Narvik; and **(g)** Mannen, Rauma. Map background credits: ©Statens kartverk, Geovekst og kommunene.

let (1740 m) in the Loen area are two mountains located north of the Jostedalsbreen ice cap. Around the Ramnanosi Mountain (1421 m), both gravitational faults and fractures were mapped in the phyllite nappes. Below a west-facing 200 m high slide scar, there are deposits from the rock avalanche and rockfall events (Blikra et al., 2006; Böhme et al., 2012, 2013).

2.2 The Jotunheimen Mountains

The Jotunheimen Mountain Range is located in the central part of southern Norway and represents one of the highest mountain areas in Norway, including its highest peak, Galdhøpiggen (2469 m). The Jotunheimen area receives less precipitation than western Norway, with normal (1961–1990) mean precipitation typically less than 1000 mm a^{-1} (Lussana, 2018). Normal mean annual air temperature (1971–2000) is below −6 °C at the highest mountain peaks to between 0 and 2 °C in the valleys (Lussana, 2020). The area has an annual range of mean monthly air temperature normally greater than 18 °C (Tveito et al., 2000). Most mountain permafrost research in southern Norway has been conducted in central and eastern Norway, especially in the Jotunheimen Mountain Range (Ødegård et al., 1992; Farbrot et al., 2011; Isaksen et al., 2011). In 1982, the first 10 m deep borehole at 1851 m elevation was drilled in Jotunheimen (Ødegård et al., 1992), and then in August 1999, the deepest permafrost borehole (129 m) in Norway was drilled in the continuous permafrost zone at Juvvasshøe (1894 m) as part of the PACE project (Fig. 1d; Sollid et al., 2000; Harris et al., 2001). Additional boreholes have been drilled at various elevations in the Juvvasshøe area on its north-eastern slope in August 2008 (Fig. 1d; Farbrot et al., 2011). The measured GTs show that permafrost occurs in all boreholes at and above 1559 m elevation. Furthermore, *GEOprecision, M-Log 5W Rock* loggers (at least 0.1 °C at 0 °C accuracy) were installed at selected sites in Jotunheimen (Hipp et al., 2014). Statistical model results (Magnin et al. 2019) suggested that the lower limit of rock wall permafrost in the Jotunheimen area is at approximately 1550 and 1150 m elevation in the south- and north-facing rock walls, respectively. We define two profiles in Jotunheimen in this study (Fig. 1d) for (1) Veslpiggen (2369 m) and (2) Galdhøe (2283 m).

2.3 Northern Norway

The geomorphology of northern Norway is generally similar to southern Norway, with multiple glaciations leading to the formation of fjords and U-valleys (Kleman et al., 2008; Olsen et al., 2013). The climate in northern Norway is mostly subarctic in the lowland and tundra type in the mountains. The climate varies from maritime in the coastal areas, with the highest annual total precipitation reaching > 2000 mm in 1961–1990 (Lussana, 2018), to a more continental character further inland, where annual total precipitation averaged less than 750 mm in 1961–1990 (Lussana, 2018). Normal mean annual air temperature (1971–2000) is between −6 and −5 °C at the highest mountains to between 2 and 6 °C in the coastal areas (Lussana, 2020). For the gentle terrain, the permafrost limits decrease from 800–900 m elevation in the western areas of northern Norway to around 200–300 m elevation further inland (Farbrot et al., 2013). Three transects in the coastal areas of northern Norway are established in this study: (1) Gámanjunni 3 (Fig. 1a), (2) Ádjit (Fig. 1e) and (3) Rombakstøtta (Fig. 1f). All sites are instrumented with *GEOprecision, M-Log 5W Rock* loggers with at least 0.1 °C at 0 °C accuracy. Gámanjunni 3 (Fig. 1a) is one of the most unstable rock slopes in Norway, recently moving up to 60 mm a^{-1} (Böhme et al., 2016b, 2019; Etzelmüller et al., 2022). The unstable part has moved approximately 150 m downslope since the end of the Holocene thermal maximum (Böhme et al., 2019; Hilger et al., 2021). Ádjit (Fig. 1e) is a mountain ridge where several periglacial and mass movement landforms were mapped below its south-western rock wall, such as active and inactive talus-derived rock glaciers (Nopper, 2015; Eriksen et al., 2018).

3 Methods

3.1 CryoGrid 2D

A transient 2D heat conduction model, CryoGrid 2D (Myhra et al., 2017), is employed to model GT evolution along the selected profiles. The subsurface temperature is modelled by solving the heat diffusion equation following Fourier's law of heat conduction with the material- and temperature-dependent thermal parameters. The effective volumetric heat capacity, which includes the latent heat effects due to water–ice phase transitions, and the thermal conductivity are functions of the volumetric contents of soil components (mineral, water or ice, air, organic) and their individual thermal properties, as defined in the one-dimensional CryoGrid 2 model (Westermann et al., 2013). In CryoGrid 2D, the MATLAB-based finite element solver MILAMIN package (Dabrowski et al., 2008) generates an unstructured triangular mesh for a given slope geometry and is used for space discretisation, whereas time discretisation is based on the finite-difference backward Euler scheme. The spatial resolution in CryoGrid 2D is prescribed by the maximum triangle area (MTA), i.e. a maximum area for the three-node triangular elements. Dirichlet boundary conditions are used at the upper model boundary, and the model is forced by GST at the air–ground interface, i.e. temperature below the snowpack. A more thorough description of the model and equations can be found in Myhra et al. (2017). Note that since CryoGrid 2D is a conductive model, convective or advective heat transport is unaccounted for. The model is constructed as a 2D cross section through a slope, assuming translational symmetry along the third dimension.

3.2 Model geometry and ground stratigraphy

The upper boundary for the selected profiles was extracted from the 0.5–1 m digital elevation models (DEMs) available from the Norwegian Mapping Authority at https://www.hoydedata.no (last access: 18 February 2021), whereas the lower boundary extends down to 6000 m below sea level. Most profiles are approximately 2.5–4 km long, except for

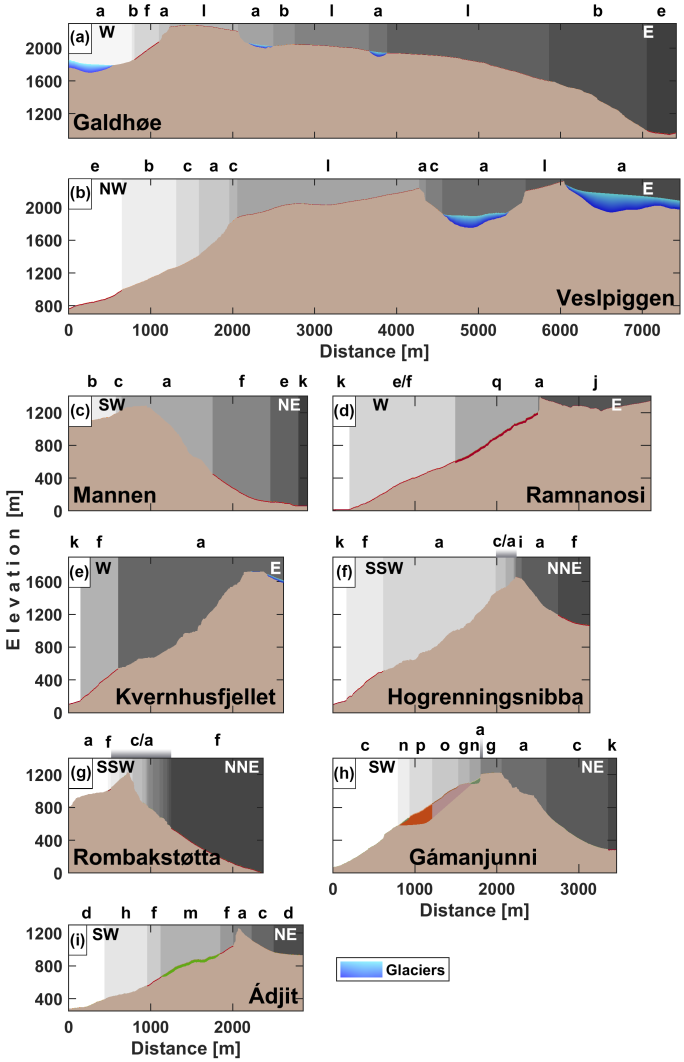

Figure 2. Slope geometry and stratigraphy. The small case letters are stratigraphy codes, described in detail in Table S1 in the Supplement. The label "c/a" indicates alternating stratigraphy of bedrock and thin colluvium. Blue patches depict glaciers or perennial snow. Different colours near the surface show various stratigraphic layers (see Table S1 for details). Note that the meshes extend down to 6000 m below sea level and the parts below the valley bottoms are not shown.

the ∼7.5 km long profiles in Jotunheimen (Fig. 2a and b). Because of the profiles in Jotunheimen, together with the profile at Kvernhusfjellet traverse glaciers, we compute glacier bed elevation by extracting glacier thickness provided by NVE, where ice thickness was estimated using a distributed model (Andreassen et al., 2015). At Kvernhusfjellet, we add a 5 m thick snow patch on the top plateau, as observed on the orthophotos from the Norwegian Public Roads Administration, the Norwegian Institute of Bioeconomy Research and the Norwegian Mapping Authority (https://www.norgeibilder.no, last access: 11 March 2021). Meshes for each profile are constructed with nodes at a 0.05 m distance at the upper boundary and an MTA that increases with depth. The constructed meshes have an MTA of 0.05 m^2 between the ground surface and 2 m depth, 0.20 m^2 at depths between 2 and 10 m, 0.50 m^2 at depths between 10 and 20 m, 5.00 m^2 at depths between 20 and 100 m, and 50 m^2 below 100 m depth. The model domains consist of approximately 500 000 vertices, except for the longer profiles in Jotunheimen, where each mesh has $\sim 1\,250\,000$ nodes. No mechanical aspect is considered in this study; hence, the meshes remain static throughout the entire simulation period.

A digital map of surface materials is available for all of Norway from the Geological Survey of Norway (NGU) at 1 : 250 000 scale. Due to the small scale of the map, we refine the geomorphological mapping along the upper profile boundaries based on the available orthophotos from https://www.norgeibilder.no (last access: 11 March 2021). The ground composition (Table S1) is based on the sediments mapped on the surface for most profiles, where we define hard vertical boundaries between the sediment classes also at depth because such an approach allows for an effective and almost automated generation of nodes for an unstructured mesh. Similar volumetric contents and layers for the NVE sediment classes are assumed as in Westermann et al. (2013) for the one-dimensional CryoGrid 2. However, we apply a higher rock porosity than Westermann et al. (2013) and follow the higher porosity of 5 % vol. to account for rock discontinuities, as in Myhra et al. (2017). The thermal conductivity for the mineral fraction is extracted from the same data as in Westermann et al. (2013) and varies for the sites between 2.3 and 3.1 $W\,m^{-1}\,K^{-1}$ (Table S2). The NVE sediment classes and their stratigraphy as defined in Westermann et al. (2013) lack a suitable representation for some sediments mapped along the profiles. Therefore, we added several sediment classes to fill this gap (Table S1). The Ádjit profile intersects a rock glacier at lower elevations, where we used a similar geometry, as presented in Eriksen et al. (2018). For Gámanjunni we use a slightly modified version of a geological profile for the unstable part (Böhme et al., 2016a), in conjunction with the geomorphological mapping outside of the geological model. The scree class is defined with the same parameters as in Myhra et al. (2019). At Ramnanosi, 30 m thick colluvium deposits are assumed just below the rock wall down to around 600 m elevation, and 4 m thick regolith is assumed at the plateau. Bedrock class (Class “a” in Table S1) is assumed below glaciers and perennial snow.

3.3 Model forcing

3.3.1 Surface air temperature

The modelled daily surface air temperature (SAT) data set for mainland Norway, hereafter seNorge, is available for 1 km^2 grid cells for the period 1957–present (Lussana, 2020). However, the seNorge data set overestimates SAT trends and often shows positive SAT trends with elevation for our study sites, leading to, for example, a 3 °C SAT increase in Jotunheimen between the 1980s and 2010s. This is the result of the inhomogeneity in the network of meteorological stations, particularly the lack of meteorological stations at mountain plateaus in some periods. Cold periods are overestimated if the gridded data set is based mainly on meteorological stations in valleys, where air temperature inversions are frequent during winter. Therefore, we choose to force the model with the regional monthly data set at 2 km spatial resolution provided by the Norwegian Meteorological Institute, described in detail in Hanssen-Bauer et al. (2006). This regional model yields robust temporal estimates at a regional scale; however, the data provide rather poor temperature series at local scales. Therefore, we superimpose a local component on the regional data. Regional SAT data sets were provided for valleys at the bottom of each profile. We use the following procedure for each profile.

1. Since we begin to run the model at the end of the Little Ice Age (LIA) in Norway and the regional SAT data sets start in 1900, we reconstruct SAT back in time by using SATs from the long-term meteorological stations described in Table S3. The latter data allow for SAT reconstruction back to 1861 for western Norway, 1864 for Jotunheimen and 1872 for northern Norway. We account for average offsets in the overlapping period between SAT from the long-term meteorological stations and the regional SAT.

2. We adjust regional SATs by subtracting offsets between the regional and local SATs from a nearby meteorological station or seNorge for valleys over the last few years.

3. We compute the average monthly lapse rate between two meteorological stations, typically one at the bottom of the valley and one at or close to the mountain plateau over the last few years. The selected SAT data are listed in Table S3.

4. We compute monthly SAT along the profiles using monthly lapse rates.

The selected last few years used in this analysis are periods when temperature measurements in the rock walls are available. This allows for a comparison of SAT with GST determined from rock wall loggers in months with minimal shortwave radiation, e.g. December, and gives more reliability. The aforementioned procedure allows for the reproduction of similar SAT trends at mountain plateaus, as provided for valleys, hence removing elevation dependency in the SAT trends present in the seNorge data. Appendix A describes decadal running mean surface air temperature (SAT10a) evolution for the highest elevations along each profile. After the generation of the SAT data sets, we account for the nival offsets and surface offsets arising from the shortwave solar radiation (see Sects. 3.3.2 and 3.3.3) by modifying SAT along the profiles.

Table 1. Assumed nF factors along the profiles.

Slope gradient [°]/sediment or vegetation class	nF factor		
	Western Norway	Jotunheimen and Rombakstøtta	Gámanjunni and Ádjit
< 30	0.25	0.40 (based on data from Gisnås et al., 2014)	0.50 (based on data from Eriksen, 2018b)
30–40	0.50	0.55	0.60
40–50	0.70	0.70	0.75
50–60	0.90		
> 60	1.00		
Blockfields (Jotunheimen)		0.70 (PACE, BH1 and BH2)	
Rock glacier (Ádjit)			0.80 (based on data from Eriksen, 2018a)
Broad-leaved forest	0.25 (Gisnås et al., 2017)		

3.3.2 Nival offsets

We lack observations of snow cover dynamics and snow depths from the rock walls in Norway. In this study, we are mostly interested in the thermal insulation effect of snow cover and not snow depth itself, especially because our permafrost model lacks an explicit snow domain. In equilibrium permafrost models such as the TTOP model (Smith and Riseborough, 2002), insulating snow effects are accounted for by using semi-empirical transfer functions, so-called freezing *n* factors (nF). The nF factors link SATs and GSTs by relating the freezing degree days at the surface to the air. In Norway, the freezing *n* factors vary between 0.1 for the attenuation effects of deep snow cover to 1.0 for very thin or absent snow cover (Gisnås et al., 2013). We follow an easy-to-implement hypothesis that snow thickness and its insulating effect on the GST depend on the slope gradient. Hence, we assign various nF values along the profiles according to the computed slope gradient; however, certain sediment or vegetation cover types have distinct values for nF (Table 1). We assume that steep slopes, i.e. steeper than 60°, are snow-free (discussed in Sect. 5.1.4). Snow redistribution towards the lower portion of the slope is not considered. Furthermore, we detect 1 m deep sinks along the profiles using fill sinks from TopoToolbox 2 (Schwanghart and Scherler, 2014) and assume that these are areas where snow may accumulate and use the same nF as for the gentlest gradient (slope < 30°) in each profile. Additionally, we assign a special nF value of 0.25, as computed by Gisnås et al. (2017), for broad-leaved forest (code 311) based on CORINE land cover 2018 (Aune-Lundberg and Strand, 2010).

For the top block at Gámanjunni (slope gradient < 30°), we compute $\mathrm{nF}=0.50$ based on the SAT and GST measurements conducted by Eriksen (2018b). For the rock glacier at Ádjit, we found an nF value of 0.80 (Eriksen, 2018a). Measurements from the three uppermost boreholes, BH1 ($\mathrm{nF}=0.78$ in 2008–2019), PACE ($\mathrm{nF}=0.89$ in 1999–2018) and BH2 ($\mathrm{nF}=0.37$ in 2008–2019), in Jotunheimen yield an average rounded nF value of 0.70 that we apply for the blockfield locations. We note that nF for the blocky terrain (blockfields and rock glaciers) is not necessarily due to nival offsets and is rather caused by air convection (discussed in Sect. 5.1.1).

3.3.3 Surface offsets

Our analysis of the measured 2 h rock wall temperature indicates that rock wall temperature in Norway is influenced by solar radiation as early as February in northern Norway and in all months of the year in southern Norway. Due to their steep vertical slopes, incoming shortwave solar radiation may not necessarily be the largest during June, as expected for a horizontal surface at the latitudes in Norway. In the case of rock walls, thawing *n* factors (nT; Smith and Riseborough, 2002) may not be able to account for surface offsets (SOs) due to the shortwave solar radiation in the months when solar radiation is maximum and SAT is still negative, which may occur in the spring months. Additionally, reflected solar radiation from the surrounding terrain is likely an important factor during spring and early summer, when snow cover may be present, or during a whole year in the rock walls above glaciers. Instead of using temperature transfer factors, we add measured average monthly SOs to SATs at the location of rock walls along profiles. Measured monthly SOs are computed as a difference between monthly mean ground surface ($\mathrm{GST}_{\mathrm{month}}$) and surface air ($\mathrm{SAT}_{\mathrm{month}}$) temperature:

$$\mathrm{SO}_{\mathrm{month}}=\mathrm{GST}_{\mathrm{month}}-\mathrm{SAT}_{\mathrm{month}}. \tag{1}$$

Note that we refer to both rock surface and soil surface temperatures as GSTs in this study. We apply the same SOs to all steep parts of slopes (> 60°) along profiles and to all months during the entire modelling period. Table 2 summarises the

Table 2. Summary of the rock wall aspects and selected logger data along profiles. "Easternmost" – aspects between 0 and 180°; "westernmost" – aspects between 180 and 360°.

Mountain, municipality	Main profile aspect of the westernmost rock wall [°]	Logger data for the westernmost rock wall	Main profile aspect of the easternmost rock wall [°]	Logger data for the easternmost rock wall
Mannen, Rauma	None		38	Two simulations: N (350°) as the main simulation and E (90°)
Hogrenningsnibba, Stryn	200	S (210°)	20	N (320°)
Kvernhusfjellet, Stryn	272	Three simulations: W (270°) as the main simulation, N (320°) and S (210°)	None	
Ramnanosi, Aurland	271	Three simulations: W (280°) as the main simulation, N (10°) and S (220°)	None	
Veslpiggen, Lom	294	W (297°)	85	Eh (89°)
Galdhøe, Lom	270	W (297°)	68	El (82°)
Gámanjunni 3, Kåfjord	260	Two simulations: S (200°) as the main simulation and W (320°)	80	N (360°)
Ádjit, Storfjord	228	S (190°)	48	N (30°)
Rombakstøtta, Narvik	202	Two simulations: E (100°) as the main simulation, because the west-facing logger is too cold, and W (270°)	37	N (25°)

aspects along profiles and selected rock wall loggers to account for the monthly SOs. Figure S1 in the Supplement shows more details about the loggers used along profiles. In this study, SOs are referred to as SOs arising mainly from solar radiation, unless other indicated.

3.4 Model initialisation, model simulations and sensitivity tests

Model simulations start around the end of the LIA in Norway when the long-term SAT data from meteorological stations are available (1861 or 1864 for the profiles in southern Norway, 1874 for the profiles in northern Norway). CryoGrid 2D is initialised in a two-step procedure: (1) by running a steady-state version of the model using the average GST for the first decade of the available data and the geothermal heat flux at the lower boundary and (2) a spin-up of the model at monthly time steps around 50 times, which yields temperature differences between the consecutive simulations on the order of 10^{-4} °C. After this initialisation procedure, we continue to run the model at monthly time steps. Accounting for at least an additional 20 years of initialisation period, we present the results of the model simulations since 1900. A zero heat flux condition is assumed along the vertical left and right boundaries. An average value of geothermal heat flux of $50\,\mathrm{mW\,m^{-2}}$ (Slagstad et al., 2009) is applied at the lower boundary at all sites, except for the profiles in Jotunheimen, where a value of $33\,\mathrm{mW\,m^{-2}}$ is used (Isaksen et al., 2001). Beneath modern glaciers or perennial snow, we apply GST of 0 °C, corresponding to the temperate bed conditions, except for the shallower glaciers or ice patches along the Galdhøe profile in Jotunheimen, where we apply cold basal conditions at −3 °C, as measured in the Juvfonne ice patch (Ødegård et al., 2017). We note, however, that the assumed temperate bed conditions should be represented by polythermal bed conditions because the thinnest parts of glaciers likely have temperatures below the pressure melting point (Etzelmüller and Hagen, 2005).

Table 3. Sensitivity simulations.

Scenario(s)	Modifications	Simulation type	Profiles
“nF − 0.1” or “nF + 0.1”	We modify nF factors by subtracting 0.1 or adding 0.1.	Uncertainty	All
“$T - 1$ °C” or “$T + 1$ °C”	We subtract or add 1 °C to the forcing data before applying nF factors.	Uncertainty	
“Without monthly offsets”	We ignore solar radiation and force the model directly with SAT; however, we still account for the nival offsets.	Test	
“N/E/S/W logger”	We test thermal influence of SOs measured in the other rock wall aspects, as listed in Table 2.	Uncertainty for Mannen and Gámanjunni; test for Kvernhusfjellet, Ramnanosi and Rombakstøtta	Mannen, Kvernhusfjellet, Ramnanosi, Gámanjunni and Rombakstøtta
“50 % water” or “200 % water”	The water fraction is reduced by 50 % or increased by 200 % compared with the values in the main simulation and the remaining fraction is added to or subtracted from the mineral fraction.	Uncertainty	Gámanjunni and Ádjit
“Bedrock”	We assume that the entire subsurface is composed of the bedrock.	Test	Ramnanosi, Hogrenningsnibba, Veslpiggen, Galdhøe and Rombakstøtta
“Without glaciers”	We remove glaciers and perennial snow along profiles.	Test	Galdhøe, Veslpiggen and Kvernhusfjellet
“Blockfields nF = 0.4”	We change the nF factor for blockfields to 0.4.	Test	Galdhøe and Veslpiggen
“Snow patch”	At Hogrenningsnibba, snow persisted until late summer in some years; hence, we add a snow patch on the top of the mountain and partly along the north-facing slope.	Uncertainty	Hogrenningsnibba
“Bedrock and glacier at NNE”	We test what happens if Hogrenningsnibba has no sediments and add a glacier at the NNE-facing slope.	Test	
“Without monthly offsets and bedrock”	We remove monthly surface offsets and assume that the subsurface consists only of bedrock.	Test	Rombakstøtta

We evaluate model sensitivity for all profiles by rerunning the model, including the initialisation steps. Certain simulations are conducted to verify the thermal influence of likely uncertainties in the model forcing or parameters (“uncertainty simulations”), and the others are “test simulations” to investigate the thermal influence of, for example, nearby glaciers, sediments or SOs in the rock walls. Uncertainty and test simulations are listed in Table 3.

4 Results

4.1 Surface offsets and logger data

Figure 3 shows the monthly SOs for rock wall loggers in Norway. The south-facing slopes usually have the maximum monthly SOs in April compared with May elsewhere. There are a few exceptions, e.g. the temperatures from the rock wall loggers at Mannen and Rombakstøtta indicate the maximum monthly offsets occur only in June. The calibration of GST forcing input using the measured SOs yields zero mean error and an RMSE below 1.40 °C for the monthly GSTs and significantly improves the correlation between the forcing data and the rock wall measurements (Figs. S2–S21).

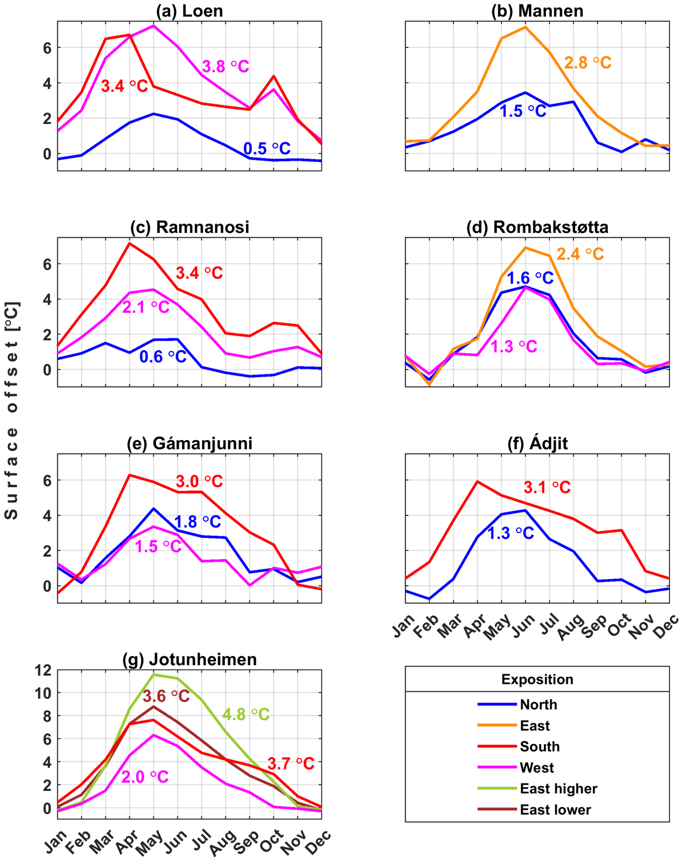

Figure 3. Monthly surface offsets between air and rock wall temperature for each site and logger exposition. Numbers along the plot lines are average values. Note that Jotunheimen has a different y axis than the other subplots.

Table S4 includes information about the measured GSTs at the study sites. Mean rock wall temperature at or below 0 °C over at least 2 consecutive years usually indicates permafrost; however, due to lateral heat fluxes and the preservation of long-term temperature signals at depth, permafrost may occur even if mean rock wall temperature is above 0 °C (Noetzli et al., 2007; Noetzli and Gruber, 2009). All recorded logger temperatures at Mannen and the W-facing logger at Ramnanosi suggest an unlikeliness of permafrost presence in these rock wall expositions over the last few years. The north-facing logger at Ramnanosi measured mean rock wall temperature at 0.02 °C (August 2016–July 2020; 1370 m); hence, permafrost was likely in the north-facing parts of the slope, at least before the measurement period started. The temperature from the north-facing logger in the Loen area indicates that permafrost is likely, whereas the temperatures from the west- and south-facing loggers are positive. In Jotunheimen, most temperatures from the rock wall loggers indicate that even cold permafrost (< -2 °C) exists in the Jotunheimen Mountains. In the Gámanjunni area, at least warm permafrost conditions can be expected in the rock walls. For Ádjit, the temperatures measured in both loggers indicate permafrost, although the south-facing rock wall is close to non-permafrost conditions. The temperatures from all loggers at Rombakstøtta, except from the east-facing logger, indicate that at least warm permafrost may be present in the rock walls.

4.2 Distribution of modelled ground temperature

We modelled GT at four sites in western Norway, two sites in Jotunheimen and three sites in northern Norway (Fig. 4). These results are also presented in Videos 1–20.

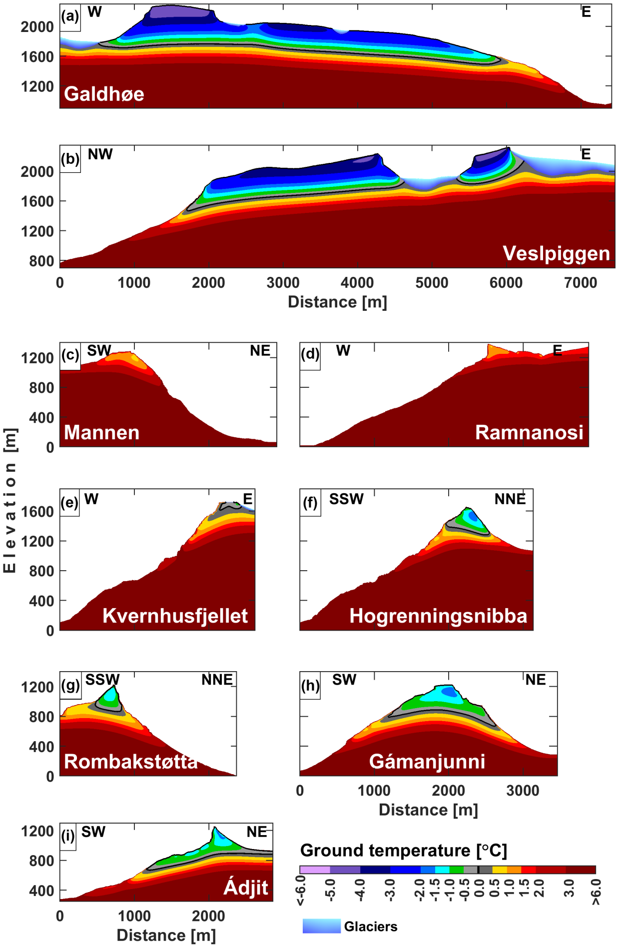

Figure 4. Simulated average annual maximum ground temperature over the 2010s.

4.2.1 The permafrost limits

Western Norway. The main simulations for the two profiles with the mountain peaks at an elevation below 1400 m (Mannen and Ramnanosi) suggest no permafrost in these mountains since 1900 (Fig. 4c and d; Videos 1–4). The simulations for the two profiles with higher mountain peaks (Hogrenningsnibba and Kvernhusfjellet) indicate that sporadic (10 %–50 % area) to discontinuous (50 %–90 % area) permafrost likely occurs in these mountains, even below glaciers and snow patches (Fig. 4e and f; Videos 5–8). The lower permafrost limits vary between 1300 m for the NNE-facing slope at Hogrenningsnibba to around 1600 m at the west-facing slope of Kvernhusfjellet over the 2010s.

Jotunheimen. For both profiles in Jotunheimen, sporadic to discontinuous permafrost is simulated down to an elevation of 1530–1590 m over the 2010s (Fig. 4a and b; Videos 9–14). Considering the simplified forcing for the gentle terrain in our modelling, a boundary between discontinuous and continuous permafrost can only be established assuming a particular isotherm, here −2 °C, as the lower limit for continuous permafrost. In that case, the continuous permafrost limit is at ∼ 1780–1860 m for the gentle terrain over the 2010s.

Northern Norway. Modelled GT field for Gámanjunni shows a colder NE-facing slope compared with the SW-facing slope, and the lower permafrost limits are approximately 100 m higher at the SW-facing slope, at an elevation of around 850 m over the 2010s (Fig. 4h; Videos 15–16).

At Ádjit, the SW-facing rock wall is warmer than the NE-facing slope at Ádjit, even though the modelled permafrost limits are lower on the SW-facing slope than on the NE-facing one, at around 700 m over the 2010s, roughly where the active rock glacier has its front (Fig. 4i; Videos 17–18). The permafrost limits at Rombakstøtta are modelled slightly higher than at the other sites in northern Norway (Fig. 4g; Videos 19–20), at approximately 900–950 and 1000 m for the NNE- and SSW-facing slopes over the 2010s.

4.2.2 Ground heat flux direction

The heat flux direction is shown in Videos 2, 4, 6, 8, 11, 14, 16, 18 and 20. The main ground heat flux direction is generally vertical beneath larger plateaus (e.g. Ramnanosi, Mannen, Galdhøe). For the latter simulations, the main heat flux direction tilts slightly outwards in simulations without monthly SOs, where relatively colder zones are simulated below rock walls. Simulations with large SOs in the rock walls show that heat flux may be forced towards the colder plateaus if SOs are large enough (e.g. Veslpiggen, Ramnanosi). The main heat flux direction is more tilted towards colder zones for the mountains, with more pronounced differences in GST between opposite mountainsides (e.g. Hogrenningsnibba, Kvernhusfjellet, Gámanjunni). The tilt between opposite mountainsides may in certain cases even be horizontal beneath the mountain peaks, with a shorter distance between two mountainsides and larger differences in GST (e.g. Ádjit, Hogrenningsnibba). If GST between the opposite mountainsides is similar (e.g. Rombakstøtta), the main heat flux direction remains vertical. Glaciers may modify the main heat flux direction below the plateaus (see Sect. 4.2.4).

4.2.3 Steepness and SOs

Even though Kvernhusfjellet and Hogrenningsnibba lie close together, the permafrost limits are at a higher elevation at the W–E Kvernhusfjellet profile than at the SSW–NNE Hogrenningsnibba profile. This difference results from the extent of the steepest parts, where we applied SOs, and is particularly clear when comparing the "Main" simulations with the "Without monthly offsets" simulations (Fig. 5c–f); i.e. ignoring SOs at the steeper Kvernhusfjellet leads to much lower GTs in the whole mountain than when ignoring SOs at the moderately steep Hogrenningsnibba. In the "Without monthly offsets" simulation for Kvernhusfjellet, permafrost is modelled down to 1300 m over the 2010s, whereas in the warmer main simulation the permafrost limit is at 1600 m over the 2010s. Moreover, the simulations with "Bedrock and glacier at NNE" for Hogrenningsnibba and "S logger" for Kvernhusfjellet show how the differences in geometry influence permafrost distribution, e.g. the permafrost limit is modelled at 150 m lower elevation in the former simulation (Videos 5 and 7). Furthermore, our results show that permafrost may underlie parts of the mountain where mean annual ground surface temperature (MAGST) is above 0 °C. For instance, the temperature from the logger at Hogrenningsnibba indicates positive MAGST at the SSW-facing slope, and permafrost underlies this slope in even the warmest simulation ("$T + 1\,°\mathrm{C}$") due to permafrost extending there from the NNE-facing slope. The Kvernhusfjellet profile lacks a substantially colder slope, since there is a warm-based glacier on the E-facing slope; hence, permafrost in the W-facing slope is unrelated to permafrost extending from a colder slope and is degrading.

Asymmetric lower permafrost limits at Gámanjunni are not related to the higher SOs applied to the SW-facing rock wall and are rather caused by the extent of steeper terrain in the profile. The NE-facing slope is rougher and consists of several smaller rock walls, whereas the SW-facing slope encompasses mainly one smoother rock wall, less than 50 m in height. The influence of geometry is especially clear in the "W logger" simulation (Fig. 5h), where we applied slightly colder forcing to the SW-facing rock walls, and the results still show lower GT in the NE-facing slope. The results for Gámanjunni show that in the simulations with SOs, the scree slope is often colder than the sun-exposed, SW-facing rock wall. The scree slope is also less coupled to atmospheric conditions due to snow cover and greater ice content; hence, permafrost degradation occurs slower than in the rock wall, further amplifying the differences in GT between the sun-exposed rock face and scree slope during warmer periods. In the simulation "Without monthly offsets", the rock wall is colder than the scree slope. For the Ádjit profile, the SW-facing rock wall is much steeper than the NE-facing slope, which is the reverse of Gámanjunni geometry. The simulation "Without monthly offsets" (Fig. 5j) shows the SW-facing slope as colder than the NE-facing slope due to the extent of the rock walls.

Permafrost temperatures at Rombakstøtta are slightly higher in parts of the NNE-facing slope ($> 60°$) than the SSW-facing slope ($< 60°$ steep), as we only applied monthly SOs on slopes steeper than 60°. In the simulation "Without monthly offsets" for Rombakstøtta, GTs are much lower on the NNE-facing rock wall than on the SSW-facing slope (Fig. 5l).

4.2.4 Thermal impact of glaciers

GTs are simulated to be higher beneath the warm-based glaciers at Veslpiggen, with no permafrost beneath the thickest parts of the glaciers (Fig. 5a). The ground below the thinner glacier sections is, nevertheless, underlain by permafrost. Removing glaciers below the Veslpiggen Plateau leads to major changes in the main heat flux direction, from the tilted heat flux (between the E-facing slope towards the blockfield-covered plateau), to the one-dimensional vertical heat flux in the "Without glaciers" simulation (Fig. 5b; Video 11). The modelled GT in the Galdhøe Plateau is much less thermally affected by glaciers than the Veslpiggen Plateau and is almost

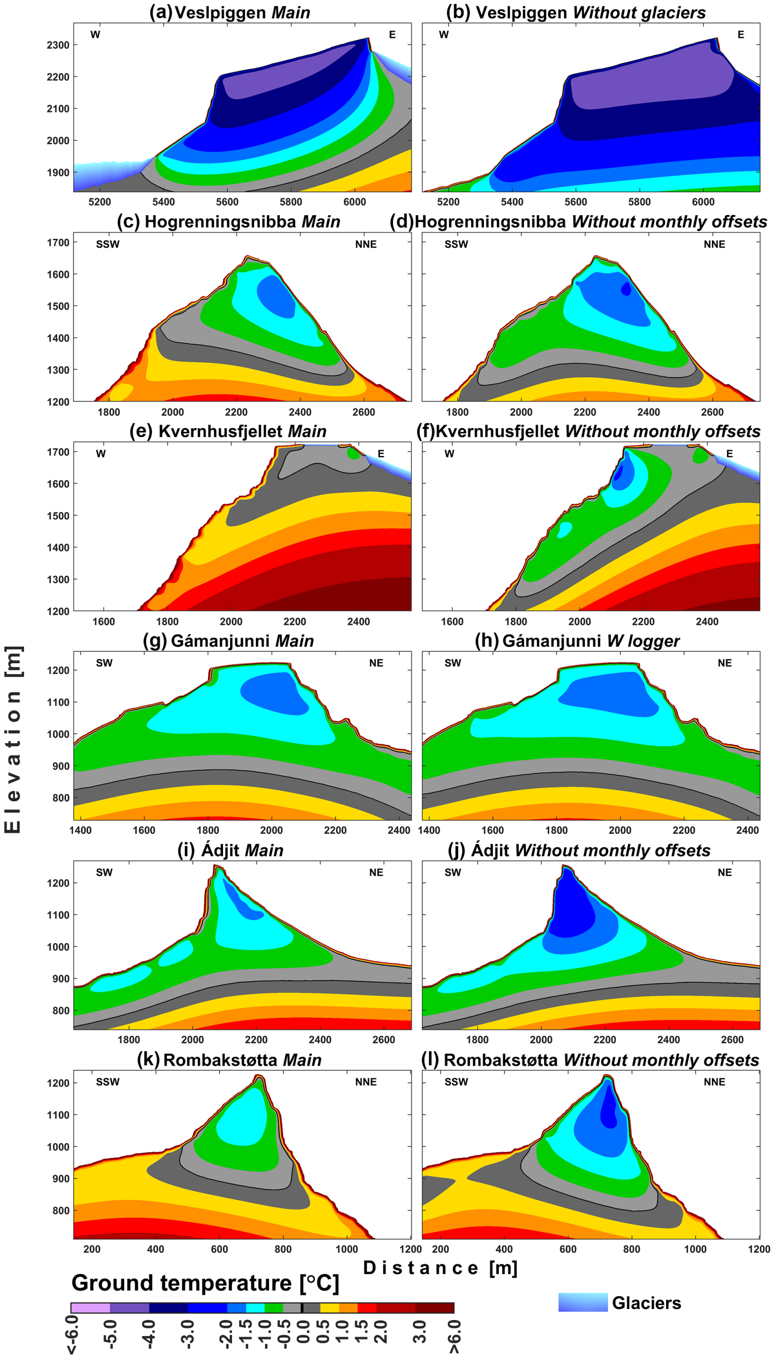

Figure 5. Simulated average annual maximum ground temperature over the 2010s for various simulations.

the same in the main simulation and the simulation without glaciers (Video 14), since there are no glaciers reaching as high up the mountainside as on the flanks below the Veslpiggen Plateau. The warm-based glacier also contributes to slightly higher GTs in Kvernhusfjellet (Video 7).

4.2.5 Model sensitivity: coldest and warmest simulations

Modelled GT is lowest in the simulations without SOs ("Without monthly offsets") or with 1 °C lower SAT ("T-1 °C") for all profiles (Videos 1–20). The coldest simulations for Mannen and Ramnanosi reveal that warm permafrost ($> -2\,^{\circ}\mathrm{C}$) or permafrost pockets could have existed in these mountains over colder periods or at the beginning of the 20th century (Videos 1 and 3). The simulations with less snow ("$\mathrm{nF}+0.1$") show almost as low GT as the "$T-1\,^{\circ}\mathrm{C}$" simulations for some profiles (e.g. Veslpiggen, Galdhøe). For Ádjit and Gámanjunni, tested uncertainties in the water content affect the results much less than the uncertainty in the GST forcing and slightly less than the uncertainty in snow conditions.

Highest GT is most often modelled in the simulations with "$T+1\,^{\circ}\mathrm{C}$", except for Jotunheimen. In Jotunheimen, the sensitivity simulations display the highest GTs for "Blockfields $\mathrm{nF}=0.4$", where snow conditions are changed substantially for the widespread blockfield-covered plateaus (Videos 9, 10, 12, 13). The assumed snow conditions at the blockfield locations at Veslpiggen have a large thermal influence on deeper GTs in the rock walls. For the Veslpiggen and Galdhøe profiles, the warmest simulation "Blockfields $\mathrm{nF}=0.4$" indicates that the coldest permafrost areas are below the NW- or W-facing rock walls, whereas in the main simulation the coldest permafrost is modelled below the blockfield-covered plateaus (Video 9 and 12). SOs arising from solar radiation and SAT forcing are thus the most important factors for modelled GT within the tested values for most profiles; however, snow conditions may have a larger influence if the nF factor is changed substantially for large areas.

4.2.6 Elevational distribution of GT at 20 m depth

We also analyse the distribution of GT in rock walls at 20 m depth, in relation to elevation for all simulations and profiles (Fig. S22). Simulations "Without monthly offsets" generally yield the coldest midsection in a single rock wall, whereas most other simulations differ from these results, except for the simulations using data from the north-facing loggers for Kvernhusfjellet and Ramnanosi, which have small average annual SOs ($\sim 0.5\,^{\circ}\mathrm{C}$). Higher rock walls ($> 50$ m high, e.g. Veslpiggen) have the highest GTs in their midsection for simulations with large SOs (Fig. 6c). For the smaller rock walls (e.g. Gámanjunni, Kvernhusfjellet), the GT at 20 m depth changes with elevation, depending on the distribution of the various terrain types in the vicinity of a single rock wall (Fig. 6b and d). GT increases with elevation if the terrain above a single rock wall is gentler than the terrain below this single rock wall, and the opposite is modelled if the terrain above is steeper than the terrain below. Thus, 20 m GT distribution in smaller rock walls is predominantly due to snow cover distribution in the rock wall vicinity. The thermal influence of snow cover on the plateau is also evident for larger rock walls below mountain plateaus (e.g. Rombakstøtta), where the GT increases with elevation from the midpoint of a rock wall section (Fig. 6). The uppermost east-facing rock wall at ~ 2300 m at Veslpiggen in Fig. 6e has glaciers below and blockfields above, and GT decreases with elevation due to the large thermal influence of the glaciers.

4.3 Ground temperature trends in rock walls

Modelled GT trends since the 1900s are shown in Fig. 7. The steepest parts of the profiles are the most responsive to both warming and cooling trends in GST. However, modelled GT in the blockfields in Jotunheimen is also strongly coupled with SAT in our simulations, since we applied a high nF factor. Furthermore, 2D effects largely influence modelled GT trends in the uppermost parts of the narrow mountain peaks (Ádjit, Rombakstøtta).

The 1900s–1930s

Modelled GT at 20 m depth increased by less than 0.1 °C per decade at the sites in southern Norway, except for Ramnanosi, which had a negative trend in SAT10a at the beginning of the 20th century (Fig. A1). The sites in northern Norway had the largest SAT10a rise at the beginning of the 20th century (Fig. A1); therefore, simulated GT increase is larger between the 1900s and 1930s than between the 1980s and 2010s.

The 1930s–1980s

Modelled GTs at 20 m depth remained similar ($< 0.05\,^{\circ}\mathrm{C}$ per decade) between the 1930s and 1980s for the sites in southern Norway. Modelled GT in northern Norway slightly decreased at depths below 20 m and increased at depths deeper than 20 m in some areas due to a rise in atmospheric temperature in the early 20th century.

The 1980s–2010s

Simulated GTs at 20 m depth increased between the 1980s and 2010s with a rate of 0.1–0.35 °C per decade (Fig. 7). The 1980s–2010s ground warming reaches deeper than the 1900s–1930s ground warming. Rombakstøtta has similar cooling and warming trends to the other sites in northern Norway; however, increases of both SAT10a and simulated GT are higher since the 1980s (Fig. 7u).

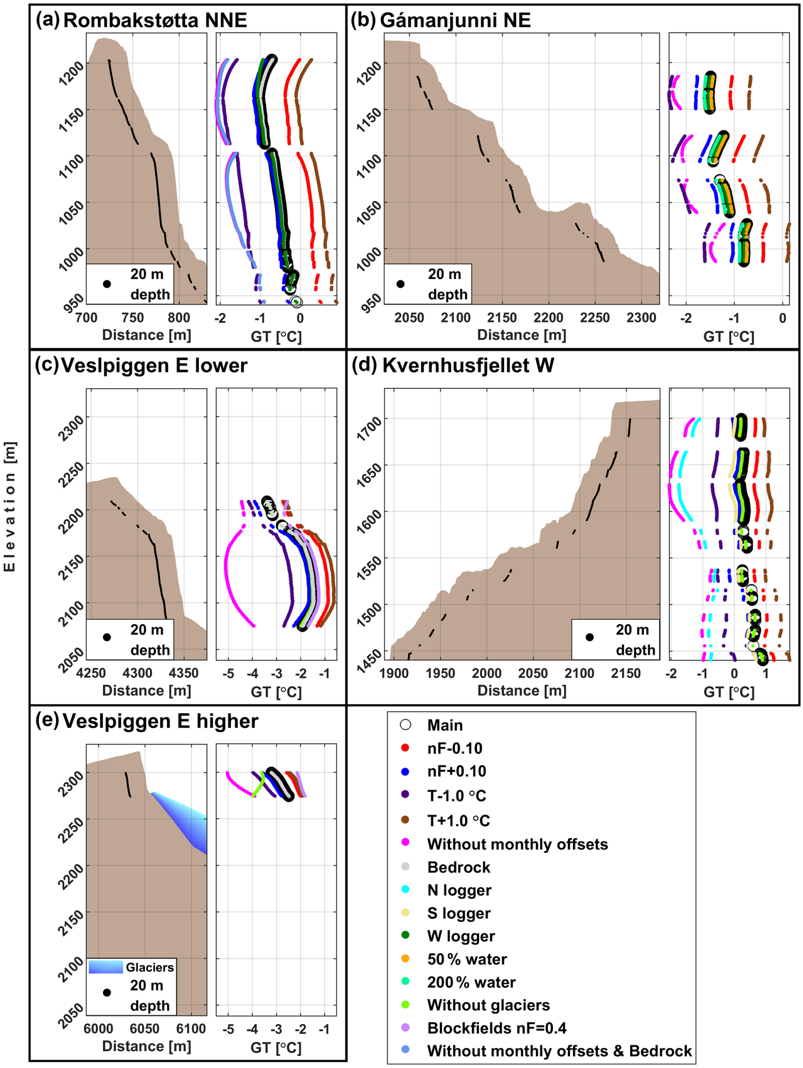

Figure 6. Simulated ground temperature (GT) in rock walls at 20 m depth for various profiles over the 2010s. Right subplots show ground temperature in nodes depicted in the left subplots.

Over the last 4 decades, SAT at the rock wall elevations along the profiles increased by 0.25–0.4 °C per decade, with the largest warming rates in Jotunheimen and at Rombakstøtta (Fig. 8a, c, e and g). We reconstructed the same SAT trends along each profile elevation wise, whereas modelled trends of GT at 20 m depth have a more complex pattern elevation wise (Fig. 8b, d, f, and h); however, the largest simulated values are still in Jotunheimen and at Rombakstøtta. The simulation results show that GT at 20 m depth increased on average by 0.2 °C per decade in the rock walls. The Jotunheimen area has the largest modelled mean 20 m GT increase (0.25 °C per decade), likely because we allowed blockfield-covered plateaus to be relatively strongly coupled with SAT; hence two-dimensional warming is more effective in rock walls below plateaus. Ádjit has larger warming rates than Gámanjunni, especially at higher elevations, pointing to the increasing importance of the two-dimensionality since the former has a sharper peak. In general, modelled warming

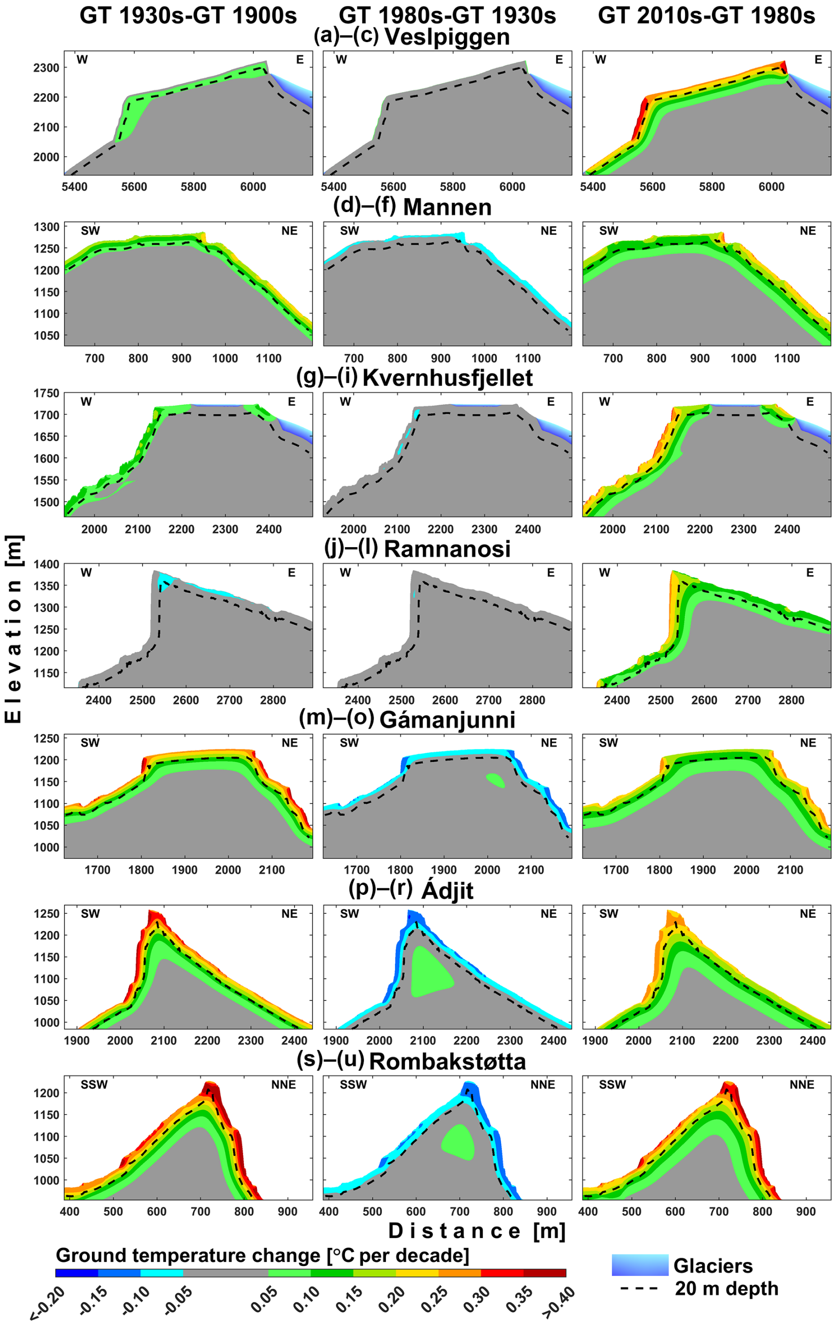

Figure 7. Rate of change in simulated decadal mean ground temperature (GT) for the various profiles between the following decades: (1) the 1900s and 1930s, (2) the 1930s and 1980s, and (3) the 1980s and 2010s.

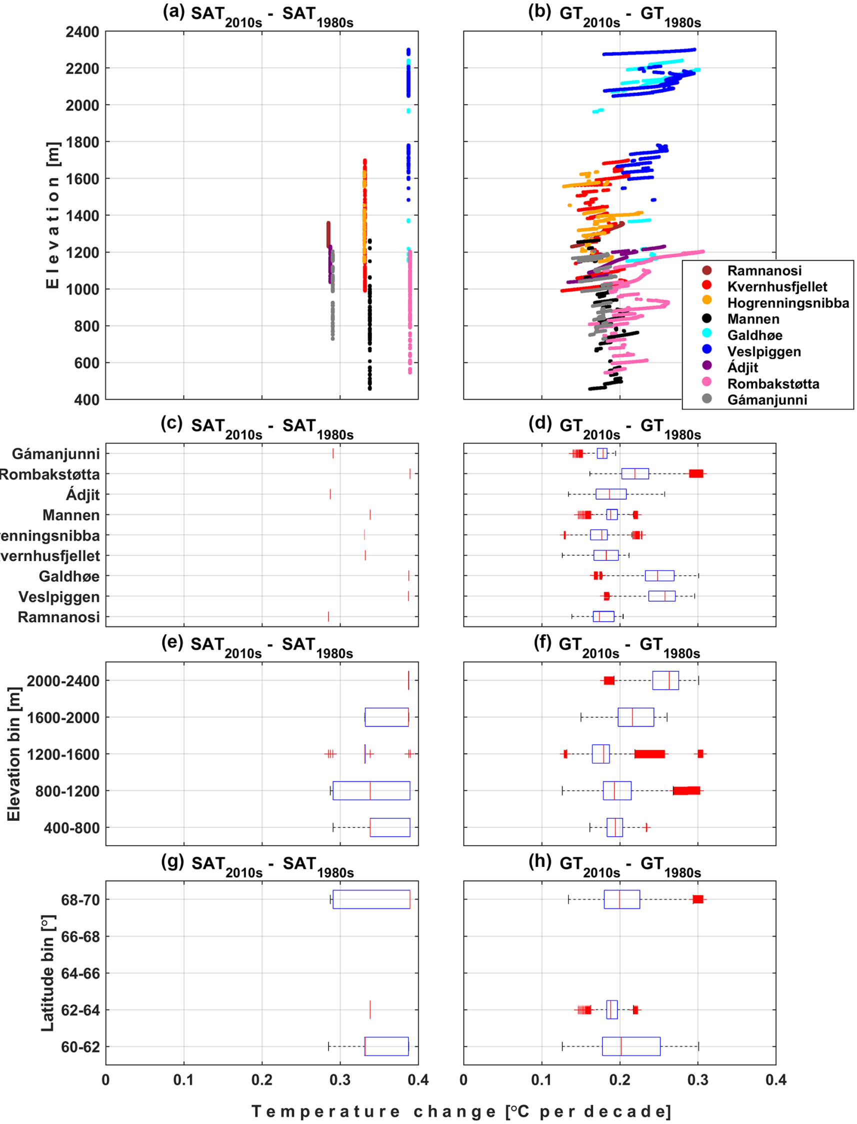

Figure 8. Modelled rates of surface air temperature (SAT) and ground temperature (GT) change at 20 m depth between the 1980s and 2010s for all nodes below steep rock slopes (slope gradient > 60°). Lower subplots: boxplots with SAT and GT rise between the 1980s and 2010s for **(c, d)** every profile, **(e, f)** 400 m elevation bins and **(g, h)** 2° latitude bins.

rates seem to increase towards the uppermost part of a single rock wall section. We simulated similar patterns in the previous simulations using the seNorge data set when SAT increase rates in some cases decreased with elevation. The 2D effects are expected to increase with elevation in a single rock wall just based on the topography of the study sites. For a 2D profile, the distance from surface above a rock wall to a 20 m depth in a rock wall below is shorter than the distance from surface below a rock wall to a 20 m depth in a rock wall above. Generally, ground warming rates at 20 m depth seem to be independent of latitude (Fig. 8h) and slightly increase with elevation (Fig. 8f).

Sensitivity of the modelled GT rise at 20 m depth between the 1980s and 2010s (Fig. S23) shows that for most simulations warming rates increase with elevation. There are, nevertheless, a few exceptions.

1. Warming rates may decrease with elevation for rock walls that are convex in the upper parts due to the assumed snow accumulation in the less steep parts.
2. For parts of rock walls where permafrost thawed at 20 m depth between the 1980s and 2010s, warming rate is larger (some simulations for Ádjit, Hogrenningsnibba, Ramnanosi, Rombakstøtta). Even small latent heat effects in permafrost slightly retard warming, and this effect disappears when permafrost is absent. However, warming retardation due to the latent heat effects depends on the ice content and results from the assumed 5 % vol. ice content for fully frozen ground; thus, for lower ice contents, latent heat effects are smaller.

Glaciers reduce ground warming in nearby steep rock faces, e.g. the east-facing rock wall in Jotunheimen has higher modelled GT increase in the simulation “Without glaciers” (Fig. S23). Otherwise, the assumed snow conditions have the greatest influence on simulated warming rates, i.e. any snow accumulation in rock walls leads to lower warming rates. Snow cover in the rock wall vicinity also influences modelled warming rates, e.g. rock walls below plateaus or rock ledges in Jotunheimen have smaller warming rates if more snow is applied above them.

5 Discussion

5.1 Limitations and strengths

5.1.1 Subsurface heat transfer

The CryoGrid 2D model is based entirely on thermal conduction, which is the dominant heat transfer process in the ground (Williams and Smith, 1989). However, non-conductive thermal processes along with discontinuities and within the cracks, such as air convection or advection by moving water, may contribute to the subsurface thermal regime (e.g. Draebing et al., 2014; Magnin and Josnin, 2021). Many discontinuities may exist in the bedrock and may be further widened by frost weathering processes, allowing for the generation of pathways for advective heat transfer to occur. The exact configuration of bedrock discontinuities is unavailable, making it unfeasible to include them in our modelling. A study by Hasler et al. (2011b) in the Swiss Alps showed that whereas heat advection by percolating water has a negligible thermal impact, air ventilation likely causes thermal offsets similar to the offsets in coarse sediments, and values of up to 3 °C are reported. Since cracks exist on the plateau above Mannen (Saintot et al., 2012) and Ramnanosi, air ventilation could lower GT in the area; however, since thick snow cover accumulates on the Mannen Plateau, plugging of the cracks with snow could prevent air ventilation (e.g. Blikra and Christiansen, 2014). Another study by Moore et al. (2011) analysed deep GT profiles and attributed their disturbed profiles to localised convection cells in the fractures, whereas seasonal water infiltration had a minor influence on GTs. Nevertheless, several studies still emphasise the importance of advective heat input for GTs in permafrost-underlain terrain (e.g. Krautblatter and Hauck, 2007; Hasler et al., 2011a; Magnin and Josnin, 2021). A study by Magnin et al. (2017a) showed, however, that non-conductive thermal processes are only relevant in the upper 6 m below the ground surface. It is also noteworthy that conductive heat transfer in discontinuities filled with ice would alter GTs, i.e. ice infills in permafrost could act as major heat sinks (Magnin and Josnin, 2021). If ice- or water-filled fractures exist inside the bedrock, this would locally delay permafrost thawing or formation due to latent heat effects (Magnin and Josnin, 2021).

Air convection is likely responsible for the observed negative thermal anomalies in coarse-sediment landforms, such as blockfields (Heggem et al., 2005), rock glaciers (Wicky and Hauck, 2020) and talus slopes (Lambiel and Pieracci, 2008; Wicky and Hauck, 2017). Studies by Juliussen and Humlum (2008) and Gruber and Hoelze (2008) show examples of how conductive heat transfer could account for the negative thermal anomalies in the blockfields. Even though views of these authors on the governing mechanisms could be implemented in our model, the thermal processes responsible are yet to be proven. In our study, negative thermal anomalies in the blockfields and rock glaciers are at least partly accounted for through the larger nF factors than in the other sediment cover types.

Furthermore, the CryoGrid 2D model considers the 2D heat diffusion, which is an advance compared with the 1D case; nevertheless, heat transfer processes in complex terrain occur three-dimensionally (Noetzli et al., 2007; Noetzli and Gruber, 2009). Myhra et al. (2017) argued that even though this is a limitation of the CryoGrid 2D model, applying it to the Norwegian mountains with flat plateaus and long valleys could be adequate. We note that our transects are only approximately suitable for two-dimensional heat conduction, yet they still follow the general characteristics of the slope and are representative of their surroundings. Magnin et al. (2017a) employed a similar 2D model to ours and validated their data against rock wall boreholes. The authors claimed that the 3D effects were likely of little importance for GT, and the 2D modelling approach was sufficient for sharp topography in the European Alps. Despite these findings, our 2D approach could potentially underestimate the GT trends in areas where the GST signal penetrates from more than two sides, as modelled in Noetzli and Gruber (2009).

5.1.2 Model forcing

The CryoGrid 2D model was forced using lapse-rate-adjusted SATs, together with the measured average monthly SOs in steep rock faces. Even though the number of meteorological stations is low in the mountains in Norway, they are still well correlated with the rock wall logger data after adjustments for the monthly SOs. There are uncertainties in lapse rates, and the reconstructed long-time forcing is especially uncertain. Moreover, we had to use the seNorge data set for certain sites, which is based on the spatial interpolation between the in situ data (Lussana et al., 2018).

Furthermore, we only force the model directly with GST, instead of including a surface energy balance, as for instance in Noetzli et al. (2007). We applied the same SOs to each year, based on the average offsets between GST and SAT, which could otherwise be modelled using surface energy balance. However, we lack data to be able to implement such an approach at the timescales used in this study. Snow cover and solar radiation are the main controlling factors for GST in the rock walls (Haberkorn et al., 2015), and snow cover governs the distribution of GST in the gentle terrain in Norway (Farbrot et al., 2011; Gisnås et al., 2014); hence, our methods account for the most important SOs measured in Norway. Magnin et al. (2017a) showed that a similar approach, i.e. without energy balance and consideration of snow accumulation in rock walls, was appropriate to reproduce temperature below steep flanks of sharp mountain peaks at depths > 6 or > 8 m by comparing the modelled temperature to the measured temperature profiles in boreholes. For shallower depths, additional effects of non-conductive heat transfer and local snow accumulations, that were ignored in the modelling, caused substantial temperature differences.

Our analysis of the 2 h temperature suggests that solar radiation is most likely the main controlling factor for SOs in Norwegian rock walls, as also shown in Magnin et al. (2019). Large increases in maximum daily temperature can be seen in the rock wall temperature series, pointing to solar radiation as the dominant source of energy that modifies GSTs. North-facing slopes in Norway can receive enough shortwave radiation to have mean annual SOs of around 0.5–1.5 °C (Fig. 3); hence, ignoring SOs would lead to much lower GTs even for this exposition. Similar ranges of average SOs were measured in the small cliffs in the north-facing loggers in northern Norway (Frauenfelder et al., 2018). Furthermore, we note that we did not apply non-nival SOs to moderately steep slopes ($< 60°$ gradient), since it is unlikely that the observed non-nival SOs are as large as in the monitored slopes. For instance, Hasler et al. (2011b) suggested that late-lying snow lowers GST in moderately steep slopes, due to the reduction of the incoming shortwave radiation.

5.1.3 Snow distribution

One of the CryoGrid 2D model limitations is the lack of a snow domain; hence, we apply nF factors for the gentle and medium-steep terrain. Preferably, snow depth should be described dynamically, both temporally and spatially, including snow redistribution by avalanching and wind. However, research concerning snow distribution on steep rock walls in Norway is lacking; hence there are large uncertainties in snow depth and its timing. Studies we reviewed from elsewhere had contrasting results about snow distribution in the steep rock walls: (1) certain studies suggest that steep slopes above a certain threshold (e.g. more than 45, 50, 60 or 70°) cannot accumulate permanent snow cover due to avalanching or wind drift (Blöschl et al., 1991; Kirnbauer et al., 1991; Blöschl and Kirnbauer, 1992; Winstral et al., 2002; Machguth et al., 2006), and (2) other studies, often using airborne or terrestrial laser scanning, show that almost any slope gradient can accumulate snow (Wirz et al., 2011; Sommer et al., 2015). The latter group of studies, nevertheless, recognises that snow cover is limited in steeper terrain and accumulates less snow than gentler terrain. Furthermore, the studies use various parameters as the most crucial to explain snow distribution in steep terrain, e.g. (1) snow-free slope angle (Blöschl and Kirnbauer, 1992; Sommer et al., 2015), (2) terrain–wind interaction (Winstral et al., 2002; Wirz et al., 2011) and (3) elevation and terrain roughness, which possibly correlates with the summer slope angle (Lehning et al., 2011). We note, however, that we used a high-resolution DEM of at least 1 m resolution to construct each profile, and 1 m DEM was considered precise enough to detect rock ledges in the Swiss Alps, where snow can accumulate (Haberkorn et al., 2017), and such areas have snow cover in our study. Snow distribution in rock walls in Norway remains to be quantified, e.g. using LIDAR-scanning, and its governing factors recognised.

5.1.4 Thermal influence of snow

Snow cover could either insulate or cool the ground. The overall effect of snow cover on GT is complex because it depends on snow thickness, duration, timing, melting processes within a snowpack, snow structure (Zhang, 2005), sun exposure (Magnin et al., 2017b), MAAT, substrate, the thickness of the active layer, and ground moisture (Throop et al., 2012) or snow density. Snow cover affects GT in both steep and gentle terrain in multiple ways.

1. As an additional buffer layer with low thermal conductivity, snow insulates the ground, given that SAT is lower than GT and snow cover is sufficiently thick, e.g. at least 0.6 m in the gentle terrain (Luetschg et al., 2008) or even 0.2 m in the rock walls (Haberkorn et al., 2015). This is likely the most important net thermal impact of snow on the GTs in Norway. Observed differences between GST and SAT are positive at most permafrost

sites in Norway (Farbrot et al., 2011), and as shown in this study (Fig. 3), all measured mean annual SOs in the rock walls are positive; hence, the overall annual cooling of the ground surface due to snow cover is not observed in Norway. We note that the installed rock wall loggers in Norway should measure only snow-free rock walls by design (Magnin et al., 2019); hence, the available measurements are insufficient to preclude cooling due to snow cover.

We assumed that rock walls are snow-free because our analysis of the measured rock wall temperature in Norway indicates only minor thermal influence of snow, as also mentioned in Magnin et al. (2019). We note, however, that the computed mean monthly SOs (Fig. 3) also account for thermal effects of snow cover if there are any; hence, rock walls are not sensu stricto snow free in this study. For instance, W- and N-facing loggers at Gámanjunni have approximately 1 °C higher temperature than the south-facing logger (Fig. 3e) in December and January, which is likely due to snow cover. The temperatures from the rock wall loggers at Rombakstøtta are probably the most influenced by snow, e.g. the temperature from the W-facing logger is lower than the temperature from the N-facing logger in May (Fig. 3d), and the temperatures from both the E- and W-facing loggers sometimes show much smaller standard deviation of daily temperatures compared with the temperature from the N-facing logger, which is likely the least snow-influenced logger in this area.

2. Snow cover increases albedo of the surface, thus reducing absorbed shortwave radiation, meaning late-lying snow would delay or reduce the spring warming of the ground (e.g. Hasler et al., 2011b; Magnin et al., 2017b). This cooling effect was concluded to be a major cooling mechanism on the thinly snow-covered rock walls in the Mont Blanc massif (Magnin et al., 2015). However, this cooling hypothesis was concluded to be of little importance in the study by Haberkorn et al. (2017), who show that sun-exposed snow-covered rock walls are typically warmer than snow-free rock walls due to reduced ground heat loss in winter, i.e. point 1 above. Moreover, snow requires large energy inputs to melt; hence GT is lower than SAT during snowmelt; however, this usually lasts for a short time and may be unimportant on annual timescales (Zhang, 2005). However, meltwater percolating inside cracks can refreeze and act as an additional heat source or favour accelerated melting of the cleft ice (Hasler et al., 2011a).

3. High emissivity of snow increases the outgoing longwave radiation; however, its high absorptivity has the opposite effect. Hence, thermal impact of emissivity and absorptivity on snow temperature is influenced by atmospheric conditions (Zhang, 2005).

4. During autumn, thin snow cover could lead to an enhanced conductive heat flux from the ground due to large thermal gradients between the cooled snow surface and warmer upper ground layers (Keller and Gubler, 1993; Luetschg et al., 2008). Furthermore, in the low-snow years, GT at the top of permafrost is relatively constant during freezeback and may be higher than GST that is coupled to SAT, leading to positive thermal offsets (Palmer et al., 2012). In addition, temporary ground cooling was observed at several sites across Switzerland during one or two winters in 2015–2017, when snow cover arrived very late and was thinner than usual (PERMOS, 2019; Noetzli et al., 2020). The latter cooling effect was not recorded at steep bedrock sites, where GT is usually insensitive or less sensitive to snow cover changes (PERMOS, 2019; Noetzli et al., 2020).

5. Deposition of snow may reduce ventilation effects in clefts (Hasler et al., 2011b).

6. If snow accumulates under rock walls or on rock ledges, the incoming shortwave radiation may be reflected diffusively towards snow-free parts of the rock wall, hence warming it. The latter effect is less investigated in permafrost studies, although its importance was emphasised in the surface energy balance modelling of the high-arctic rock walls in Svalbard by Schmidt et al. (2021) and mentioned in Fiddes et al. (2015). We speculate that the reflected shortwave from surrounding snow-covered surfaces may be important in some rock wall aspects in Norway because measured rock wall temperatures at 2 h intervals often show a distinct daily temperature distribution due to shortwave solar radiation during late winter or spring. Such a temperature increase is even measured in February in northern Norway. A similar temperature increase is not observed at the same magnitude during autumn, when snow is less common. We recognise, however, that this seasonality could be related to cloud cover, issues with lapse rate or cooling effects of thin snow cover during autumn. Additionally, rock walls just above glaciers, e.g. in Jotunheimen, may likely be affected by reflected solar radiation from the glaciers all year round, and measurements from the east-facing rock walls just above the glaciers show particularly large SOs (Fig. 3g). Hasler et al. (2011b) also state that south- and east-facing rock faces above glaciers in the Swiss Alps experience extreme solar radiation. Nevertheless, the observed SOs in Jotunheimen could be a result of the dark rocks in this area, which have a lower albedo compared with the bedrock at the other sites presented in this study.

5.2 Comparison to borehole data, geophysical surveys and other studies

5.2.1 Western Norway

At Mannen, both the geophysical surveys presented in Etzelmüller et al. (2022) and our thermal modelling suggest that permafrost may only occur sporadically in this area. Nevertheless, high resistivity values ($> 20\,\mathrm{k\Omega m}$) measured in this area could also reflect very good water drainage conditions, due to highly fractured bedrock or even ion-poor pore water (Dalsegg and Rønning, 2012).

5.2.2 The Jotunheimen Mountains

Results from thermal simulations, both the modelled GTs and deeper warming rates, are in good agreement with the available borehole data in the Jotunheimen Mountains (Fig. S24 and Table S5), although there are variations in snow conditions between the boreholes; hence, we compared the measurements to various snow sensitivity simulations. For the BH5 borehole in Jotunheimen (Fig. 1d) and nearby gentle slopes, geophysical surveys performed in 1999 and 2010, together with numerical modelling, indicated the degradation of permafrost over the intervening decade (Isaksen et al. 2011). We compared the modelled subsurface thermal fields for Galdhøe to the geophysical surveys from 1999 and 2010, and our results show a similar pattern of possible permafrost degradation in this marginal permafrost area (Fig. S25). The results are especially similar for the sensitivity simulation with less snow (“nF + 0.1”).

5.2.3 Northern Norway

Three-dimensional GT modelling of the Polvartinden Mountain, around 30 km north-east of Ádjit, which suggested the lower permafrost limits at 600–650 m over the last few years (Frauenfelder et al., 2018), is in agreement with our results. Furthermore, the local permafrost limit at an elevation of around 700 m, derived from various temperature measurements at the Jettan rockslide (Blikra and Christiansen, 2014), 12 km NW of Gámanjunni, is in accordance with our modelled permafrost limit for less sun-exposed slopes. The simulations by Etzelmüller et al. (2022) for Gámanjunni show a slightly different subsurface GT field, due to different model forcing. However, geophysical surveys reproduce the main patterns of the modelled subsurface thermal field at Gámanjunni presented in our study and Etzelmüller et al. (2022). The geophysical surveys at Gámanjunni indicate (1) the thermal influence of the NW and SW facing rock walls, (2) higher resistivity (i.e. cooler conditions) in the scree below the SW-facing rock wall and (3) a warmer subsurface below the snow-covered plateau. In comparison with Etzelmüller et al. (2022), our thermal fields show that (1) and (2) agree even better with the geophysical surveys because we accounted for the additional surface offsets in the SW-facing rock wall. The conductive thermal field is slightly perturbed by the non-conductive heat transfer mechanisms in larger fractures. Etzelmüller et al. (2022) argued that comparison of the modelled ground temperature and geophysical surveys is useless at smaller scales, due to high resistivity variations in rough terrain, influenced by cracks and fractures, strong topographic variations and local water infiltration.

5.3 Thermal regime in steep slopes

Due to the strong coupling of GST and SAT in rock walls, rock walls may have lower GT compared with the surrounding terrain, and permafrost aggradation may occur much faster in them than in other types of terrain in the decreasing SAT conditions, as shown by Myhra et al. (2017). However, sun-exposed large rock walls may allow more heat to enter the mountain. One example is Kvernhusfjellet, where the lower limit of permafrost is modelled at 1620 m over the last few years, which is higher than at the moderately steep Hogrenningsnibba, where the modelled permafrost limit has been at 1450 m. In Norway, permafrost research on moderately steep terrain is yet to be conducted, since there are large uncertainties in both snow distribution and SOs in moderately steep terrain in Norway. However, our results agree with the conclusions of Magnin et al. (2019) that the permafrost limits may be higher in the sun-exposed rock walls than in the less-steep terrain.

We constructed meshes for various topographies and extended the previously presented 2D modelling for Norway (Myhra et al., 2017), mainly by including SOs. Whereas previous results mostly showed the midsection along a single rock wall as the coldest, our simulations show the midsection, or more precisely the lower portions of the midsection, in some cases as the warmest along the rock wall (at 20 m depth), barring the north-facing rock walls. The sensitivity simulations where we omitted SOs show the same results as in Myhra et al. (2017) with the much colder midsections. Because the rock wall data from Norway indicated average annual SOs of at least 0.5 °C, the colder midsections in the north-facing slopes are less pronounced in the main simulations when compared with the simulations without SOs. Our results also show that scree slopes may be warmer than rock walls if SOs are large enough, e.g. 3 °C. The latter is in discordance with the study by Myhra et al. (2019), where rock walls had a cooling effect on scree slopes; however, we note that they still agree for rock walls with minimal SOs. The simulated subsurface thermal fields are more similar to the results from 3D modelling in the European Alps (Noetzli and Gruber, 2009), especially for Hogrenningsnibba, which has the most similar geometry to the one presented in that study. Our simulations show similar distribution of the isotherms to the ones from the European Alps, except that the isotherms inside Hogrenningsnibba are less inclined. This is expected since the difference in rock surface temperature between the north- and south-facing slopes is smaller than in the European Alps, as discussed in Magnin et al. (2019). Slope steepness is, however, also an important factor influencing the subsurface thermal field. Ádjit is the narrowest ridge presented in this study and although the measured mean annual GST difference between the north- and south-facing slopes is below 2 °C, almost horizontal heat flux direction between the opposite mountainsides is often modelled. This suggests an increasing sensitivity of the subsurface thermal fields to small differences in forcing for the steep and narrow terrain. For instance, the modelled subsurface thermal field for the nearby less steep and less narrow Polvartinden indicates almost horizontal isotherms (Frauenfelder et al., 2018). We note, however, that the differences in SOs for various aspects presented in the latter study were smaller, around 1 °C. The modelled GT in the Hogrenningsnibba profile also indicates that permafrost may underlie a warmer mountainside with positive MAGSTs, due to permafrost occurrence in a colder mountainside, as shown in the studies of Noetzli et al. (2007) and Noetzli and Gruber (2009).

The importance of multi-dimensionality for the rates of GT rise was previously investigated in the studies by Noetzli et al. (2007) and Noetzli and Gruber (2009), where it was shown that surface warming penetrates steeper topography from several sides, thus leading to a faster pace of ground warming compared with flatter topography. Our study also suggests that multi-dimensionality in mountain ridges is an important factor, although we only investigated a 2D case. The simulated rise in GT increases with elevation, generally when the terrain is more exposed to surface warming penetration. The modelled warming rate of on average 0.25 °C per decade in rock walls in Jotunheimen over the 1980s–2010s is slightly higher than the warming rate of 0.2 °C per decade measured at 20 m depth in the deep borehole at Juvvasshøe since 1999 (Smith et al., 2021). GT in this borehole is strongly coupled with SAT, and the borehole has an nF factor of around 0.9.

5.4 Geomorphological implications

Our study focuses on rock wall permafrost evolution in Norway since the end of the Little Ice Age. The results indicate a substantial increase of GT at 20 m depth since the 1980s at all sites in Norway. Although the mechanical implications of this warming are not considered in our modelling, the ground thermal regime itself has an important influence on geomorphological processes in periglacial regions (e.g. Berthling and Etzelmüller, 2011) and ultimately landscape development (e.g. Egholm et al., 2015). The ground thermal regime and its temporal development in steep slopes is associated with the weakening of rock bonds, the widening of cracks and the potential for frost weathering processes. Several authors have linked permafrost degradation and destabilisation of slopes (e.g. Davies et al., 2000, 2001; Gruber and Haeberli, 2007; Krautblatter et al., 2013). Conductive warming of ice-filled fractures, which stabilise permafrost-underlain mountains (e.g. Dramis et al., 1995), may result in (1) loss of joint bonding and reduction of shear strength of the joint due to water release through ice melting and (2) shear strength changes due to mechanical ice properties that are a function of the normal stress and temperature (Davies et al., 2001). Furthermore, advective heat transport by percolating meltwater may result in rapid, local degradation of rock wall permafrost, which can trigger rockfalls even in cold permafrost areas (Hasler et al., 2011a). In addition, rock-mechanical properties depend on rock temperature (Krautblatter et al., 2013); hence, thawing can lead to a substantial drop in rock strength. Frost weathering processes caused by ice segregation or volumetric expansion of in situ water contribute to the generation of weakness planes or fracture widening in frost-affected rocks (Gruber and Haeberli, 2007; Krautblatter et al., 2013). It is uncertain how the modelled spatial and temporal variations in GT may affect slope stability. Our results suggest that ground warming increases with elevation within a single rock wall section; hence, this may indicate that instability risk increases with elevation for a single rock wall section. However, GT may be highest in the middle of the rock wall; hence, this part may be more susceptible to permafrost degradation in the sun-exposed rock walls. Furthermore, shaded rock walls may act as “refrigerators” in the landscape due to low snow cover within the rock walls and small amounts of solar radiation (e.g. Myhra et al., 2017). Thus, these landscape areas are locations for steep thermal gradients on the transition of snow-free steep rock walls and snow-covered more gentle terrain. This is exemplified in other studies and formerly addressed by Myhra et al. (2019) for the upper parts of talus slopes or rock glaciers below shaded rock walls, for cirques (Sanders et al., 2012) and below coastal cliffs in Arctic settings (Ødegård and Sollid, 1993; Wangensteen et al., 2007; Schmidt et al., 2021). All these settings influence frost weathering, as these strong thermal gradients favour frost segregation and frost cracking (Hales and Roering, 2007). Similar processes are also discussed for snow patches in relation to nivation processes (Berrisford, 1991). Thus, especially the constant change of ground thermal regime associated with rock walls and their vicinity facilitates material production and further geomorphological transport processes.

6 Conclusions

From this study, the following conclusions could be drawn.

1. Permafrost is likely discontinuous along most of the modelled profiles. Rock walls at the highest elevations in the Jotunheimen Mountains are in the continuous permafrost zone. The simulations suggest no permafrost in Mannen and Ramnanosi. However, convective heat transfer along discontinuities at both Mannen and Ram-

nanosi could lower GT; hence, both sites could be underlain by sporadic permafrost.

2. Rock walls in northern Norway experienced larger GT variations after LIA than rock walls in southern Norway, since both the 1930s atmospheric warming and the 1970s–80s cooling were more pronounced in the north. All simulations show increasing GT since the 1980s. Rock walls in Norway are warming by 0.2 °C per decade on average at 20 m depth over the last 3 decades.

3. Many of the modelled sites lie close to the lower boundary of mountain permafrost; hence, the modelled GT is sensitive to the changes in the forcing. Within the tested forcing, uncertainties in the SAT led to the largest changes in the modelled GT. Neglecting SOs may lead to much lower GT in the rock walls, even in Norway.

4. The rock wall exposition and its size appear to be important modifying factors for permafrost distribution in the mountains. High rock walls, higher than 50 m, or several small rock walls (< 50 m high) allow effective ground cooling and lead to lower permafrost limits in the mountain if SOs are not too large (e.g. Gámanjunni). High rock walls or several small rock walls may also allow more heat to enter a mountain and sun-exposed rock walls may even have higher permafrost limits than moderately steep terrain (e.g. Kvernhusfjellet).

5. The elevational distribution of GT at 20 m depth is influenced by the assumed snow conditions above and below rock walls; this is especially pronounced for smaller rock walls. Larger rock walls and in some cases even smaller rock walls may have the coldest or warmest midsection depending on SOs. The north-facing rock walls usually have small SOs; hence their midsection is coldest. The rock walls with large SOs have warmest midsection.

6. The main ground heat flux direction is often one dimensional inside the mountains in Norway, especially below mountain plateaus or mountains with minimal difference in GST forcing between the opposite mountainsides (e.g. Rombakstøtta). The narrow ridges in Norway are, however, sensitive to even small differences in GSTs between opposite mountain faces (e.g. Ádjit).

7. Ground heat flux is modified in rock walls in Jotunheimen by blockfields and glaciers. GST in blockfields may be relatively strongly coupled with SAT, leading to lower GT and higher rates of GT increase (at 20 m depth) in rock walls close to blockfields. Glaciers reduce the magnitude of increases in GT in nearby parts of rock walls; however, in view of their potential future retreat, warming rates may increase in the closest parts of rock walls.

8. In rock walls with large SOs, plateaus above or talus below may be colder than the rock wall, forcing ground heat flux towards colder plateaus or talus slopes.

Appendix A: Surface air temperature trends

Atmospheric temperature has in general had a positive trend in Norway since the end of the LIA, with the largest changes occurring over the last 40 years. Figure A1 shows the decadal running mean surface air temperature (SAT10a) evolution for the highest elevations along each profile. In the first decade of the 20th century, SAT10a were -0.59 to -1.75 °C lower than over the last decade (2011–2020).

The warming during the early 20th century was largest in northern Norway, which experienced at least 1 °C warming between the 1900s and 1930s, whereas western Norway had around 0.4–0.7 °C warming in the same period. Ramnanosi is the site with the largest cooling trend at the beginning of the 20th century. Jotunheimen had only a small cooling between these decades. SAT10a was 0.5–0.7 °C lower in northern and western Norway between the 1930s and 1980s. In Jotunheimen, SAT10a increased between the 1930s and 1980s by around 0.4 °C, although we note that there was a slight cooling in the area in the early 1980s; however, it vanishes when the results are presented as a mean value for the whole 1980s. SAT10a increased by 0.86–1.16 °C at all study sites after the 1970s–1980s cooling. The recent warming is largest in Jotunheimen and at Rombakstøtta.

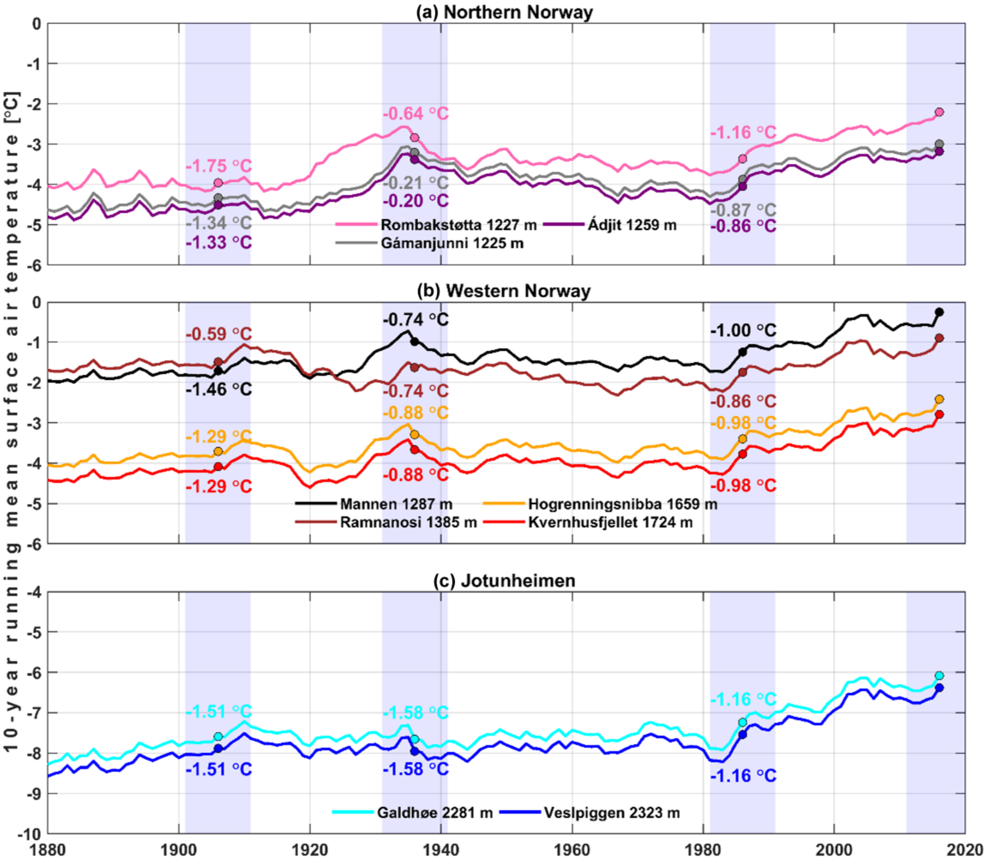

Figure A1. Decadal running mean surface air temperature (SAT10a) for peak elevations along each of the constructed profiles in northern and western Norway, together with Jotunheimen. Numbers along the plot lines are mean decadal temperature offsets in the 1900s, 1930s and 1980s relative to the 2010s. Data from Hanssen-Bauer et al. (2006), Lussana (2020) and meteorological stations.

Data availability. The data can be found at Zenodo: https://doi.org/10.5281/Zenodo.8014400 (Czekirda et al., 2023a).

Video supplement. Videos are available at Zenodo: https://doi.org/10.5281/Zenodo.8014756 (Czekirda et al., 2023b).

Supplement. The supplement related to this article is available online at: https://doi.org/10.5194/tc-17-2725-2023-supplement.

Author contributions. JC performed the simulations and prepared the paper, with contributions from all co-authors. BE prepared the first version of the forcing data and supervised the study. JC, BE and SW contributed to the conceptualisation of this study and developed the methods. KI prepared the regional SAT data sets and contributed to the analysis of the SAT trends. FM contributed to the discussion on the thermal regime in steep slopes.

Competing interests. The contact author has declared that none of the authors has any competing interests.

Acknowledgements. This study uses rock wall loggers installed by Tobias Hipp and Bas Altena within the CRYOLINK project in 2011, together with rock wall loggers installed later during the project "CryoWALL – Permafrost slopes in Norway" (243784/CLE). Both projects were funded by the Research Council of Norway. Installation and data retrieval from the loggers were actively supported by the Geological Survey of Norway (NGU) and the Norwegian Water Resources and Energy Directorate (NVE). Particular thanks are due to Reginald L. Hermanns (NGU) and Lars Harald Blikra (NVE). Paula Hilger, Thorben Dunse (both the University College of Western Norway), Ove Brynhildsvoll, Trond Eiken, Jaroslav Obu, Bas Altena, Juditha Aga, Harald Wathne Hestad and Erling Thokle Hovden (all University of Oslo) helped with retrieving the rock wall logger data. Ole Einar Tveito from the Norwegian Meteorological Institute assisted in preparing the climatic data. Kristin Sæterdal Myhra (the University College of Western Norway) provided the CryoGrid 2D code, and ice thickness data for the selected glaciers in Norway were provided by Liss Marie Andreassen (NVE). Thomas Barnes (University of Oslo) proofread the paper. Three anonymous referees provided insightful reviews and suggestions that improved the paper. We want to thank the mentioned institutions and individuals.

Financial support. This study was funded by the Department of Geosciences, University of Oslo, Norway. Additional funding was provided by the project "CryoWALL – Permafrost slopes in Norway" (243784/CLE), funded by the Research Council of Norway.

Review statement. This paper was edited by Ylva Sjöberg and reviewed by three anonymous referees.

References

Allen, S. K., Gruber, S., and Owens, I. F.: Exploring Steep Bedrock Permafrost and its Relationship with Recent Slope Failures in the Southern Alps of New Zealand, Permafrost Periglac., 20, 345–356, https://doi.org/10.1002/ppp.658, 2009.

Andreassen, L. M., Huss, M., Melvold, K., Elvehøy, H., and Winsvold, S. H.: Ice thickness measurements and volume estimates for glaciers in Norway, J. Glaciol., 61, 763–775, https://doi.org/10.3189/2015JoG14J161, 2015.

Aune-Lundberg, L. and Strand, G.-H.: CORINE Land Cover classes. Examination of the content of CLC classes in Norway, Norwegian Forest and Landscape Institute, Ås, Norway, Report 05/2010, 42 pp., 2010.

Berrisford, M. S.: Evidence for enhanced mechanical weathering associated with seasonally late-lying and perennial snow patches, Jotunheimen, Norway, Permafrost Periglac., 2, 331–340, https://doi.org/10.1002/ppp.3430020408, 1991.

Berthling, I. and Etzelmüller, B.: The concept of cryo-conditioning in landscape evolution, Quaternary Res., 75, 378–384, https://doi.org/10.1016/j.yqres.2010.12.011, 2011.

Blikra, L. H. and Christiansen, H. H.: A field-based model of permafrost-controlled rockslide deformation in northern Norway, Geomorphology, 208, 34–49, https://doi.org/10.1016/j.geomorph.2013.11.014, 2014.

Blikra, L. H., Longva, O., Braathen, A., Anda, E., Dehls, J., and Stalsberg, K.: Rock slope failures in Norwegian fjord areas: examples, spatial distribution and temporal pattern, in: Landslides from Massive Rock Slope Failure, edited by: Evans, S. G., Mugnozza, G. S., Strom, A., Hermanns, R. L., NATO Science Series, vol. 49, Springer, Dordrecht, the Netherlands, https://doi.org/10.1007/978-1-4020-4037-5_26, 2006.

Blöschl, G. and Kirnbauer, R.: An analysis of snow cover patterns in a small alpine catchment, Hydrol. Process., 6, 99–109, https://doi.org/10.1002/hyp.3360060109, 1992.

Blöschl, G., Kirnbauer, R., and Gutknecht, D.: Distributed Snowmelt Simulations in an Alpine Catchment: 1. Model Evaluation on the Basis of Snow Cover Patterns, Water Resour. Res., 27, 3171–3179, https://doi.org/10.1029/91WR02250, 1991.

Boeckli, L., Brenning, A., Gruber, S., and Noetzli, J.: A statistical approach to modelling permafrost distribution in the European Alps or similar mountain ranges, The Cryosphere, 6, 125–140, https://doi.org/10.5194/tc-6-125-2012, 2012.

Böhme, M., Hermanns, R. L., Fischer, L., Oppikofer, T., Bunkholt, H., Derron, M. H., Carrea, D., Jaboyedoff, M., and Eiken, T.: Detailed assessment of the deep-seated gravitational deformation at Stampa above Flåm, Norway, Landslides and Engineered Slopes: Protecting Society through Improved Understanding, Taylor & Francis Group, London, 647–652, ISBN 978-0-415-62123-6, 2012.

Böhme, M., Hermanns, R. L., Oppikofer, T., Fischer, L., Bunkholt, H. S. S., Eiken, T., Pedrazzini, A., Derron, M.-H., Jaboyedoff, M., Blikra, L. H., and Nilsen, B.: Analyzing complex rock slope deformation at Stampa, western Norway, by integrating geomorphology, kinematics and numerical modeling, Eng. Geol., 154, 116–130, https://doi.org/10.1016/j.enggeo.2012.11.016, 2013.

Böhme, M., Bunkholt, H. S. S., Dehls, J. F., Oppikofer, T., Hermanns, R., Dalsegg, E., Kristensen, L., Lauknes, T. R., and Eriksen, H. Ø.: Geologisk modell og fare-og risikoklassifisering av det ustabile fjellpartiet Gamanjunni 3 i Manndalen, Troms, Norges Geologiske Undersøkelse, Trondheim, Norway, Report 2016.031, 63 pp., 2016a (in Norwegian).

Böhme, M., Bunkholt, H. S. S., Oppikofer, T., Dehls, J. F., Hermanns, R. L., Eriksen, H. Ø., Lauknes, T. R., and Eiken, T.: Using 2D InSAR, dGNSS and structural field data to understand the deformation mechanism of the unstable rock slope Gamanjunni 3, northern Norway, in: Proceedings of the 12th International Symposium on Landslides, Napoli, Italy, 12–19 June 2016, 443–449, ISBN 978-1-138-02988-0, 2016b.

Böhme, M., Hermanns, R. L., Gosse, J., Hilger, P., Eiken, T., Lauknes, T. R., and Dehls, J. F.: Comparison of monitoring data with paleo-slip rates: Cosmogenic nuclide dating detects acceleration of a rockslide, Geology, 47, 339–342, https://doi.org/10.1130/G45684.1, 2019.

Czekirda, J., Etzelmüller, B., Westermann, S., Isaksen, K., and Magnin, F.: Data: Post-Little Ice Age rock wall permafrost evolution in Norway, Zenodo [data set], https://doi.org/10.5281/zenodo.8014400, 2023a.

Czekirda, J., Etzelmüller, B., Westermann, S., Isaksen, K., and Magnin, F.: Videos: Post-Little Ice Age rock wall permafrost evolution in Norway, Zenodo [video], https://doi.org/10.5281/zenodo.8014756, 2023b.

Dabrowski, M., Krotkiewski, M., and Schmid, D. W.: MILAMIN: MATLAB-based finite element method solver for large problems, Geochem. Geophy. Geosy., 9, Q04030, https://doi.org/10.1029/2007gc001719, 2008.

Dalsegg, E. and Rønning, J. S.: Geofysiske målinger på Mannen i Rauma kommune, Møre og Romsdal, Norges geologiske undersøkelse, Trondheim, Norway, Report 2012.024, 18 pp., 2012 (in Norwegian).

Davies, M. C. R., Hamza, O., Lumsden, B. W., and Harris, C.: Laboratory measurement of the shear strength of ice-filled rock joints, Ann. Glaciol., 31, 463–467, https://doi.org/10.3189/172756400781819897, 2000.

Davies, M. C. R., Hamza, O., and Harris, C.: The effect of rise in mean annual temperature on the stability of rock slopes containing ice-filled discontinuities, Permafrost Periglac., 12, 137–144, https://doi.org/10.1002/ppp.378, 2001.

Draebing, D., Krautblatter, M., and Dikau, R.: Interaction of thermal and mechanical processes in steep permafrost rock walls: A conceptual approach, Geomorphology, 226, 226–235, https://doi.org/10.1016/j.geomorph.2014.08.009, 2014.

Dramis, F., Govi, M., Guglielmin, M., and Mortara, G.: Mountain Permafrost and Slope Instability in the Italian Alps – the Val-Pola Landslide, Permafrost Periglac., 6, 73–81, https://doi.org/10.1002/ppp.3430060108, 1995.

Egholm, D. L., Andersen, J. L., Knudsen, M. F., Jansen, J. D., and Nielsen, S. B.: The periglacial engine of mountain erosion – Part 2: Modelling large-scale landscape evolution, Earth Surf. Dynam., 3, 463–482, https://doi.org/10.5194/esurf-3-463-2015, 2015.

Eriksen, H. Ø.: Instrumentation and temperature data (2014–2017) for the Ádjet Mountain in Skibotn, Troms, Figshare [data set], https://doi.org/10.6084/m9.figshare.6225056.v3, 2018a.

Eriksen, H. Ø.: Instrumentation and temperature data (2013–2017), Gámanjunni 3 Rockslide and Rock Glacier, Manndalen, Troms, Figshare [data set], https://doi.org/10.6084/m9.figshare.6254750.v1, 2018b.

Eriksen, H. Ø., Rouyet, L., Lauknes, T. R., Berthling, I., Isaksen, K., Hindberg, H., Larsen, Y., and Corner, G. D.: Recent Acceleration of a Rock Glacier Complex, Ádjet, Norway, Documented by 62 Years of Remote Sensing Observations, Geophys. Res. Lett., 45, 8314–8323, https://doi.org/10.1029/2018GL077605, 2018.

Etzelmüller, B. and Hagen, J. O.: Glacier-permafrost interaction in Arctic and alpine mountain environments with examples from southern Norway and Svalbard, Geological Society, London, Special Publications, 242, 11–27, https://doi.org/10.1144/gsl.Sp.2005.242.01.02, 2005.

Etzelmüller, B., Berthling, I., and Sollid, J. L.: The distribution of permafrost in Southern Norway; a GIS approach, in: Proceedings of the Seventh International Conference on Permafrost, Yellowknife, Canada, 23–27 June 1998, 251–258, 1998.

Etzelmüller, B., Berthling, I., and Sollid, J. L.: Aspects and concepts on the geomorphological significance of Holocene permafrost in southern Norway, Geomorphology, 52, 87–104, https://doi.org/10.1016/S0169-555X(02)00250-7, 2003.

Etzelmüller, B., Guglielmin, M., Hauck, C., Hilbich, C., Hoelzle, M., Isaksen, K., Noetzli, J., Oliva, M., and Ramos, M.: Twenty years of European mountain permafrost dynamics – the PACE legacy, Environ. Res. Lett., 15, 104070, https://doi.org/10.1088/1748-9326/abae9d, 2020.

Etzelmüller, B., Czekirda, J., Magnin, F., Duvillard, P.-A., Ravanel, L., Malet, E., Aspaas, A., Kristensen, L., Skrede, I., Majala, G. D., Jacobs, B., Leinauer, J., Hauck, C., Hilbich, C., Böhme, M., Hermanns, R., Eriksen, H. Ø., Lauknes, T. R., Krautblatter, M., and Westermann, S.: Permafrost in monitored unstable rock slopes in Norway – new insights from temperature and surface velocity measurements, geophysical surveying, and ground temperature modelling, Earth Surf. Dynam., 10, 97–129, https://doi.org/10.5194/esurf-10-97-2022, 2022.

Farbrot, H., Isaksen, K., and Etzelmüller, B.: Present and past distribution of mountain permafrost in Gaissane Mountains, Northern Norway, in: Proceedings of the Ninth International Conference on Permafrost, Fairbanks, Alaska, 29 June–3 July 2008, 427–432, 2008.

Farbrot, H., Hipp, T. F., Etzelmüller, B., Isaksen, K., Ødegård, R. S., Schuler, T. V., and Humlum, O.: Air and Ground Temperature Variations Observed along Elevation and Continentality Gradients in Southern Norway, Permafrost Periglac., 22, 343–360, https://doi.org/10.1002/ppp.733, 2011.

Farbrot, H., Isaksen, K., Etzelmüller, B., and Gisnås, K.: Ground Thermal Regime and Permafrost Distribution under a Changing Climate in Northern Norway, Permafrost Periglac., 24, 20–38, https://doi.org/10.1002/ppp.1763, 2013.

Fiddes, J., Endrizzi, S., and Gruber, S.: Large-area land surface simulations in heterogeneous terrain driven by global data sets: application to mountain permafrost, The Cryosphere, 9, 411–426, https://doi.org/10.5194/tc-9-411-2015, 2015.

Fischer, L., Kääb, A., Huggel, C., and Noetzli, J.: Geology, glacier retreat and permafrost degradation as controlling factors of slope instabilities in a high-mountain rock wall: the Monte Rosa east face, Nat. Hazards Earth Syst. Sci., 6, 761–772, https://doi.org/10.5194/nhess-6-761-2006, 2006.

Fischer, L., Purves, R. S., Huggel, C., Noetzli, J., and Haeberli, W.: On the influence of topographic, geological and cryospheric factors on rock avalanches and rockfalls in high-mountain areas, Nat. Hazards Earth Syst. Sci., 12, 241–254, https://doi.org/10.5194/nhess-12-241-2012, 2012.

Frauenfelder, R., Isaksen, K., Lato, M. J., and Noetzli, J.: Ground thermal and geomechanical conditions in a permafrost-affected high-latitude rock avalanche site (Polvartinden, northern Norway), The Cryosphere, 12, 1531–1550, https://doi.org/10.5194/tc-12-1531-2018, 2018.

Gisnås, K., Etzelmüller, B., Farbrot, H., Schuler, T. V., and Westermann, S.: CryoGRID 1.0: Permafrost Distribution in Norway estimated by a Spatial Numerical Model, Permafrost Periglac., 24, 2–19, https://doi.org/10.1002/ppp.1765, 2013.

Gisnås, K., Westermann, S., Schuler, T. V., Litherland, T., Isaksen, K., Boike, J., and Etzelmüller, B.: A statistical approach to represent small-scale variability of permafrost temperatures due to snow cover, The Cryosphere, 8, 2063–2074, https://doi.org/10.5194/tc-8-2063-2014, 2014.

Gisnås, K., Etzelmüller, B., Lussana, C., Hjort, J., Sannel, A. B. K., Isaksen, K., Westermann, S., Kuhry, P., Christiansen, H. H., Frampton, A., and Akerman, J.: Permafrost Map for Norway, Sweden and Finland, Permafrost Periglac., 28, 359–378, https://doi.org/10.1002/ppp.1922, 2017.

Gruber, S. and Haeberli, W.: Permafrost in steep bedrock slopes and its temperature-related destabilization following climate change, J. Geophys. Res.-Earth, 112, F02S18, https://doi.org/10.1029/2006jf000547, 2007.

Gruber, S. and Hoelze, M.: The cooling effect of coarse blocks revisited: a modeling study of a purely conductive mechanism, in: Proceedings of the Ninth International Conference on Permafrost, Fairbanks, Alaska, 29 June–3 July 2008, 557–561, 2008.

Gruber, S., Hoelzle, M., and Haeberli, W.: Permafrost thaw and destabilization of Alpine rock walls in the hot summer of 2003, Geophys. Res. Lett., 31, L13504, https://doi.org/10.1029/2004gl020051, 2004.

Haberkorn, A., Phillips, M., Kenner, R., Rhyner, H., Bavay, M., Galos, S. P., and Hoelzle, M.: Thermal regime of rock and its relation to snow cover in steep alpine rock walls: Gemsstock, Central Swiss Alps, Geogr. Ann. A, 97, 579–597, https://doi.org/10.1111/geoa.12101, 2015.

Haberkorn, A., Wever, N., Hoelzle, M., Phillips, M., Kenner, R., Bavay, M., and Lehning, M.: Distributed snow and rock temperature modelling in steep rock walls using Alpine3D, The Cryosphere, 11, 585–607, https://doi.org/10.5194/tc-11-585-2017, 2017.

Haeberli, W., Huggel, C., Kaab, A., Zgraggen-Oswald, S., Polkvoj, A., Galushkin, I., Zotikov, I., and Osokin, N.: The Kolka-Karmadon rock/ice slide of 20 September 2002: an extraordinary event of historical dimensions in North Ossetia, Russian Caucasus, J. Glaciol., 50, 533–546, https://doi.org/10.3189/172756504781829710, 2004.

Hales, T. C. and Roering, J. J.: Climatic controls on frost cracking and implications for the evolution of bedrock landscapes, J. Geophys. Res.-Earth, 112, F02033, https://doi.org/10.1029/2006JF000616, 2007.

Hanssen-Bauer, I., Tveito, O., and Szewczyk-Bartnicka, H.: Comparison of grid-based and station-based regional temperature and precipitation series, Norwegian Meteorological Institute, Oslo, Norway, Report 04/2006, 26 pp., 2006.

Harris, C., Haeberli, W., Vonder Mühll, D., and King, L.: Permafrost monitoring in the high mountains of Europe: the PACE Project in its global context, Permafrost Periglac., 12, 3–11, https://doi.org/10.1002/ppp.377, 2001.

Hasler, A., Gruber, S., Font, M., and Dubois, A.: Advective Heat Transport in Frozen Rock Clefts: Conceptual Model, Laboratory Experiments and Numerical Simulation, Permafrost Periglac., 22, 378–389, https://doi.org/10.1002/ppp.737, 2011a.

Hasler, A., Gruber, S., and Haeberli, W.: Temperature variability and offset in steep alpine rock and ice faces, The Cryosphere, 5, 977–988, https://doi.org/10.5194/tc-5-977-2011, 2011b.

Heggem, E. S. F., Juliussen, H., and Etzelmüller, B.: Mountain permafrost in Central-Eastern Norway, Norsk Geogr. Tidsskr. – Norwegian Journal of Geography, 59, 94–108, https://doi.org/10.1080/00291950510038377, 2005.

Hilger, P., Hermanns, R. L., Czekirda, J., Myhra, K. S., Gosse, J. C., and Etzelmüller, B.: Permafrost as a first order control on long-term rock-slope deformation in (Sub-) Arctic Norway, Quaternary Sci. Rev., 251, 106718, https://doi.org/10.1016/j.quascirev.2020.106718, 2021.

Hipp, T., Etzelmüller, B., Farbrot, H., Schuler, T. V., and Westermann, S.: Modelling borehole temperatures in Southern Norway – insights into permafrost dynamics during the 20th and 21st century, The Cryosphere, 6, 553–571, https://doi.org/10.5194/tc-6-553-2012, 2012.

Hipp, T., Etzelmüller, B., and Westermann, S.: Permafrost in Alpine Rock Faces from Jotunheimen and Hurrungane, Southern Norway, Permafrost Periglac., 25, 1–13, https://doi.org/10.1002/ppp.1799, 2014.

Hock, R., Rasul, G., Adler, C., Cáceres, B., Gruber, S., Hirabayashi, Y., Jackson, M., Kääb, A., Kang, S., Kutuzov, S., Milner, A., Molau, U., Morin, S., Orlove, B., and Steltzer, H.: High Mountain Areas, in: IPCC Special Report on the Ocean and Cryosphere in a Changing Climate, edited by: Pörtner, H.-O., Roberts, D. C., Masson-Delmotte, V., Zhai, P., Tignor, M., Poloczanska, E., Mintenbeck, K., Alegrììa, A., Nicolai, M., Okem, A., Petzold, J., Rama, B., and Weyer, N. M., Cambridge University Press, Cambridge, UK and New York, NY, USA, 131–202, https://doi.org/10.1017/9781009157964.004, 2019.

Huggel, C., Salzmann, N., Allen, S., Caplan-Auerbach, J., Fischer, L., Haeberli, W., Larsen, C., Schneider, D., and Wessels, R.: Recent and future warm extreme events and high-mountain slope stability, Philos. T. R. Soc. A, 368, 2435–2459, https://doi.org/10.1098/rsta.2010.0078, 2010.

Isaksen, K., Holmlund, P., Sollid, J. L., and Harris, C.: Three deep Alpine-permafrost boreholes in Svalbard and Scandinavia, Permafrost Periglac., 12, 13–25, https://doi.org/10.1002/ppp.380, 2001.

Isaksen, K., Sollid, J. L., Holmlund, P., and Harris, C.: Recent warming of mountain permafrost in Svalbard and Scandinavia, J. Geophys. Res.-Earth, 112, F02S04, https://doi.org/10.1029/2006JF000522, 2007.

Isaksen, K., Ødegård, R. S., Etzelmüller, B., Hilbich, C., Hauck, C., Farbrot, H., Eiken, T., Hygen, H. O., and Hipp, T. F.: Degrading Mountain Permafrost in Southern Norway: Spatial and Temporal Variability of Mean Ground Temperatures, 1999–2009, Permafrost Periglac., 22, 361–377, https://doi.org/10.1002/ppp.728, 2011.

Juliussen, H. and Humlum, O.: Thermal regime of openwork block fields on the mountains Elgåhogna and Sølen, central-eastern Norway, Permafrost Periglac., 19, 1–18, https://doi.org/10.1002/ppp.607, 2008.

Keller, F. and Gubler, H.: Interaction between snowcover and high mountain permafrost Murtel/Corvatsch, Swiss Alps, in: Proceedings of the Sixth International Conference on Permafrost, Beijing, China, 5–9 July 1993, 332–337, 1993.

Kirnbauer, R., Blöschl, G., Waldhäusl, P., and Hochstöger, F.: An analysis of snow cover patterns as derived from oblique aerial photographs, in: Proc. Vienna Symp. – Snow, Hydrology and Forests in High Alpine Areas, Vienna, Austria, 11–24 August 1991, 91–99, 1991.

Kleman, J., Stroeven, A. P., and Lundqvist, J.: Patterns of Quaternary ice sheet erosion and deposition in Fennoscandia and a theoretical framework for explanation, Geomorphology, 97, 73–90, https://doi.org/10.1016/j.geomorph.2007.02.049, 2008.

Krautblatter, M. and Hauck, C.: Electrical resistivity tomography monitoring of permafrost in solid rock walls, J. Geophys. Res.-Earth, 112, F02S20, https://doi.org/10.1029/2006JF000546, 2007.

Krautblatter, M., Funk, D., and Günzel, F. K.: Why permafrost rocks become unstable: a rock-ice-mechanical model in time and space, Earth Surf. Proc. Land., 38, 876–887, https://doi.org/10.1002/esp.3374, 2013.

Kristensen, L., Czekirda, J., Penna, I., Etzelmüller, B., Nicolet, P., Pullarello, J. S., Blikra, L. H., Skrede, I., Oldani, S., and Abellan, A.: Movements, failure and climatic control of the Veslemannen rockslide, Western Norway, Landslides, 18, 1963–1980, https://doi.org/10.1007/s10346-020-01609-x, 2021.

Lambiel, C. and Pieracci, K.: Permafrost distribution in talus slopes located within the alpine periglacial belt, Swiss Alps, Permafrost Periglac., 19, 293–304, https://doi.org/10.1002/ppp.624, 2008.

Lebrouc, V., Schwartz, S., Baillet, L., Jongmans, D., and Gamond, J. F.: Modeling permafrost extension in a rock slope since the Last Glacial Maximum: Application to the large Sechilienne landslide (French Alps), Geomorphology, 198, 189–200, https://doi.org/10.1016/j.geomorph.2013.06.001, 2013.

Lehning, M., Grünewald, T., and Schirmer, M.: Mountain snow distribution governed by an altitudinal gradient and terrain roughness, Geophys. Res. Lett., 38, L19504, https://doi.org/10.1029/2011GL048927, 2011.

Luetschg, M., Lehning, M., and Haeberli, W.: A sensitivity study of factors influencing warm/thin permafrost in the Swiss Alps, J. Glaciol., 54, 696–704, https://doi.org/10.3189/002214308786570881, 2008.

Lussana, C.: seNorge_2018 daily total precipitation amount 1957–2017, version 18.12, Zenodo [data set], https://doi.org/10.5281/zenodo.2082320, 2018.

Lussana, C.: seNorge observational gridded datasets, seNorge_2018, version 20.05, Norwegian Meteorological Institute, Oslo, Norway, Report 07/2020, 33 pp., 2020.

Lussana, C., Tveito, O. E., and Uboldi, F.: Three-dimensional spatial interpolation of 2 m temperature over Norway, Q. J. Roy. Meteor. Soc., 144, 344–364, https://doi.org/10.1002/qj.3208, 2018.

Machguth, H., Paul, F., Hoelzle, M., and Haeberli, W.: Distributed glacier mass-balance modelling as an important component of modern multi-level glacier monitoring, Ann. Glaciol., 43, 335–343, https://doi.org/10.3189/172756406781812285, 2006.

Magnin, F., Deline, P., Ravanel, L., Noetzli, J., and Pogliotti, P.: Thermal characteristics of permafrost in the steep alpine rock walls of the Aiguille du Midi (Mont Blanc Massif, 3842 m a.s.l), The Cryosphere, 9, 109–121, https://doi.org/10.5194/tc-9-109-2015, 2015.

Magnin, F., Etzelmüller, B., Westermann, S., Isaksen, K., Hilger, P., and Hermanns, R. L.: Permafrost distribution in steep rock slopes in Norway: measurements, statistical modelling and implications for geomorphological processes, Earth Surf. Dynam., 7, 1019–1040, https://doi.org/10.5194/esurf-7-1019-2019, 2019.

Magnin, F. and Josnin, J.-Y.: Water Flows in Rock Wall Permafrost: A Numerical Approach Coupling Hydrological and Thermal Processes, J. Geophys. Res.-Earth, 126, e2021JF006394, https://doi.org/10.1029/2021JF006394, 2021.

Magnin, F., Josnin, J.-Y., Ravanel, L., Pergaud, J., Pohl, B., and Deline, P.: Modelling rock wall permafrost degradation in the Mont Blanc massif from the LIA to the end of the 21st century, The Cryosphere, 11, 1813–1834, https://doi.org/10.5194/tc-11-1813-2017, 2017a.

Magnin, F., Westermann, S., Pogliotti, P., Ravanel, L., Deline, P., and Malet, E.: Snow control on active layer thickness in steep alpine rock walls (Aiguille du Midi, 3842 m asl, Mont Blanc massif), Catena, 149, 648–662, https://doi.org/10.1016/j.catena.2016.06.006, 2017b.

Moore, J. R., Gischig, V., Katterbach, M., and Loew, S.: Air circulation in deep fractures and the temperature field of an alpine rock slope, Earth Surf. Proc. Land., 36, 1985–1996, https://doi.org/10.1002/esp.2217, 2011.

Myhra, K. S., Westermann, S., and Etzelmüller, B.: Modelled Distribution and Temporal Evolution of Permafrost in Steep Rock Walls Along a Latitudinal Transect in Norway by CryoGrid 2D, Permafrost Periglac., 28, 172–182, https://doi.org/10.1002/ppp.1884, 2017.

Myhra, K. S., Westermann, S., and Etzelmüller, B.: Modeling Conductive Heat Flow Between Steep Rock Walls and Talus Slopes – Thermal Processes and Geomorphological Implications, Front. Earth Sci., 7, 192, https://doi.org/10.3389/feart.2019.00192, 2019.

Noetzli, J. and Gruber, S.: Transient thermal effects in Alpine permafrost, The Cryosphere, 3, 85–99, https://doi.org/10.5194/tc-3-85-2009, 2009.

Noetzli, J., Gruber, S., Kohl, T., Salzmann, N., and Haeberli, W.: Three-dimensional distribution and evolution of permafrost temperatures in idealized high-mountain topography, J. Geophys. Res.-Earth, 112, F02S13, https://doi.org/10.1029/2006jf000545, 2007.

Noetzli, J., Christiansen, H., Deline, P., Gugliemin, M., Isaksen, K., Romanovsky, V., Smith, S., Zhao, L., and Streletskiy, D.: Permafrost thermal state, in: State of the Climate in 2019, B. Am. Meteorol. Soc., 101, 20–22, https://doi.org/10.1175/BAMS-D-20-0104.1, 2020.

Nopper, H.: Geomorphological study of the rock-slope failure at Adjet, Storfjord, Troms, Master's thesis, The Arctic University of Norway, Tromsø, Norway, 2015.

Ødegård, R. S. and Sollid, J. L.: Coastal cliff temperatures related to the potential for cryogenic weathering processes, western Spitsbergen, Svalbard, Polar Res., 12, 95–106, https://doi.org/10.3402/polar.v12i1.6705, 1993.

Ødegård, R. S., Sollid, J. L., and Liestøl, O.: Ground temperature measurements in mountain permafrost, Jotunheimen, southern Norway, Permafrost Periglac., 3, 231–234, https://doi.org/10.1002/ppp.3430030310, 1992.

Ødegård, R. S., Nesje, A., Isaksen, K., Andreassen, L. M., Eiken, T., Schwikowski, M., and Uglietti, C.: Climate change threatens archaeologically significant ice patches: insights into their age, internal structure, mass balance and climate sensitivity, The Cryosphere, 11, 17–32, https://doi.org/10.5194/tc-11-17-2017, 2017.

Olsen, L., Sveian, H., Ottesen, D., and Rise, L.: Quaternary glacial, interglacial and interstadial deposits of Norway and adjacent onshore and offshore areas, in: Quaternary Geology of Norway, edited by: Olsen, L., Fredin, O., and Olesen, O., Geological Survey of Norway, Trondheim, Norway, Special Publication, 13, 79–144, 2013.

Palmer, M. J., Burn, C. R., and Kokelj, S. V.: Factors influencing permafrost temperatures across tree line in the uplands east of the Mackenzie Delta, 2004–2010, Can. J. Earth Sci., 49, 877–894, https://doi.org/10.1139/e2012-002, 2012.

PERMOS: Permafrost in Switzerland 2014/2015 to 2017/2018, edited by: Noetzli, J., Pellet, C., and Staub, B., Glaciological Report (Permafrost) No. 16-19 of the Cryospheric Commission of the Swiss Academy of Sciences, Fribourg, Switzerland, 104 pp., https://doi.org/10.13093/permos-rep-2019-16-19, 2019.

Ravanel, L. and Deline, P.: Climate influence on rockfalls in high-Alpine steep rockwalls: The north side of the Aiguilles de Chamonix (Mont Blanc massif) since the end of the 'Little Ice Age', Holocene, 21, 357–365, https://doi.org/10.1177/0959683610374887, 2011.

Ravanel, L., Allignol, F., Deline, P., Gruber, S., and Ravello, M.: Rock falls in the Mont Blanc Massif in 2007 and 2008, Landslides, 7, 493–501, https://doi.org/10.1007/s10346-010-0206-z, 2010.

Ravanel, L., Magnin, F., and Deline, P.: Impacts of the 2003 and 2015 summer heatwaves on permafrost-affected rock-walls in the Mont Blanc massif, Sci. Total Environ., 609, 132–143, https://doi.org/10.1016/j.scitotenv.2017.07.055, 2017.

Saintot, A., Oppikofer, T., Derron, M.-H., and Henderson, I.: Large gravitational rock slope deformation in Romsdalen valley (Western Norway), Revista de la Asociación Geológica Argentina, 69, 354–371, 2012.

Sanders, J. W., Cuffey, K. M., Moore, J. R., MacGregor, K. R., and Kavanaugh, J. L.: Periglacial weathering and headwall erosion in cirque glacier bergschrunds, Geology, 40, 779–782, https://doi.org/10.1130/g33330.1, 2012.

Schmidt, J. U., Etzelmüller, B., Schuler, T. V., Magnin, F., Boike, J., Langer, M., and Westermann, S.: Surface temperatures and their influence on the permafrost thermal regime in high-Arctic rock walls on Svalbard, The Cryosphere, 15, 2491–2509, https://doi.org/10.5194/tc-15-2491-2021, 2021.

Schwanghart, W. and Scherler, D.: Short Communication: TopoToolbox 2 – MATLAB-based software for topographic analysis and modeling in Earth surface sciences, Earth Surf. Dynam., 2, 1–7, https://doi.org/10.5194/esurf-2-1-2014, 2014.

Slagstad, T., Balling, N., Elvebakk, H., Midttømme, K., Olesen, O., Olsen, L., and Pascal, C.: Heat-flow measurements in Late Palaeoproterozoic to Permian geological provinces in south and central Norway and a new heat-flow map of Fennoscandia and the Norwegian–Greenland Sea, Tectonophysics, 473, 341–361, https://doi.org/10.1016/j.tecto.2009.03.007, 2009.

Smith, M. W. and Riseborough, D. W.: Climate and the limits of permafrost: a zonal analysis, Permafrost Periglac., 13, 1–15, https://doi.org/10.1002/ppp.410, 2002.

Smith, S. L., Romanovsky, V. E., Isaksen, K., Nyland, K. E., Kholodov, A. L., Shiklomanov, N. I., Streletskiy, D. A., Farquharson, L. M., Drozdov, D. S., Malkova, G. V., and Christiansen, H. H.: Permafrost, in: State of the Climate in 2020, B. Am. Meteorol. Soc., 102, 290–292, https://doi.org/10.1175/BAMS-D-21-0086.1, 2021.

Sollid, J. L., Holmlund, P., Isaksen, K., and Harris, C.: Deep permafrost boreholes in western Svalbard, northern Sweden and southern Norway, Norsk Geogr. Tidsskr. – Norwegian Journal of Geography, 54, 186–191, https://doi.org/10.1080/002919500448567, 2000.

Sollid, J. L., Isaksen, K., Eiken, T., and Ødegård, R. S.: The transition zone of mountain permafrost on Dovrefjell, southern Norway, in: Proceedings of the Eighth International Conference on Permafrost, Zürich, Switzerland, 21–25 July 2003, 1085–1090, 2003.

Sommer, C. G., Lehning, M., and Mott, R.: Snow in a Very Steep Rock Face: Accumulation and Redistribution During and After a Snowfall Event, Front. Earth Sci., 3, 73, https://doi.org/10.3389/feart.2015.00073, 2015.

Steiger, C., Etzelmüller, B., Westermann, S., and Myhra, K. S.: Modelling the permafrost distribution in steep rock walls in Norway, Norwegian Journal of Geology/Norsk Geologisk Forening, 96, 329–341, https://doi.org/10.17850/njg96-4-04, 2016.

Throop, J., Lewkowicz, A. G., and Smith, S. L.: Climate and ground temperature relations at sites across the continuous and discontinuous permafrost zones, northern Canada, Can. J. Earth Sci., 49, 865–876, https://doi.org/10.1139/e11-075, 2012.

Tveito, O., Førland, E., Heino, R., Hanssen-Bauer, I., Alexandersson, H., Dahlström, B., Drebs, A., Kern-Hansen, C., Jónsson, T., and Vaarby Laursen, E.: Nordic temperature maps, Norwegian Meteorological Institute, Oslo, Norway, Report 09/00 KLIMA, 54 pp., 2000.

Wangensteen, B., Eiken, T., Ødegård, R. S., and Ludvig Sollid, J.: Measuring coastal cliff retreat in the Kongsfjorden area, Svalbard, using terrestrial photogrammetry, Polar Res., 26, 14–21, https://doi.org/10.1111/j.1751-8369.2007.00002.x, 2007.

Westermann, S., Schuler, T. V., Gisnås, K., and Etzelmüller, B.: Transient thermal modeling of permafrost conditions in Southern Norway, The Cryosphere, 7, 719–739, https://doi.org/10.5194/tc-7-719-2013, 2013.

Wicky, J. and Hauck, C.: Numerical modelling of convective heat transport by air flow in permafrost talus slopes, The Cryosphere, 11, 1311–1325, https://doi.org/10.5194/tc-11-1311-2017, 2017.

Wicky, J. and Hauck, C.: Air Convection in the Active Layer of Rock Glaciers, Front. Earth Sci., 8, 335, https://doi.org/10.3389/feart.2020.00335, 2020.

Williams, P. J. and Smith, M. W.: The frozen earth: fundamentals of geocryology, Cambridge University Press, Cambridge, UK, https://doi.org/10.1017/CBO9780511564437, 1989.

Winstral, A., Elder, K., and Davis, R. E.: Spatial Snow Modeling of Wind-Redistributed Snow Using Terrain-Based Parameters, J. Hydrometeorol., 3, 524–538, https://doi.org/10.1175/1525-7541(2002)003<0524:Ssmowr>2.0.Co;2, 2002.

Wirz, V., Schirmer, M., Gruber, S., and Lehning, M.: Spatio-temporal measurements and analysis of snow depth in a rock face, The Cryosphere, 5, 893–905, https://doi.org/10.5194/tc-5-893-2011, 2011.

Zhang, T.: Influence of the seasonal snow cover on the ground thermal regime: An overview, Rev. Geophys., 43, RG4002, https://doi.org/10.1029/2004RG000157, 2005.

Paper III

Spatiotemporal variations in frost cracking measures in two dimensions: A case study for rock walls in Jotunheimen, southern Norway

Justyna Czekirda, Alan W. Rempel, Bernd Etzelmüller, Sebastian Westermann

Published in *Geomorphology*, Vol. 453, 109112, 2024.
doi: 10.1016/j.geomorph.2024.109112

Geomorphology 453 (2024) 109112

Contents lists available at ScienceDirect

Geomorphology

journal homepage: www.journals.elsevier.com/geomorphology

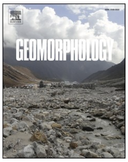

Spatiotemporal variations in frost cracking measures in two dimensions: A case study for rock walls in Jotunheimen, southern Norway

Justyna Czekirda [a,*], Alan W. Rempel [b], Bernd Etzelmüller [a], Sebastian Westermann [a]

[a] Department of Geosciences, University of Oslo, 0316 Oslo, Norway
[b] Department of Earth Sciences, University of Oregon, Eugene, OR 97403, USA

ARTICLE INFO

Keywords:
Rock walls
Frost weathering
Permafrost
Periglacial weathering
Frost crack modeling

ABSTRACT

The ground thermal regime has a profound impact on geomorphological processes and has been suggested to be particularly important for weathering processes in periglacial environments. Several frost-related damage indices have hitherto been developed to link climate and frost weathering potential in bedrock, although only for individual points or grid cells. Here, we model ground temperature and frost weathering potential in steep rock walls in the Jotunheimen Mountains, southern Norway, along a two-dimensional profile line for the Younger Dryas Stadial-Preboreal transition (c. 11.5 ka), the Holocene Thermal Maximum (c. 7.5 ka), the Little Ice Age (1750), and the 2010s. We use an established heat flow model and frost-cracking index based on the ice segregation theory. A central innovation of our model treatment is the implementation of ensemble simulations using distributions of automatically mapped crack radii in a rock wall, whereas previous frost damage models considered only a single characteristic crack radius. Our results allowed for the identification of sites with enhanced frost weathering. Such sites are typically found between rock walls and retreating glaciers, as well as in areas where snow depth changes abruptly, resulting in large thermal gradients. Hence, frost weathering may be highly active during glacier retreat, enhancing the damage to rock walls during deglaciation by adding to the damage from stress release. The coldest climates of the Younger Dryas Stadial-Preboreal transition and the Little Ice Age were generally most favorable for frost cracking. Such timing compares well with the knowledge about the timing of rockfall accumulations in Norway.

1. Introduction

Frost action dominates geomorphological processes in periglacial environments (e.g. Ballantyne, 2018). Although the efficiency of frost weathering and thus the periglacial imprint for long-term and large-scale landscape evolution have been questioned by recent research (André, 2003; French, 2016), geomorphological processes in cold, unglaciated areas are believed to be conditioned by seasonal and perennial ground ice despite the operation of azonal processes (Berthling and Etzelmüller, 2011). Recently, Egholm et al. (2015) explained the existence of high-elevation, low-relief surfaces, e.g. in southern Norway, by large-scale periglacial landscape evolution, the so-called "periglacial buzzsaw", over several million years through a combination of frost cracking and diffusive frost creep. Backwearing in cirques is thought to be a particularly effective mode of landscape smoothing (Oskin and Burbank, 2005; Steer et al., 2012), where denudation is likely driven by a combination of glacial and periglacial processes.

Rock wall retreat is a component of long-term landscape evolution in periglacial landscapes and exemplifies detachment-limited erosion, which mainly depends on the shear strength and weathering-susceptibility of rock instead of transport capacity. Compressional tectonics generates major flaws and joints in bedrock. Glacial debuttressing in recently glaciated areas may also lead to fracture formation (Ballantyne, 2002). Subsequently, pre-existing fractures are widened or new fractures are generated by chemical or physical weathering, such as thermal cracking due to thermal expansion stresses and weathering due to frost action. These processes further increase material detachability from rock faces, ultimately leading to gravity-driven material transport, especially when bedrock permafrost thaws (Krautblatter et al., 2013; Murton et al., 2006). Rock wall permafrost is exceptionally vulnerable due to its rapid thermal response to atmospheric warming, exacerbated by low ice contents, three-dimensional effects, and shallow snow cover (Boeckli et al., 2012; Gruber and Haeberli, 2007; Myhra et al., 2017; Noetzli et al., 2007). The occurrence of rock falls induced by thawing

---

* Corresponding author.
E-mail address: justyna.czekirda@geo.uio.no (J. Czekirda).

https://doi.org/10.1016/j.geomorph.2024.109112
Received 11 April 2023; Received in revised form 16 February 2024; Accepted 21 February 2024

permafrost has increased in the European Alps since the end of the last century (Fischer et al., 2012; Ravanel and Deline, 2011), particularly during unusually hot summers (Gruber et al., 2004).

Traditionally, the drivers for frost weathering were mainly related to freeze-thaw cycles and the 9 % volumetric expansion of water when it freezes to ice in situ, so-called "freeze-thaw weathering" (e.g. McGreevy and Whalley, 1982). Such a process requires a closed system and saturated conditions, with most damage expected to occur very close to 0 °C; damage at lower temperatures in undersaturated conditions while fluid migration pathways are present requires a different mechanism. Accordingly, some studies have considered volumetric expansion as a frost weathering process that may be effective close to the surfaces of saturated rocks subject to rapid freezing, particularly in water-filled joints, or in rocks with small specific surface areas (e.g. Matsuoka, 1990; Matsuoka and Murton, 2008). Other studies have argued against the importance of "freeze-thaw weathering" due to volumetric expansion in nature (e.g. Hallet et al., 1991) and instead invoke segregated ice growth as a much more effective and pervasive frost-damage mechanism. Ice segregation in rocks refers to ice growth due to water migration (i.e. "cryosuction"), induced by chemical-potential gradients, towards the freezing front. This is the same mechanism responsible for frost heave in fine-grained soils. In the "ice-lensing model" of Walder and Hallet (1985), frost-induced rock damage results from the temperature-dependent buildup of ice pressure inside slowly growing cracks. Their results showed that frost cracking is most effective at ground temperatures between approximately −15 and − 4 °C, with the exact temperature range depending on initial crack size and the hydraulic- and fracture-mechanical properties of bedrock. At higher temperatures, ice pressure and thus the stress-intensity factor are too low for crack growth, whereas at lower temperatures, the low hydraulic conductivity of partially ice-clogged fluid pathways inhibits the water supply needed for crack growth. Walder and Hallet (1985) emphasized that freeze–thaw oscillations are not required for effective frost weathering and instead the main limiting factor for crack growth is water transport, although freeze–thaw cycles may often help to enhance water supply (Walder and Hallet, 1986). This theoretical model for ice-induced crack growth was later tested by measuring microfracture activity in the laboratory for sandstone specimens subject to freezing, with results confirming that most frost damage occurred in a frost-cracking window (FCW), which fell between −6 and − 3 °C (Hallet et al., 1991). Laboratory experiments by Murton et al. (2006) using wet chalk specimens showed that: (1) frost damage was associated with ice segregation during thawing cycles, and not freezing cycles themselves, (2) fractures caused by frost weathering were parallel to the cooling surfaces, (3) ice lenses were formed, and (4) the depth of fractures depended on whether they resulted from bi- or unidirectional freezing. Duca et al. (2014) conducted the first laboratory study using hard, intact rock specimens of gneiss and showed that ice segregation also operates in harder rock types, although the microcracking they observed occurred between −2.7 and − 0.5 °C, which is a higher temperature range than previous studies (e.g. Matsuoka and Murton, 2008) would have predicted for such hard rocks.

Tracking the growth of each crack within a landscape would be a daunting task, and instead efforts to gauge the contribution of frost damage to landscape evolution have motivated the development of several one-dimensional frost-cracking indices that attempt to link key climate attributes with frost-cracking potential due to ice segregation in rocks. Anderson (1998) implemented the first frost-cracking index, which accounts for a correlation between frost damage and the time spent within an assumed FCW. Hales and Roering (2007) based their frost-weathering index on the premise that, in addition to time spent within the FCW, the temperature gradient is important for controlling the chemical potential gradients that facilitate water transport during frost cracking. Anderson et al. (2013) extended the latter model with a penalty function to address limits on water availability that increase with the distance between unfrozen reservoirs and potential frost-cracking sites. Lastly, in Rempel et al. (2016) a temperature-dependent hydraulic conductivity was introduced, with frost damage assumed to correlate with the porosity changes that accompany gradients in water flux when the temperature is low enough for ice growth to extend cracks.

The mentioned frost cracking indices assume that heat flow occurs one-dimensionally, whereas various ground temperature modeling studies implement realistic three-dimensional heat flow inside steep mountains (Noetzli and Gruber, 2009; Noetzli et al., 2007). Different rock surface temperatures depending on the aspect of rock faces have been measured in southern Norway (Czekirda et al., 2023; Hipp et al., 2014; Magnin et al., 2019), certainly influencing ground temperature distribution and thus frost weathering processes. To our knowledge, only a few studies explicitly mention such lateral effects as important in their study areas. Studies of coastal cliff temperatures in Svalbard related the large frost weathering potential in the area to thermal gradients due to snow cover variations (Ødegård and Sollid, 1993; Ødegård et al., 1995). Farbrot et al. (2007) calculated relatively high retreat rates (0.4–0.6 mm a^{-1}) in rock walls above talus-derived rock glaciers in the Tröllaskagi Peninsula in northern Iceland, which were attributed to large thermal gradients between the isothermal snowpack arising from maritime climate and colder permafrost-underlain rock walls. In addition, the study by Myhra et al. (2019) showed large thermal gradients between shaded rock walls and talus slopes, implying that such boundary areas may be important spots for frost weathering.

We hypothesize that lateral effects are important for frost weathering processes in rock walls. This study aims to increase knowledge about the importance of the lateral effects on frost weathering processes in rock walls, exemplified by those situated in the alpine periglacial environment of the Jotunheimen Mountains in southern Norway. The following research objectives are set: (1) extend the existing one-dimensional frost-weathering index proposed by Rempel et al. (2016), described in more detail in Section 3.1, to two-dimensional configurations; (2) model ground temperature in two dimensions (Section 3.2); (3) run the frost damage model based on the modeled subsurface thermal fields (Section 3.3); and (4) evaluate the spatiotemporal patterns of frost weathering. In contrast to previous studies (Rempel et al., 2016; Walder and Hallet, 1985) that are formulated in terms of a single characteristic/initial crack size, we account for the population of initial crack radii in a rock wall by using ensemble-based modeling.

2. Site description

We focus on two rock walls below the Veslpiggen (or Vesle Galdhøpiggen) Plateau, located in the Galdhøpiggen massif, western Jotunheimen, central southern Norway (Fig. 1). The Galdhøpiggen massif is one of the highest mountain areas in Norway. The study area is within the tectonic unit of the Jotun-Valdres Nappe Complex with high-grade intrusive rocks. The bedrock in the area is composed of pyroxene granulite with a composition from gabbroic to quartz mangeritic (Lutro and Tveten, 2012). Rock walls below the Veslpiggen Plateau probably formed as a result of the cumulative operation of various geomorphological processes during the multiple local glaciations and non-glacial periods throughout the Quaternary, similar to other larger-scale erosional bedrock landforms in Norway (Fredin et al., 2013). The most important geomorphological processes in those rock walls have probably been glacial and periglacial erosion, possibly with some contribution from debuttressing effects. These processes were probably not effective during the full-scale Pleistocene glaciations because other studies suggest that these mostly cold-based ice sheets were non-erosive in Norway, except in the deep valleys and fjords (Kleman et al., 2008). Hughes et al. (2015) suggest a deglaciation onset in the study area around 12 ka (the Younger Dryas Stadial), a rapid ice retreat from 10 ka and completion of the ice-sheet glaciation around 9.5 ka (the Boreal period) when the local valley at an elevation of around 800 m was completely deglaciated. All glaciers in Norway melted away during the

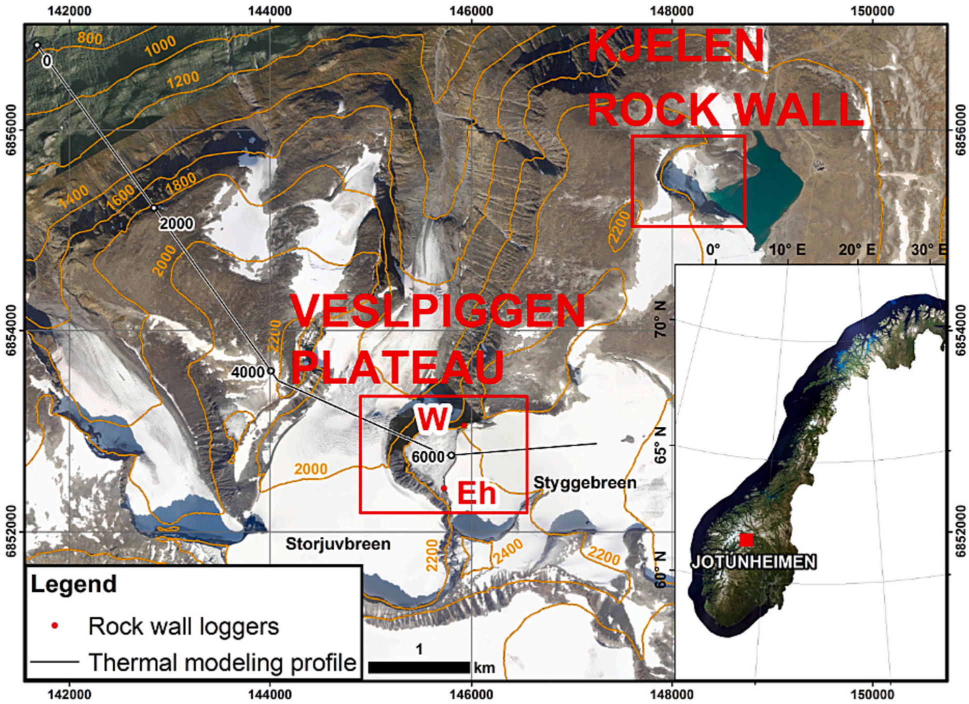

Fig. 1. The Veslpiggen modeling profile. Red points show the location of rock wall loggers in the various expositions: Eh – east-facing logger at a higher elevation, W – west-facing logger. Numbers along the modeling profile indicate distance in meters. Map background courtesy of © Statens kartverk, Geovekst og kommunene. UTM zone 33 N.

relatively warm period of the Holocene Thermal Maximum, although the timing of the disappearance varies (Nesje et al., 2008). Glaciers reformed during the Neoglaciation that in Norway began around 6–5 ka. The maximum Holocene glacier extent was reached during the Little Ice Age period, which culminated around 1750 in Norway. There has been extensive permafrost research in the gentle terrain of the nearby Juvflye area. Several boreholes have been drilled in the area (Farbrot et al., 2011; Ødegård et al., 1992), including a deep PACE borehole (129 m) in the continuous permafrost zone at 1894 m elevation (Harris et al., 2001). At the highest elevations (above ~1850 m) permafrost has likely been present throughout the entire Holocene (Lilleøren et al., 2012). Magnin et al. (2019)'s statistical model results suggest that the lower limit of rock wall permafrost in the Jotunheimen area is at approximately 1550 and 1150 m elevation for south- and north-facing rock walls, respectively.

The two rock walls along the two-dimensional model profile (Fig. 1) have easterly (elevation of 2280–2300 m) and westerly aspects (elevation of 2150–2190 m). The Veslpiggen Plateau is covered by blockfields and underlain by continuous permafrost, as confirmed by ground temperature modeling (Czekirda et al., 2023). The east-facing flank of the plateau is at present covered by the Styggebreen Glacier (Fig. 1) up to an elevation of 2275 m, which influences the ground thermal regime within the rock wall (Czekirda et al., 2023). The rock walls in the study area are monitored by shallow (10 cm depth) temperature loggers (Fig. 1) (Magnin et al., 2019), which allowed for calibration and estimation of ground surface temperature (GST). Our estimated mean annual ground surface temperature (MAGST) for the east-facing rock wall is −1.3 °C (2300 m) for the 2010s with an annual amplitude of 12.1 °C. MAGST is lower at the lower west-facing rock wall and is estimated at −3.3 °C (2180 m) for the 2010s with an annual amplitude of 9.3 °C. The blockfields on the plateau are likely colder and have estimated MAGST of −4.2 °C (2320 m; the 2010s) and a smaller annual amplitude of 5.4 °C due to the insulating effect of snow cover and lower amount of incoming shortwave solar radiation.

3. Methods and data

3.1. 2D frost damage model

Intermolecular interactions cause liquid water to wet both ice and rock/soil surfaces so that "premelted" liquid can persist in porous geological materials even when the temperature is several degrees below the normal bulk melting temperature of $T_m = 273.15$ K (Dash et al., 2006). This behavior is crucial to models of ice segregation, both because the premelted liquid forms connected pathways that can supply ice growth and allow the frozen mass to often exceed the initial moisture capacity of the unfrozen rock, and because the intermolecular interactions responsible for premelting produce a net thermomolecular pressure that increases as the temperature T is reduced, enabling the propagation of cracks at temperatures well below T_m. The dynamics of ice segregation can be formulated in terms of standard conservation laws. Differences between the thermomolecular pressure and the stresses that resist the expansion of segregated ice set the distribution of liquid pressures, leading to liquid pressure gradients that commonly run parallel to temperature gradients (Dash et al., 2006; Rempel et al., 2016); liquid water migration to the solidification front follows as a direct consequence. Frost damage associated with crack growth becomes possible at temperatures that are sufficiently low, or equivalently at undercoolings $\Delta T = T_m - T$ that are sufficiently high, for the thermomolecular pressure exerted by the ice on the rock matrix to promote the stress concentrations at crack tips that are necessary to propagate fractures (Rempel et al., 2016; Walder and Hallet, 1985). However, as the temperature drops, ice formation also causes the hydraulic conductivity in the frozen rock matrix to drop substantially, so that the water flux parallel to the temperature gradients must decrease as well (Rempel et al., 2016).

The key assumption of Rempel et al. (2016)'s model is that frost weathering potential is correlated with ice growth at sufficient undercoolings for the thermomolecular pressure to propagate fractures. Accepting this premise, mass balance considerations then imply that the spatiotemporal porosity changes that must result from gradients in the liquid water supply to growing segregated ice can be interpreted as a measure of frost weathering potential. It should be noted, however, that some ice expansion can be accommodated elastically, and is hence reversible, so modeled porosity changes do not necessarily gauge frost damage directly and resulting predictions should thus be interpreted as a qualitative measure of damage. In this work, the following assumptions from the original model are retained (Rempel et al., 2016):

1) Frost damage can occur only when the net thermomolecular pressure against the rock matrix is greater than a critical cracking pressure P_c, which dictates the upper-temperature limit for frost cracking ΔT_c. We term ΔT_c as the "undercooling for frost cracking", i.e. the absolute temperature difference between T_m and the upper-temperature threshold for the onset of frost-induced porosity increase. Following linear elastic fracture mechanics, we expect P_c to depend on the mode I (tensile) fracture toughness through "the critical stress-intensity factor" K_{IC}, and the crack radius c, so that

$$\Delta T_c \approx \frac{T_m}{\rho L} P_c \approx \frac{T_m}{\rho L} \frac{\sqrt{\pi}}{2} \frac{K_{IC}}{\sqrt{c}}, \tag{1}$$

where ρ is the ice density (920 kg m^{-3}), and L is the specific latent heat of fusion (334 kJ kg^{-1}).

2) The generalized Clapeyron equation approximates the undercooling ΔT as proportional to the difference ΔP between ice pressure against the crack walls and the lower liquid pressure in water films that enables liquid water supply. Thus, the model assumes that liquid water must be available when ice is present.
3) Liquid water flow is redistributed according to Darcy's law with a temperature-dependent permeability $k(T)$ that is parametrized using the power-law function

$$k(T) = k_c \left(\frac{\Delta T_c}{\Delta T}\right)^{\alpha}, \tag{2}$$

where α is the unitless power-law exponent (here 4), and k_c denotes the permeability at ΔT_c, typically between 10^{-24} and 10^{-16} m^2. Eq. (2) implies that k decreases dramatically as temperature drops and ice formation inhibits water movement. This assumption justifies the lack of an explicit lower temperature limit for frost cracking in the model, i.e. the equivalent of the lower temperature threshold in FCW. The unfrozen hydraulic permeability k_0 can be used to estimate k_c as

$$k_c \equiv k_0 \left(\frac{\Delta T_f}{\Delta T_c}\right)^{\alpha} \tag{3}$$

where ΔT_f – the undercooling for ice formation – is set to 0.1 °C to obtain the results described below.

4) Saturated conditions are idealized as always prevailing in rock pores (Rempel et al., 2016).

In Rempel et al. (2016), the model described above is applied in one dimension. We derived a two-dimensional version of the model by using the same underlying equations (see Appendix A. Frost damage model derivation) that satisfy the mass balance constraint. We compute spatiotemporal porosity changes Δn in two dimensions for each node with Cartesian coordinates x and y at time t:

$$\Delta n(x,y,t) = \frac{D \Delta T_c^{\alpha-1}}{\alpha} \int_{t_c}^{t} \Delta T(x,y,t)^{-\alpha} \left[\frac{\alpha}{\Delta T(x,y,t)} (\nabla T(x,y,t))^2 + \nabla^2 T(x,y,t)\right] dt \tag{4}$$

where the symbols denote: D – the frost weathering diffusivity, ∇T – the temperature gradient [°C m^{-1}] and $\nabla^2 T$ – the Laplacian [°C m^{-2}]. Here, D is defined as:

$$D = \frac{\rho L}{T_m \mu} \alpha k_c \Delta T_c \tag{5}$$

where μ denotes the dynamic viscosity of water (1.8 mPa s). The accumulated porosity change for one year is defined as:

$$\Delta n(x,y) = \frac{D \Delta T_c^{\alpha-1}}{\alpha} \int_{\Delta T > \Delta T_c, 1\,year} \Delta T(x,y)^{-\alpha} \left[\frac{\alpha}{\Delta T(x,y)} (\nabla T(x,y))^2 + \nabla^2 T(x,y)\right] dt. \tag{6}$$

The integration limits allow us to only track the frost-induced porosity change for days when the ground temperature at a given node is below the threshold value of –ΔT_c. The implied frost damage is thus a function of: (1) rock strength parameters through ΔT_c that dictates when frost cracking starts (Eq. (1)), (2) D that determines the rock susceptibility to frost damage (Eq. (5)), (3) ground temperature, and (4) α that shapes the hydraulic permeability decline with decreases in ground temperature. The second term in Eq. (6) has a minor influence on porosity changes, and its contribution is exactly zero in idealized cases where the annual temperature forcing is periodic and sensible heat changes dominate (Carslaw and Jaeger, 1959). In this study, we account for latent heat effects and therefore we keep the second term, although its influence remains minor, because most freezing takes place at higher temperatures and sensible heat changes tend to be more important than latent heat effects in the temperature range where frost cracking occurs.

3.2. Ground temperature modeling

We run the CryoGrid 2D heat conduction model with the effects of latent heat (Myhra et al., 2017) for four time slices (10-year periods) around: (1) the Younger Dryas-Preboreal transition (YD/PB, c. 11.5 ka), (2) the Holocene Thermal Maximum (HTM, c. 7.5 ka), (3) the Little Ice Age (LIA, 1750), and (4) the 2010s.

Simulations for the 2010s: We mostly use the methods for ground temperature modeling presented in Czekirda et al. (2023). The ground thermal modeling in the latter study was based on runs with monthly time steps forced by the regional monthly data set provided by the Norwegian Meteorological Institute (Hanssen-Bauer et al., 2006) as well as meteorological station data or the seNorge observational gridded datasets (Lussana, 2020). In the previous simulations, the model was run at monthly time steps, which we consider insufficient for this study. Hence, we rerun the model using the output from the monthly time steps as the initial temperature for the daily runs. We run the model only for the 2010s. We adjust daily air temperature data from the seNorge datasets (Lussana, 2020) and/or data from meteorological stations if available, so the mean monthly air temperature in this study is the same as in Czekirda et al. (2023). This procedure minimizes the difference in comparison to previous runs and avoids the issues with lapse rate in the seNorge datasets. Other methods are the same as in Czekirda et al. (2023), where mesh, ground stratigraphy, meteorological data and other parameters are described in detail. We only use the main thermal scenario from the aforementioned study, where several thermal sensitivity simulations were run.

We created a 2D-model profile for the Jotunheimen site by drawing a transect across the mountain. Elevation at the upper boundary of the two-dimensional domain was extracted from a digital elevation model (Fig. 2A). Furthermore, we needed to define the stratigraphy of the model domain, and we used the surface deposits map with some refinements based on the orthophotos to specify the volumetric contents of the subsurface (Fig. 2B; Table 1).

Simulations for the Younger Dryas, the Holocene Thermal Maximum and the Little Ice Age: As long-term air temperature, we use the TraCE-21 ka dataset (Liu et al., 2009), filled with NGRIP ice core data (NGRIP, 2004) for the HTM. Mean annual surface air temperature (SAT) was computed along the profile using the long-term air temperature datasets and the 2010s lapse rates. Subsequently, we compute monthly SATs using the 2010s air temperature amplitudes. Finally, GST, which the CryoGrid 2D requires as forcing, is estimated using slope gradient-dependent nF-factors to account for snow cover (Smith and Riseborough, 2002) and site- and aspect-specific monthly surface offsets to account for the incoming shortwave solar radiation in rock walls (Czekirda et al., 2023) (Fig. 2B). We run the first steady-state simulation for the permafrost model at the local deglaciation onset and assume a warm-based ice sheet with the basal temperature at the ice melting point (T_m). We derived the deglaciation dynamics for each site from the DATED-1 dataset, which contains time-slice maps of the Eurasian Ice Sheet margins for every one-thousand-year transition (Hughes et al., 2015). For each map, we computed ice thickness h for a distance x from the ice divide assuming a perfectly plastic parabolic ice sheet with radius

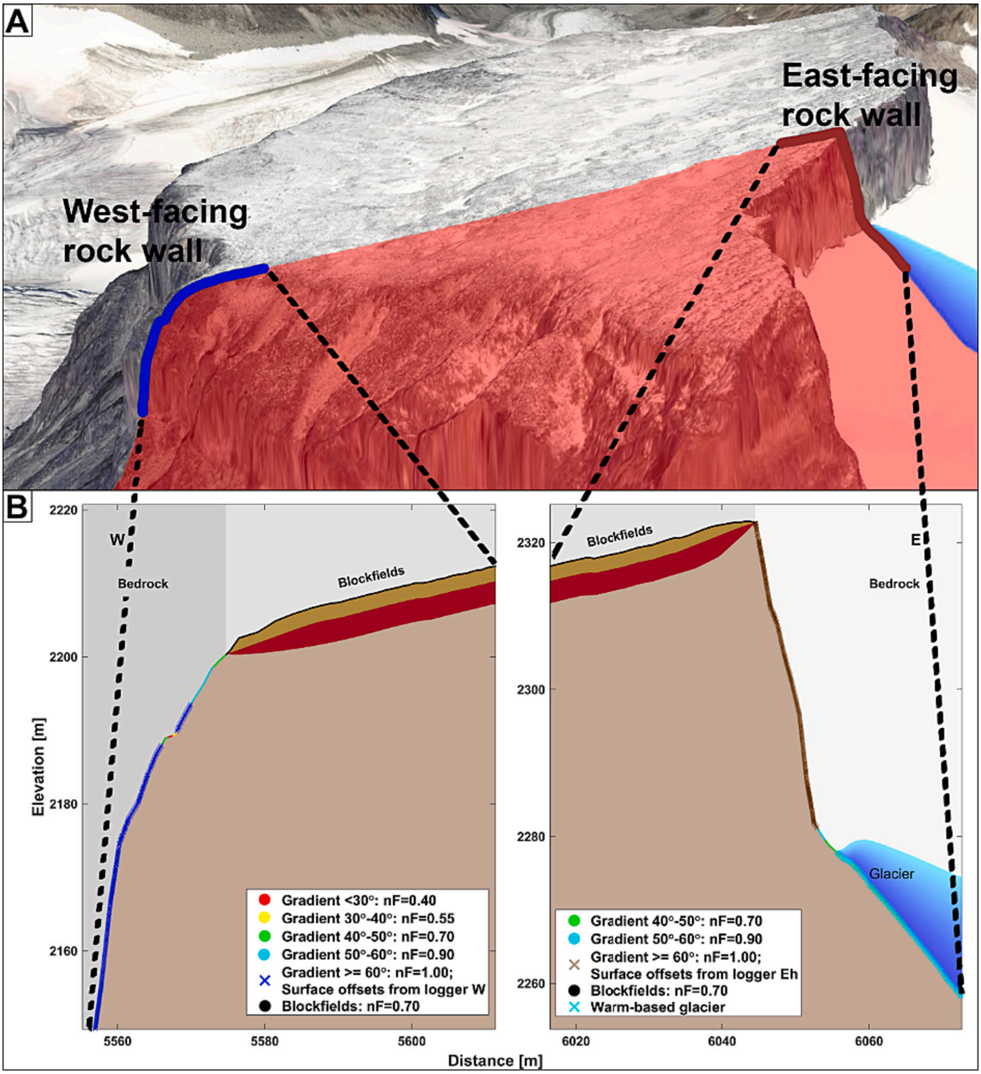

Fig. 2. **A**: The 2D-model profile (red transparent polygon) draped over surface topography. 2.5D background courtesy of: © Statens kartverk, Geovekst og kommunene. **B**: Model domain and forcing assumptions for surface nodes along the model profile. nF – freezing n-factor. The volumetric contents of the soil constituents for various subsurface layers are listed in Table 1.

Table 1
Assumed depths of subsurface layers, along with volumetric fractions of the soil constituents for each layer: θ_w – volumetric water content; θ_m – volumetric mineral content; θ_a – volumetric air content; z – depth. The row colors correspond to the subsurface colors depicted in Fig. 2B.

z [m]	θ_w [-]	θ_m [-]	θ_a [-]
Bedrock			
>0	0.05	0.95	0.00
Blockfields			
<2	0.10	0.60	0.30
2–5	0.40	0.60	0.00
>5	0.05	0.95	0.00

L (Paterson, 1994):

$$h = \left(\frac{2\tau_0}{\rho g}(L - x)\right)^{1/2} \tag{7}$$

where the basal shear stress τ_0=150 kPa (Vie, 2012) and g is the acceleration due to gravity. Subsequently, we interpolated the one-thousand-year ice thicknesses to yearly estimates. The onset of deglaciation for the highest peaks at the Veslpiggen Plateau occurred around 12 ka. We proceed with transient runs at yearly time steps until the YD/PB transition (11.5 ka), HTM (7.5 ka) and LIA (1750). During deglaciation, we use T_m for ice-covered parts along the profile and GST for unglaciated parts. We run the permafrost model at daily steps for 10 years at the mentioned end periods using the same SAT amplitudes as for the 2010s, accounting for the SAT offset between the 2010s and YD/PB, HTM or LIA. The derived offset is −4.7 °C between the YD/PB and 2010s, +1 °C between the HTM and 2010s and − 3 °C between the LIA and 2010s. The elevation of the Fennoscandian Ice Sheet at 11.5 ka is modeled at 2180 m. We remove glaciers in Jotunheimen in 9.5–8.5 ka and 7.5–6.5 ka according to the glacier variations in the Smørstabbtindan area (Matthews and Dresser, 2008; Nesje, 2009).

3.3. Frost damage modeling

Mechanical and hydraulic properties of bedrock: We estimated K_{IC} from uniaxial compressive strength σ_C using an equation from Chang et al. (2002). The study site has orthopyroxene gneiss bedrock with an assumed σ_C between 90 and 225 MPa, based on the value for amphibiotic gneiss from Hanssen (1988). These yield estimated K_{IC} values between 1.44 and 2.01 MPa m$^{1/2}$. In our simulations, we choose a uniform mean value of 1.7 MPa m$^{1/2}$. Crystalline bedrock at the study site has low unfrozen permeability with an assumed uniform value of 5×10^{-17} m^2 (Nilsen and Thidemann, 1993).

Note that the frost damage model was formulated to account for homogenous crack radii as defined in Eq. (1) to set the upper temperature limit for frost damage. In reality, a population of cm-scale, mode I cracks is expected within a single rock wall, and hence a choice must be made for the characteristic crack radius c that is most relevant for the onset of significant frost weathering. In our study, rather than pick a single value for c we take advantage of the statistical distribution of crack radii that is approximated from the mapped crack lengths observed in a selected rock wall. To avoid manual digitalization of fracture traces, which is both time-consuming and somewhat associated with a subjective interpretation, we employed MATLAB-based software for ridge detection using the complex shearlet transform to automatically detect fractures based on an orthomosaic (Prabhakaran et al., 2019). We conducted fieldwork to collect drone imagery from the 260 m high Kjelen rock wall (See Fig. 1 for the location), created an ultra-high quality dense point cloud in the photogrammetric Agisoft Metashape software using this imagery (Fig. 3A), and subsequently exported a 10 × 10 m orthomosaic with 1 cm^2 resolution for a section where the drone was closest to the rock wall (Fig. 3B). Fig. 3B shows the mapped cracks and the algorithm gave satisfactory results for our rock wall section.

The histogram of the mapped crack radii is depicted in Fig. 4A. We fitted a log-normal probability density function (PDF) to the data (Fig. 4A), which yielded the parameters $\mu = 1.58$ and $\sigma = 0.76$, which are used in the statistical formulae included on Fig. 4A for crack dimensions measured in cm. Fig. 4B shows ΔT_c as a function of crack radius computed from Eq. (1) assuming fracture toughness $K_{IC} = 1.7$ MPa m$^{1/2}$. Fig. 4C shows the distribution of the ensemble sample with 500 random numbers from the fitted log-normal distribution.

Computation of porosity changes: We implemented the frost damage model as presented in Section 3.1 and verified the implementation by comparing it with 1D runs shown by Rempel et al. (2016). We note that we do not aim at the application of the frost damage model in a transient way for longer periods, and present the results as annual means for the four time periods 11.5 ka (YD/PB), 7.5 ka (HTM), 1750 (LIA) and the 2010s. We accumulate porosity change in each vertex in the finite element mesh for each year in each time period using Eq. (6) and subsequently compute an annual mean for a 10-year period. We run the model for the population of crack radii that define ΔT_c shown in Fig. 4C. By performing the statistical runs, we assume that there is no interaction between various cracks and that each crack grows independently of others, i.e. each model run for various ΔT_c is run independently.

4. Results

4.1. Ground temperature modeling

The YD/PB was a cool period, and SAT was estimated to be −4.7 °C lower than in the 2010s (Fig. 5), and the modeled ground temperature in the rock walls is between −9 and − 5 °C. The HTM was a warmer period, with SAT estimated to be +1 °C higher than in the 2010s. The modeled rock wall temperature is between −4 and 0 °C for that period, which is even higher than over the 2010s when the modeled rock wall temperature is between −5 and − 1 °C. During the LIA, the modeled rock wall temperature is between −7 and − 4 °C. In general, the west-facing rock wall has lower modeled ground temperature than the east-facing rock wall, and its temperature is quite similar to the blockfields on the plateau, whereas the east-facing rock wall is up to 4 °C warmer than the blockfields on the adjacent plateau (Fig. 5). The difference in ground temperature between the east-facing and west-facing rock walls is around 1–3 °C. With the modeled thermal regime range for rock walls since deglaciation in mind, i.e. mean ground temperature range between −9 and 0 °C, we proceed with a description of the modeled porosity changes.

4.2. Frost damage modeling

We present the results of the porosity model for the YD/PB for two cases: (1) one in which ΔT_c is only computed for the median crack radius of 4.86 cm (Fig. 6A), (2) and one in which Δn is computed as a mean of the ensemble-based simulations for the sample of ΔT_c (Fig. 6B). Figs. 7 and 8 illustrate the same results for the remaining decennia. We also computed the average Δn with depth for various zones presented in Fig. 6: zones 1 and 6 include blockfields, zones 2 and 8 include moderately steep slopes, zones 3 and 7 include rock walls with various expositions, zones 4 and 9 include parts of rock walls that were or still are just at an elevation of an ice sheet or a glacier, zones 5 and 10 include previously or currently glaciated portions of the profile. The average profiles of porosity change Δn with depth in the various zones are shown in Fig. 9. Fig. 10 depicts average profiles of Δn with depth for zones with

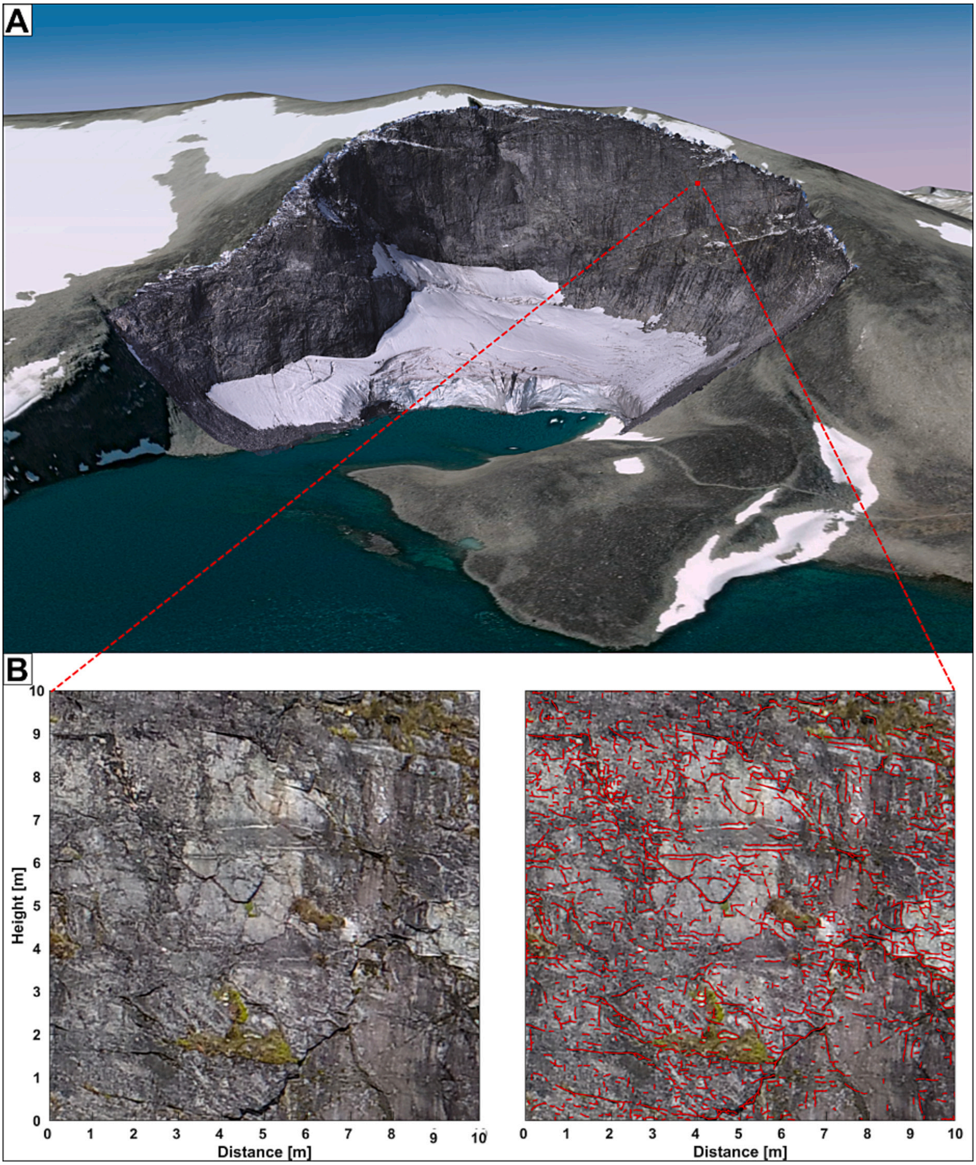

Fig. 3. **A**: Dense point cloud from the 260-m-high Kjelen rock wall (See Fig. 1 for the location), together with the location of the selected rock wall section (tiny red rectangle) draped over 2.5D background courtesy of © Mapbox, © OpenStreetMap, © Maxar. **B**: Orthomosaic (left image) and automatically mapped cracks (red lines) draped over the orthomosaic (right image).

rock walls.

ΔT_c is 6.1 °C for the median crack radius of 4.86 cm, meaning that frost-induced porosity increase only occurs for ground temperatures lower than −6.1 °C, i.e. the optimal thermal conditions for frost cracking require quite low ground temperatures. Hence, the results from the median crack radius simulations suggest that the frost cracking potential was greatest during the YD/PB period (Figs. 6A, 7, 9A). Over the HTM, frost cracking was least active due to the highest modeled ground temperatures, except in areas where we assumed that the present-day glacier was absent in that period. The modeled frost cracking potential for the LIA and 2010s falls between the large frost cracking potential in the YD/PB and the smallest frost cracking potential in the HTM, with the LIA frost damage slightly smaller than the YD/PB frost potential. Since ensemble simulations allow for frost cracking operating across wider climatic conditions, the computed Δn is always larger and reaches deeper than in the median crack radius simulations (Figs. 6B, 8, 9B). The evolution of frost cracking potential also shows that the temporal differences in Δn are much smaller in the ensemble simulations than in the

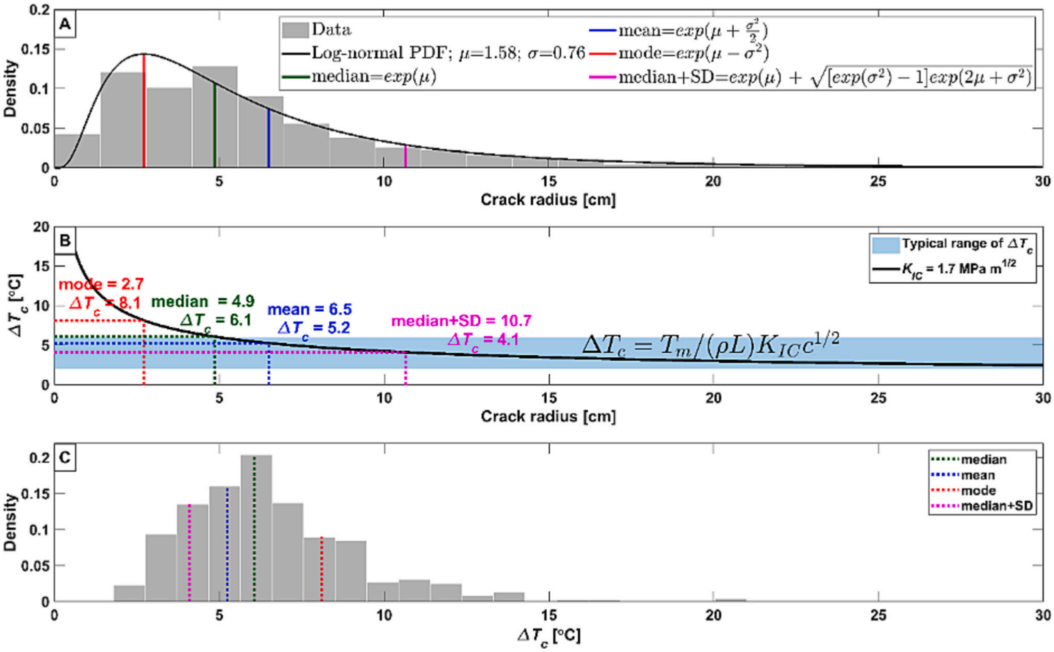

Fig. 4. **A:** Distribution of crack radii and a fitted log-normal probability density function (PDF) with parameters μ and σ. SD – standard deviation. **B**: Undercooling for frost cracking ΔT_c as a function of crack radius c for fracture toughness K_{IC}=1.7 MPa m$^{1/2}$. Physical constants in the equation are: T_m – the bulk melting temperature (273.15 K), ρ – the ice density (920 kg m^{-3}), L – the specific latent heat of fusion for water (334 kJ kg^{-1}). **C**: Distribution of undercooling for frost cracking ΔT_c sample used in the ensemble simulations.

median crack radius simulations (Fig. 9). In contrast to the median crack radius simulations, the YD/PB is not necessarily the period with the largest frost cracking potential according to the ensemble simulations, depending on the zone. The LIA period also has a large frost-cracking potential in the ensemble simulations. The HTM is usually the period with the smallest potential weathering in the rock walls, according to the ensemble simulations.

Ensemble simulations are averaged values from 500 simulations with various crack radii and we evaluated which crack radius is the most similar to average ensemble values (Fig. 10B). The results suggest that a crack radius of around 8 to 9 cm dominates the mean computed in the ensemble simulations. A crack radius of around 8 to 9 cm corresponds to ΔT_c between 4.5 and 4.7 °C and could be approximated by *median* + *a*SD*, where coefficient a=0.55–0.7. It seems reasonable to assume that the median crack radius is the most important for frost damage potential; however, our results suggest otherwise, indicating that ΔT_c from the median crack radius simulations is 1.5 °C too high. Therefore, the median crack radius simulations show the biggest frost damage potential for colder climate conditions, whereas the ensemble simulations favor slightly warmer climate conditions for shaded rock walls and colder climate conditions for sun-exposed rock walls.

Our two-dimensional profiles show that frost damage always decreases with depth in an exponential way (Figs. 9 and 10). Our results do not reproduce spikes in frost damage potential at a particular depth, as shown in Rempel et al. (2016)'s study. We modeled a more rapid decrease with depth than shown for the one-dimensional profiles in Rempel et al. (2016). Two-dimensional temperature gradients are expected to have a sharper decrease with depth than 1D profiles due to the surface topography in our study.

We assumed in the ground temperature modeling that the snow distribution depends on the slope gradient and rock walls (slope gradient >60°) are snow-free. In addition, we added surface offsets arising from incoming shortwave solar radiation in the rock wall sections. Hence, along our profiles rock walls are the areas with the largest GST amplitudes, both in winter and summer. The amplitude of the MAGST is around 12 °C at the east-facing rock wall, around 9 °C at the west-facing rock wall and around 5 °C at the blockfield-covered plateau. For moderately steep slopes, we ignore surface offsets for the summer period. The assumptions from the ground temperature modeling influence the results and rock walls generally have the largest frost weathering potential along profiles, larger than blockfields and moderately steep slopes (Fig. 9). However, the east-facing moderately steep slopes may have larger frost cracking potential than the east-facing rock walls at certain depths, according to the median crack radius simulations. According to the ensemble simulations, the east-facing sun-exposed rock wall has the largest and deepest frost cracking potential, except for Zones 4 and 9.

Furthermore, the climate conditions do not seem to be a limiting factor for frost cracking in the uppermost 1 m of the subsurface, yielding very similar results for various periods and zones in the ensemble and median crack radius simulations (Figs. 9 and 10). The differences at depth seem to be more pronounced. Nevertheless, there are areas where frost cracking potential is much larger close to the surface than anywhere else, even in the uppermost 1 m, namely in Zones 4 and 9 (Figs. 9 and 10). All simulations show that critical points for frost cracking are concentrated in the vicinity of the melting ice sheet, the glacier and anywhere where we anticipate a sharp transition in snow conditions, resulting in large ground thermal gradients in these areas (the black areas in Figs. 6–8). The temperature at the glacier bed was assumed to be 0 °C; hence, the areas between the rock walls and the melting ice sheet on the west-facing rock wall (YD/PB) and the glacier on the east-facing rock wall (except HTM) have particularly large ground thermal

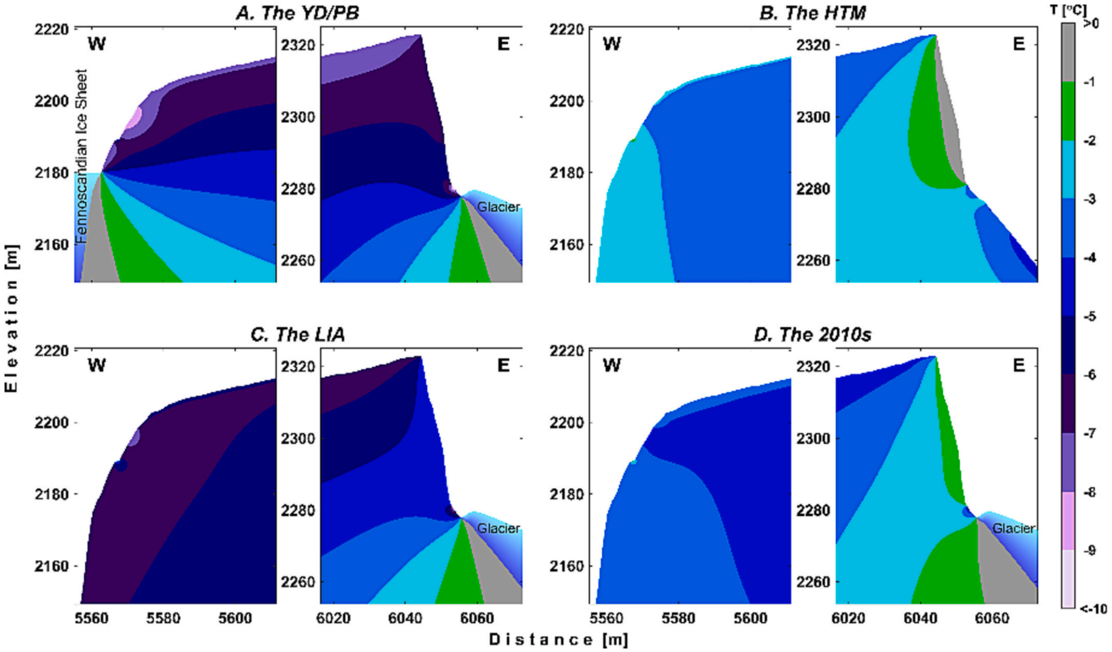

Fig. 5. Mean modeled ground temperature over four decennia: **A**. The Younger Dryas/Preboreal (YD/PB) transition, **B**. The Holocene Thermal Maximum (HTM), **C**. The Little Ice Age (LIA), and **D**. The 2010s.

gradients, resulting in large frost cracking potential. In addition, our assumption relating the snow distribution to slope gradient leads to a sharp transition in MAGST in the areas where slope gradient abruptly changes, and thus results in large thermal gradients in these areas close to the surface, where most frost cracking takes place. This is also the case between the blockfield and rock walls, where cornice snow may accumulate. The critical zones for enhanced frost weathering are most pronounced in the YD/PB and become weaker in the later periods. Nevertheless, they are still quite pronounced (e.g. the median crack radius simulations for the YD/PB vs HTM).

5. Discussion

5.1. Model limitations

We implemented two numerical models that each have their limitations: (1) a ground-temperature model, and (2) a frost-damage model. Both models are in two dimensions, which is an advance in comparison to one-dimensional models; however, the ground heat flow occurs in three dimensions in complex mountainous terrain (Noetzli and Gruber, 2009; Noetzli et al., 2007). Furthermore, uncertainties in the ground temperature modeling arise from our assumptions about the exclusively conductive heat transfer in the subsurface (i.e. neglecting advective heat transport from water fluxes), the model forcing, the assumed winter and summer surface offsets, and the assumed snow distribution (see more details in Czekirda et al., 2023). Furthermore, we assumed a simple parabolic ice-sheet profile during the YD and PB, which is certainly not always realistic (e.g. Patton et al., 2017; Stroeven et al., 2016), especially when ice flow is more governed by the subglacial topography during the thinning of the ice sheet with time. However, we assume the approach is sufficient for the aims and objectives of this study.

The employed frost damage model is a simple model that does not track the porosity evolution of individual cracks, as in e.g. Walder and Hallet (1986) or Sanders et al. (2012). The frost damage model instead focuses on larger geomorphological scales, and at the slope scale considered in our study, our choice of a simpler model is justified. The applied model is based on an assumed correlation between ice accumulation that is accommodated by porosity changes and frost damage. This reasoning is strictly justified when porosity changes due to non-reversible crack propagation are considered (Rempel et al., 2016), whereas more generally some poroelastic deformation is expected and could be relieved following thaw (Vlahou and Worster, 2010).

We note that the frost damage model was developed to describe fully saturated conditions and assumes that a water source is always available. Nevertheless, Rempel et al. (2016) argued that the porosity changes modeled in their study only required a small water supply from nearby pores and that this can be supplied by cannibalizing existing ice in regions where the ice pressure is insufficient to propagate cracks. The values of porosity changes modeled in our study are even smaller, hence the required water supply is quite small. Water flow is of central importance to the rock damage model, while in contrast, the thermal model assumes that water movement is unimportant as a heat transport mechanism because conductive transport can take place through the entire rock volume, whereas advective heat transport is constrained by relatively small pore volumes and low Darcy transport rates (i.e. the thermal *Peclet* number is small). Put another way, water flow and freezing of water drawn to the freezing front are important at the crack scale; however, they are omitted in the model scale of meters and tens of meters. As the small cracks comprise only a very small volume of a block, the impact on the freezing dynamics is negligible. In addition, ice segregation occurs at quite low ground temperatures in our study, hence the water movement at a larger scale is limited and its influence on the ground temperature is likely of minor importance.

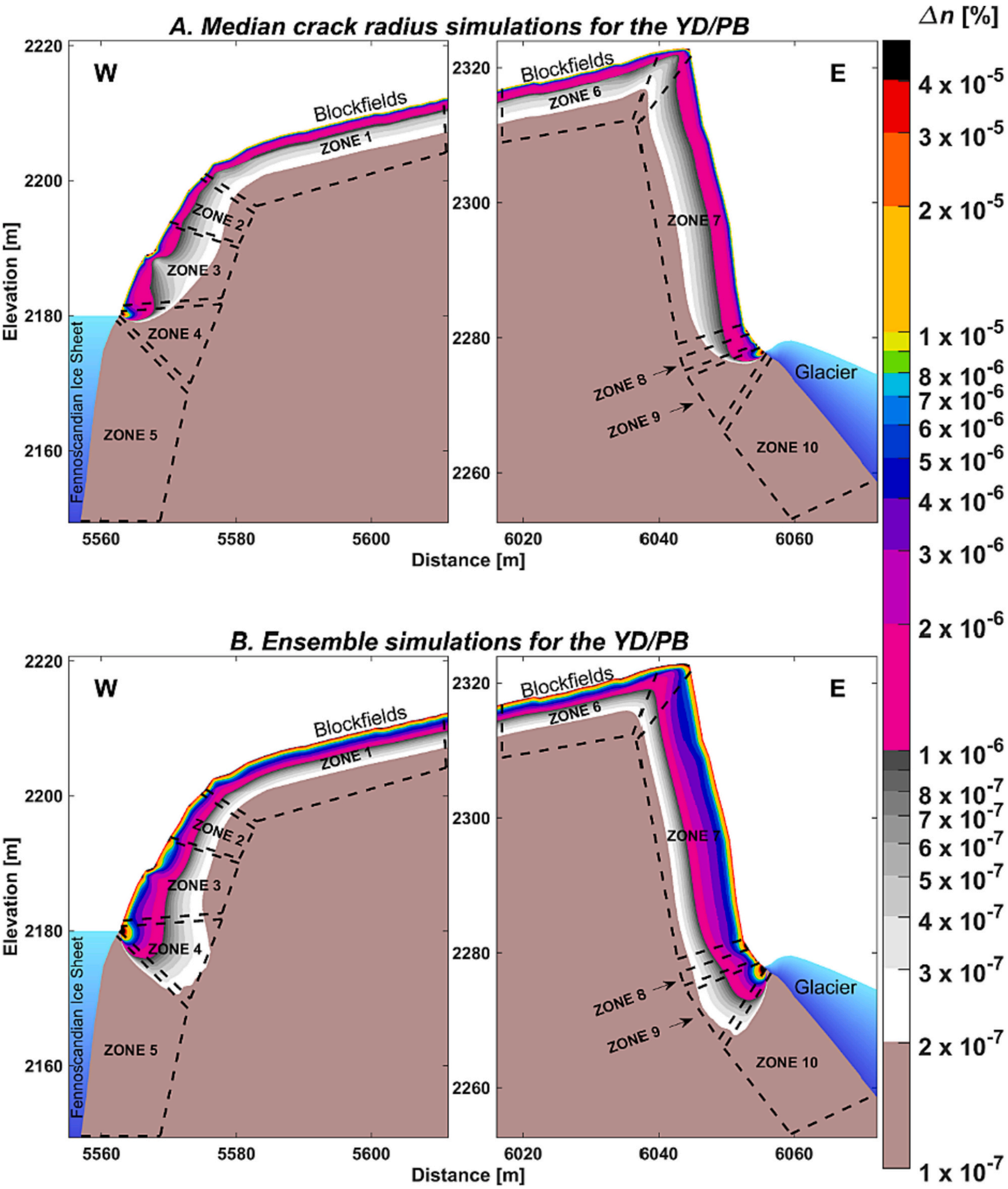

Fig. 6. Porosity changes Δ*n* in the Veslpiggen Plateau over the Younger Dryas/Preboreal (YD/PB) transition computed based on the undercooling for frost cracking for: **A**: Median crack radius simulations. **B**: Ensemble simulations. Note the logarithmic scale.

5.2. Model improvements and their feasibility

The main difference between this study using the 2D approach and other studies using the 1D approach (Draebing et al., 2022; Hales and Roering, 2007; Rempel et al., 2016; Savi et al., 2015) is that the lateral effects across areas with high thermal gradients could be simulated. Myhra et al. (2019) modeled large thermal gradients between the shaded rock walls and talus slopes below based on the conductive 2D ground temperature modeling, implying that frost weathering may be very active in such transition zones. Berrisford (1991)'s investigations suggested a high potential for weathering at the average annual retreat position for snow patches in Jotunheimen. Furthermore, this finding is crucial for supporting the nivation processes and associated landforms (Christiansen, 1998). In our modeling, sharp transitions in snow depth

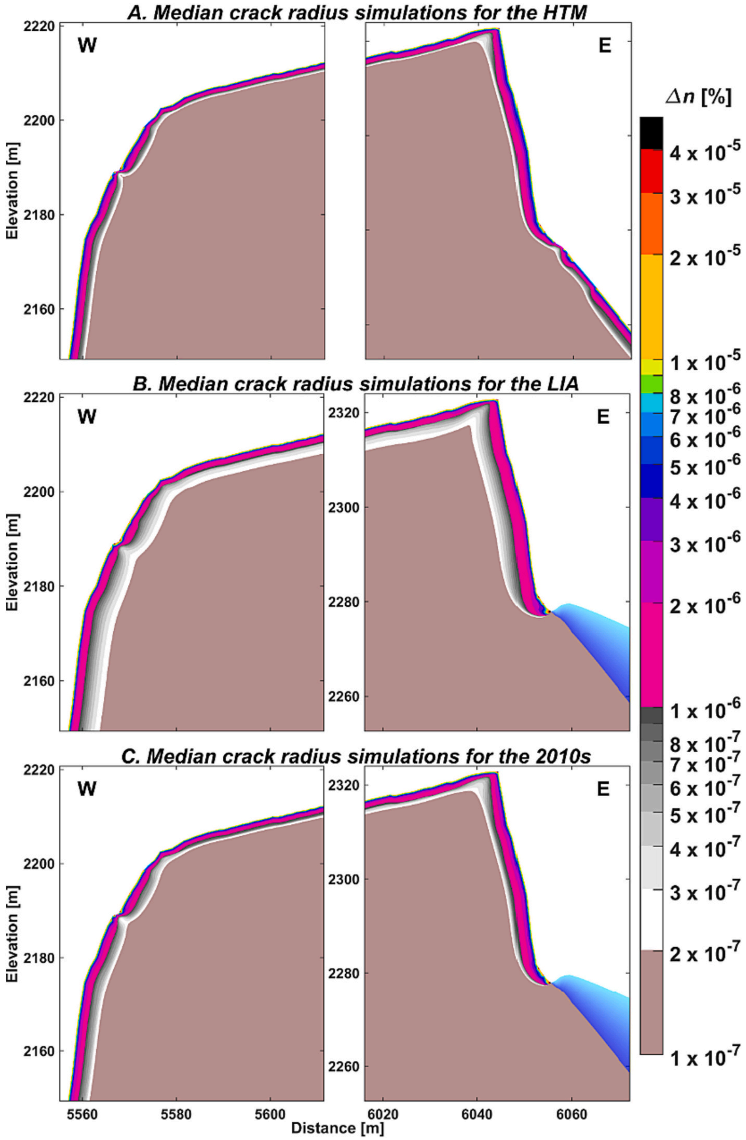

Fig. 7. Porosity changes Δn in the Veslpiggen Plateau computed based on undercooling for frost cracking for the median crack radius for various decennia. HTM – The Holocene Thermal Maximum. LIA – The Little Ice Age. Note the logarithmic scale.

along the profiles led to quite large thermal gradients, indicating that spatial heterogeneities in snow cover could be sufficient to generate transition zones with elevated frost damage. The latter is in accordance with the studies of coastal cliff temperatures in Svalbard, where larger frost weathering potential is related to thermal gradients due to snow cover variations (Ødegård et al., 1995; Ødegård and Sollid, 1993). Furthermore, the most pronounced frost weathering potential is modeled between glaciers and rock walls in our study, which agrees well with the study of Hartmeyer et al. (2020) concerning glaciated cirques in the Central Alps of Austria, where ice segregation led to high rockfall activity in recently deglaciated areas.

To our knowledge, no other frost weathering modeling study to date has attempted to account for heterogenous crack radii. We did not attempt to fully describe interactions between cracks, although we recognize that liquid water is likely to be redistributed between various cracks according to their sizes, and not necessarily only according to their temperatures. As ground temperature drops, ice growth is expected to start in the largest cracks, and subsequently in smaller ones with progressing temperature decrease (Anderson et al., 2013). Frost damage would also start in the largest cracks because the smaller cracks require greater ice pressure to grow (Rempel et al., 2016), hence their undercooling for frost cracking has larger values (Fig. 4). However, it is

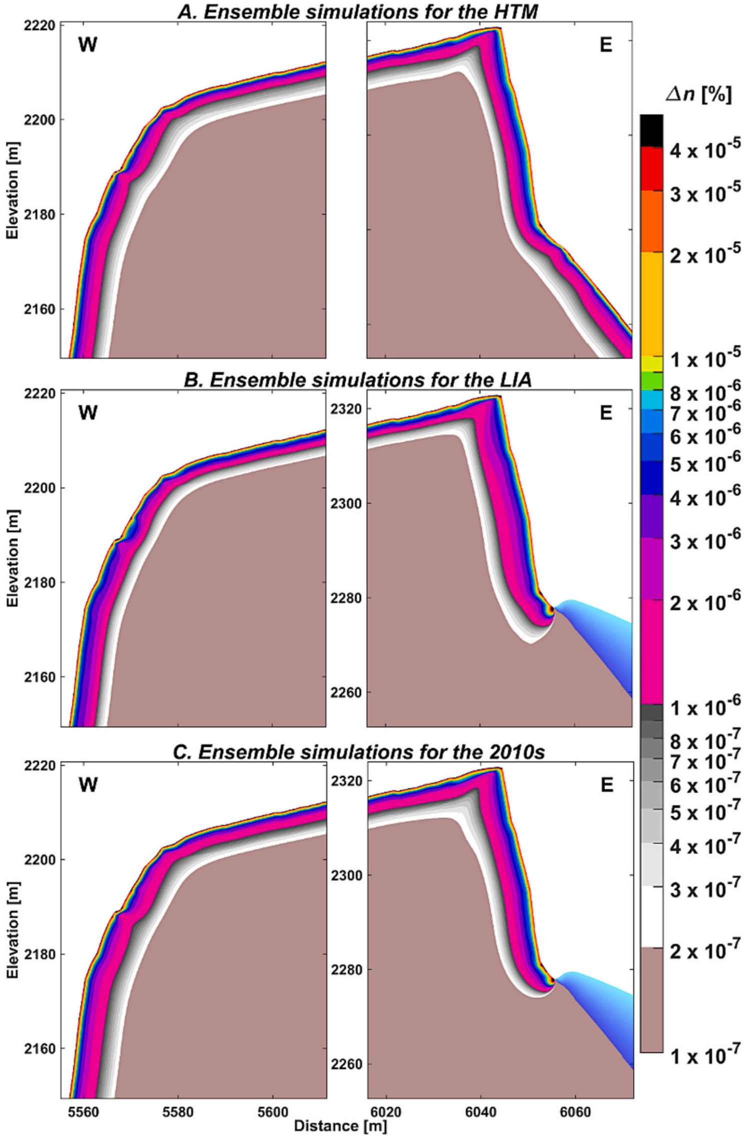

Fig. 8. Porosity changes Δn in the Veslpiggen Plateau computed based on undercooling for frost cracking from the ensemble simulations for various decennia. HTM – The Holocene Thermal Maximum. LIA – The Little Ice Age. Note the logarithmic scale.

uncertain whether liquid water would feed the smaller cracks at lower ground temperatures, because the larger cracks may suck water from the smaller cracks, as laboratory experiments suggest for isothermal frost damage (Rempel and Van Alst, 2013). The mean values from the ensemble approach are governed by larger crack radii than the median crack radius, which might be viewed as suggestive of such a water redistribution process, although we emphasize that our approach was not formulated to account explicitly for such crack growth interactions. Further model developments are needed to better account for the interaction of the various crack radii, ideally tested by laboratory experiments or field observations, although the collection of suitable validation data may be challenging, as shown in other frost weathering studies (Matsuoka and Murton, 2008).

5.3. Spatiotemporal distribution of frost damage

In general, studies show that frost weathering is more intense in north-facing rock walls since they have lower ground temperatures and may have higher moisture content (Coutard and Francou, 1989; Sass, 2005a). Even though we cannot discuss the relevance of moisture content, our results showed that the sun-exposed rock walls should have more frost damage, in agreement with Draebing and Mayer (2021), who

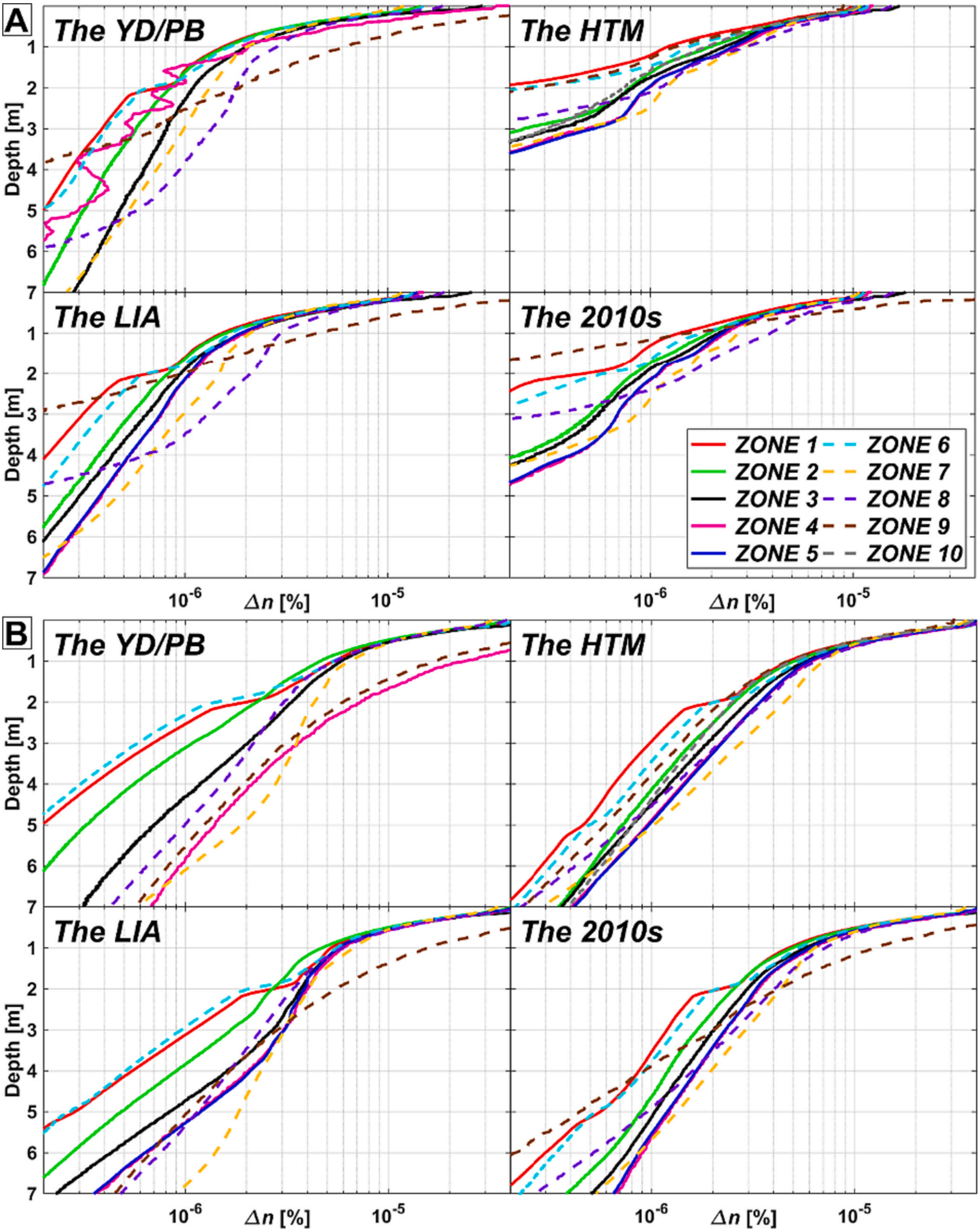

Fig. 9. Average profiles of porosity change Δn with depth in zones shown in Fig. 6 for: **A**: Median crack radius simulations. **B**: Ensemble simulations. YD/PB – The Younger Dryas/Preboreal. HTM – The Holocene Thermal Maximum. LIA – The Little Ice Age. Note the logarithmic scale.

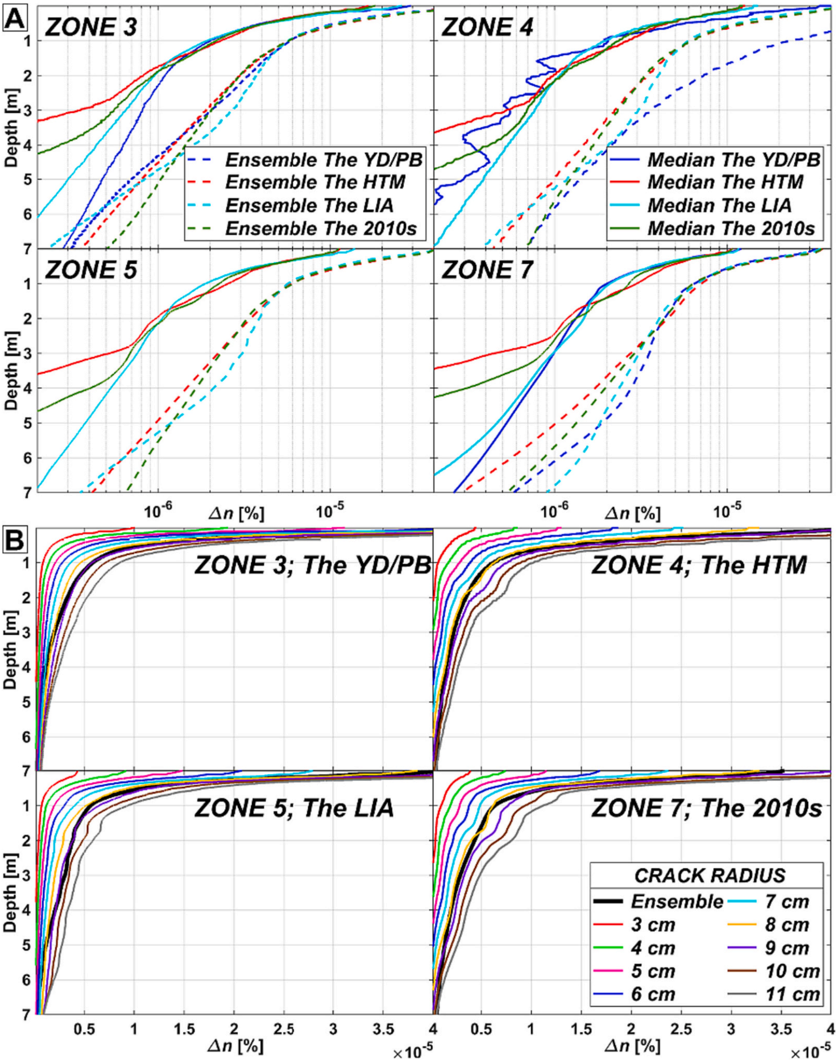

Fig. 10. Average profiles of porosity change Δn with depth in zones encompassing rock walls shown in Fig. 6. **A**: Temporal changes in each zone. Note the logarithmic scale. **B**: Simulations for various crack radii and ensemble simulations. YD/PB – The Younger Dryas/Preboreal. HTM – The Holocene Thermal Maximum. LIA – The Little Ice Age.

also used the model by Rempel et al. (2016). The large frost cracking potential in the east-facing rock wall in Jotunheimen likely arises from the largest MAGST amplitudes in this exposition. The latter is retained from the original 1D frost damage model as shown in the examples by Rempel et al. (2016). We also showed that rock walls have generally more effective frost cracking than other terrain types due to the largest MAGST amplitudes. Our modeling could be extended by running the model at sub-daily time steps to further show that also sub-daily temperature variations would be larger in rock walls than in other terrain types, where deeper snow cover decreases daily temperature amplitudes (e.g. Anderson et al., 2013).

The warmest modeled period of the HTM was the period with the smallest frost-weathering potential in the rock walls, according to both the median crack radius and ensemble simulations. The ongoing atmospheric warming will soon bring climatic conditions to those in the HTM, implying that frost weathering potential in the rock walls in Jotunheimen will be reduced in the future. Kellerer-Pirklbauer (2017) discussed a similar future with smaller frost weathering in the rock walls in the Alps in Austria.

5.4. Geomorphological implications

Frost weathering plays an important role in rock wall retreat and comprises a large contribution to rockfall supply onto talus slopes (Krautblatter and Dikau, 2007). Frost weathering leads to intensification of rockfall processes (Blikra and Nemec, 1998), although in detail segregation ice weathering acts primarily as a preconditioning mechanism (Curry, 2023), enabling rockfall events to be triggered by other factors such as seasonal thawing of the active layer as segregation ice melts out (Sass, 2005b), deepening of the active layer (Gruber et al., 2004; Ravanel and Deline, 2011), adverse weather such as persistent heavy rainfall and snowmelt (Sandersen et al., 1997), or earthquakes that may result from enhanced seismic activity during glacio-isostatic rebound (Bellwald et al., 2019; Cossart et al., 2014). Frost weathering has been mentioned as a possible destabilizing factor for rock avalanches in Norway by Blikra et al. (2006), although it is uncertain whether frost weathering contributes to larger events, because frost weathering processes operate mostly in the upper few meters (Krautblatter et al., 2013; Rempel et al., 2016), as our results also suggest. Hence, larger rock slope failures in permafrost-underlain terrain are much more influenced by long-term permafrost changes, and the delay in the rock material release may be as long as millennia when permafrost finally degrades (Matthews et al., 2018; Hilger et al., 2021). Rockfalls often recur seasonally and therefore we assume they are much more related to the frost weathering processes in periglacial environments.

According to our results, the frost weathering potential was largest between the relatively warmer ice sheets or glaciers and relatively colder rock walls or moderately steep slopes in the YD/PB, when ground temperatures were lowest since deglaciation. This aspect agrees well with the knowledge about rockfall accumulations outside Norway since deglaciation, i.e. that most sediments accumulated soon after deglaciation (e.g. Rapp, 1960; Ballantyne and Kirkbride, 1987; Hinchliffe and Ballantyne, 1999), although it is uncertain whether these sediments should be considered as due to stress release in response to deglaciation or periglacial due to the enhanced frost weathering (Ballantyne, 2002; Ballantyne and Harris, 1994; Hinchliffe and Ballantyne, 1999). However, the mentioned processes may be connected. Rock walls affected by glacial debuttressing would be highly fractured near the surface, priming them for even more efficient frost weathering (Ballantyne and Kirkbride, 1987; Hales and Roering, 2009). Messenzehl et al. (2017) investigated the influence of various factors on rockfall distribution at a regional scale in the Turtmann Valley in the Swiss Alps. They concluded that ice segregation is probably the most important breakdown mechanism in the study area, even more important than time since deglaciation and mechanical factors, implying that debuttressing effects may be overestimated in some areas. Other studies focus on more intense ice segregation weathering as permafrost aggrades during deglaciation (e.g. Draebing et al., 2022). Our results indicate potentially large periglacial activity in rock walls during deglaciation, specifically where large temperature differences exist between rock walls and melting ice sheets or glaciers. The results suggest not only a large frost cracking potential close to the surface, but also possibly a larger frost weathering potential at depth in such areas. The enhanced frost weathering at sites with large thermal gradients could progressively weaken entire rock walls during an ice sheet/glacier retreat, when abundant meltwater would be available from the melting ice sheet/glacier. Ongoing glacier retreat already increases rockfalls from newly deglaciated rock wall faces in the European Alps (Fischer et al., 2006) and in the Peruvian Andes (Stuart-Smith et al., 2021), perhaps partly due to meltout or warming of ice lenses formed in rock faces adjacent to previous glacier surfaces.

In southern Norway, most rockfall material accumulated during the climatic deterioration over the YD (Blikra and Nemec, 1998) and generally after deglaciation (Matthews and Nesje, 2023). Those studies compare favorably with the large frost cracking in the YD modeled in our study. The enhanced frost weathering at that time was likely also important for the development of relict talus-derived rock glaciers in Norway (Lilleøren and Etzelmüller, 2011). Blikra and Longva (1995) discussed that the Quaternary deposits in the Møre-Romsdal district in Norway probably accumulated due to intense frost weathering in the YD with deep permafrost conditions. The early Holocene and the HTM were probably periods with limited rockfall activity (Blikra and Nemec, 1998), which coincides with the lowest modeled frost cracking potential during the HTM in our study. The rockfall activity increased again in the second half of the Holocene (Blikra and Nemec, 1998; Nesje, 2002; Nesje et al., 1994), likely due to climatic deterioration and hence the increased frost weathering activity during colder and perhaps wetter phases of the mid-Holocene (Neo-glaciation). Several rockfall events and colluvial processes occurred in Jotunheimen during the late Holocene over the last 4000 years (Støren et al., 2008). Our results could explain more intense periglacial weathering in the relatively colder climate of the LIA. McCarroll et al. (2001)'s study claimed that rockfall accumulation rates in the Jotunheimen region were substantially higher in the coldest phase of the LIA, implying that periglacial processes and thus climate variations are sufficient to explain the origin of the talus in this area with no need for glacial debuttressing effects. In a transition period, heat waves may exert a particularly strong influence on the stability of steep rock walls as long as parts of the rock wall are frozen. The timing of small rock-slope failures (excluding rockfalls) in the Jotunheimen area was different than the mentioned rockfall activity and peaked in the mid- to late-Holocene due to permafrost degradation (Matthews et al., 2018).

Frost weathering has long been an interest within the research on the development of glacial cirques, where the bergschrund, the randkluft or both have been identified as the key locations for effective erosion in lower parts of headwalls (e.g. Gardner, 1987; Evans, 2021). In such zones, intensely frost-weathered material is further transported by glacier through quarrying, thereby allowing for high erosion rates in glaciated cirques. Thermal conditions in such zones are certainly important for cirque erosion and the variations in elevation of glacier surfaces led to the exposure of several hundred meters of cirque headwalls to frost weathering throughout the Quaternary (Gardner, 1987). One-dimensional modeling of ice segregation weathering has already been proven to be useful for understanding the role of frost weathering in cirque erosion (Sanders et al., 2012). Further attempts using the two-dimensional approach as shown here may allow for even more progress, as large thermal gradients along cirque headwall are probable (e.g. Fisher, 1955).

6. Conclusions

We have modeled ground temperature in two dimensions in a mountain plateau in the Jotunheimen Mountains in Norway. Based on the modeled thermal fields, we computed frost damage potential in 2D using an established numerical model. We derived and presented the first frost cracking index applied to rock walls in two dimensions. In addition, we mapped crack radii in a nearby rock wall and ran ensemble simulations to account for the distribution of crack radii. We demonstrated limitations of the modeling and highlighted the importance of developing more advanced frost cracking indices that account more fully for interactions between populations of crack radii in rock walls and their two-/three-dimensional nature.

The key findings of our modeling are summarized as follows:

(1) Sites of enhanced frost weathering are concentrated in the vicinity of the melting ice sheet, the local glaciers and anywhere else where sharp transitions in snow conditions occur, resulting in large temperature gradients in these areas.
(2) Sites of enhanced frost weathering due to lateral effects are not strongly controlled by the climatic conditions as long as they are within the periglacial domain. However, the location of such sites changes due to evolving snow and glacier coverage.
(3) If only one crack radius is modeled, we recommend replacing the median crack radius with a larger crack radius, since ice growth in larger cracks can be more effective at promoting frost damage.
(4) Simulated porosity changes indicate that in addition to glacial debuttressing processes, frost weathering can weaken the bedrock while the ice sheet/glacier melts. This could be particularly important both for deglaciation and ongoing contemporary mountain glacier retreat around the world, and could potentially increase material detachability from rock faces in newly deglaciated areas.

(5) Our modeled frost weathering potential compares favorably with most of the published studies concerning the timing of rockfall accumulations in southern Norway.

Funding

This study was funded through Justyna Czekirda's doctoral research fellow position at the Department of Geosciences, University of Oslo, Norway.

CRediT authorship contribution statement

Justyna Czekirda: Conceptualization, Formal analysis, Methodology, Software, Visualization, Writing – original draft. **Alan W. Rempel:** Conceptualization, Formal analysis, Methodology, Writing – review & editing. **Bernd Etzelmüller:** Conceptualization, Methodology, Supervision, Writing – review & editing. **Sebastian Westermann:** Methodology, Writing – review & editing.

Declaration of competing interest

The authors declare that they have no known competing financial interests or personal relationships that could have appeared to influence the work reported in this paper.

Data availability

Data will be made available on request.

Acknowledgments

We thank Luc Girod for collecting drone imagery from the Kjelen rock wall and Trond Eiken for additional help during the fieldwork.

Appendix A. Frost damage model derivation

In the present study, we model the porosity changes using Supplementary Eq. (5) in Rempel et al. (2016), which is applicable to two- and three-dimensional cases:

$$\frac{\partial n}{\partial t} = \frac{\rho L}{T_m \mu}\left[\frac{dk}{dT}\,(\nabla T)^2 + k\nabla^2 T\right], \tag{A.1}$$

where n is the porosity, ρ is the ice density (920 kg m^{-3}), L is the specific latent heat of fusion for water (334 kJ kg^{-1}), T_m is the bulk melting temperature (273.15 K), and μ is the water dynamic viscosity (here 1.8 mPa s). The temperature-dependent permeability $k(T)$ is parametrized using the power-law function:

$$k(T) = k_c\left(\frac{\Delta T_c}{\Delta T}\right)^{\alpha} \tag{A.2}$$

where α is the unitless power-law exponent between 2 and 5, k_c denotes the permeability at ΔT_c, typically between 10^{-24} and 10^{-16} m^2. ΔT_c is the upper-temperature limit for frost cracking. The first derivative of $k(T)$ with respect to T is:

$$\frac{dk(T)}{dT} = \frac{k_c \alpha}{\Delta T_c}\left(\frac{\Delta T_c}{\Delta T}\right)^{\alpha+1} \tag{A.3}$$

Using Eqs. (A.2) and (A.3) in Eq. (A.1), we may then express:

$$\frac{\partial n}{\partial t} = \frac{\alpha \rho L k_c}{T_m \mu \Delta T_c}\left(\frac{\Delta T_c}{\Delta T}\right)^{\alpha+1}(\nabla T)^2 + \frac{\rho L k_c}{T_m \mu}\left(\frac{\Delta T_c}{\Delta T}\right)^{\alpha}\nabla^2 T \tag{A.4}$$

where D – "the frost weathering diffusivity" is:

$$D = \frac{\alpha \rho L k_c \Delta T_c}{T_m \mu} \tag{A.5}$$

Using Eq. (A.5) in Eq. (A.4), we find:

$$\frac{\partial n}{\partial t} = \frac{D \Delta {T_c}^{\alpha-1} \Delta T^{-\alpha}}{\alpha}\left[\frac{\alpha}{\Delta T}\,(\nabla T)^2 + \nabla^2 T\right] \tag{A.6}$$

For a node in two dimensions with the Cartesian coordinates x and y at the time t, the model for porosity changes becomes:

$$\Delta n(x,y,t) = \frac{D \Delta {T_c}^{\alpha-1}}{\alpha}\int_{t_c}^{t} \Delta T(x,y,t)^{-\alpha}\left[\frac{\alpha}{\Delta T(x,y,t)}\,(\nabla T(x,y,t))^2 + \nabla^2 T(x,y,t)\right]dt \tag{A.7}$$

The accumulated porosity change for one year can thus be written as:

$$\Delta n(x,y) = \frac{D \Delta {T_c}^{\alpha-1}}{\alpha}\int_{\Delta T > \Delta T_c, 1\ year} \Delta T(x,y)^{-\alpha}\left[\frac{\alpha}{\Delta T(x,y)}\,(\nabla T(x,y))^2 + \nabla^2 T(x,y)\right]dt \tag{A.8}$$

References

Anderson, R.S., 1998. Near-surface thermal profiles in alpine bedrock: implications for the frost weathering of rock. Arctic and Alpine Research 30 (4), 362–372. https://doi.org/10.2307/1552008.

Anderson, R.S., Anderson, S.P., Tucker, G.E., 2013. Rock damage and regolith transport by frost: an example of climate modulation of the geomorphology of the critical zone. Earth Surf Proc Land 38 (3), 299–316. https://doi.org/10.1002/esp.3330.

André, M.-F., 2003. Do periglacial landscapes evolve under periglacial conditions? Geomorphology 52 (1–2), 149–164. https://doi.org/10.1016/s0169-555x(02)00255-6.

Ballantyne, C.K., 2002. Paraglacial geomorphology. Quaternary Science Reviews 21 (18), 1935–2017. https://doi.org/10.1016/S0277-3791(02)00005-7.

Ballantyne, C.K., 2018. Periglacial Geomorphology. Wiley-Blackwell.

Ballantyne, C.K., Harris, C., 1994. The periglaciation of Great Britain. UK:Cambridge University Press, Cambridge.

Ballantyne, C.K., Kirkbride, M.P., 1987. Rockfall activity in upland britain during the loch lomond stadial. Geogr J. 153 (1), 86–92. https://doi.org/10.2307/634474.

Bellwald, B., Hjelstuen, B.O., Sejrup, H.P., Stokowy, T., Kuvås, J., 2019. Holocene mass movements in west and mid-Norwegian fjords and lakes. Mar. Geol. 407, 192–212. https://doi.org/10.1016/j.margeo.2018.11.007.

Berrisford, M.S., 1991. Evidence for enhanced mechanical weathering associated with seasonally late-lying and perennial snow patches, Jotunheimen. Norway. Permafrost Periglac 2 (4), 331–340. https://doi.org/10.1002/ppp.3430020408.

Berthling, I., Etzelmüller, B., 2011. The concept of cryo-conditioning in landscape evolution. Quatern. Res. 75 (2), 378–384. https://doi.org/10.1016/j.yqres.2010.12.011.

Blikra, L.H., Longva, O., 1995. Frost-shattered debris facies of Younger Dryas age in the coastal sedimentary successions in western Norway: palaeoenvironmental implications. Palaeogeogr. Palaeoclimatol. Palaeoecol. 118 (1), 89–110. https://doi.org/10.1016/0031-0182(94)00141-T.

Blikra, L.H., Nemec, W., 1998. Postglacial colluvium in western Norway: depositional processes, facies and palaeoclimatic record. Sedimentology 45 (5), 909–960. https://doi.org/10.1046/j.1365-3091.1998.00200.x.

Blikra, L.H., Longva, O., Braathen, A., Anda, E., Dehls, J., Stalsberg, K., 2006. Rock slope failures in Norwegian fjord areas: Examples, spatial distribution and temporal pattern. In: Landslides from Massive Rock Slope Failure. Springer, pp. 475–496.

Boeckli, L., Brenning, A., Gruber, S., Noetzli, J., 2012. A statistical approach to modelling permafrost distribution in the European Alps or similar mountain ranges. Cryosphere 6 (1), 125–140. https://doi.org/10.5194/tc-6-125-2012.

Carslaw, H.S., Jaeger, J.C., 1959. Conduction of Heat in Solids. Clarendon Press.

Chang, S.-H., Lee, C.-I., Jeon, S., 2002. Measurement of rock fracture toughness under modes I and II and mixed-mode conditions by using disc-type specimens. Eng. Geol. 66 (1), 79–97. https://doi.org/10.1016/S0013-7952(02)00033-9.

Christiansen, H.H., 1998. Nivation forms and processes in unconsolidated sediments. NE Greenland. Earth Surf Proc Land 23 (8), 751–760. https://doi.org/10.1002/(SICI)1096-9837(199808)23:8<751::AID-ESP886>3.0.CO;2-A.

Cossart, E., Mercier, D., Decaulne, A., Feuillet, T., Jónsson, H.P., Sæmundsson, Þ., 2014. Impacts of post-glacial rebound on landslide spatial distribution at a regional scale in northern Iceland (Skagafjörður). Earth Surf. Process. Landforms 39, 336–350. https://doi.org/10.1002/esp.3450.

Coutard, J.-P., Francou, B., 1989. Rock temperature measurements in two alpine environments: implications for frost shattering. Arctic and Alpine Research 21 (4), 399–416. https://doi.org/10.2307/1551649.

Curry, A., 2023. Talus slopes. In *Reference Module in Earth Systems and Environmental Sciences. Elsevier*. https://doi.org/10.1016/B978-0-323-99931-1.00047-7.

Czekirda, J., Etzelmüller, B., Westermann, S., Isaksen, K., Magnin, F., 2023. Post-Little Ice Age rock wall permafrost evolution in Norway. The Cryosphere 17 (7), 2725–2754. https://doi.org/10.5194/tc-17-2725-2023.

Dash, J.G., Rempel, A.W., Wettlaufer, J.S., 2006. The physics of premelted ice and its geophysical consequences. Rev. Mod. Phys. 78 (3), 695–741. https://doi.org/10.1103/RevModPhys.78.695.

Draebing, D., Mayer, T., 2021. Topographic and geologic controls on frost cracking in Alpine rockwalls. J. Geophys. Res. Earth 126 (6), e2021JF006163. https://doi.org/10.1029/2021JF006163.

Draebing, D., Mayer, T., Jacobs, B., McColl, S.T., 2022. Alpine Rockwall erosion patterns follow elevation-dependent climate trajectories. Communications Earth & Environment 3 (1), 21. https://doi.org/10.1038/s43247-022-00348-2.

Duca, S., Occhiena, C., Mattone, M., Sambuelli, L., Scavia, C., 2014. Feasibility of ice segregation location by acoustic emission detection: A laboratory test in gneiss. Permafrost Periglac 25 (3), 208–219. https://doi.org/10.1002/ppp.1814.

Egholm, D.L., Andersen, J.L., Knudsen, M.F., Jansen, J.D., Nielsen, S.B., 2015. The periglacial engine of mountain erosion – part 2: Modelling large-scale landscape evolution. Earth Surf. Dynam. 3 (4), 463–482. https://doi.org/10.5194/esurf-3-463-2015.

Evans, I.S., 2021. Glaciers, rock avalanches and the 'buzzsaw' in cirque development: why mountain cirques are of mainly glacial origin. Earth Surf. Process. Landforms 46, 24–46. https://doi.org/10.1002/esp.4810.

Farbrot, H., Etzelmüller, B., Gudmundsson, A., Humlum, O., Kellerer-Pirklbauer, A., Eiken, T., Wangensteen, B., 2007. Rock glaciers and permafrost in Tröllaskagi, Northern Iceland. Zeitschrift für Geomorphologie, Supplementary Issues 51, 1–16. https://doi.org/10.1127/0372-8854/2007/0051S2-0001.

Farbrot, H., Hipp, T.F., Etzelmüller, B., Isaksen, K., Ødegård, R.S., Schuler, T.V., Humlum, O., 2011. Air and ground temperature variations observed along elevation and continentality gradients in Southern Norway. Permafrost Periglac 22 (4), 343–360. https://doi.org/10.1002/ppp.733.

Fischer, L., Kääb, A., Huggel, C., Noetzli, J., 2006. Geology, glacier retreat and permafrost degradation as controlling factors of slope instabilities in a high-mountain rock wall: the Monte Rosa east face. Nat. Hazards Earth Syst. Sci. 6 (5), 761–772. https://doi.org/10.5194/nhess-6-761-2006.

Fischer, L., Purves, R.S., Huggel, C., Noetzli, J., Haeberli, W., 2012. On the influence of topographic, geological and cryospheric factors on rock avalanches and rockfalls in high-mountain areas. Nat Hazard Earth Sys 12 (1), 241–254. https://doi.org/10.5194/nhess-12-241-2012.

Fisher, J.E., 1955. Internal Temperatures of a Cold Glacier and Conclusions Therefrom. Journal of Glaciology 2 (18), 583–591. https://doi.org/10.3189/002214355793702163.

Fredin, O., Bergstrøm, B., Eilertsen, R., Hansen, L., Longva, O., Nesje, A., & Sveian, H. (2013). Glacial landforms and Quaternary landscape development in Norway. *Quaternary Geology of Norway, edited by: Olsen, L., Fredin, O., and Olesen, O., Geological Survey of Norway Special Publication, Geological Survey of Norway, Trondheim, 525.*

French, H.M., 2016. Do periglacial landscapes exist? A discussion of the upland landscapes of northern interior Yukon. Canada. Permafrost Periglac 27 (2), 219–228. https://doi.org/10.1002/ppp.1866.

Gardner, J.S., 1987. Evidence for Headwall Weathering zones, Boundary Glacier, Canadian Rocky Mountains. J. Glaciol. 33 (113), 60–67. https://doi.org/10.3189/S0022143000005359.

Gruber, S., Haeberli, W., 2007. Permafrost in steep bedrock slopes and its temperature-related destabilization following climate change. J Geophys Res-Earth 112 (F2). https://doi.org/10.1029/2006jf000547.

Gruber, S., Hoelzle, M., Haeberli, W., 2004. Permafrost thaw and destabilization of Alpine rock walls in the hot summer of 2003. Geophys. Res. Lett. 31 (13) https://doi.org/10.1029/2004gl020051.

Hales, T.C., Roering, J.J., 2007. Climatic controls on frost cracking and implications for the evolution of bedrock landscapes. J. Geophys. Res. Earth 112 (F2). https://doi.org/10.1029/2006JF000616.

Hales, T.C., Roering, J.J., 2009. A frost "buzzsaw" mechanism for erosion of the eastern Southern Alps. New Zealand. Geomorphology 107 (3), 241–253. https://doi.org/10.1016/j.geomorph.2008.12.012.

Hallet, B., Walder, J.S., Stubbs, C.W., 1991. Weathering by segregation ice growth in microcracks at sustained subzero temperatures: Verification from an experimental study using acoustic emissions. Permafrost Periglac 2 (4), 283–300. https://doi.org/10.1002/ppp.3430020404.

Hanssen, T.H., 1988. Rock properties. In: Norwegian Tunnelling Today, vol. Publication No. 5. Tapir Publishers, University of Trondheim, pp. 41–44.

Hanssen-Bauer, I., Tveito, O., Szewczyk-Bartnicka, H., 2006. Comparison of grid-based and station-based regional temperature and precipitation series. *Met.No Report, 4/2006*. Retrieved from. https://www.met.no/publikasjoner/met-report/met-report-2006/_/attachment/download/dd9d9481-5986-4790-9154-54dd5a4ceae7:4b95bfe33dcc6651f34bed4e1e36399cb19bbdef/MET-report-04-2006.pdf.

Harris, C., Haeberli, W., Vonder Mühll, D., King, L., 2001. Permafrost monitoring in the high mountains of Europe: the PACE Project in its global context. Permafrost Periglac 12 (1), 3–11. https://doi.org/10.1002/ppp.377.

Hartmeyer, I., Delleske, R., Keuschnig, M., Krautblatter, M., Lang, A., Schrott, L., Otto, J. C., 2020. Current glacier recession causes significant rockfall increase: the immediate paraglacial response of deglaciating cirque walls. Earth Surf. Dynam. 8 (3), 729–751. https://doi.org/10.5194/esurf-8-729-2020.

Hilger, P., Hermanns, R.L., Czekirda, J., Myhra, K.S., Gosse, J.C., Etzelmüller, B., 2021. Permafrost as a first order control on long-term rock-slope deformation in (Sub-) Arctic Norway. Quat. Sci. Rev. 251, 106718. https://doi.org/10.1016/j.quascirev.2020.106718.

Hinchliffe, S., Ballantyne, C.K., 1999. Talus accumulation and Rockwall retreat, Trotternish, Isle of Skye. Scotland. Scottish Geographical Journal 115 (1), 53–70. https://doi.org/10.1080/00369229918737057.

Hipp, T., Etzelmüller, B., Westermann, S., 2014. Permafrost in Alpine Rock Faces from Jotunheimen and Hurrungane. Southern Norway. *Permafrost Periglac* 25 (1), 1–13. https://doi.org/10.1002/ppp.1799.

Hughes, A.L.C., Gyllencreutz, R., Lohne, Ø.S., Mangerud, J., Svendsen, J.-I., 2015. DATED-1: Compilation of Dates and Time-slice Reconstruction of the Build-up and Retreat of the Last Eurasian (British-Irish, Scandinavian, Svalbard-Barents-Kara Seas) Ice Sheets 40-10 ka. Department of Earth Science, University of Bergen and Bjerknes Centre for Climate Research, PANGAEA [dataset]. https://doi.org/10.1594/PANGAEA.848117.

Kellerer-Pirklbauer, A., 2017. Potential weathering by freeze-thaw action in alpine rocks in the European Alps during a nine year monitoring period. Geomorphology 296, 113–131. https://doi.org/10.1016/j.geomorph.2017.08.020.

Kleman, J., Stroeven, A.P., Lundqvist, J., 2008. Patterns of Quaternary ice sheet erosion and deposition in Fennoscandia and a theoretical framework for explanation. Geomorphology 97 (1), 73–90. https://doi.org/10.1016/j.geomorph.2007.02.049.

Krautblatter, M., Dikau, R., 2007. Towards a uniform concept for the comparison and extrapolation of Rockwall retreat and rockfall supply. Geogr. Ann. Ser. B 89 (1), 21–40. https://doi.org/10.1111/j.1468-0459.2007.00305.x.

Krautblatter, M., Funk, D., Günzel, F.K., 2013. Why permafrost rocks become unstable: a rock-ice-mechanical model in time and space. Earth Surf Proc Land 38 (8), 876–887. https://doi.org/10.1002/esp.3374.

Lilleøren, K.S., Etzelmüller, B., 2011. A regional inventory of rock glaciers and ice-cored moraines in Norway. Geogr. Ann. Ser. B 93 (3), 175–191. https://doi.org/10.1111/j.1468-0459.2011.00430.x.

Lilleøren, K.S., Etzelmüller, B., Schuler, T.V., Gisnås, K., Humlum, O., 2012. The relative age of mountain permafrost — estimation of Holocene permafrost limits in Norway. Global Planet. Change 92-93, 209–223. https://doi.org/10.1016/j.gloplacha.2012.05.016.

Liu, Z., Otto-Bliesner, B.L., He, F., Brady, E.C., Tomas, R., Clark, P.U., Carlson, A.E., Lynch-Stieglitz, J., Curry, W., Brook, E., Erickson, D., Jacob, R., Kutzbach, J., Cheng, J., 2009. Transient simulation of last deglaciation with a new mechanism for Bølling-Allerød warming. Science 325 (5938), 310–314. https://doi.org/10.1126/science.1171041.

Lussana, C., 2020. *seNorge observational gridded datasets. seNorge_2018, version 20.05*. [dataset]. https://arxiv.org/abs/2008.02021.

Lutro, O., & Tveten, E. (2012). Berggrunnskart (EN Bedrock map) Galdhøpiggen 1518 II, M 1: 50.000. Retrieved from https://www.ngu.no/upload/Publikasjoner/Kart/B50/galdhopiggen.pdf.

Magnin, F., Etzelmüller, B., Westermann, S., Isaksen, K., Hilger, P., Hermanns, R.L., 2019. Permafrost distribution in steep rock slopes in Norway: measurements, statistical modelling and implications for geomorphological processes. Earth Surf Dynam 7 (4), 1019–1040. https://doi.org/10.5194/esurf-7-1019-2019.

Matsuoka, N., 1990. Mechanisms of rock breakdown by frost action: an experimental approach. Cold Reg. Sci. Technol. 17 (3), 253–270. https://doi.org/10.1016/S0165-232X(05)80005-9.

Matsuoka, N., Murton, J., 2008. Frost weathering: recent advances and future directions. Permafrost Periglac 19 (2), 195–210. https://doi.org/10.1002/ppp.620.

Matthews, J.A., Dresser, P.Q., 2008. Holocene glacier variation chronology of the Smørstabbtindan massif, Jotunheimen, southern Norway, and the recognition of century- to millennial-scale European Neoglacial events. The Holocene 18 (1), 181–201. https://doi.org/10.1177/0959683607085608.

Matthews, J.A., Nesje, A., 2023. Scandinavia. In: Periglacial Landscapes of Europe. Springer, pp. 365–426.

Matthews, J.A., Winkler, S., Wilson, P., Tomkins, M.D., Dortch, J.M., Mourne, R.W., Hill, J.L., Owen, G., Vater, A.E., 2018. Small rock-slope failures conditioned by Holocene permafrost degradation: a new approach and conceptual model based on Schmidt-hammer exposure-age dating, Jotunheimen, southern Norway. Boreas 47 (4), 1144–1169. https://doi.org/10.1111/bor.12336.

McCarroll, D., Shakesby, R.A., Matthews, J.A., 2001. Enhanced rockfall activity during the Little Ice Age: further lichenometric evidence from a Norwegian talus. Permafrost Periglac 12 (2), 157–164. https://doi.org/10.1002/ppp.359.

McGreevy, J.P., Whalley, W.B., 1982. The geomorphic significance of rock temperature variations in cold environments: a discussion. Arct. Alp. Res. 14 (2), 157–162. https://doi.org/10.2307/1551114.

Messenzehl, K., Meyer, H., Otto, J.-C., Hoffmann, T., Dikau, R., 2017. Regional-scale controls on the spatial activity of rockfalls (Turtmann Valley, Swiss Alps) — A multivariate modeling approach. Geomorphology 287, 29–45. https://doi.org/10.1016/j.geomorph.2016.01.008.

Murton, J.B., Peterson, R., Ozouf, J.-C., 2006. Bedrock fracture by ice segregation in cold regions. Science 314 (5802), 1127–1129. https://doi.org/10.1126/science.1132127.

Myhra, K.S., Westermann, S., Etzelmüller, B., 2017. Modelled distribution and temporal evolution of permafrost in steep rock walls along a latitudinal transect in Norway by CryoGrid 2D. Permafrost Periglac 28 (1), 172–182. https://doi.org/10.1002/ppp.1884.

Myhra, K.S., Westermann, S., Etzelmüller, B., 2019. Modeling conductive heat flow between steep rock walls and talus slopes–thermal processes and geomorphological implications. *Frontiers*. Earth Sci. 7 (192) https://doi.org/10.3389/feart.2019.00192.

Nesje, A., 2002. A large rockfall avalanche in Oldedalen, inner Nordfiord, western Norway, dated by means of a sub-avalanche Salix sp. tree trunk. Norwegian Journal of Geology/Norsk Geologisk Forening 82 (1), 59–62.

Nesje, A., 2009. Latest Pleistocene and Holocene alpine glacier fluctuations in Scandinavia. Quaternary Science Reviews 28 (21), 2119–2136. https://doi.org/10.1016/j.quascirev.2008.12.016.

Nesje, A., Blikra, L.H., Anda, E., 1994. Dating rockfall-avalanche deposits from degree of rock-surface weathering by Schmidt-hammer tests: a study from Norangsdalen, Sunnmøre. Norway. Norsk Geologisk Tidsskrift 74 (2), 108–113.

Nesje, A., Bakke, J., Dahl, S.O., Lie, Ø., Matthews, J.A., 2008. Norwegian mountain glaciers in the past, present and future. Global Planet. Change 60 (1), 10–27. https://doi.org/10.1016/j.gloplacha.2006.08.004.

Nilsen, B., Thidemann, A., 1993. Rock engineering. Norwegian Institute of Technology, Department of Hydraulic Engineering.

Noetzli, J., Gruber, S., 2009. Transient thermal effects in Alpine permafrost. The Cryosphere 3 (1), 85–99. https://doi.org/10.5194/tc-3-85-2009.

Noetzli, J., Gruber, S., Kohl, T., Salzmann, N., Haeberli, W., 2007. Three-dimensional distribution and evolution of permafrost temperatures in idealized high-mountain topography. J Geophys Res-Earth 112 (F2). https://doi.org/10.1029/2006jf000545.

North Greenland Ice Core Project Members (NGRIP), 2004. North Greenland Ice Core Project Oxygen Isotope Data. In: IGBP PAGES/World. Data Center for Paleoclimatology, Data Contribution Series # 2004–059. NOAA/NGDC Paleoclimatology Program, Boulder CO, USA.

Ødegård, R., Etzelmüller, B., Vatne, G., Sollid, J., 1995. Near-surface spring temperatures in an Arctic coastal cliff: Possible implications of rock breakdown. In: Slaymaker, O. (Ed.), Steepland Geomorphology. John Wiley & Sons, pp. 89–102.

Ødegård, R.S., Sollid, J.L., 1993. Coastal cliff temperatures related to the potential for cryogenic weathering processes, western Spitsbergen. Svalbard. Polar Research 12 (1), 95–106. https://doi.org/10.3402/polar.v12i1.6705.

Ødegård, R.S., Sollid, J.L., Liestøl, O., 1992. Ground temperature measurements in mountain permafrost, Jotunheimen, southern Norway. Permafrost Periglac 3 (3), 231–234. https://doi.org/10.1002/ppp.3430030310.

Oskin, M., Burbank, D.W., 2005. Alpine landscape evolution dominated by cirque retreat. Geology 33 (12), 933–936. https://doi.org/10.1130/g21957.1.

Paterson, W.S.B., 1994. 12 - Flow of ice shelves and ice streams. In: Paterson, W.S.B. (Ed.), The Physics of Glaciers, Third edition. Pergamon, pp. 289–316. https://doi.org/10.1016/B978-0-08-037944-9.50018-2.

Patton, H., Hubbard, A., Andreassen, K., Auriac, A., Whitehouse, P.L., Stroeven, A.P., Shackleton, C., Winsborrow, M., Heyman, J., Hall, A.M., 2017. Deglaciation of the Eurasian ice sheet complex. Quat. Sci. Rev. 169, 148–172. https://doi.org/10.1016/j.quascirev.2017.05.019.

Prabhakaran, R., Bruna, P.O., Bertotti, G., Smeulders, D., 2019. An automated fracture trace detection technique using the complex shearlet transform. Solid Earth 10 (6), 2137–2166. https://doi.org/10.5194/se-10-2137-2019.

Rapp, A., 1960. Recent development of mountain slopes in Karkevagge and Surroundings, Northern Scandinavia. Geografiska Annaler 42 (2/3), 65–200. https://doi.org/10.2307/520126.

Ravanel, L., Deline, P., 2011. Climate influence on rockfalls in high-Alpine steep rockwalls: the north side of the Aiguilles de Chamonix (Mont Blanc massif) since the end of the 'Little Ice Age'. Holocene 21 (2), 357–365. https://doi.org/10.1177/0959683610374887.

Rempel, A.W., Van Alst, L.J., 2013. Potential gradients produced by pore-space heterogeneities: application to isothermal frost damage and submarine hydrate anomalies. In: Poromechanics V Proceedings of the Fifth Biot Conference on Poromechanics, pp. 813–822. https://doi.org/10.1061/9780784412992.098.

Rempel, A.W., Marshall, J.A., Roering, J.J., 2016. Modeling relative frost weathering rates at geomorphic scales. Earth Planet. Sci. Lett. 453, 87–95. https://doi.org/10.1016/j.epsl.2016.08.019.

Sanders, J.W., Cuffey, K.M., Moore, J.R., MacGregor, K.R., Kavanaugh, J.L., 2012. Periglacial weathering and headwall erosion in cirque glacier bergschrunds. Geology 40 (9), 779–782. https://doi.org/10.1130/g33330.1.

Sandersen, F., Bakkehøi, S., Hestnes, E., Lied, K., 1997. The influence of meteorological factors on the initiation of debris flows, rockfalls, rockslides and rockmass stability. Norges Geotekniske Institutt 201, 97–114.

Sass, O., 2005a. Rock moisture measurements: techniques, results, and implications for weathering. Earth Surf Proc Land 30 (3), 359–374. https://doi.org/10.1002/esp.1214.

Sass, O., 2005b. Temporal Variability of Rockfall in the Bavarian Alps, Germany. Arct. Antarct. Alp. Res. 37 (4), 564–573. https://doi.org/10.1657/1523-0430(2005)037[0564:TVORIT]2.0.CO;2.

Savi, S., Delunel, R., Schlunegger, F., 2015. Efficiency of frost-cracking processes through space and time: an example from the eastern Italian Alps. Geomorphology 232, 248–260. https://doi.org/10.1016/j.geomorph.2015.01.009.

Smith, M.W., Riseborough, D.W., 2002. Climate and the limits of permafrost: a zonal analysis. Permafrost Periglac 13 (1), 1–15. https://doi.org/10.1002/ppp.410.

Steer, P., Huismans, R.S., Valla, P.G., Gac, S., Herman, F., 2012. Bimodal Plio–Quaternary glacial erosion of fjords and low-relief surfaces in Scandinavia. Nat. Geosci. 5 (9), 635–639. https://doi.org/10.1038/ngeo1549.

Støren, E.N., Dahl, S.O., Lie, Ø., 2008. Separation of late-Holocene episodic paraglacial events and glacier fluctuations in eastern Jotunheimen, central southern Norway. The Holocene 18 (8), 1179–1191. https://doi.org/10.1177/0959683608096593.

Stroeven, A.P., Hättestrand, C., Kleman, J., Heyman, J., Fabel, D., Fredin, O., Goodfellow, B.W., Harbor, J.M., Jansen, J.D., Olsen, L., Caffee, M.W., Fink, D., Lundqvist, J., Rosqvist, G.C., Strömberg, B., Jansson, K.N., 2016. Deglaciation of Fennoscandia. Quaternary Science Reviews 147, 91–121. https://doi.org/10.1016/j.quascirev.2015.09.016.

Stuart-Smith, R.F., Roe, G.H., Li, S., Allen, M.R., 2021. Increased outburst flood hazard from Lake Palcacocha due to human-induced climate change. Nat. Geosci. 14, 85–90. https://doi.org/10.1038/s41561-021-00686-4.

Vie, E.H., 2012. *Kvartærgeologisk kartlegging og rekonstruksjon av isavsmeltinga i Grødalen, Sunndalsfjella* [MSc thesis, University of Bergen].

Vlahou, I., Worster, M.G., 2010. Ice growth in a spherical cavity of a porous medium. J. Glaciol. 56 (196), 271–277. https://doi.org/10.3189/002214310791968494.

Walder, J., Hallet, B., 1985. A theoretical model of the fracture of rock during freezing. GSA Bull. 96 (3), 336–346. https://doi.org/10.1130/0016-7606(1985)96<336:ATMOTF>2.0.CO;2.

Walder, J.S., Hallet, B., 1986. The physical basis of frost weathering: toward a more fundamental and unified perspective. Arctic and Alpine Research 18 (1), 27–32. https://doi.org/10.2307/1551211.

III

APPENDIX

A. SUPPLEMENTARY FIGURES AND TABLES

Table A.1: Assumed mechanical and hydraulic properties of bedrock in Norway. k_0 - unfrozen hydraulic permeability, σ_c - uniaxial compressive strength, K_{IC} - fracture toughness, ΔT_c - undercooling for frost cracking.

Bedrock	k_0 $[\mathrm{m}^2]$	σ_c [MPa]	K_{IC} $[\mathrm{MPa\,m}^{1/2}]$	ΔT_c $[^\circ\mathrm{C}]$
Aluminium silicate gneiss	3×10^{-16}	121	1.57	5.52
Amphibole gneiss	3×10^{-16}	163	1.75	6.15
Amphibole schist	3×10^{-16}	123	1.58	5.55
Amphibolite	3×10^{-16}	123	1.58	5.55
Anorthosite	3×10^{-15}	125	1.59	5.58
Arkose	1×10^{-14}	175	1.80	6.33
Augengneiss	3×10^{-16}	161	1.74	6.12
Banded gneiss	3×10^{-16}	121	1.57	5.52
Calcareous mica schist	2×10^{-15}	116	1.55	5.44
Calcareous phyllite	2×10^{-15}	51	1.27	4.46
Chert	1×10^{-14}	110	1.52	5.35
Chlorite schist	3×10^{-16}	116	1.55	5.44
Claystone	1×10^{-14}	40	1.22	4.30
Conglomerate	1×10^{-14}	84	1.41	4.96
Diorite	3×10^{-15}	144	1.67	5.87
Dolomite	1×10^{-14}	110	1.52	5.35

Continued on next page

Bedrock	k_0 $[\mathbf{m}^2]$	σ **[MPa]**	K_{IC} $[\mathbf{MPa\,m}^{1/2}]$	ΔT_c [°**C**]
Dolomite marble	2×10^{-15}	66	1.33	4.69
Gabbro	3×10^{-15}	239	2.07	7.30
Garnet mica schist	2×10^{-15}	103	1.49	5.25
Granite	3×10^{-15}	162	1.74	6.14
Granitic gneiss	3×10^{-16}	121	1.57	5.52
Granodiorite	3×10^{-15}	106	1.50	5.29
Granodioritic gneiss	3×10^{-16}	121	1.57	5.52
Graphite schist	2×10^{-15}	40	1.22	4.30
Greenschist	3×10^{-16}	76	1.38	4.84
Greenstone	3×10^{-16}	79	1.39	4.89
Greywacke	1×10^{-14}	120	1.56	5.50
Marble	2×10^{-15}	66	1.33	4.69
Meta-arkose	2×10^{-15}	148	1.68	5.93
Metagabbro	3×10^{-16}	163	1.75	6.15
Metagreywacke	2×10^{-15}	148	1.68	5.93
Metasandstone	2×10^{-15}	148	1.68	5.93
Mica gneiss	3×10^{-16}	78	1.38	4.87
Mica schist	2×10^{-15}	116	1.55	5.44
Monzodiorite	3×10^{-15}	145	1.67	5.88
Monzonite	3×10^{-15}	145	1.67	5.88
Norite	3×10^{-15}	242	2.09	7.34
Orthopyroxene gneiss	3×10^{-16}	121	1.57	5.52
Peridotite	3×10^{-15}	109	1.52	5.34
Phyllite	2×10^{-15}	51	1.27	4.46
Quartz arenite	1×10^{-14}	121	1.57	5.52
Quartz schist	2×10^{-15}	116	1.55	5.44
Quartzite	2×10^{-15}	148	1.68	5.93
Rhyolite	1×10^{-14}	167	1.76	6.21
Sandstone	1×10^{-14}	122	1.57	5.53

Continued on next page

Bedrock	$k_0\left[\mathbf{m}^2\right]$	σ **[MPa]**	$K_{IC}\left[\mathbf{MPa\,m}^{1/2}\right]$	ΔT_c **[°C]**
Shale	2×10^{-15}	51	1.27	4.46
Siltstone	1×10^{-14}	122	1.57	5.53
Tonalitic gneiss	3×10^{-16}	121	1.57	5.52
Trondhjemite	3×10^{-15}	106	1.50	5.29
Tuffite	1×10^{-14}	51	1.27	4.46
Volcanic breccia	1×10^{-14}	80	1.39	4.90

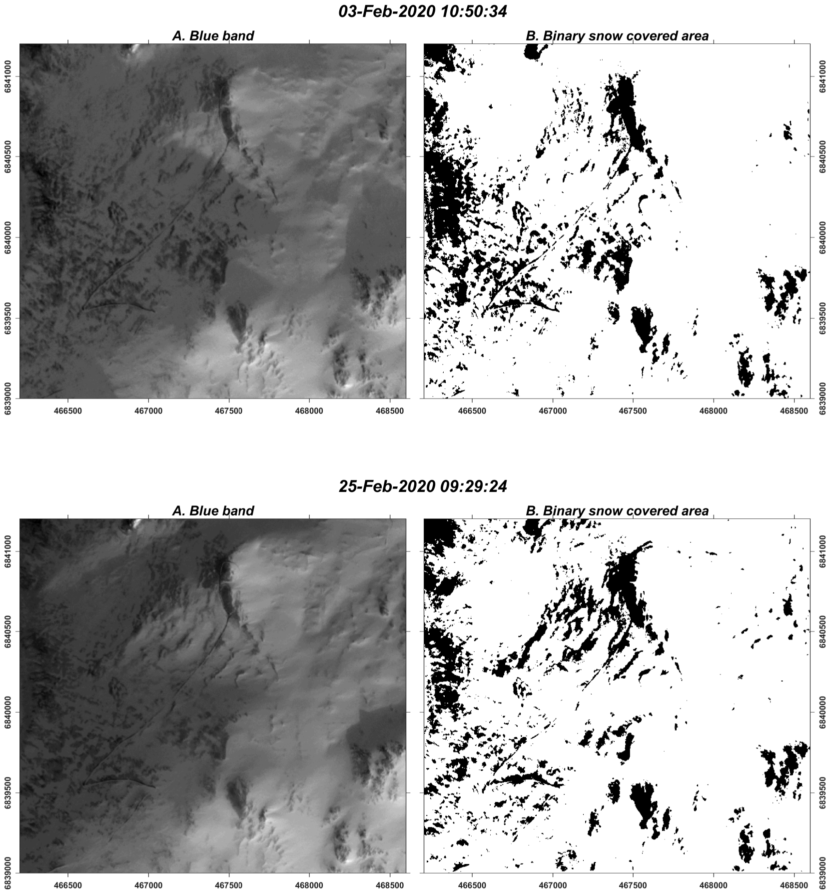

Figure A.1: Examples of snow classification. Satellite image courtesy of Planet Labs, Inc.

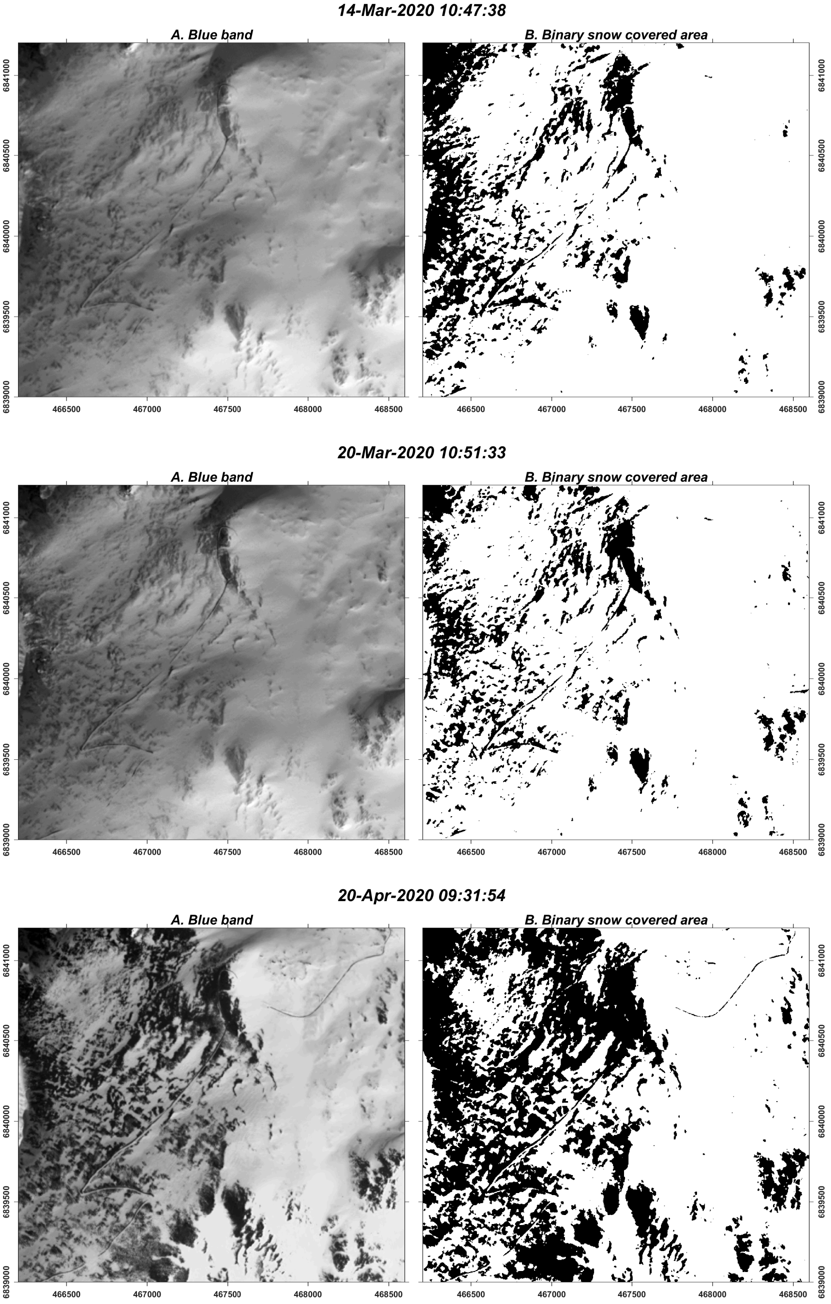

Figure A.2: Examples of snow classification. Satellite image courtesy of Planet Labs, Inc.

26-Apr-2020 09:25:30

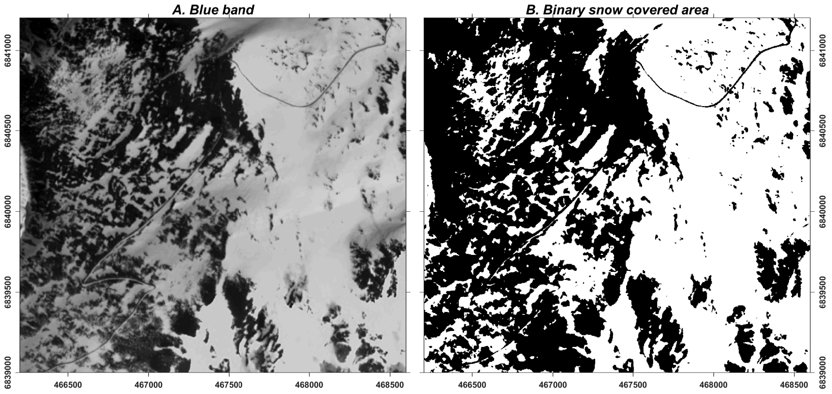

25-May-2020 10:49:38

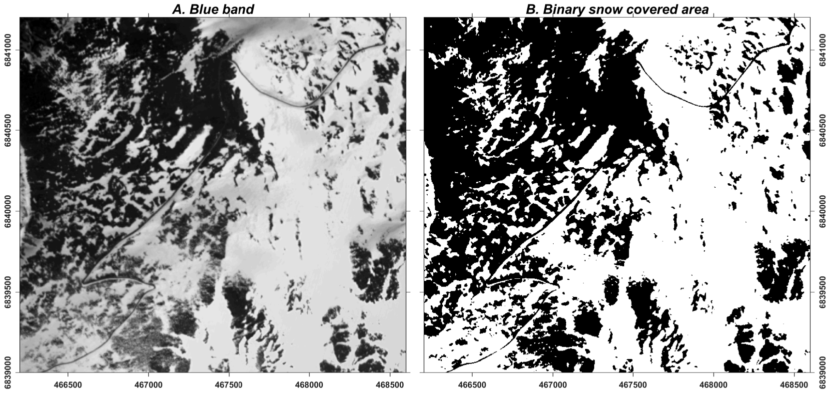

31-May-2020 07:23:19

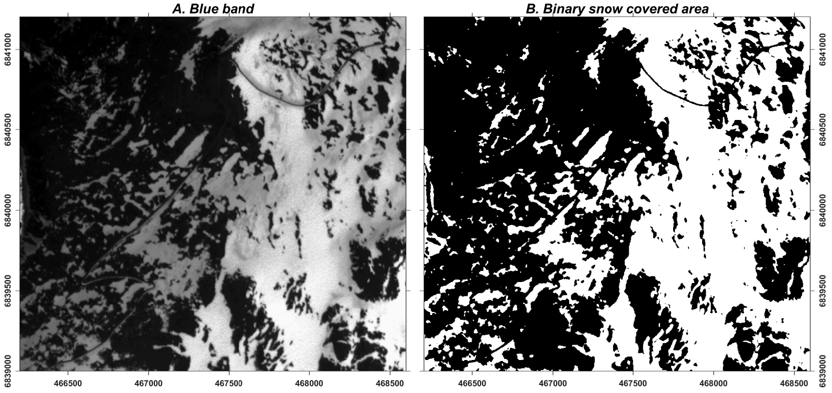

Figure A.3: Examples of snow classification. Satellite image courtesy of Planet Labs, Inc.

09-Jun-2020 07:18:18

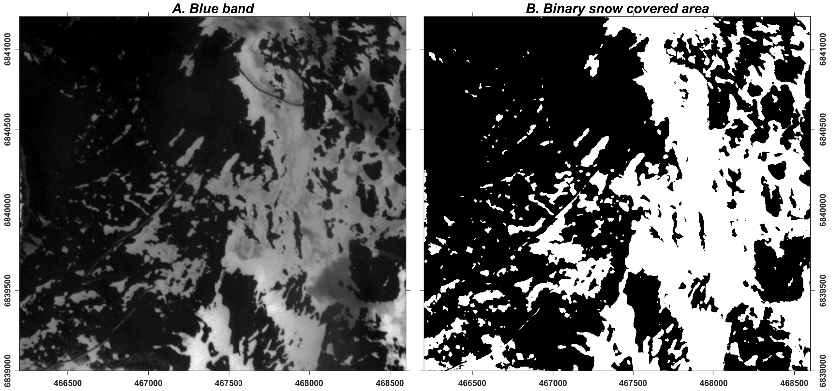

14-Jun-2020 09:27:31

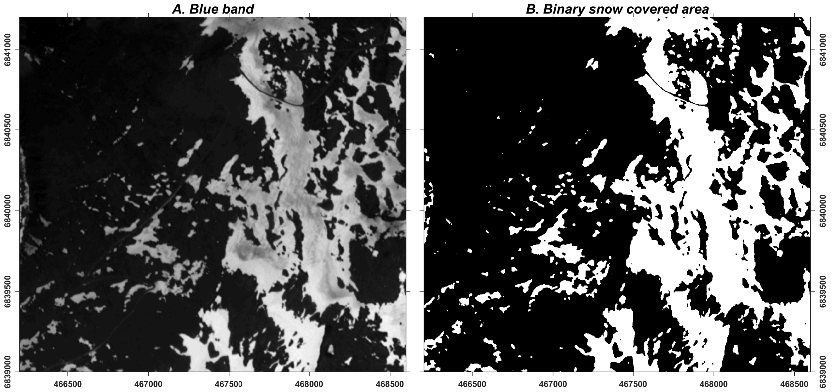

18-Jun-2020 10:25:21

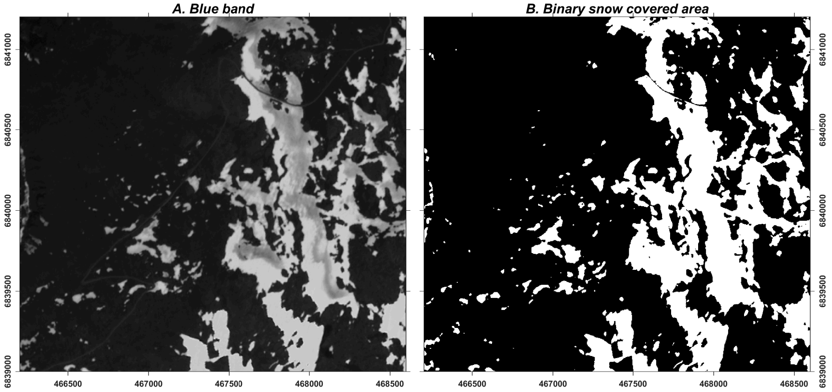

Figure A.4: Examples of snow classification. Satellite image courtesy of Planet Labs, Inc.

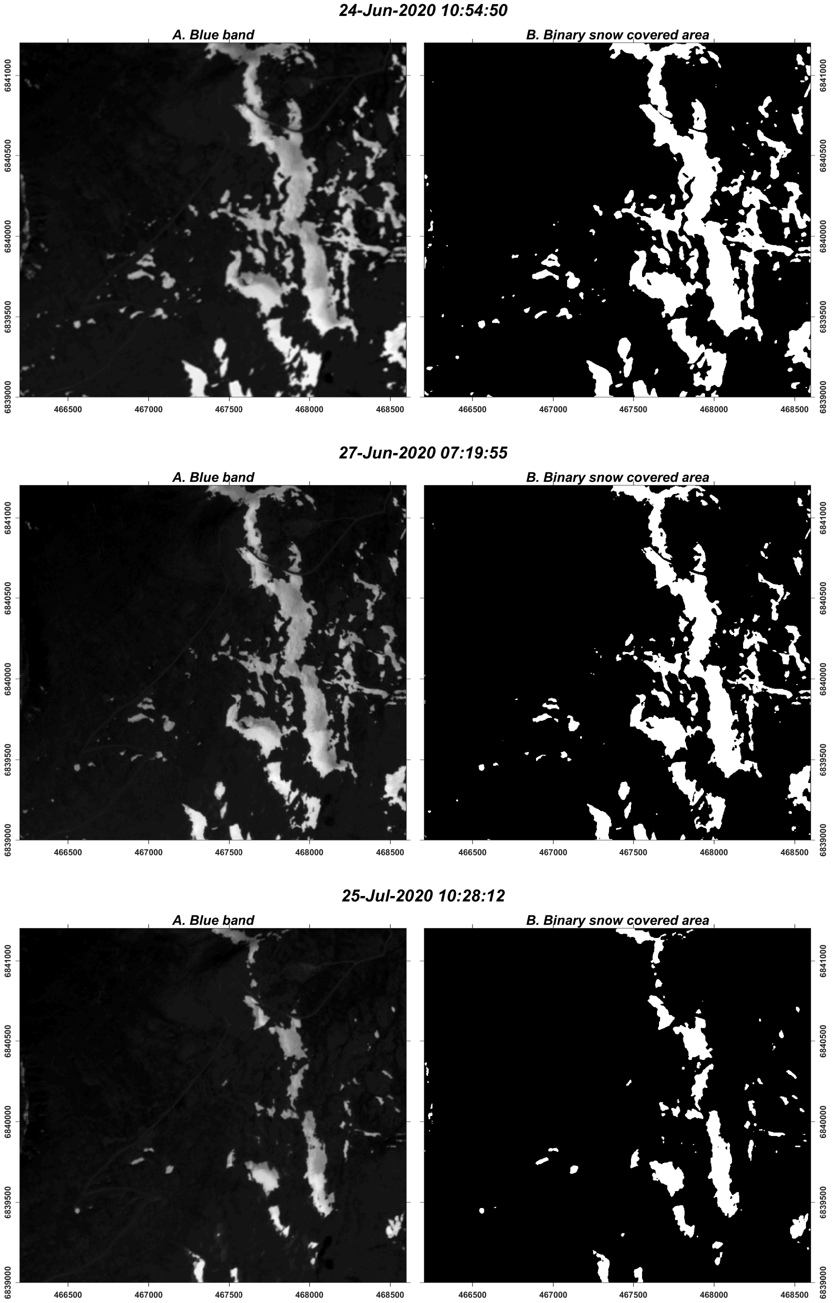

Figure A.5: Examples of snow classification. Satellite image courtesy of Planet Labs, Inc.

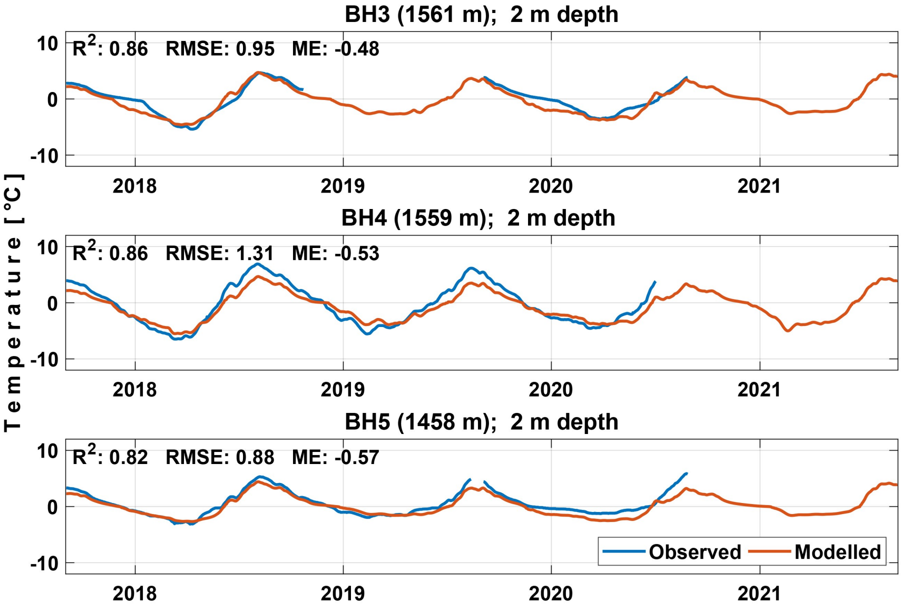

Figure A.6: Modelled and observed *GT* for the boreholes in Juvflye, the Jotunheimen Mountains.

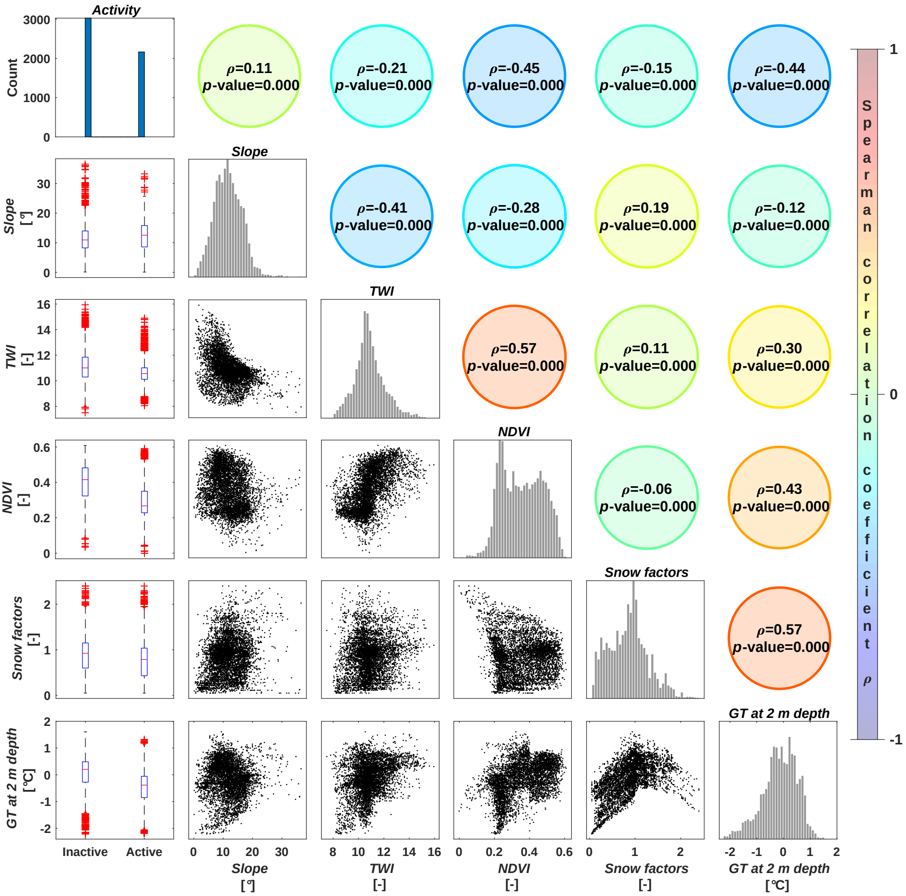

Figure A.7: Activity and environmental variables. **First column:** Boxplots with the distribution of values for active and inactive areas. **Diagonal:** Distribution of data for a given variable. **Lower triangular:** Scatter plots with the relationship between the variables. **Upper triangular:** Spearman rank-order correlation ρ and their p-values.

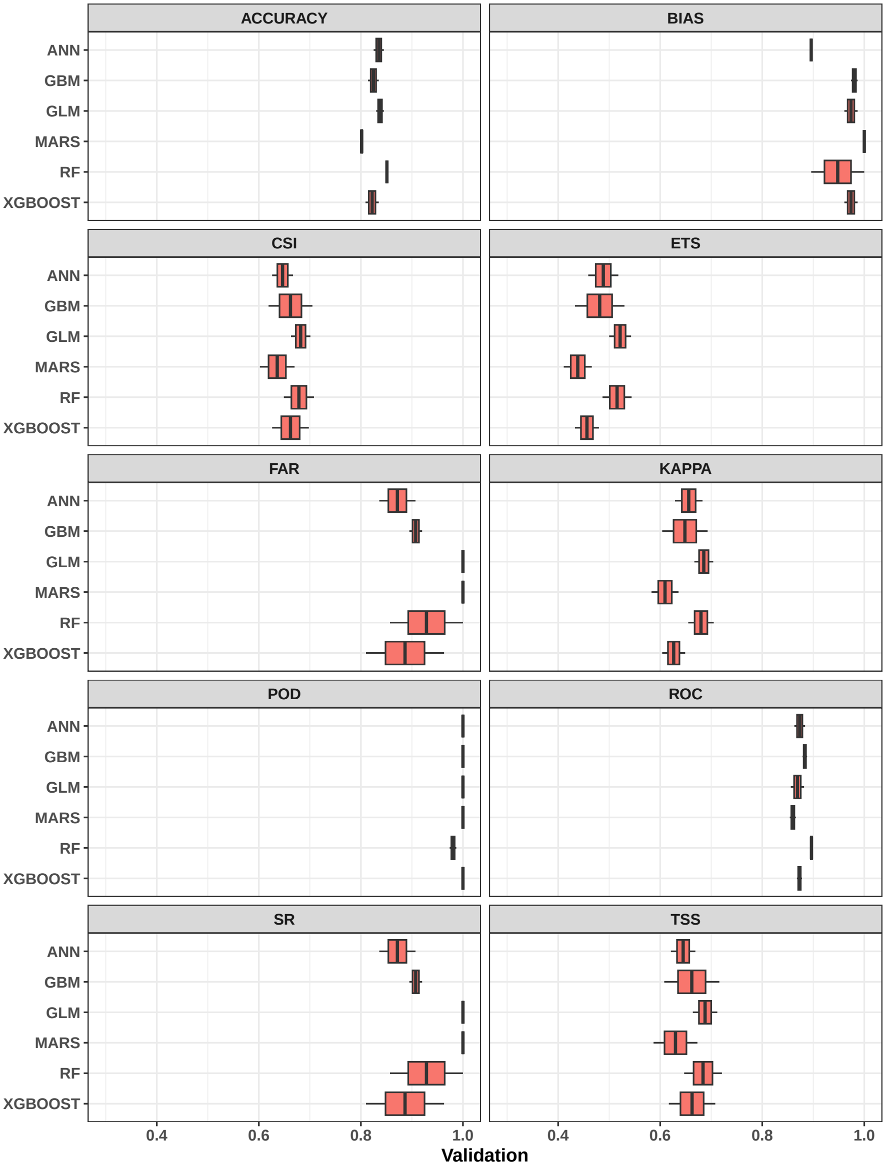

Figure A.8: Model performance for ANN - Artificial Neutral Networks, GBM - Generalised Boosted Regression, GLM - Generalised Linear Model, MARS - Multivariate Adaptive Regression Splines, RF - Random Forest and XGBoost - eXtreme Gradient Boosting. Evaluation metrics: ACCURACY - Accuracy (fraction correct), BIAS - Bias score (frequency bias), CSI - Critical success index (threat score), ETS - Equitable threat score (Gilbert skill score), FAR - False alarm ratio, KAPPA - Cohen's Kappa (Heidke skill score), POD - Probability of detection (hit rate), ROC - Relative Operating Characteristic, SR - Success ratio and TSS - True kill statistic (Hanssen and Kuipers discriminant, Peirce's skill score). Evaluation scores for the validation data set are shown.

B. PUBLICATIONS

B.1 PEER-REVIEWED JOURNAL PUBLICATIONS

Czekirda, J., Westermann, S., Etzelmüller, B., and Jóhannesson, T. (2019). Transient Modelling of Permafrost Distribution in Iceland. *Frontiers in Earth Science*, 7. doi: 10.3389/feart.2019.00130

Etzelmüller, B., Patton, H., Schomacker, A., **Czekirda, J.**, Girod, L., Hubbard, A., Lilleøren, K. S., and Westermann, S. (2020). Icelandic permafrost dynamics since the Last Glacial Maximum–model results and geomorphological implications. *Quaternary Science Reviews*, 233. doi: 10.1016/j.quascirev.2020.106236

Hilger, P., Hermanns, R. L., **Czekirda, J.**, Myhra, K. S., Gosse, J. C., and Etzelmüller, B. (2021). Permafrost as a first order control on long-term rock-slope deformation in (Sub-)Arctic Norway. *Quaternary Science Reviews*, 251. doi: 10.1016/j.quascirev.2020.106718

Kristensen, L., **Czekirda, J.**, Penna, I., Etzelmüller, B., Nicolet, P., Pullarello, J. S., Blikra, L. H., Skrede, I., Oldani, S., and Abellan, A. (2021). Movements, failure and climatic control of the Veslemannen rockslide, Western Norway. *Landslides*, 18, 1963–1980. doi: 10.1007/s10346-020-01609-x

Etzelmüller, B., **Czekirda, J.**, Magnin, F., Duvillard, P. A., Ravanel, L., Malet, E., Aspaas, A., Kristensen, L., Skrede, I., Majala, G. D., Jacobs, B., Leinauer, J., Hauck, C., Hilbich, C., Böhme, M., Hermanns, R., Eriksen, H. Ø., Lauknes, T. R., Krautblatter, M., and Westermann, S. (2022). Permafrost in monitored unstable rock slopes in Norway

– new insights from temperature and surface velocity measurements, geophysical surveying, and ground temperature modelling. *Earth Surface Dynamics*, 10, 97–129. doi: 10.5194/esurf-10-97-2022

Czekirda, J., Etzelmüller, B., Westermann, S., Isaksen, K., and Magnin, F. (2023). Post-Little Ice Age rock wall permafrost evolution in Norway. *The Cryosphere*, 17, 2725–2754. doi: 10.5194/tc-17-2725-2023

Etzelmüller, B., Isaksen, K., **Czekirda, J.**, Westermann, S., Hilbich, C., and Hauck, C. (2023). Rapid warming and degradation of mountain permafrost in Norway and Iceland. *The Cryosphere*, 17, 5477–5497. doi: 10.5194/tc-17-5477-2023

Czekirda, J., Rempel, A. W., Etzelmüller, B., and Westermann, S. (2024). Spatiotemporal variations in frost cracking measures in two dimensions: A case study for rock walls in Jotunheimen, southern Norway. *Geomorphology*, 453, 109112. doi: 10.1016/j.geomorph.2024.109112

B.2 CONFERENCE PUBLICATIONS

Czekirda, J., Westermann, S., and Etzelmüller, B. (2019). The CryoGrid permafrost models: examples of applications. The CSDMS 2019 annual meeting: CSDMS 3.0 - Bridging Boundaries, 21–23rd May 2019, Boulder, Colorado, USA. Poster, Presenting author J. Czekirda.

Czekirda, J., Westermann, S., and Etzelmüller, B. (2019). 2D thermal modelling of unstable rock walls in Norway: Examples from Mannen and Gámanjunni 3. The 1st Southern Hemisphere Conference on Permafrost, 4–14th December 2019, Queenstown, New Zealand. Oral presentation, Presenting author J. Czekirda.

Czekirda, J., Westermann, S., and Etzelmüller, B. (2020). 2D thermal modelling of unstable rock walls in Norway: Examples from Mannen and Gámanjunni 3. The 34th Nordic Geological Winter Meeting, 8–10th January 2020, Oslo, Norway. Oral presentation, Presenting author J. Czekirda.

Czekirda, J., Etzelmüller, B., Westermann, S., Isaksen, K., and Magnin, F. (2022). Modelling of rock wall permafrost development in Norway post the Little Ice Age. The 35th Nordic Geological Winter Meeting, 11–13th May 2022, Reykjavík, Iceland. Oral presentation, Presenting author J. Czekirda.

Czekirda, J., Etzelmüller, B., Westermann, S., Isaksen, K., and Magnin, F. (2022). Spatio-temporal variations in rock wall temperature in Norway post the Little Ice Age. The EGU General Assembly, 23–27th May 2022, Vienna, Austria and Online. Oral presentation, Presenting author J. Czekirda.

Czekirda, J., Etzelmüller, B., Rempel, A. W., and Westermann, S. (2022). 2D-frost weathering indices for rock walls. The 10th International Conference on Geomorphology (10th ICG), 12–16th September 2022, Coimbra, Portugal. Oral presentation, Presenting author J. Czekirda.

Czekirda, J., Rempel, A. W., Etzelmüller, B., and Westermann, S. (2023). Relative frost damage index applied to periglacial rock walls in two dimensions. The 6th European Conference on Permafrost (EUCOP 2023), 18–22nd June 2023, Puigcerdà, Spain. Poster, Presenting author J. Czekirda.